Adıyaman University
Journal of Science

Dec. 2022

Volume: 12 Issue: 2

An international peer reviewed journal of science

PHYSIC
SCIENCE
BIOLOGY
MATHEMATICS
CHEMISTRY

ADYU J SCI

ISSN 2147-1630
e-ISSN 2146-586X

An open access, peer reviewed, international journal of science. Biannual (June & December). ISSN 2147-1630 | e-ISSN 2146-586X. Publisher: Adıyaman University.

Publication language: English (with Turkish title and abstract)

Issue published date: 30.12.2022

Privilege owner: On Behalf of Rectorate of Adıyaman University, Prof. Dr. Mehmet TURGUT (Rector)

Web site: EN: https://dergipark.org.tr/en/pub/adyujsci
TR: https://dergipark.org.tr/tr/pub/adyujsci

Table of Contents (İçindekiler)

Volume (Cilt): 12 Number (Sayı): 2
December (Aralık) 2022

BIOLOGY

CHEMISTRY

MATHEMATICS

PHYSICS

Electrochemical Properties of Low Bi Doped $La_{0.60}Dy_{0.10}Sr_{0.30}Mn_{(1-x)}Bi_xO_3$ Perovskite Materials
Düşük Bi Katkılı Manyetikalorik $La_{0.60}Dy_{0.10}Sr_{0.30}Mn_{(1-x)}Bi_xO_3$ Perovskite Malzemelerin Elektrokimyasal Özellikleri

Mustafa Zeki KURT

315-323

Adıyaman University Journal of Science
https://dergipark.org.tr/en/pub/adyujsci
DergiPark AKADEMİK
ISSN 2147-1630
e-ISSN 2146-586X

Wave Solution Analysis of a Nonlinear Mathematical Model on Fluid Mechanics

Tolga AKTÜRK[1], Volkan ÇAKMAK[2,*]

[1]*Ordu University Faculty of Education, Department of Mathematics and Science Education, Cumhuriyet Campus,52200, Ordu, Türkiye*
tolgaakturk@odu.edu.tr, ORCID: 0000-0002-8873-0424
[2]*Ordu University Faculty of Education, Department of Mathematics and Science Education, Cumhuriyet Campus,52200, Ordu, Türkiye*
volkancakmak_@hotmail.com, ORCID: 0000-0002-3262-9327

Received: 09.05.2022 **Accepted:** 08.09.2022 **Published:** 30.12.2022

Abstract

This study obtains some wave solutions of the B-type Kadomtsev Petviashvili equation by applying the modified exponential function method (MEFM). Thanks to this method, the exact solutions of the non-linear partial differential equations will be obtained and there will be an opportunity to examine the physical structure of these solutions. Due to the nature of MEFM, two different cases are presented here that have been analyzed to obtain more solutions in this structure. More wave solutions can be obtained by analyzing different situations. When the resulting solutions are analyzed, hyperbolic, trigonometric, and rational functions are observed. It has been checked whether the solution functions found with Wolfram Mathematica software provide the B type Kadomtsev Petviashvili equation and graphs simulating the wave solution behavior with the determined appropriate parameters are presented.

Keywords: Modified Exponential Function Method (MEFM); B-type Kadomtsev Petviashvili Equation; Wave Solutions.

* Corresponding Author DOI: 10.37094/adyujsci.1114265

Akışkanlar Mekaniği Üzerine Doğrusal Olmayan Bir Matematiksel Modelin Dalga Çözümü Analizi

Öz

Bu çalışmada, modifiye edilmiş üstel fonksiyon metodu uygulanarak B tipi Kadomtsev Petviashvili denkleminin bazı dalga çözümleri elde edilmiştir. Modifiye edilmiş üstel fonksiyon yönteminin doğası gereği, bu yapıdaki çözümlerden daha fazla elde etmek için incelenilmiş olan iki farklı durum burada sunulmuştur. Farklı durumlar da incelenerek daha fazla dalga çözümü elde edilebilir. Ortaya çıkan çözümler analiz edildiğinde hiperbolik, trigonometrik ve rasyonel fonksiyonlar gözlemlenmiştir. Wolfram Mathematica yazılımı ile bulunan çözüm fonksiyonlarının B tipi Kadomtsev Petviashvili denklemini sağlayıp sağlamadığı kontrol edilmiş ve belirlenen uygun parametrelerle dalga çözümünün üç boyutlu kontur, yoğunluk ve iki boyutlu grafiklerin analizi sunulmuştur.

Anahtar Kelimeler: Geliştirilmiş Üstel Fonksiyon Metodu (GÜFM); B tipi Kadomtsev Petviashvili; Dalga Çözümleri.

1. Introduction

All events encountered in natural and applied sciences such as physics, engineering, health, etc., are represented by mathematical models. These models are generally stated in nonlinear partial differential equations (NPDE). Therefore, it is important to obtain the solutions to such equations. There are various methods to investigate the solutions of such equations in scientific studies in the literature. Some of these methods are the modified extended tanh-function method [1], the generalized tanh function method [2], the trial equation method [3-5], the generalized Bernoulli sub-equation function method [6-8], the first integral method [9], the quintic B-spline collocation method [10-12], the modified exponential function method (MEFM) [13-17],

In this paper, the B type Kadomtsev Petviashvili equation [18-24] which marine scientists are using for oceanic investigation is considered as follows,

$$u_{xxxy} + a(u_x u_y)_x + (u_x + u_y + u_z)_t - (u_{xx} + u_{zz}) = 0, \tag{1}$$

where a is a real non-zero parameter. A mathematical model given as Eqn. (1) is encountered in fluid mechanics, a branch of physics [18-29].

In the second part of this study, method is introduced and detailed information is given about the steps of the process. NPDEs have been reduced to nonlinear ordinary differential equations (NODEs) to implement this method. In the third chapter, the solutions obtained by applying the determined method B type Kadomtsev Petviashvili Equation graphs simulating of

these results are presented for two cases. In the conclusion part of the study, the obtained results are given.

2. Modified Exponential Function Method (MEFM)

In this section, the general form of the nonlinear mathematical model is as follows;

$$P\left(U,U_x,U_y,U_z,U_t,U_{xx},U_{xt},U_{yy},U_{xxz},\cdots\right)=0, \tag{2}$$

where $U=U(x,y,z,t)$ is the function that is thought to provide the nonlinear mathematical model.

Step 1. Taking the independent variables given in Eqn. (1) into consideration, the wave transformation given below is considered,

$$U(x,y,z,t)=U(\xi),\ \xi=k\left(x+y+z-ct\right), \tag{3}$$

c represents the frequency of the wave, and k the height of the wave. If the necessary derivative terms in Eqn. (2) are arranged according to Eqn. (1) are obtained by using wave Eqn. (3) and written instead,

$$N\left(U,U',\left(U'\right)^2,U'',U''',\cdots\right)=0. \tag{4}$$

Step 2: According to MEFM, the default solution function of Eqn. (1) is as follows;

$$U\left(\xi\right)=\frac{\sum_{i=0}^{n}A_i\left[\exp\left(-\Omega\left(\xi\right)\right)\right]^i}{\sum_{j=0}^{m}B_j\left[\exp\left(-\Omega\left(\xi\right)\right)\right]^j}=\frac{A_0+A_1\exp\left(-\Omega\right)+\cdots+A_n\exp\left(n\left(-\Omega\right)\right)}{B_0+B_1\exp\left(-\Omega\right)+\cdots+B_m\exp\left(m\left(-\Omega\right)\right)}, \tag{5}$$

where $A_i,B_j,\left(0\le i\le n,0\le j\le m\right)$ are constants. The balance procedure determines the relationship between m and n, which are the upper bounds of the sum symbols in the method's solution Eqn. (5). By applying the balance procedure to Eqn. (4), the relationship between the constants m and n, which ensures the equivalence of the term containing the highest order derivative and the nonlinear term, is determined, and the general structure of the solution function is formed by giving values to these constants.

$$\Omega'\left(\xi\right)=\exp\left(-\Omega\left(\xi\right)\right)+\mu\exp\left(\Omega\left(\xi\right)\right)+\lambda, \tag{6}$$

when the Eqn. (6) is solved, the following families are obtained by He et al [13]:

Condition 1: If $\mu\neq0,\ \lambda^2-4\mu>0,$

$$\Omega\left(\xi\right)=\ln\left(\frac{-\sqrt{\lambda^2-4\mu}}{2\mu}\tanh\left(\frac{\sqrt{\lambda^2-4\mu}}{2}\left(\xi+E\right)\right)-\frac{\lambda}{2\mu}\right). \tag{7}$$

Condition 2: If $\mu \neq 0,\ \lambda^2 - 4\mu < 0,$

$$\Omega(\xi) = \ln\left(\frac{\sqrt{-\lambda^2 + 4\mu}}{2\mu} \tan\left(\frac{\sqrt{-\lambda^2 + 4\mu}}{2}(\xi + E) \right) - \frac{\lambda}{2\mu} \right). \tag{8}$$

Condition 3: If $\mu = 0,\ \lambda \neq 0$ and $\lambda^2 - 4\mu > 0,$

$$\Omega(\xi) = -\ln\left(\frac{\lambda}{\exp(\lambda(\xi + E)) - 1} \right). \tag{9}$$

Condition 4: If $\mu \neq 0,\ \lambda \neq 0$ and $\lambda^2 - 4\mu = 0,$

$$\Omega(\xi) = \ln\left(-\frac{2\lambda(\xi + E) + 4}{\lambda^2(\xi + E)} \right). \tag{10}$$

Condition 5: If $\mu = 0,\ \lambda = 0$ and $\lambda^2 - 4\mu = 0,$

$$\Omega(\xi) = \ln(\xi + E). \tag{11}$$

Step 3: After Eqn. (6) is solved, when Eqn. (5) is written in its place, an algebraic equation system consisting of coefficients is obtained. After this system of equations is solved with the Mathematica program, the relations between the coefficients of the solution function satisfying the Eqn. (4) are obtained. Therefore, the solution obtained in each case is checked and the traveling wave solution satisfying Eqn. (1) is found.

3. Application

When Eqn. (3) is applied to Eqn. (1) and after one integration with respect to ξ, the following nonlinear ordinary differential equation is get,

$$k^2 U''' + ak\left(U'\right)^2 - (3c + 2)U' = 0. \tag{12}$$

If $U' = V$ is Eqn. (12),

$$k^2 V'' + akV^2 - (3c + 2)V = 0. \tag{13}$$

If the balance procedure is applied between the terms V'' and V^2 in Eqn. (13),

$$M+2=N. \tag{14}$$

If $M=1$ then $N=3$ is obtained from the Eqn. (14). Thus, the upper limits of the sum symbols in the sought solution function in Eqn. (5) are determined. Accordingly, the terms required in the Eqn. (15) are given.

$$\begin{aligned} V(\xi)&=\frac{\psi}{\varphi}=\frac{A_0+A_1e^{-\Omega(\xi)}+A_2e^{-2\Omega(\xi)}+A_3e^{-3\Omega(\xi)}}{B_0+B_1e^{-\Omega(\xi)}},\\ V'(\xi)&=\frac{\psi'\varphi-\psi\varphi'}{\varphi^2},\\ V''(\xi)&=\frac{\psi''\varphi^3-\varphi^2\psi'\varphi'-(\psi\varphi''+\psi'\varphi')\varphi^2+2(\psi')^2\psi\varphi}{\varphi^4}. \end{aligned} \tag{15}$$

Case 1:

$$A_0=-\frac{6B_0k\mu}{a},\ A_1=-\frac{6k(B_0\lambda+B_1\mu)}{a},\ A_2=-\frac{6k(B_1\lambda+B_0)}{a},\ A_3=-\frac{6B_1k}{a},$$

$$c=\frac{1}{3}\left(k^2(\lambda^2-4\mu)-2\right).$$

By using these coefficients, solutions of the mathematical model are presented and analyzed by considering the previously mentioned family cases.

Family 1:

$$V_{1,1}(\xi)=\frac{6k\mu(\lambda^2-4\mu)}{a\left(\sqrt{\lambda^2-4\mu}\sinh\left(\frac{1}{2}\phi\right)+\lambda\cosh\left(\frac{1}{2}\phi\right)\right)^2}, \tag{16}$$

where $\left(\phi=\sqrt{\lambda^2-4\mu}\,(E+\xi)\right)$. Integrating Eqn. (16) with respect to ξ,

$$U_{1,1}(\xi)=\frac{3k\left(2\mu\sqrt{\lambda^2-4\mu}\sinh\left((\mathrm{E}+\xi)\sqrt{\lambda^2-4\mu}\right)+\lambda^3-4\lambda\mu\right)}{a\left(2\mu\cosh\left((\mathrm{E}+\xi)\sqrt{\lambda^2-4\mu}\right)+\lambda^2-2\mu\right)}, \tag{17}$$

is obtained.

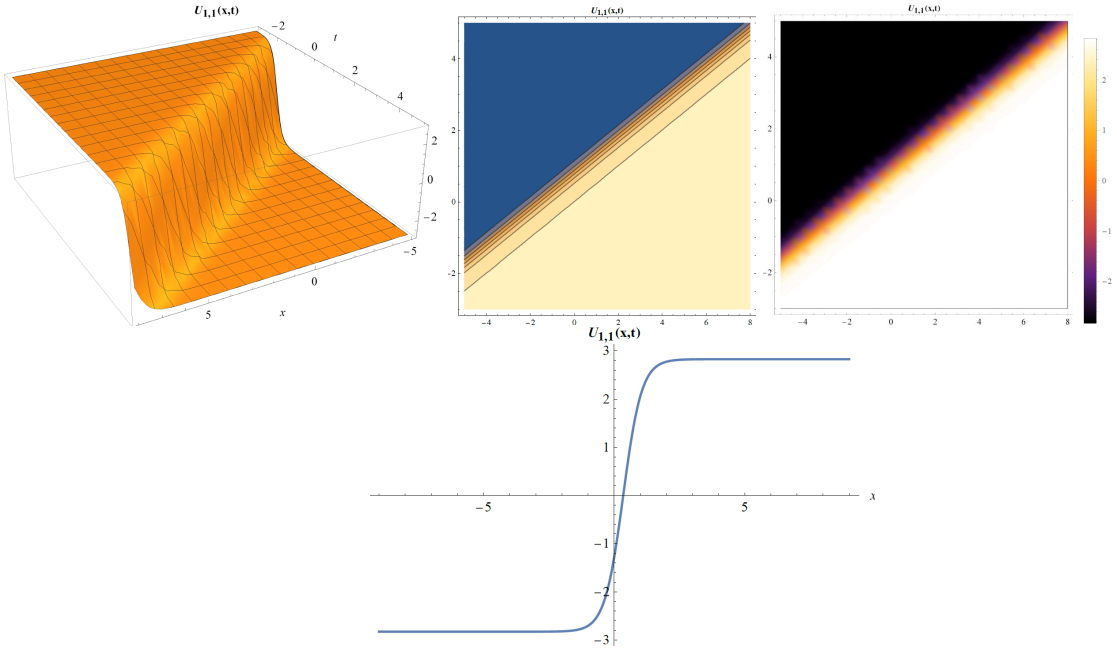

Figure 1: Graphs simulating the behavior of Eqn. (17) for the values $a=3$, $c=2$, $\mathrm{E}=0.82$, $k=1$, $\lambda=2\sqrt{3}$, $\mu=1$, $y=0.01, z=0.01$ and two-dimensional graph for $t=1$

Family 2:

$$V_{1,2}(\xi)=\frac{6k\mu\left(\lambda^2-4\mu\right)}{a\left(\lambda\cos\left(\frac{1}{2}\phi\right)-\sqrt{4\mu-\lambda^2}\sin\left(\frac{1}{2}\phi\right)\right)^2}, \tag{18}$$

where $\left(\phi=\sqrt{-\lambda^2+4\mu}\left(E+\xi\right)\right)$. Integrating Eqn. (18) with respect to ξ,

$$U_{1,2}(\xi)=\frac{3k\left(-2\mu\sqrt{4\mu-\lambda^2}\sin\left((\mathrm{E}+\xi)\sqrt{4\mu-\lambda^2}\right)+\lambda^3-4\lambda\mu\right)}{a\left(2\mu\cos\left((\mathrm{E}+\xi)\sqrt{4\mu-\lambda^2}\right)+\lambda^2-2\mu\right)}, \tag{19}$$

is obtained.

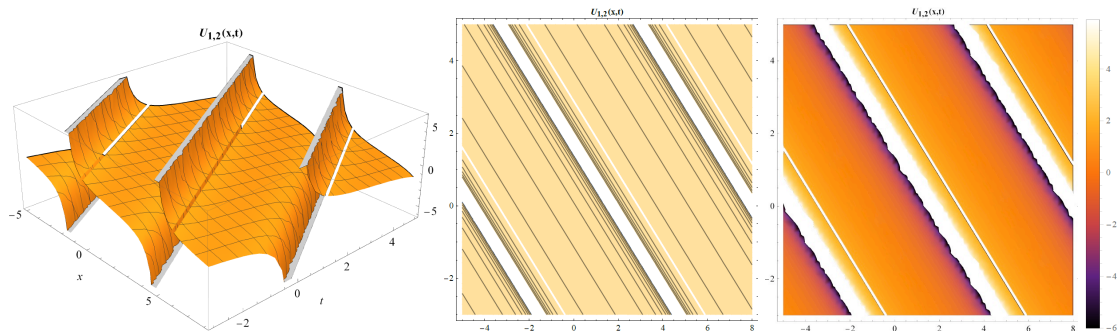

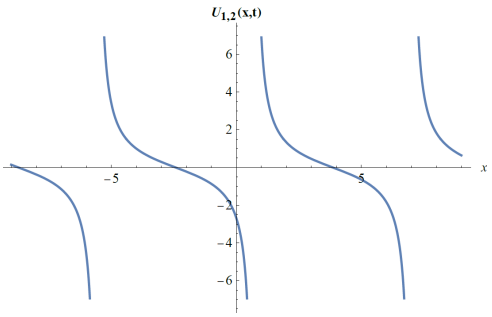

Figure 2: Graphs simulating the behavior of Eqn. (19) for the values $a=3$, $c=-1$, $\mathrm{E}=0.82$, $k=1$, $\lambda=\sqrt{11}$, $\mu=3$, $y=0.01$, $z=0.01$,and two-dimensional graph for $t=1$

Family 3:

$$V_{1,3}(\xi)=\frac{3k\lambda^2}{a-a\cosh(\lambda(\mathrm{E}+\xi))}. \tag{20}$$

Integrating Eqn. (20) with respect to ξ,

$$U_{1,3}(\xi)=\frac{3k\lambda\coth\left(\frac{1}{2}\lambda(\mathrm{E}+\xi)\right)}{a}. \tag{21}$$

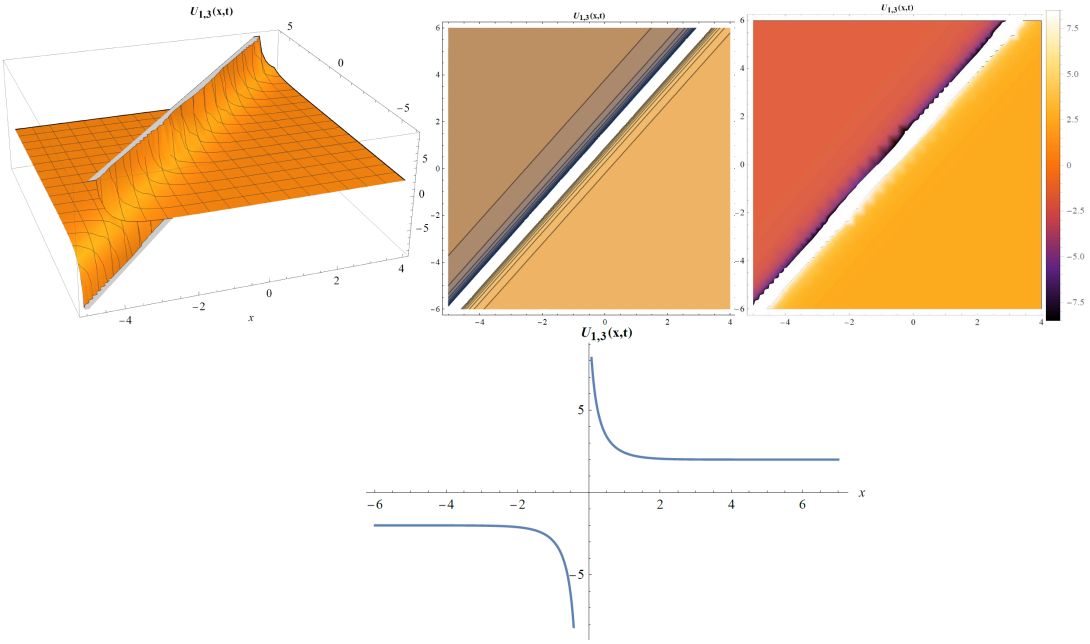

Figure 3: Graphs simulating the behavior of Eqn. (21) for the values $a=3$, $c=0.\overline{6}$, $\mathrm{E}=0.82$, $k=1$, $\lambda=2$, $\mu=0$, $y=0.01$, $z=0.01$ and two-dimensional graph for $t=1$

Family 4:

$$V_{1,4}(\xi)=\frac{3k\left(\lambda^2\left(1-\frac{4}{(\lambda(\mathrm{E}+\xi)+2)^2}\right)-4\mu\right)}{2a}. \tag{22}$$

Integrating Eqn. (22) with respect to ξ,

$$U_{1,4}(\xi)=\frac{3k\left(\lambda(\lambda(\mathrm{E}+\xi)+2)+\frac{4\lambda}{\lambda(\mathrm{E}+\xi)+2}-4\mu\xi\right)}{2a}. \tag{23}$$

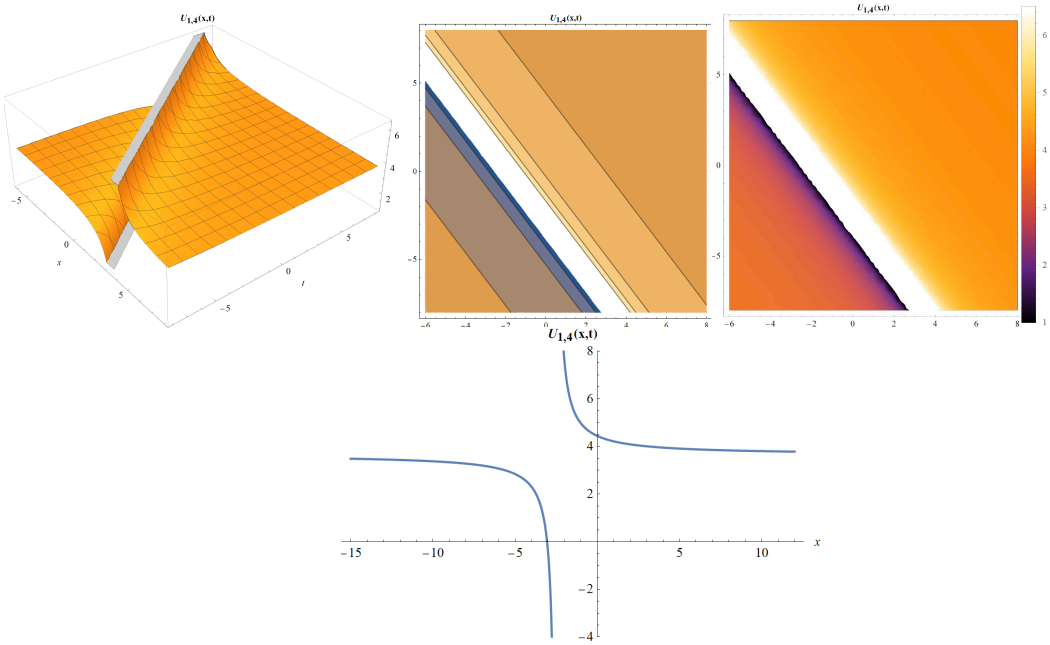

Figure 4: Graphs simulating the behavior of Eqn. (23) for the values $a=3$, $c=-0.\overline{6}$, $\mathrm{E}=0.82$, $\lambda=2$, $k=1$, $\mu=1$, $y=0.01$, $z=0.01$ and two-dimensional graph for $t=1$

Family 5:

$$V_{1,5}(\xi)=-\frac{6k}{a(\mathrm{E}+\xi)^2}. \tag{24}$$

Integrating Eqn. (24) with respect to ξ,

$$U_{1,5}(\xi)=\frac{6k}{a(\mathrm{E}+\xi)}, \tag{25}$$

is obtained.

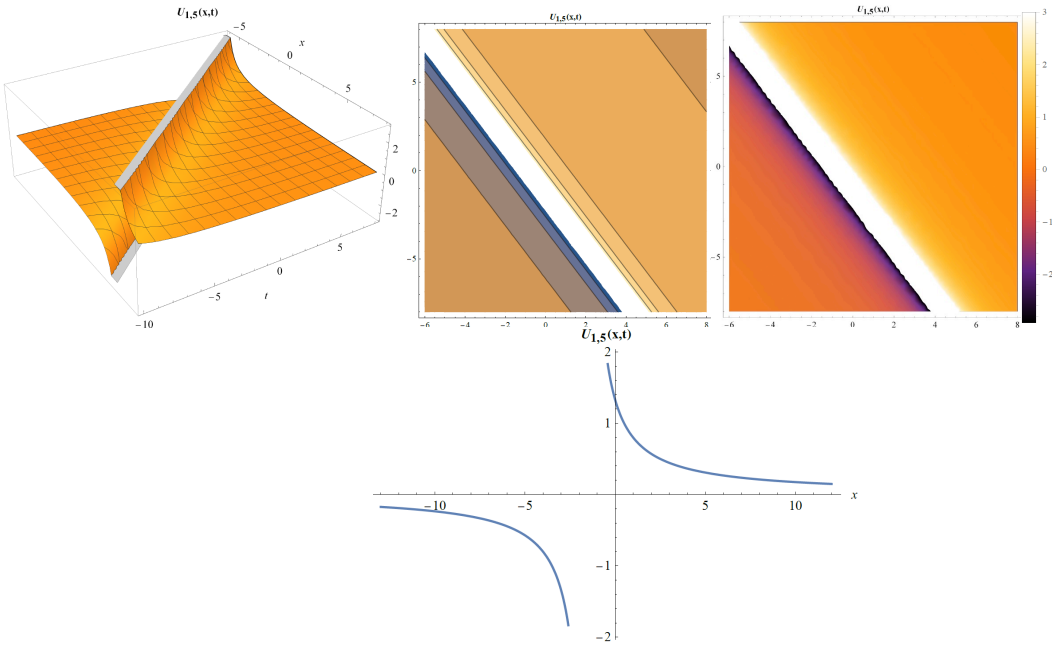

Figure 5: Graphs simulating the behavior of Eqn. (25) for the values $a=3$, $c=-0.\overline{6}$, $\mathrm{E}=0.82$, $\lambda=0$, $k=1$, $\mu=0$, $y=0.01$, $z=0.01$ and two-dimensional graph for $t=1$

Case 2:

$$A_0=-\frac{B_0\left(3c+3k^2\lambda^2+2\right)}{2ak},\ A_1=-\frac{B_1\left(3c+3k^2\lambda^2+2\right)}{2ak}-\frac{6B_0k\lambda}{a},$$

$$A_2=-\frac{6k\left(B_1\lambda+B_0\right)}{a},\ A_3=-\frac{6B_1k}{a},\quad \mu=\frac{3c+k^2\lambda^2+2}{4k^2}.$$

By using these coefficients, the traveling wave solutions of the nonlinear differential equation are presented and analyzed by considering the previously mentioned family cases.

Family 1:

$$V_{2,1}(\xi)=-\frac{3c+\dfrac{3k^2\left(\lambda\sqrt{\lambda^2-4\mu}\tanh\left(\frac{1}{2}(\mathrm{E}+\xi)\sqrt{\lambda^2-4\mu}\right)+\lambda^2-4\mu\right)^2}{\left(\sqrt{\lambda^2-4\mu}\tanh\left(\frac{1}{2}(\mathrm{E}+\xi)\sqrt{\lambda^2-4\mu}\right)+\lambda\right)^2}+2}{2ak},\tag{26}$$

where $\left(\beta=\sqrt{\lambda^2-4\mu}\ ,\tau=\tanh\left(\frac{1}{2}\beta\left(E+\xi\right)\right)\right)$. Integrating Eqn. (26) with respect to ξ,

$$U_{2,1}(\xi)=-\frac{\beta\left(2(3c+2)\mu\xi+3\lambda k^2\left(\lambda^2-8\mu\right)\right)\tau+2(3c+2)\lambda\mu\xi+12k^2\mu\tanh^{-1}(\tau)\left(\beta^2\tau+\lambda\beta\right)+3k^2\beta^4}{4ak\mu\left(\beta\tau+\lambda\right)},\tag{27}$$

is obtained.

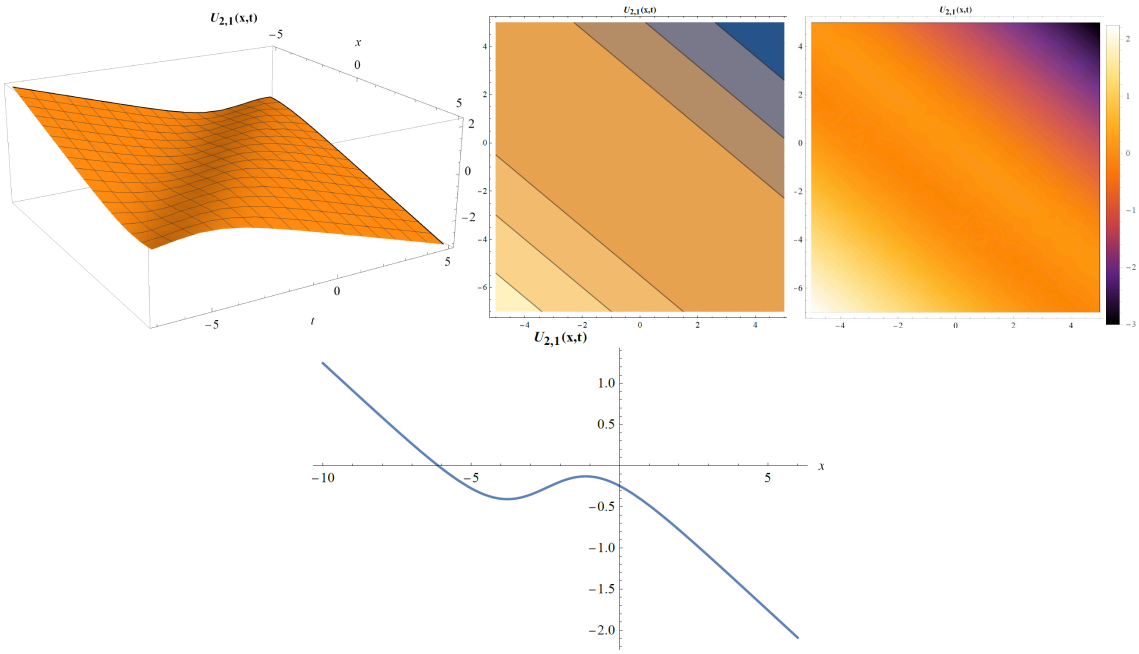

Figure 6: Graphs simulating the behavior of Eqn. (27) for the values $a=3$, $c=-1$, $\mathrm{E}=0.75$, $\lambda=3$, $k=1$, $\mu=2$, $y=0.01$, $z=0.01$ and two-dimensional graph for $t=1$

Family 2:

$$V_{2,2}(\xi)=-\frac{3c+\dfrac{3k^2\left(-\lambda\sqrt{4\mu-\lambda^2}\,\tan\left(\frac{1}{2}(\mathrm{E}+\xi)\sqrt{4\mu-\lambda^2}\right)+\lambda^2-4\mu\right)^2}{\left(\lambda-\sqrt{4\mu-\lambda^2}\,\tan\left(\frac{1}{2}(\mathrm{E}+\xi)\sqrt{4\mu-\lambda^2}\right)\right)^2}+2}{2ak}, \tag{28}$$

where $\left(\varsigma=\mu\tau\sin(q\tau),\ \omega=2\mu\cos(q\tau),\ \tau=\sqrt{-\lambda^2+4\mu},\ q=(\mathrm{E}+\xi)\right)$. Integrating Eqn. (28) with respect to ξ,

$$U_{2,2}(\xi)=-\frac{\omega\left((3c+2)\xi+3k^2q\left(-\tau^2\right)\right)+(3c+2)\xi\left(\lambda^2-2\mu\right)+3k^2\left(-\tau^2\right)\left(\lambda^2q-2\mu q-2\lambda\right)+12k^2\varsigma}{2ak\left(\omega+\lambda^2-2\mu\right)}. \tag{29}$$

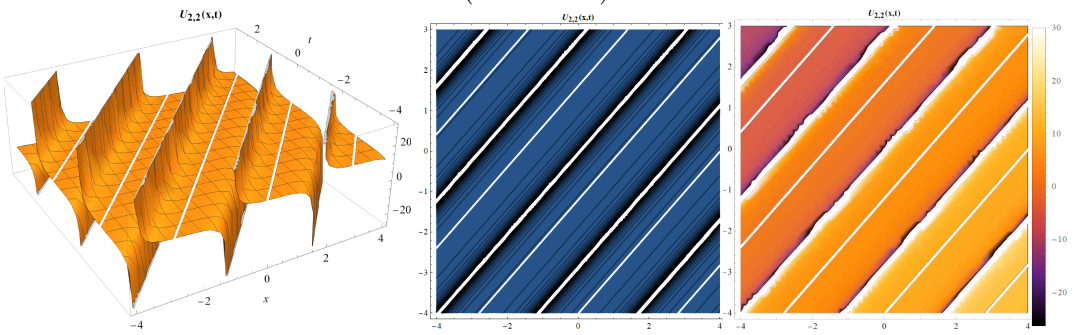

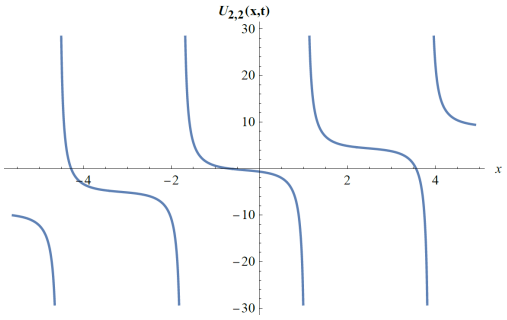

Figure 7: Graphs simulating the behavior of Eqn. (29) for the values $a=3$, $c=1$, $\mathrm{E}=0.75$, $\lambda=3$, $k=1$, $\mu=3.5$, $y=0.01$, $z=0.01$ and two-dimensional graph for $t=1$

Family 3:

$$V_{2,3}(\xi)=-\frac{3c+3k^2\lambda^2\coth^2\left(\frac{1}{2}\lambda(\mathrm{E}+\xi)\right)+2}{2ak}. \tag{30}$$

Integrating Eqn. (30) with respect to ξ,

$$U_{2,3}(\xi)=\frac{6k^2\lambda\left(\coth\left(\frac{1}{2}\lambda(\mathrm{E}+\xi)\right)-\left(\frac{1}{2}\lambda(\mathrm{E}+\xi)\right)\right)-(3c+2)\xi}{2ak}. \tag{31}$$

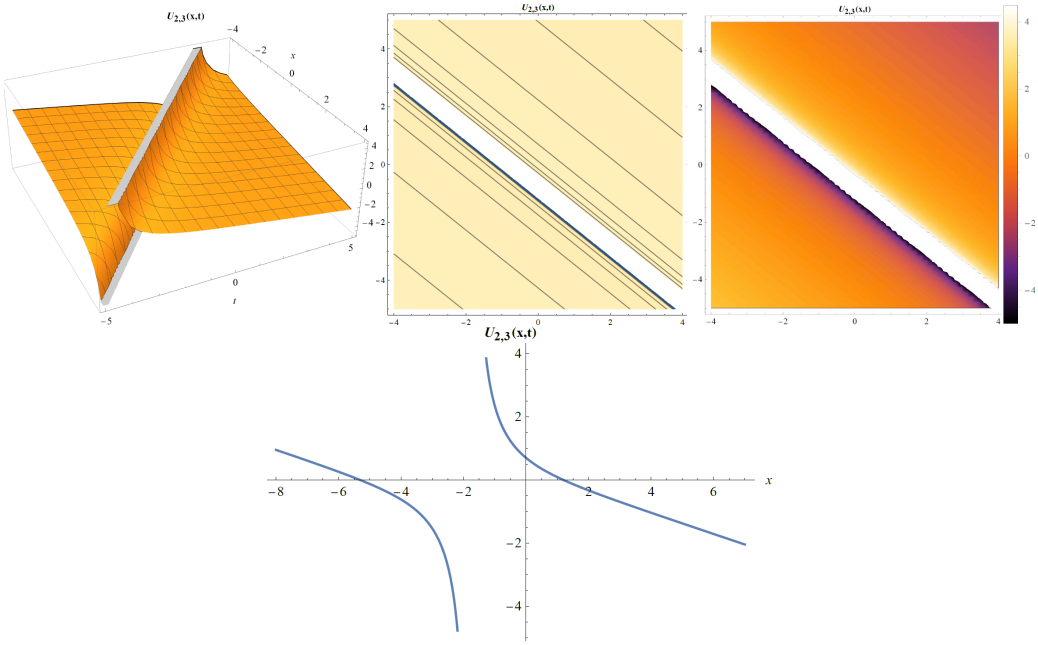

Figure 8: Graphs simulating the behavior of Eqn. (31) for the values $a=3$, $c=-1$, $\mathrm{E}=0.75$, $\lambda=1$, $k=1$, $\mu=0$, $y=0.01$, $z=0.01$ and two-dimensional graph for $t=1$

Family 4:

$$V_{2,4}(\xi) = -\frac{3c + \dfrac{12k^2\lambda^2}{(\lambda(\mathrm{E}+\xi)+2)^2} + 2}{2ak}. \tag{32}$$

Integrating Eqn. (32) with respect to ξ,

$$U_{2,4}(\xi) = \frac{6k\lambda}{a(\lambda(\mathrm{E}+\xi)+2)} - \frac{(3c+2)\xi}{2ak}. \tag{33}$$

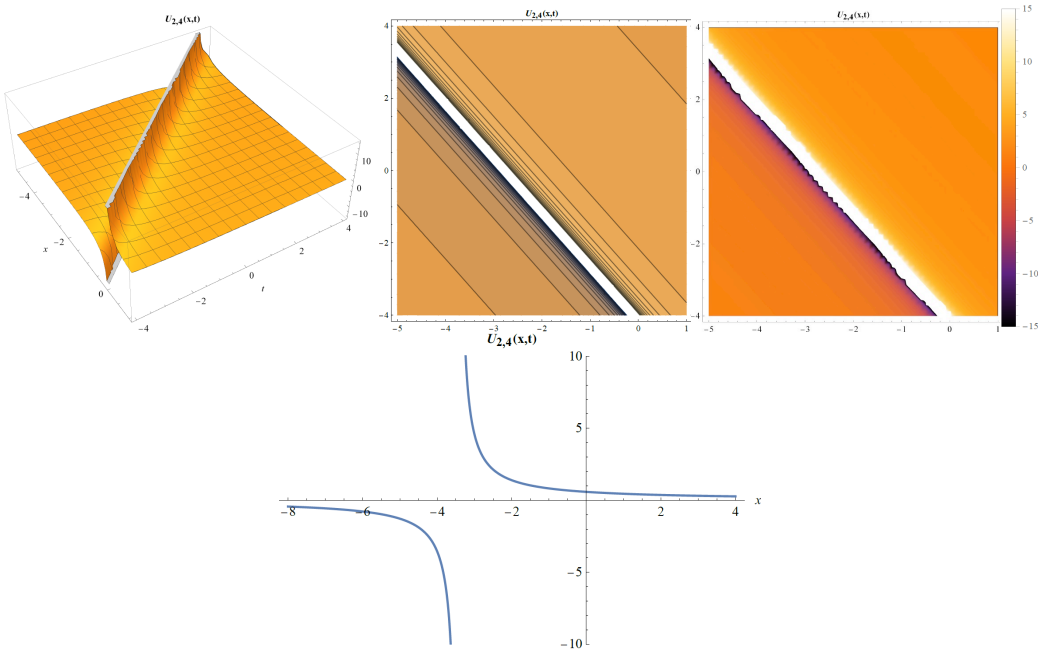

Figure 9: Graphs simulating the behavior of Eqn. (33) for the values $a=3$, $c=-0.\overline{6}$, $\mathrm{E}=0.75$, $\lambda=1$, $k=1$, $\mu=0.25$, $y=0.01$, $z=0.01$ and two-dimensional graph for $t=1$

Family 5:

$$V_{2,5}(\xi) = -\frac{3c + \dfrac{12k^2}{(\mathrm{E}+\xi)^2} + 2}{2ak}. \tag{34}$$

Integrating Eqn. (34) with respect to ξ,

$$U_{2,5}(\xi) = \frac{6k}{a(\mathrm{E}+\xi)} - \frac{(3c+2)\xi}{2ak}, \tag{35}$$

is obtained.

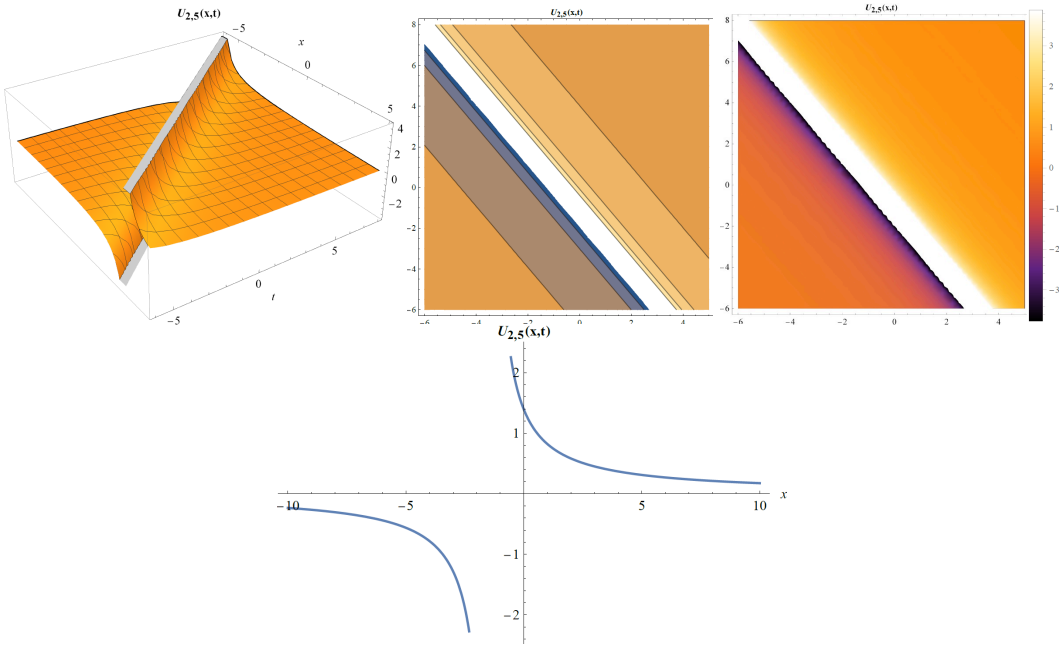

Figure 10: Graphs simulating the behavior of Eqn. (35) for the values $a = 3$, $c = -0.\overline{6}$, $E = 0.75$, $\lambda = 0$, $k = 1$, $\mu = 0$, $y = 0.01, z = 0.01$ and two-dimensional graph for $t = 1$

4. Conclusion

This article has been applied to the B-type Kadomtsev Petviashvili equation representing fluid mechanics, which is a nonlinear mathematical model of the developed exponential function method. In this research, it was seen that the analytical solutions found under the conditions were obtained according to the method provided by the Eqn. (1). When the mobile solution functions obtained were evaluated, it was determined that they were soliton, periodic and rational functions. All calculations related to the method and solution function graphs representing the nonlinear mathematical model were made using the Mathematica 12.0.0 software program. It has been observed that two and three-dimensional graphs obtained by determining the appropriate parameters are suitable for the physical behavior of wave solutions. In addition, contour graphics and density graphics were found with the help of software program for analytical solutions. It has been observed that hyperbolic functions are obtained when the solutions of equations with similar structures are investigated with other solution methods in the literature [18-24]. Using this method, different traveling wave solutions can be obtained if more cases are investigated, and different coefficient values are taken. When the obtained solutions are analyzed, it can be stated that MEFM is effective method for finding the traveling wave solutions of nonlinear partial differential equations. The resulting solution functions help us learn more about the physical phenomenon that represented fluid mechanics.

References

[1] Elwakil, S.A., El-Labany, S.K., Zahran, M.A., Sabry, R., *Modified extended tanh-function method for solving nonlinear partial differential equations*, Physics Letters A, 299 (2-3), 179-188, 2002.

[2] Zheng, X., Chen, Y., Zhang, H., *Generalized extended tanh-function method and its application to (1+1)-dimensional dispersive long wave equation*, Physics Letters A, 311 (2-3), 145-157, 2003.

[3] Liu, C.S., *Trial equation method to nonlinear evolution equations with rank inhomogeneous: mathematical discussions and its applications*, Communications in Theoretical Physics, 45 (2), 219-223, 2006.

[4] Bulut, H., Baskonus, H.M., Pandir Y., *The modified trial equation method for fractional wave equation and time fractional generalized Burgers equation*, In Abstract and Applied Analysis Hindawi, Vol. 2013, 2013.

[5] Gurefe, Y., Misirli, E., Sonmezoglu, A., Ekici, M., *Extended trial equation method to generalized nonlinear partial differential equations*, Applied Mathematics and Computation, 219 (10), 5253-5260, 2013.

[6] Yang, X.F., Deng, Z.C., Wei, Y.A., *Riccati-Bernoulli sub-ODE method for nonlinear partial differential equations and its application*, Advances in Difference Equations, 2015 (1), 1-17, 2015.

[7] Baskonus, H.M., Bulut, H., *Regarding on the prototype solutions for the nonlinear fractional-order biological population model*, In AIP Conference Proceedings AIP Publishing LLC, 1738, 2016.

[8] Abdelrahman, M.A., *A note on Riccati-Bernoulli Sub-ODE method combined with complex transform method applied to fractional differential equations*, Nonlinear Engineering, 7 (4), 279-285, 2018.

[9] Hosseini, K., Gholamin, P., *Feng's first integral method for analytic treatment of two higher dimensional nonlinear partial differential equations*, Differential Equations and Dynamical Systems, 23 (3), 317-325, 2015.

[10] Kutluay, S., Karta, M., Yağmurlu, N.M., *Operator time-splitting techniques combined with quintic B-spline collocation method for the generalized Rosenau–KdV equation*, Numerical Methods for Partial Differential Equations, 35, 2221–2235, 2019.

[11] Yağmurlu, N.M., Karakaş, A.S., *Numerical solutions of the equal width equation by trigonometric cubic B-spline collocation method based on Rubin–Graves type linearization*, Numerical Methods for Partial Differential Equations, 36 (5), 1170-1183, 2020.

[12] Özer, S., Yağmurlu, N.M., *Numerical solutions of nonhomogeneous Rosenau type equations by quintic B-spline collocation method*, Mathematical Methods in the Applied Sciences, 45 (9), 5545–5558, 2022.

[13] He, J.H., Wu, X.H., *Exp-function method for nonlinear wave equations*, Chaos, Solitons & Fractals, 30 (3), 700-708, 2006.

[14] Baskonus, H.M., Askin, M., *Travelling wave simulations to the modified Zakharov-Kuzentsov model arising in plasma physics*, In Litteris et Artibus, Lviv Polytechnic Publishing House. 2016.

[15] Gurefe, Y., Misirli, E., *Exp-function method for solving nonlinear evolution equations with higher order nonlinearity*, Computers & Mathematics with Applications, 61 (8), 2025-2030, 2011.

[16] Misirli, E., Gurefe, Y., *The Exp-function method to solve the generalized Burgers-Fisher equation*, Nonlinear Science Letters A, 323-328, 2010.

[17] Misirli, E., Gurefe, Y., *Exact solutions of the Drinfel'd–Sokolov–Wilson equation using the exp-function method*, Applied Mathematics and Computation, 216 (9), 2623-2627, 2010.

[18] Gao, X., *Bäcklund transformation and shock-wave-type solutions for a generalized (3+1)-dimensional variable-coefficient B-type Kadomtsev–Petviashvili equation in fluid mechanics*, Ocean Engineering, 245–247, 2015.

[19] Cheng, L., Zhang, Y., *Multiple wave solutions and auto-Bäcklund transformation for the (3+1)-dimensional generalized B-type Kadomtsev–Petviashvili equation*, Computers and Mathematics with Applications, 70(5), 765-775, 2015.

[20] Ma, W.X., Zhu, Z.N., *Solving the (3+1)-dimensional generalized KP and BKP equations by the exp-function algorithm*, Applied Mathematics and Computation, 218, 11871–11879, 2012.

[21] Nisar, K.S., Ilhan, O.A., Abdulazeez, S.T., Manafian, J., Mohammed, S.A., Osman, M.S., *Novel multiple soliton solutions for some nonlinear PDEs via multiple Exp-function method*, Results in Physics 21,103769, 2021.

[22] Asaad, M.G., Ma, W.X., *Pfaffian solutions to a (3+1)-dimensional generalized B-type Kadomtsev–Petviashvili equation and its modified counterpart*, Applied Mathematics and Computation 218, 5524–5542, 2012.

[23] Cao, X., *Lump Solutions to the (3+1)-Dimensional Generalized b-type Kadomtsev-Petviashvili Equation*, Advances in Mathematical Physics, 5, 7843498, 2018.

[24] Wazwaz, A.M., *Distinct Kinds of Multiple-Soliton Solutions for a (3+1)-Dimensional Generalized B-type Kadomtsev-Petviashvili Equation*, Physica Scripta, 84, 5, 055006, 2011.

[25] Yokuş, A., Durur, H., Duran, S., *Ample felicitous wave structures for fractional foam drainage equation modeling for fluid-flow mechanism*, Computational and Applied Mathematics, 41, 174, 2022.

[26] Duran, S., Yokuş, A., Durur, H., Kaya, D., *Refraction simulation of internal solitary waves for the fractional Benjamin–Ono equation in fluid dynamics*, Modern Physics Letters B, Vol. 35, 26, 2150363, 2021.

[27] Yokuş, A., *Simulation of bright–dark soliton solutions of the Lonngren wave equation arising the model of transmission lines*, Modern Physics Letters B,Vol. 35, 32, 2150484, 2021.

[28] Duran, S., Kaya, D., *Breaking analysis of solitary waves for the shallow water wave system in fluid dynamics*, The European Physical Journal Plus, 136, 980, 2021.

[29] Yokuş, A., Durur, H., Duran, S., *Simulation and refraction event of complex hyperbolic type solitary wave in plasma and optical fiber for the perturbed Chen-Lee-Liu equation*, Optical and Quantum Electronics 53, 402, 2021.

Adıyaman University Journal of Science
https://dergipark.org.tr/en/pub/adyujsci
DergiPark AKADEMİK
ISSN 2147-1630
e-ISSN 2146-586X

Blending of Poly(methyl methacrylate) with Poly(1,3-diphenyl-1H-pyrazol-5-yl methacrylate): Investigation of its Optical Properties

Adnan KURT[1,*], Murat KOCA[2]

[1]*Adıyaman University, Faculty of Science and Arts, Department of Chemistry, 02040, Adıyaman, Türkiye*
akurt@adiyaman.edu.tr, ORCID: 0000-0001-8516-6525
[2]*Adıyaman University, Faculty of Pharmacy, Department of Pharm. Chemistry, 02040, Adıyaman, Türkiye*
mkoca@adiyaman.edu.tr, ORCID: 0000-0001-9377-2461

Received: 29.04.2022 **Accepted:** 21.09.2022 **Published:** 30.12.2022

Abstract

In the present study, a new blend polymer consisting of a pyrazole-derived polymer poly(1,3-diphenyl-1H-pyrazol-5-yl methacrylate) and poly(methyl methacrylate) was prepared with solution mixing method. The blend polymer was spectrally characterized with FTIR and ^{1}H-NMR techniques. TGA analysis showed that the blend polymer was stable up to 275.4 °C. A thin film of blend polymer was prepared by using spin coating technique. The UV measurements were obtained as a function of wavelength (300 – 700 nm). The optical and dispersion parameters were reported in detail. Transmittance was increased depending on the increasing wavelength whereas the reflectance decreased. The Transmittance value at 700 nm was measured as 97.55%, meaning the blend polymer was transparent. The refractive index at 700 nm was 1.37. The Urbach energy (E_u) and the optical band gap constant (E_g) were calculated to be 0.831 eV and 3.737 eV, respectively. The type of electronic transitions for polymer was determined as indirect allowed transition.

Keywords: Blend polymer; Pyrazole; Methyl methacrylate; UV absorptions; Optical properties; Dispersion parameters.

* Corresponding Author DOI: 10.37094/adyujsci.1110956

Poli(metil metakrilat) ile Poli(1,3-difenil-1H-pirazol-5-il metakrilat)'ın Blendleşmesi: Optik Özelliklerinin Araştırılması

Öz

Mevcut çalışmada, pirazol türevli bir polimer olan poli(1,3-difenil-1H-pirazol-5-il metakrilat) ve poli(metil metakrilat) içeren yeni bir blend polimer, çözelti karıştırma yöntemiyle hazırlandı. Hazırlanan blend polimer FTIR ve ^{1}H-NMR teknikleri ile spektral olarak karakterize edildi. TGA analizi blend polimerin 275.4 °C'ye kadar stabil olduğunu gösterdi. Spin kaplama tekniği kullanılarak blend polimer ince filmi hazırlandı. UV ölçümleri dalga boyunun (300-700 nm) bir fonksiyonu olarak kaydedildi. Optik ve dağılım parametreleri detaylı olarak rapor edildi. Artan dalga boyuna bağlı olarak geçirgenlik artarken yansıma azaldı. Geçirgenlik değeri 700 nm'de %97,55 olarak ölçüldü, bu da blend polimerin oldukça geçirgen olduğu anlamına gelmektedir. Kırılma indisi değeri 700 nm'de 1.37 olarak hesaplandı. Urbach enerjisi (E_u) ve optik bant aralığı sabiti (E_g) sırasıyla 0.831 eV ve 3.737 eV olarak belirlendi. Polimerin elektronik geçiş türünün dolaylı izinli geçiş olduğu görüldü.

Anahtar Kelimeler: Blend polimer; Pirazol; Metil metakrilat; UV absorpsiyon; Optik özellikler; Dispersiyon parametreleri.

1. Introduction

Polymer blends are one of the most important research topics in polymer chemistry. The chemical structures, properties and processing techniques of polymer blends have been investigated in scientific and technological platforms for years [1]. Polymer blends play an important role in our lives due to their high elasticity, low cost, light, transparent and easy processing. Thanks to these mentioned features; polymer blends have a wide application and usage potential in electronics, packaging, automotive, daily life materials, household appliances, etc. Therefore, polymer blends have shown a continuous development and become an ideal candidate for today's modern technologies [2]. Generally, a polymer blend is a physical mixture of at least two or more different homopolymers. By blending, a new material is obtained that differs in properties from its homopolymers. Polymer blends can be classified as plastic, thermoplastic, elastomer, etc. according to the physical properties of their components. In addition, the final properties of a polymer blend are highly dependent on the morphology, miscibility, and phase behavior of its partners [3]. If a well-defined blend with the desired properties can be achieved, this blending technique becomes a faster and more cost-effective technique without the need for the synthesis of new monomers or the use of new polymerization methods [1]. Many studies investigating PMMA-based blend polymers and their various

properties can be seen widely in the literature. For example, one of these studies was reported by Bubmann et al. in which they prepared the transparent terminally phenolic OH-functionalized polycarbonate and epoxy-functionalized polymethylmethacrylate (PC/PMMA) blends with enhanced mechanical properties via reactive compounding of functionalized polymers [4]. In another study, Le and coworkers reported that the multiphase blends were prepared by melt processing of poly(L-lactide) and poly(methyl methacrylate) at various compositions to identify their morphologies, phase relationships and biomaterial compatibility for tissue engineering studies [5]. Aid and friends studied the miscibility of poly(vinylidene fluoride)-PVDF/PMMA blends at different approaches such as experimental tests using physico-chemical and rheological methods, thermodynamics using Flory-Huggins parameters and numerical simulation using Fluent Ansys software to describe the coalescence phenomenon [6].

The optical properties of polymer molecules are quite remarkable in addition to the many physical and chemical properties of these molecules such as thermal, mechanical, rheological, dielectric, etc. Among the optical properties of polymers, some parameters such as transmittance, reflectance, absorbance, refractive index, optical band energy, and dispersion parameters are widely studied [7-9]. These properties are highly dependent on the chemical structure of the polymer or copolymer, the formulation of the polymeric material (colorants, fillers, plasticizers, stabilizers and other additives), crystallinity and amorphous structure of the polymer. In addition to these, the mechanical, thermal or chemical degradation of the polymer, the mechanical conditions that the polymer is exposed to during production or processing, heat treatments, environmental conditions, solvents and chemical interactions significantly change the optical properties of polymers.

Many techniques can be used to determine the optical properties of polymers. However, among these, Ultraviolet-Visible spectroscopy is a technique that can give very effective, reliable and fast results in the optical characterization (absorbance, transmittance, reflectance) of polymers [10]. Optical measurements of polymers at different wavelengths are taken in UV-vis spectroscopy, and many different optical parameters can be easily determined by using the obtained data in the methods or equations available in the literature. There are many publications to investigate the optical properties of different chemically derived blend polymers. Some of those, Tikish and friends investigated the electrical and optical properties of polypyrrole and polyaniline blends [11]. Takahashi and coworkers reported a paper on the optical properties of ethylene–vinyl acetate copolymer and poly(methyl methacrylate) blends at different compositions [12]. In a study reported by our research group, we prepared a blend polymer based poly(ethyl methacrylate) and poly(2-hydroxy-3-phenoxypropyl methacrylate). The compatibility, thermal

degradation kinetics, degradation mechanism and electro optic properties of that blend polymer was studied [13].

The synthesis of many heterocyclic polymers with different functional groups and also preparation of blend polymers of these polymers with commercial ones are seen in in the literature. However, the synthesis and characterization of the blend polymer containing pyrazole-derived poly(1,3-diphenyl-1H-pyrazol-5-yl methacrylate) polymer with poly(methyl methacrylate) and especially the optical properties of this blend polymer have not been found in the literature. Pyrazole-derived molecules have been the subject of widespread study in many fields with their small molecule forms as well as their polymeric macromolecular structures. Especially, pyrazole-derived polymers are one of the most important members of heterocyclic polymers. The pyrazole ring consists of a five-membered lactam ring containing two nitrogen atoms in its chemical structure [14]. In addition, the pyrazole molecule also has a dense pi bond structure. There has been an increasing trend of studies on pyrazole derivatives in recent years. The fact that both two pi bonds and heteroatoms are present in the structure of these molecules have made these molecules particularly important electro-optic properties in addition to their pharmacological properties [15, 16]. From this point, the main purpose of this study is to synthesize and characterize a new blend polymer consisting of a pyrazole-derived polymer poly(1,3-diphenyl-1H-pyrazol-5-yl methacrylate) and poly(methyl methacrylate). The miscibility of two polymers in terms of different chemical structures has been tested. Thus, it is aimed to develop new pyrazole-derived polymeric systems and contribute to the heterocyclic polymer class. Another aim is to determine some important optical parameters such as transmittance, reflectance, optical band gap, Urbach energy, dispersion parameters of new blend polymer thin film prepared by spin coating technique.

2. Materials and Methods

2.1. Sample preparation

Methyl methacrylate, benzoyl peroxide, tetrahydrofuran (THF), chloroform, and ethyl alcohol were purchased from Sigma-Aldrich. Methyl methacrylate (MMA) was passed through an alumina column to separate it from the inhibitors. Then, poly(MMA) was synthesized by free radical polymerization using 1.00 g of MMA, 3 ml of THF, and 0.01 g benzoyl peroxide (1 %wt of MMA) at 60 ºC for 24 h. After that, polymer was precipitated in ethyl alcohol, filtrated, and dried. Synthesis and characterization of pyrazol derived polymer poly(1,3-diphenyl-1H-pyrazol-5-yl methacrylate), poly(DPMA), was reported in our previous study [17]. Blend of poly(MMA) with poly(DPMA) was prepared by solution method in THF. In the present work, we set the

weight fraction of poly(MMA) to poly(DPMA) blend as 50% : 50%, respectively. For this process, poly(DPMA) homopolymer (0.100 g) was first added to a 50 ml single necked reaction flask and dissolved by adding THF (3 mL). Then the calculated amount of poly(MMA) homopolymer (0.100 g) was added to this solution. The solution containing both homopolymers was stirred on a magnetic stirrer at room temperature for 24 hours. At the end of this period, the blend polymer solution was precipitated in ethyl alcohol, filtered and dried in a vacuum oven. A suitable schematic illustration for the preparation of the blend polymer was given in Fig. 1.

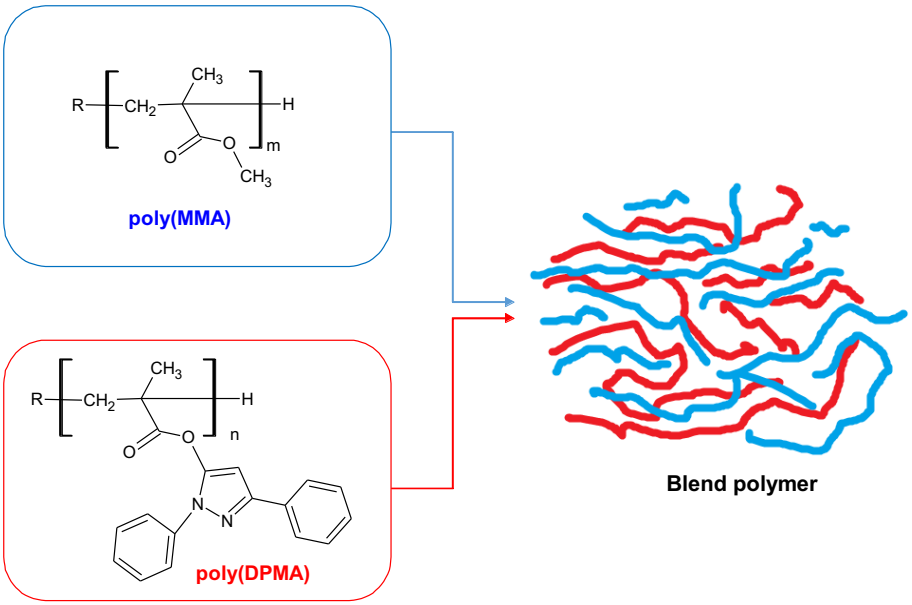

Figure 1: Preparation of the poly(DPMA)/poly(MMA) blend polymer

2.2. Characterization

At the spectral characterizations of poly(DPMA)/poly(MMA) blend polymer, a high resolution Bruker Avance III HD 300 MHz NMR Spectrometer and a Perkin Elmer Spectrum 100 FTIR Spectrometer (with ATR unit) were used. TGA analysis was performed on a Seiko SII 7300 TG/DTA thermobalance heated from ambient temperature to 500 ºC at heating rate of 15 ºC/min in nitrogen flow of 25 mL/min. Blend polymer thin film was prepared by spin coating technique. For this purpose, a Laurell WS-400-6NPP-Lite spin coater was used. In this process, blend polymer (0.015 g) was dissolved in 0,5 mL of THF and coated onto a glass at the conditions of 5 bar argon gas pressure and 1500 rpm for 50 seconds. The thickness of film was measured to be 6 µm using a digital micrometer supplied by Mitutoyo Corporation Ltd Japan. After that, the UV measurements of blend thin film was obtained by using a Perkin Elmer Lambda 25 UV/VIS spectrophotometer at wavelengths of 300 - 700 nm.

3. Results and Discussion

FTIR spectra of poly(MMA), blend polymer and poly(DPMA) were shown in Fig. 2(a-c), respectively. In the FTIR spectrum of the blend polymer (Fig. 2b), the characteristic signals for both homopolymers are seen. It is important to observe the absorbance's of aromatic C-H stretching (3160-3029 cm^{-1}) and the aromatic C=C stretching (1595 cm^{-1}) which are characteristic for poly(DPMA) in blend polymer apart from the standard poly(MMA) signals.

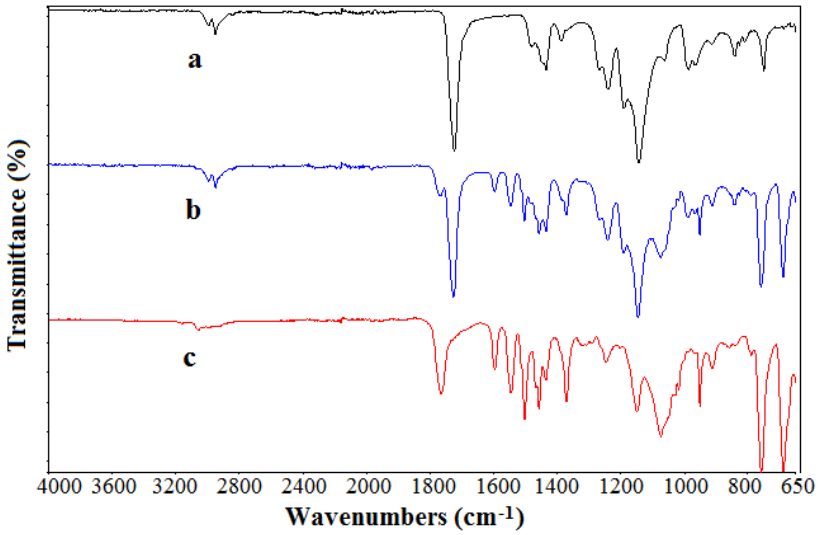

Figure 2: FTIR spectra of a) poly(MMA), b) blend polymer, c) poly(DPMA)

So, these signals clearly show that the blend polymer has accomplished and the presence of both homopolymers in the blend. A second important change is occurred in the ester carbonyl region. The methacrylic ester carbonyl stretching in the blend polymer is seemed at 1768 cm^{-1} and 1726 cm^{-1} reasoned from the ester carbonyl bands of poly(DPMA) and that of poly(MMA), respectively. In the blend polymer, the vibration energy of ester carbonyls of both polymers are relatively shifted due to possible intermolecular secondary interactions. This situation gives an important clue about the miscibility of the blend polymer.

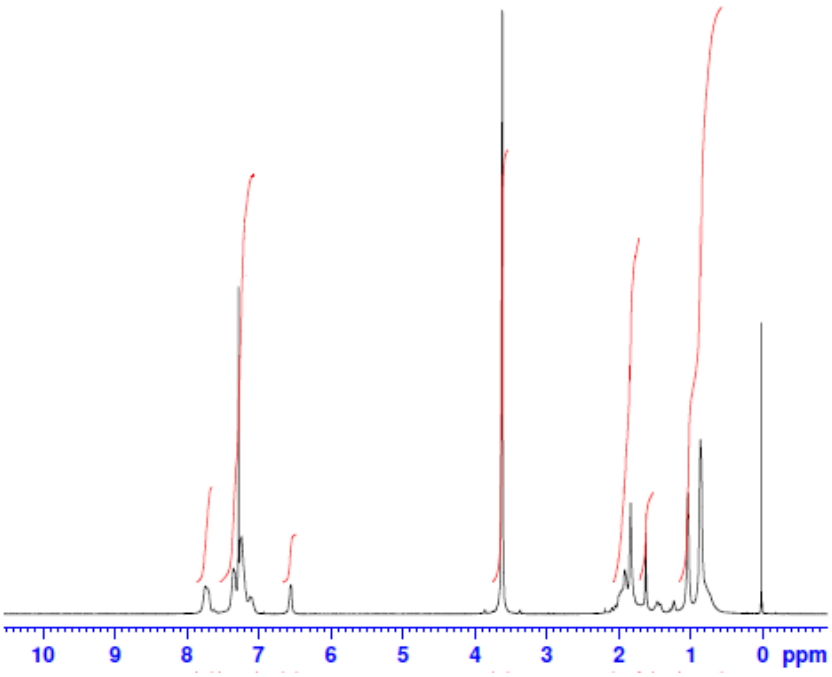

Figure 3: ^{1}H-NMR spectra of blend polymer

Another proof of the success of blend polymer synthesis is the ^{1}H-NMR spectrum. This spectrum is shown in Fig. 3 where the signals belonging to both poly(MMA) and poly(DPMA) units are seen. Accordingly, the 7.74 – 7.19 ppm signals and also 6.56 ppm signal are recorded for the aromatic =CH protons in phenyl groups and aliphatic =CH proton in the pyrazole group for poly(DPMA), respectively. The signal at 3.62 ppm is attributed to $-COOCH_3$ protons in poly(MMA). Methylene and methyl protons on the blend polymer main chains reasoned from both units are observed at 1.92 – 0.86 ppm.

Thermal analysis of blend polymer was accomplished by thermogravimetric analysis (TGA). The thermal decomposition process was performed on a temperature range of room temperature to 500 °C. Fig. 4 shows the TGA thermogram of blend polymer. As can be seen, the decomposition of blend polymer is occurred in three stages. The first one, with up to 12% weight loss at ~290 - 340 °C usually caused by volatile hydrocarbons, the second decomposition stage is about between 340 – 390 °C with up to 44% weight loss, and the third one is ~ 390 – 460 °C with up to 94% weight loss. The initial decomposition temperature of the blend polymer is measured as 275.4 °C. In our previous study, this value was determined as 238.8 °C for the poly(1,3-diphenyl-1H-pyrazol-5-yl methacrylate) homopolymer [17]. As a result of the blending of this homopolymer with poly(MMA), an increase in thermal stability occurred. In addition, the final decomposition temperature of the blend polymer was determined as 460 °C and the temperature of 50% decomposition was 401.1 °C. The % mass losses of the blend polymer at different

temperatures such as 350 °C, 400 °C and 450 °C were also recorded as 15.53%, 49.90% and 90.94%, respectively.

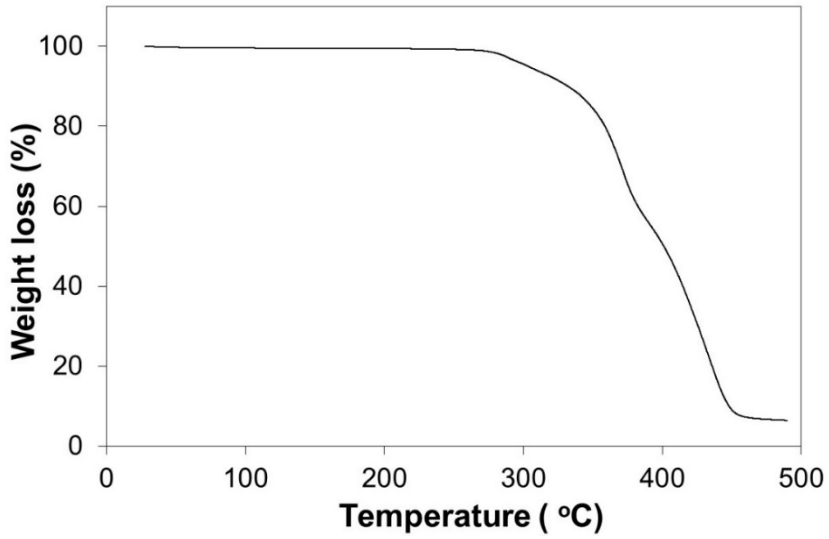

Figure 4: TGA thermogram of blend polymer

The UV measurements of poly(DPMA)/poly(MMA) blend polymer were recorded at the wavelengths of 300 - 700 nm for determining the optical properties. Therefore, firstly, the absorbance (A) and transmittance (T) measurements were directly measured by UV and then the reflectance (R) values were calculated by the equation of (R = 1 - T - A) [18]. Transmittance and reflectance spectra of blend polymer were shown in Fig. 5 and Fig. 6, respectively. The transmittance values showed a general increase depending on the increase in wavelength. While this increasing trend is quite sharp in the 300-330 nm range, the increase in the next wavelengths gradually decreases and reaches almost constant value.

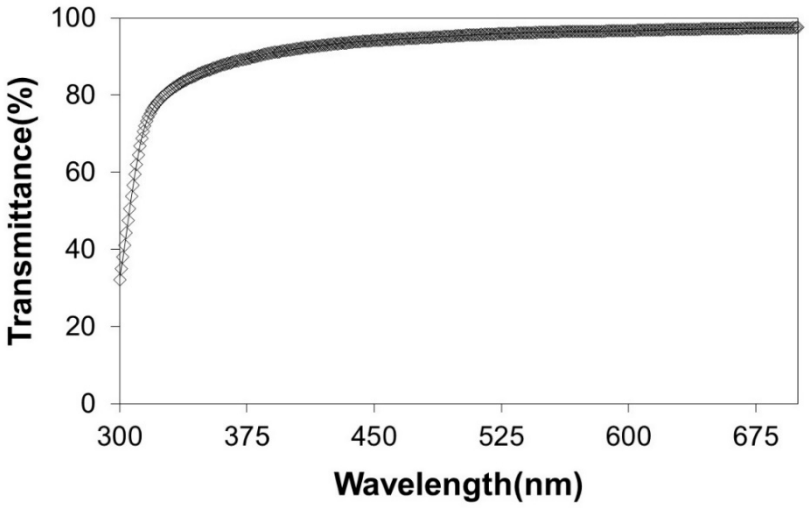

Figure 5: Transmittance spectra of blend polymer thin film

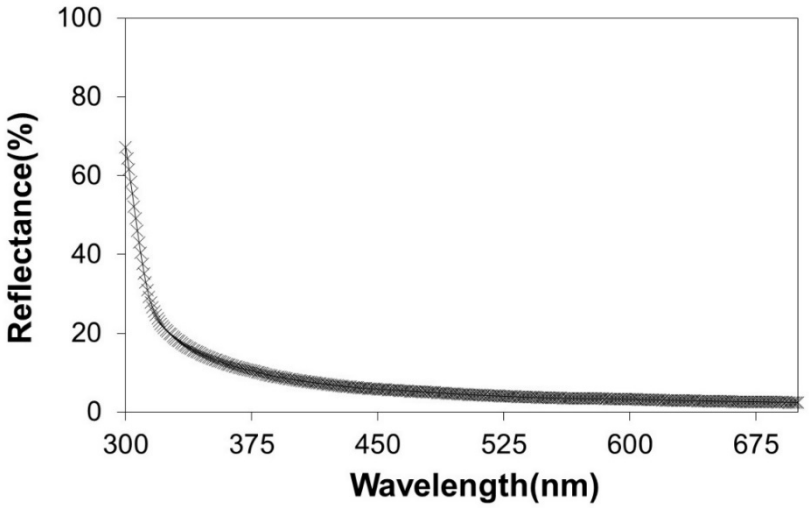

Figure 6: Reflectance spectra of blend polymer thin film

An opposite behavior of the transmittance values was observed in the reflectance values. A rather drastic decrease in reflectance values was observed, especially at low wavelengths (up to 320 nm). However, depending on the increase in wavelength, a slowdown occurs in this decrease rate and an almost constant value is obtained towards 700 nm. The transmittance and reflectance values at 700 nm were measured as 97.55% and 2.43%, respectively. The presence of pyrazole groups in the structure of the prepared blend polymer and also the presence of intense pi-bonds in these groups cause the absorption at low wavelengths to be higher [19].

The refractive index (n) is very important for the optical characterization of polymers. It is possible to determine this parameter with the following formula using the transmittance and reflectance values [20]:

$$n = \left[\frac{1 + R}{1 - R}\right] + \left[\frac{4R}{(1 - R)^2} - k^2\right]^{1/2} \quad (1)$$

where k is the extinction coefficient and equal to, $k = \alpha\lambda/4\pi$. In this formula, α is the absorption coefficient which is obtained as: $\alpha = 2.303A/d$ where A is the absorbance and d is the film thickness. Fig. 7 shows the relationship between the refractive index and the wavelength. There is a significant decrease in the refractive index depending on the increase in wavelength. While this decrease is quite evident especially at low wavelengths, the downward trend towards the next wavelengths gets lighter [21]. The refractive index value at 700 nm is measured as 1.37. This value is the expected value for methacrylate-derived polymers [22].

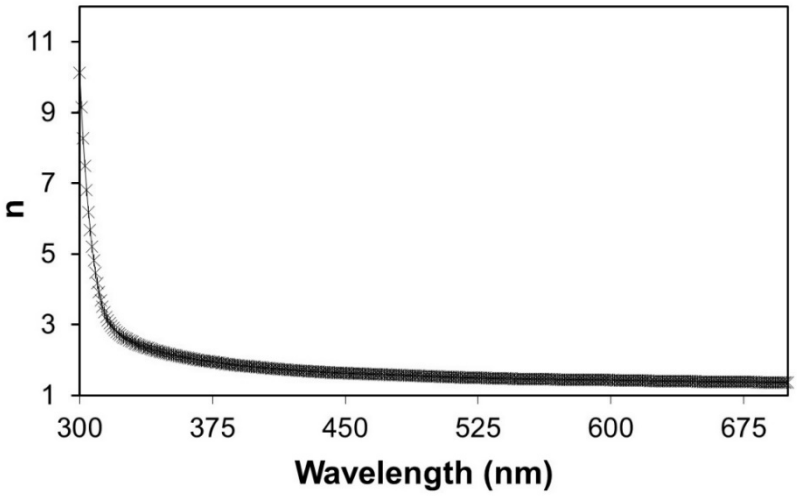

Figure 7: Refractive index dispersion of blend polymer thin film

The dependence of the dispersion energy parameters on the refractive index were well defined by Wemple and DrDomenico with the following equation [23].

$$n^2(h\nu) = 1 + \frac{E_o E_d}{E_o^2 - (h\nu)} \quad (2)$$

These parameters are E_o, the single – oscillator energy and E_d, the dispersion energy. From these parameters, E_o responsible from the electronic excitations in the molecules and illustrates the average of the optical band gap whereas E_d shows the average strength of inter-band optical transition [24]. Figure 8 shows the $(n^2-1)^{-1}$ vs. $(h\nu)^2$ plots. The linear fit of this figure yields a slope corresponds to $(E_oE_d)^{-1}$ and intercept is E_o/E_d. Finally, the single – oscillator energy (E_o) and the dispersion energy (E_d) values for blend polymer are calculated to be 3.982 eV and 3.488 eV, respectively. These values are given in Table 1.

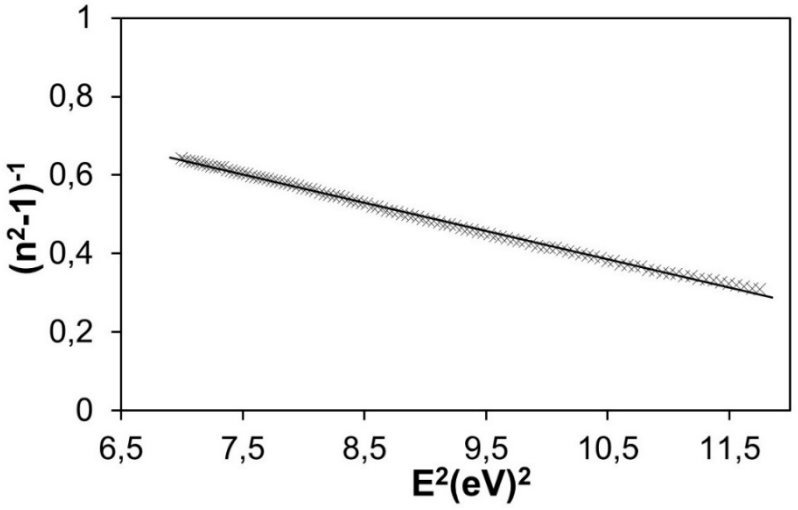

Figure 8: Variation of $(n^2-1)^{-1}$ as a function of E^2 of blend polymer thin film

Wemple and DrDomenico have defined the moments of imaginary part of the complex dielectric constant (M_{-1} and M_{-3}) with the single oscillator energy parameters (E_o and E_d). These moments can be determined from following relation [23, 25]:

$$E_o^2 = \frac{M_{-1}}{M_{-3}} \qquad E_d^2 = \frac{(M_{-1})^3}{M_{-3}} \tag{3}$$

Table 1 includes the moments M_{-1} and M_{-3} are calculated as 0.876 and 0.055, respectively. These parameters are also given in Table 1.

The average inter-band oscillator wavelength (λ_o) and oscillator strength (S_o) may be obtained from the single-term Sellmeier equation [26]. This is expressed as:

$$n^2(\lambda) - 1 = \frac{S_0.\lambda_0^2}{1 - (\lambda_0/\lambda)^2} \tag{4}$$

Figure 9 shows the $(n^2-1)^{-1}$ vs. λ^{-2} plots. From the slope and intercept of this figure, the average inter-band oscillator wavelength (λ_o) and oscillator strength (S_o) is calculated as 311.7 nm and 9.02×10^{12} m^{-2}. Table 1 also gives these values.

Table 1: Optical results of blend polymer thin film

E_u (eV)	**E_g (eV)**	**E_0 (eV)**	**E_d (eV)**	**M_{-1}**	**M_{-3} $(eV)^{-2}$**
0,831	3,737	3,982	3,488	0,876	0,055
$S_0.10^{12}(m^{-2})$	**λ_0(nm)**	**σ**	**α_0**	**n (700 nm)**	**T% (700 nm)**
9,02	311,7	0,0309	$3,46.10^{-7}$	1,37	97,55

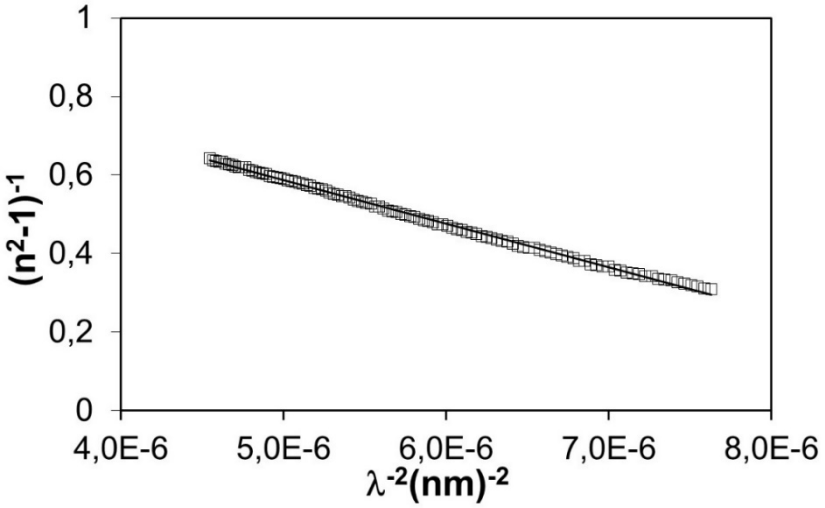

Figure 9: Variation of $(n^2-1)^{-1}$ as a function of $(\lambda)^{-2}$ of blend polymer thin film

The interband transitions of polymers may be obtained by analyzing the absorption data at the fundamental edge by [27]:

$$(\alpha h\nu) = B(h\nu - E_g)^n \quad (5)$$

where E_g is the optical band gap, B is a constant, and n is an index that shows the electronic transition types [24]. For the prepared blend polymer, the electronic transition type is the indirect allowed transition (n=2). So, the $(\alpha h\nu)^{1/2}$ vs $(h\nu)$ values are plotted as shown in Fig. 10. The slope of this line gives the B constant, which is 0.0189, whereas the intercept corresponds *$(-B.E_g)$*. When the value of B is written in the intercept, the optical band gap (E_g) is calculated as 3.737 for blend polymer.

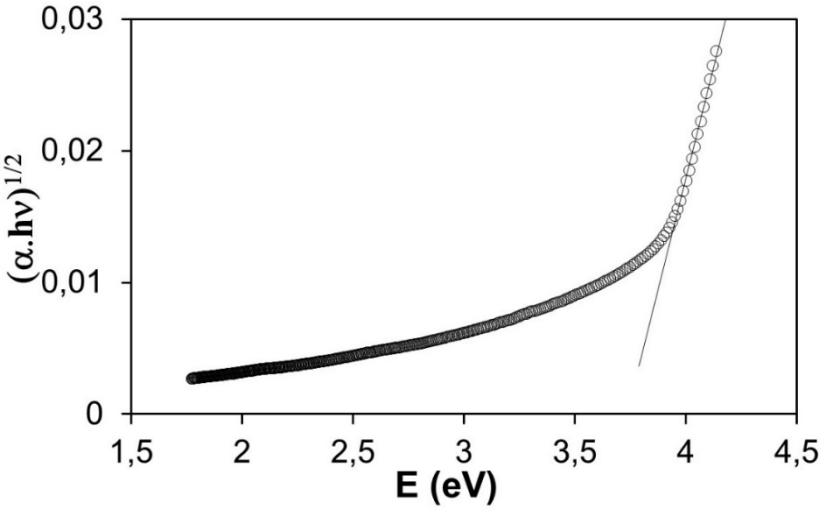

Figure 10: Plots of $(\alpha h\nu)^{1/2}$ vs: E of blend polymer thin film

On the other hand, some local defects may occur in polymeric materials when exposed to UV radiation. One effect of these defects is to trap electrons and prevent their direct transition to the conduction band [28]. Urbach energy is defined as a measure of the size of these defects and expressed [29]:

$$\alpha = \alpha_0 \exp(E/E_u) \quad (6)$$

where α_0 is a constant and E_u is the Urbach energy. Fig. 11 shows the (lnα) vs E plots. The slope of this figure equal to $1/E_u$ and from this Urbach energy value of blend polymer is found to be 0.831 eV. Also, α_0 constant is 3.46×10^{-7}.

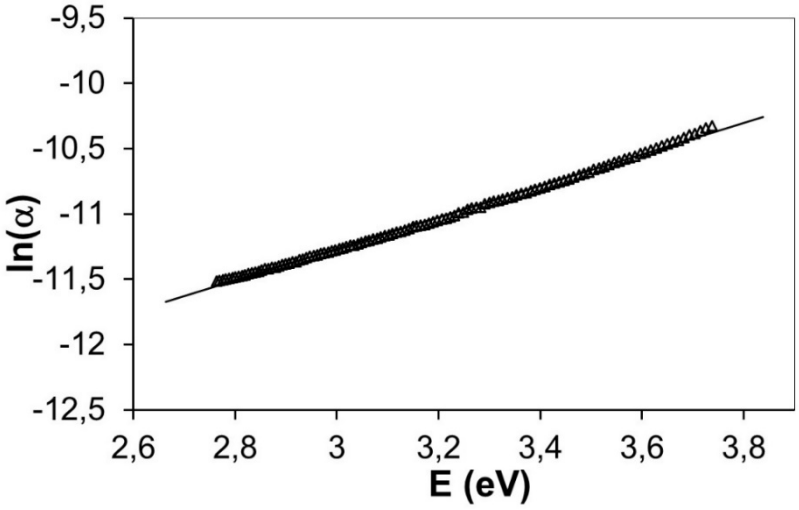

Figure 11: Plots of ln(α) vs: E of blend polymer thin film

Steepness parameter which is a constant corresponds the broadening of absorption edge and characterizes the sates usually caused by electron-phonon interactions [30] in the Urbach spacing. The slope of line in Fig. 11 also gives σ/kT at a constant temperature. Where k is the Boltzmann constant, T is the temperature, σ is the steepness parameter. When the Boltzmann constant are taken as 8.167×10^{-5} eV.K^{-1} and the temperature is 298 K, the steepness parameter of blend polymer is determined as 0.0309.

4. Conclusion

UV/VIS measurements of newly prepared blend polymer [poly(DPMA)/poly(MMA)] thin film were obtained to determine the electro optic parameters. Transmittance was increased depending on the increase in wavelength whereas the reflectance values were decreased. The refractive index at 700 nm was 1.37. The optical band gap (E_g) and the Urbach energy (E_u) were

determined as 3.737 eV and 0.831 eV, respectively. The electronic transition type was indirect allowed transition. The average inter-band oscillator wavelength (λ_o) and oscillator strength (S_o) were found to be 311.7 nm and $9.02x10^{12}$ m^{-2}, respectively. The oscillator energy (E_o) was 3.982 eV and the dispersion energy (E_d) was 3.488 eV. TGA analysis showed that the blend polymer was stable up to 275.4 °C.

Acknowledgments

This work was financially supported by the Adıyaman University Scientific Research Projects Unit with project number (ADYÜBAP/FEFMAP/2021-0002).

References

[1] Zainal, N.F.A., Chan, C.H., *Crystallization and melting behavior of compatibilized polymer blends*, eds: Ajitha A.R., Thomas, S., Compatibilization of polymer blends, Elsevier, 391pp. 2020.

[2] Mishra, J., Tiwari, S.K., Abolhasani, M.M., Azimi, S., Nayak, G.C., Fundamental of polymer blends and its thermodynamics, EDS: Mishra, R.K., Thomas, S., Kalarikkal, N.*, In woodhead publishing series in composites science and engineering, micro and nano fibrillar composites (MFCs and NFCs) from polymer blends*, Woodhead Publishing, 27pp. 2017.

[3] Sabzi, F. Gas transport through polymer blends, eds: Thomas, S., Wilson, R., Kumar S, A., George, S.C., *Transport properties of polymeric membranes*, Elsevier, 517pp. 2018.

[4] Bubmann, T., Seidel, A., Ruckdäsche, H., Altstädt, V., *Transparent PC/PMMA blends with enhanced mechanical properties via reactive compounding of functionalized polymers,* Polymers, 14(1), 73, 2022.

[5] Le, K.P., Lehman, R., Remmert, J., Vanness, K., Ward, P.M.L., Idol, J.D., *Multiphase blends from poly(L-lactide) and poly(methyl methacrylate)*, Journal of Biomaterials Science. Polymer Edition, 17(1-2), 121-137, 2006.

[6] Aid, S., Eddhahak, A., Khelladi, S., Ortega, Z., Chaabani, S., Tcharkhtchi, A., *On the miscibility of PVDF/PMMA polymer blends: Thermodynamics, experimental and numerical investigations*. Polymer Testing, Elsevier, 73, 222-231, 2019.

[7] Kurt, A., Gunduz, B., Koca, M., *A detailed study on the optical properties of 3-benzoyl-7-hydroxy coumarin compound in different solvents and concentrations*, Macedonian Journal of Chemistry and Chemical Engineering, 38(2), 227-236, 2019.

[8] Kurt, A., Koca, M., *Optical properties of poly(2-(5-bromo benzofuran-2-yl)-2-oxoethyl methacrylate)/organoclay nanocomposites*, The Arabian Journal for Science and Engineering, 40, 2975–2984, 2015.

[9] Van Krevelen, D.W., Te Nijenhuis, K., Optical properties, eds: Van Krevelen, D.W., Te Nijenhuis, K., *Properties of polymers (Fourth Edition),* Elsevier, 287pp. 2009.

[10] Su, W.F., *Characterization of polymer. In: Principles of polymer design and synthesis*. *Lecture notes in chemistry,* Springer, Berlin, Heidelberg, 82pp. 2013.

[11] Tikish, T.A., Kumar, A., Kim, J.Y., *Electrical and optical properties of polypyrrole and polyaniline blends*, Polymer Science - Series A, 62, 680–690, 2020.

[12] Takahashi, S., Okada, H., Nobukawa, S., Yamaguchi, M., *Optical properties of polymer blends composed of poly(methyl methacrylate) and ethylene–vinyl acetate copolymer,* European Polymer Journal, 48(5), 974-980, 2012.

[13] Kurt, A., Koca, M., *Blending of poly(ethyl methacrylate) with poly(2-hydroxy-3-phenoxypropyl methacrylate): thermal and optical properties,* The Arabian Journal for Science and Engineering, 39, 5413–5420, 2014.

[14] Marzouk, M.I., Sayed, G.H., Abd ElHalim, M.S., Mansour, S.Y., *Synthesis and characterization of novel pyrazolone derivatives,* European Journal of Chemistry, 5(1), 24-32, 2014.

[15] Koca, M., Kurt, A., *Investigation of optical properties of a novel pyrazole containing polymer poly(1,3-diphenyl-1H-pyrazol-5-yl methacrylate) thin film,* Russian Journal of Physical Chemistry A, 96, 159-165, 2022.

[16] Karrouchi, K., Radi, S., Ramli, Y., Taoufik, J., Mabkhot, Y.N., Al-Aizari, F.A., Ansar, M., *Synthesis and pharmacological activities of pyrazole derivatives: A Review*, Molecules, 23(1), 134, 2018.

[17] Kurt, A., Koca, M., *Synthesis, characterization and thermal degradation kinetics of a new pyrazole derived methacrylate polymer, poly(1,3-diphenyl-1H-pyrazol-5-yl methacrylate),* Acta Chimica Slovenica, 69(2), 466-477, 2022.

[18] Aziz, S.B., Brza, M.A., Nofal, M.M., Abdulwahid, R.T., Hussen, S.A., Hussein, A.M., Karim, W.O., *A comprehensive review on optical properties of polymer electrolytes and composites,* Materials, 13(17), 3675, 2020.

[19] Rawat, A., Mahavar, H., Chauhan, S., Tanwar, A., Singh, P., *Optical band gap of polyvinylpyrrolidone/polyacrylamide blend thin films,* Indian Journal of Pure and Applied Physics, 50(2), 100-104, 2012.

[20] Atyia, H.E., *Influence of deposition temperature on the structural and optical properties of $InSbSe_3$ films*, Journal of Optoelectronics and Advanced Materials, 8(4), 1359-1366, 2006.

[21] Rodriguez, J., Gomez, M., Ederth, J., Niklasson, G.A., Granqvist, C.G., *Thickness dependence of the optical properties of sputter deposited Ti oxide films,* Thin Solid Films, 365(1), 119-125, 2000.

[22] Kurt, A., *Influence of $AlCl_3$ on the optical properties of new synthesized 3-armed poly(methyl methacrylate) films,* Turkish Journal of Chemistry, 34(1), 67-69, 2010.

[23] Wemple, S.H., DrDomenico, M., *Behavior of the electronic dielectric constant in covalent and ionic materials,* Physical Review B, 3, 1338-1351, 1971.

[24] Veena, G., Lobo, B., *Dispersive parameters of oxidized PVA-PVP blend films,* Turkish Journal of Physics, 43, 337–354, 2019.

[25] Ammar, A.H. *Studies on some structural and optical properties of $Zn_xCd_{1-x}Te$ thin films,* Applied Surface Science, 201, 9-19, 2002.

[26] DrDomenico, M., Wemple, S.H., *Oxygen-octahedra ferroelectrics I. Theory of electro-optical and nonlinear optical effects,* Journal of Applied Physics, 40, 720-734, 1969.

[27] Tauc, J., *Amorphous and liquid semiconductors,* Plenum Press, New York, 1974.

[28] Akshay, V.R., Arun, B., Mandal, G., Vasundhara, M., *Visible range optical absorption, Urbach energy estimation and paramagnetic response in Cr-doped TiO_2 nanocrystals derived by a sol–gel method,* Physical Chemistry Chemical Physics, 21(24), 12991-13004, 2019.

[29] Urbach, F., *The long wavelength edge of photographic sensitivity and electronic*

absorption of solids, Physical Review, 92(5), 1324-1330, 1953.

[30] Abu El-Fadl, A., Soltan, A.S., Shaalan, N.M., *Temperature dependence of the indirect band gap, steepness parameter and related optical constants of* $[K_x(NH_4)_{1-x}]_2ZnCl_4$ *mixed crystals,* Optics & Laser Technology, 39(7), 1310-1318, 2007.

Adıyaman University Journal of Science
https://dergipark.org.tr/en/pub/adyujsci
DergiPark AKADEMİK
ISSN 2147-1630
e-ISSN 2146-586X

Parameter Estimation Procedures for Log Exponential-Power Distribution with Real Data Applications

Mustafa Ç. KORKMAZ[1], Kadir KARAKAYA[2*], Yunus AKDOĞAN[3]

[1]*Artvin Çoruh University, Faculty of Education, Department of Measurement and Evaluation, Artvin, Türkiye*
mustafacagataykorkmaz@gmail.com, ORCID: 0000-0003-3302-0705
[2]*Selçuk University, Science Faculty, Department of Statistics, Konya, Türkiye*
kkarakaya@selcuk.edu.tr, ORCID: 0000-0002-0781-3587
[3]*Selçuk University, Science Faculty, Department of Statistics, Konya, Türkiye*
yakdogan@selcuk.edu.tr, ORCID: 0000-0003-3520-7493

Received: 14.02.2022 **Accepted:** 28.09.2022 **Published:** 30.12.2022

Abstract

In this study, some estimation techniques are investigated to estimate two parameters of the log exponential-power distribution. The maximum likelihood, quantile, least squares, weighted least squares, Anderson-Darling, and Cramer-von Mises estimation methods are studied in detail. The efficiency of these estimators is validated through Monte Carlo simulation experiments. Also, four real data applications are performed and Kolmogorov-Smirnov statistic results for all estimators are presented.

Keywords: Point estimation; Log exponential-power distribution; Maximum likelihood estimators; Practical data application.

* Corresponding Author DOI: 10.37094/adyujsci.1073616

Gerçek Veri Uygulamaları ile Log Exponential-Power Dağılımı için Parametre Tahmin Prosedürleri

Öz

Bu makalede, log exponential-power dağılımının iki parametresini tahmin etmek için çeşitli tahmin yöntemleri araştırılmıştır. En çok olabilirlik, kuantil, en küçük kareler, ağırlıklandırılmış en küçük kareler, Anderson-Darling ve Cramer-von Mises tahmin yöntemleri detaylı olarak incelenmiştir. Bu tahmin edicilerin performanslarını değerlendirmek için Monte Carlo simülasyon deneyleri yapılmıştır. Ayrıca dört gerçek veri uygulaması gerçekleştirilmiş ve tüm tahmin ediciler Kolmogorov-Smirnov istatistiği sonuçları sunulmuştur.

Anahtar Kelimeler: Nokta tahmini; Log exponential-power dağılımı; En çok olabilirlik tahmini; Gerçek veri uygulaması.

1. Introduction

The log exponential-power (LEP) model was introduced by [1], applying the $X=\exp(-T)$ transformation where distribution of the T random variable is exponential-power distribution suggested by [2]. Korkmaz et al. [1] investigates some of the mathematical features of the LEP distribution such as moments, coefficient of skewness and kurtosis, order statistics, quantiles, entropies, etc. The LEP distribution is a unit distribution and is an alternative to distributions such as Beta and Kumaraswamy [3]. The probability density function (pdf) and cumulative distribution function of $LEP(\alpha,\beta)$ distribution are presented as:

$$f(x,\alpha,\beta)=\frac{\alpha\beta}{x}e^{\alpha(-\log x)^{\beta}}\left(-\log x\right)^{\beta-1}e^{1-\exp\left\{\alpha(-\log x)^{\beta}\right\}},\quad x\in(0,1) \tag{1}$$

and

$$F(x,\alpha,\beta)=e^{1-\exp\left\{\alpha(-\log x)^{\beta}\right\}},\quad x\in(0,1), \tag{2}$$

where $\alpha>0$ and $\beta>0$ are model parameters. The following is the LEP model's hazard rate function (hrf):

$$h(x,\alpha,\beta)=\frac{\alpha\beta}{x\left(e^{\exp\left\{\alpha(-\log x)^{\beta}\right\}-1}-1\right)}e^{\alpha(-\log x)^{\beta}}\left(-\log x\right)^{\beta-1},\quad x\in(0,1). \tag{3}$$

It is presented in [1] that the hrf of the LEP distribution has unimodal, increasing, U-shaped, bathtub or N-shaped. Figure 1 shows the hrf and pdf plots of the LEP model for different parameter options.

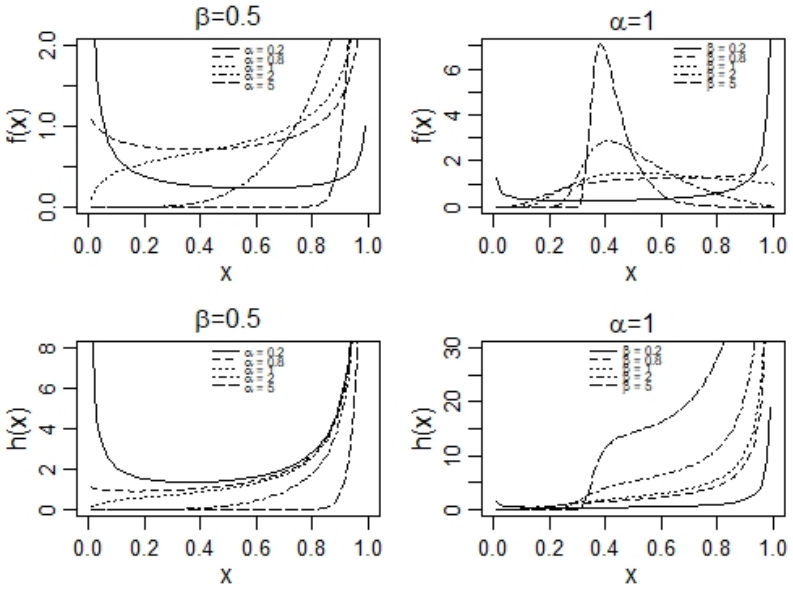

Figure 1: The pdf and hrf plots of the LEP model for some parameter values

Other issues studied in the study of [1] can be listed as follows: Only the maximum likelihood estimator approach was studied in estimate procedure. The LEP distribution was also used to develop a novel quantile regression model. The regression model parameters were also estimated using the maximum likelihood technique. In some scenarios, extensive simulation studies were conducted for the estimation of two distribution parameters.

The goal of this work is to use simulations to evaluate six alternative estimators for the parameters of the LEP distribution. The maximum likelihood estimators (MLE), least squares estimators (LSE), quantile estimators (QE), weighted least squares estimators (WLSE), Anderson-Darling estimators (AD), and Cramer-von Mises estimators (CVM) are examined for point estimation. The remainder of this paper is structured as follows: Six estimate procedures are presented in Section 2. In Section 3, simulation experiment is conducted to assess the performance of these estimators using some criteria such as bias and mean square error (MSE). Four practical data applications are considered in Section 4. Lastly, there are some concluding remarks in Section 5.

2. Different Parameter Estimation Procedures

In this section, six different estimate procedures are discussed for estimating the unknown parameters of the LEP distribution. These methods and details are described in the subsections below.

2.1. Maximum likelihood estimation

In this subsection, the MLE of the LEP distribution is provided. Let $\boldsymbol{\Theta} = (\alpha, \beta)^T$ be the parameter vector and $x_1, x_2, \ldots, x_n$ random sample from the LEP distribution. The log-likelihood function is presented as

$$\ell(\boldsymbol{\Theta}) = n + n\log\alpha + n\log\beta + \alpha\sum_{i=1}^{n}(-\log x_i)^{\beta} + (\beta-1)\sum_{i=1}^{n}\log(-\log x_i) - \sum_{i=1}^{n}e^{\alpha(-\log x_i)^{\beta}}. \quad (4)$$

Then, differentiating (4), for the MLEs, say $\hat{\alpha}$ and $\hat{\beta}$, the normal equations are obtained by

$$\frac{\partial\ell(\boldsymbol{\Theta})}{\partial\alpha} = \frac{n}{\alpha} + \sum_{i=1}^{n}(-\log x_i)^{\beta} - \sum_{i=1}^{n}(-\log x_i)^{\beta}e^{\alpha(-\log x_i)^{\beta}} = 0$$

and

$$\frac{\partial\ell(\boldsymbol{\Theta})}{\partial\beta} = \frac{n}{\beta} + \alpha\sum_{i=1}^{n}\log(-\log x_i)(-\log x_i)^{\beta} - \alpha\sum_{i=1}^{n}\log(-\log x_i)(-\log x_i)^{\beta}e^{\alpha(-\log x_i)^{\beta}} = 0.$$

The numerical technique should be required to acquire the $\hat{\alpha}$ and $\hat{\beta}$. The quasi-Newton or Newton-Raphson algorithms can be utilized for this aim.

2.2. Quantile estimation

The quantile estimation method also known as the percentile estimation method is introduced by [4]. Let $x_{(1)}, x_{(2)}, \ldots, x_{(n)}$ be the order statistics of random sample of size n from the LEP distribution and let $q_i = \frac{i}{n+1}$ for $i = 1, 2\ldots, n$ is the estimation of the $F(x_{(i)}, \alpha, \beta)$. Then, by minimizing the function

$$QE(\boldsymbol{\Theta}) = \sum_{i=1}^{n}\left(x_{(i)} - \exp\left(-\frac{\log(1-\log q_i)}{\alpha}\right)^{1/\beta}\right)^2,$$

according to the model parameters, the QE of the α and β parameters, say $\hat{\alpha}_{QE}$ and $\hat{\beta}_{QE}$, can be determined.

2.3. Least squares estimation

The LSE of α and β, say $\hat{\alpha}_{LSE}$ and $\hat{\beta}_{LSE}$, can be obtained by minimizing the function

$$LSE(\Theta)=\sum_{i=1}^{n}\left(\exp\left(1-\exp\left(\alpha\left(-\log\left(x_{(i)}\right)\right)^{\beta}\right)\right)-\frac{i}{n+1}\right)^{2}.$$

2.4. Weighted least squares estimation

The weighted least squares estimation method is the weighted version of the LSE method. By minimizing the function

$$WLSE(\Theta)=\sum_{i=1}^{n}\frac{(n+2)(n+1)^{2}}{i(n-i+1)}\left(\exp\left(1-\exp\left(\alpha\left(-\log\left(x_{(i)}\right)\right)^{\beta}\right)\right)-\frac{i}{n+1}\right)^{2},$$

the WLSEs of α and β, say $\hat{\alpha}_{WLSE}$ and $\hat{\beta}_{WLSE}$ can be derived.

2.5. Anderson-Darling estimation

The ADE of α and β, say $\hat{\alpha}_{AD}$ and $\hat{\beta}_{AD}$, are determined by minimizing the function

$$\begin{aligned}AD(\Theta)=-n-\sum_{i=1}^{n}\frac{2i-1}{n}\Bigg\{&\log\left(\exp\left(1-\exp\left(\alpha\left(-\log\left(x_{(i)}\right)\right)^{\beta}\right)\right)\right)\\&+\log\left(1-\exp\left(1-\exp\left(\alpha\left(-\log\left(x_{(i)}\right)\right)^{\beta}\right)\right)\right)\\&+\log\left(\exp\left(1-\exp\left(\alpha\left(-\log\left(x_{(i)}\right)\right)^{\beta}\right)\right)\right)+\log\left(1-\exp\left(1-\exp\left(\alpha\left(-\log\left(x_{(i)}\right)\right)^{\beta}\right)\right)\right)\Bigg\}.\end{aligned}$$

2.6. Cramer-von Mises estimation

The CVME of α and β, say $\hat{\alpha}_{CVM}$ and $\hat{\beta}_{CVM}$, are determined by minimizing the function

$$CVM(\Theta)=\frac{1}{12n}+\sum_{i=1}^{n}\left[\exp\left(1-\exp\left(\alpha\left(-\log\left(x_{(i)}\right)\right)^{\beta}\right)\right)-\frac{2i-1}{2n}\right]^{2}.$$

All equations belonging to the above estimation procedures have no explicit solutions. As a result, they must be solved numerically using well-known software such as R , Matlab, and S-Plus utilizing Newton-Raphson and quasi-Newton techniques. Numerical optimization approaches will be used to solve these functions.

3. Simulation Procedure

In this section, the empirical results have been given to see the performance of the pointed out estimators. *N=1000* samples size *n=20, 25, ... ,1000* are generated from a random variable using the LEP distribution. The data generation from the LEP distribution is conducted as follows:

If the random variable U follows the standard uniform distribution, then $X \sim \exp\left\{-\left(\frac{\log\left(1-\log\left(U\right)\right)}{\alpha}\right)\wedge\left(1/\beta\right)\right\}$ follows the LEP distribution. The true values of the first and second Monte Carlo simulation studies are $\Theta=(0.5,0.5)$ and $\Theta=(2,2)$ respectively. Moreover, the empirical mean, bias, and MSE belonging to related estimators have been obtained for comparisons between estimation methods. By setting $\varepsilon=\alpha$ or β, the related bias and MSE are calculated by

$$Bias_{\varepsilon}(n)=\frac{1}{N}\sum_{i=1}^{N}\left(\varepsilon_i-\hat{\varepsilon}_i\right),\quad MSE_{\varepsilon}(n)=\frac{1}{N}\sum_{i=1}^{N}\left(\varepsilon_i-\hat{\varepsilon}_i\right)^2, \tag{5}$$

respectively. Figures 2 and 3 present the results of simulation studies. Figures 2 and 3 show that as the sample size increases, the empirical means go to the true parameter values, all estimators are asymptotically unbiased, and all MSEs go to zero. Simultaneously, as the sample size increases, the empirical results get closer.

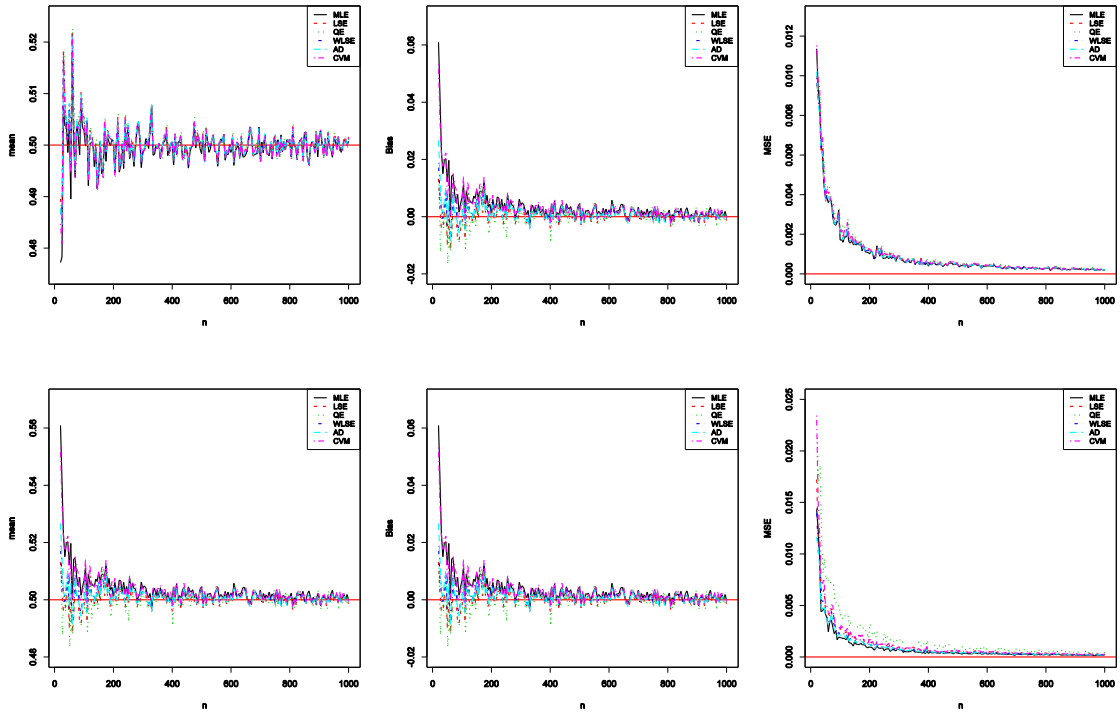

Figure 2: The α (top) and β (bottom) parameters results for $\Theta=(0.5,0.5)$

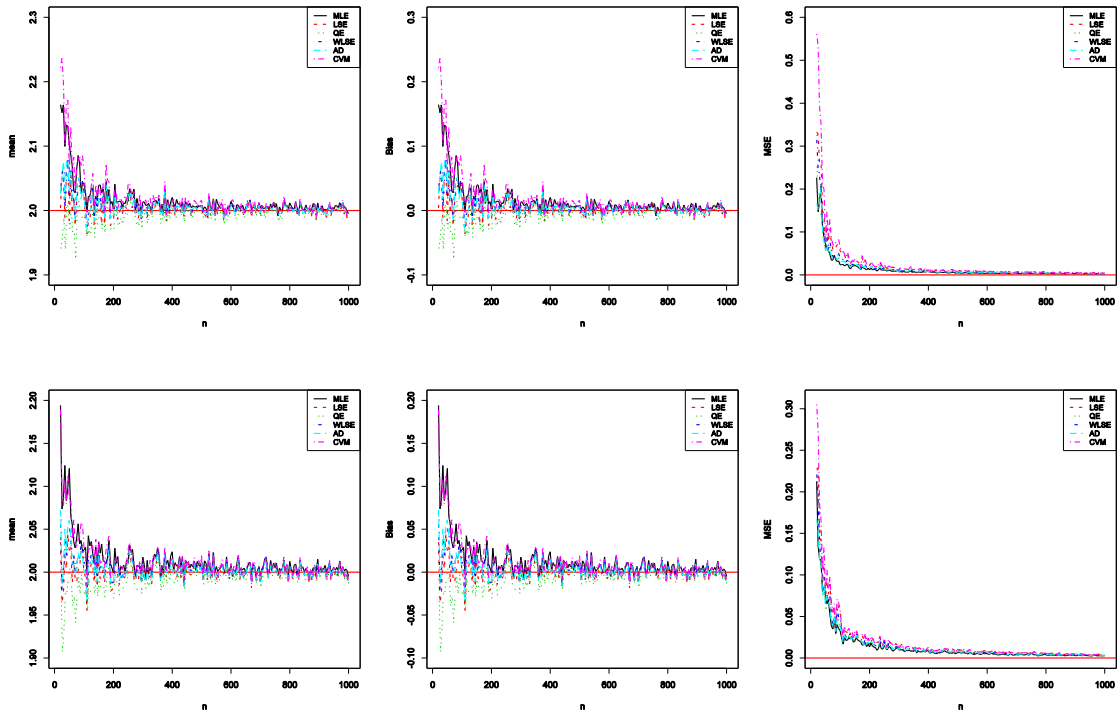

Figure 3: The α (top) and β (bottom) parameters' results for $\Theta = (2, 2)$

4. Real Data Applications

In this section, four practical data applications for the LEP distribution are addressed. The LEP distribution is fitted to four practical datasets by estimating the parameters using the six estimators discussed in the previous sections. The MLE, LSE, QE, WLSE, AD, and CVM the parameters α and β of LEP distribution are achieved by BFGS algorithm and reported in Table 1. Table 1 also shows the Kolmogorov-Smirnov statistics (KS) and related p values for all estimators.

The first data is taken from [5] and represents the flood levels for the Susquehanna River at Harrisburg, Pennsylvania. The data are 0.654, 0.613, 0.315, 0.449, 0.297, 0.402, 0.379, 0.423, 0.379, 0.3235, 0.269, 0.740, 0.418, 0.412, 0.494, 0.416, 0.338, 0.392, 0.484 and 0.265. Recently, this data has been examined in [6, 7].

The second data set comes from [8] and show the strengths of 1.5 cm glass fibers, which were first measured by researchers at the UK National Physical Laboratory. The data are 0.17, 0.13, 0.16, 0.14, 0.20, 0.15, 0.13, 0.11, 0.15, 0.12, 0.12, 0.15, 0.12, 0.16, 0.21, 0.20, 0.23, 0.16, 0.12, 0.10, 0.32, 0.33, 0.33, 0.36, 0.38, 0.20 and 0.26.

The third data set is taken from [9] and consist of 48 rock samples from a petroleum reservoir. The detailed information about data given in [9]. Recently, this data has been examined

in [10, 11]. The data are 0.0903296, 0.2036540, 0.2043140, 0.2808870, 0.1976530, 0.3286410, 0.1486220, 0.1623940, 0.2627270, 0.1794550, 0.3266350, 0.2300810, 0.1833120, 0.1509440, 0.2000710, 0.1918020, 0.1541920, 0.4641250, 0.1170630, 0.1481410, 0.1448100, 0.1330830, 0.2760160, 0.4204770, 0.1224170, 0.2285950, 0.1138520, 0.2252140, 0.1769690, 0.2007440, 0.1670450, 0.2316230, 0.2910290, 0.3412730, 0.4387120, 0.2626510, 0.1896510, 0.1725670, 0.2400770, 0.3116460, 0.1635860, 0.1824530, 0.1641270, 0.1534810, 0.1618650, 0.2760160, 0.2538320 and 0.2004470.

The fourth data set comes from [9] and show total milk production in the first birth of 107 cows from SINDI race. Recently, this data has been examined in [12, 13]. The data are 0.4365, 0.4260, 0.5140, 0.6907, 0.7471, 0.2605, 0.6196, 0.8781, 0.4990, 0.6058 ,0.6891 ,0.5770, 0.5394, 0.1479, 0.2356, 0.6012, 0.1525, 0.5483, 0.6927, 0.7261, 0.3323, 0.0671, 0.2361, 0.4800, 0.5707, 0.7131, 0.5853, 0.6768 ,0.5350, 0.4151 ,0.6789, 0.4576, 0.3259, 0.2303, 0.7687, 0.4371 ,0.3383, 0.6114, 0.3480, 0.4564, 0.7804, 0.3406, 0.4823, 0.5912 ,0.5744, 0.5481, 0.1131, 0.7290, 0.0168, 0.5529 ,0.4530, 0.3891, 0.4752, 0.3134, 0.3175 ,0.1167, 0.6750 ,0.5113,0.5447, 0.4143, 0.5627, 0.5150, 0.0776, 0.3945 ,0.4553, 0.4470, 0.5285, 0.5232, 0.6465, 0.0650, 0.8492, 0.8147, 0.3627, 0.3906, 0.4438, 0.4612, 0.3188, 0.2160, 0.6707, 0.6220, 0.5629, 0.4675, 0.6844, 0.3413,0.4332, 0.0854, 0.3821, 0.4694, 0.3635, 0.4111, 0.5349, 0.3751, 0.1546, 0.4517 ,0.2681, 0.4049, 0.5553, 0.5878 ,0.4741 ,0.3598, 0.7629, 0.5941, 0.6174, 0.6860, 0.0609, 0.6488 and 0.2747.

Table 1: Parameter estimation and KS results for four data sets based on the six estimators

		Parameter		**KS**	
Data	**Estimators**	α	β	Statistics	p-values
First	**MLE**	0.6593	2.9191	0.1366	0.8494
	LSE	0.6573	2.7806	0.1360	0.8529
	QE	0.2719	2.1158	0.5264	0.0001
	WLSE	0.6507	2.6582	0.1390	0.8339
	AD	0.6581	2.8151	0.1359	0.8535
	CVM	0.6679	3.0180	0.1317	0.8783
Second	**MLE**	0.0413	4.3744	0.1120	0.8870
	LSE	0.0584	3.7762	0.1063	0.9202
	QE	0.0330	4.3681	0.1699	0.4164
	WLSE	0.0566	3.8574	0.1044	0.9296
	AD	0.0530	3.9659	0.1050	0.9271
	CVM	0.0512	3.9894	0.0990	0.9537
Third	**MLE**	0.0938	3.5262	0.0966	0.7607
	LSE	0.0757	3.9984	0.0655	0.9859
	QE	0.0466	3.5564	0.4307	0.0000
	WLSE	0.0782	3.9342	0.0664	0.9837
	AD	0.0816	3.8366	0.0659	0.9850
	CVM	0.0709	4.1299	0.0633	0.9906

Fourth	**MLE**	0.6396	0.9669	0.1746	0.0029
	LSE	0.8227	1.6112	0.1075	0.1685
	QE	0.6623	1.0339	0.1437	0.0240
	WLSE	0.8150	1.6911	0.1116	0.1389
	AD	0.6815	1.1128	0.1280	0.0597
	CVM	0.8281	1.6353	0.1107	0.1451

5. Concluding Remarks

The LEP distribution proposed by [1] is explored in this work with relation to several point estimations. The two unknown parameters of the LEP distribution are estimated using six estimators. For two different parameter values and sample sizes, extensive Monte Carlo simulations are conducted. It is observed that when the size of the sample increases, the mean of all estimators neared the real parameter value, their biases and MSEs decreased and approached zero. In addition, the estimations and KS results for all estimators for four real data are examined.

Conflicts of Interest

No conflict of interest was declared by the authors.

References

[1] Korkmaz, M.Ç., Altun, E., Alizadeh, M., El-Morshedy, M., *The Log Exponential-Power Distribution: Properties, Estimations and Quantile Regression Model*, Mathematics, 9 (21), 2634, 2021.

[2] Smith, R.M., Bain, L.J., *An exponential power life-testing distribution*, Communication in Statistics Theory Methods, 4, 469–481, 1975.

[3] Kumaraswamy, P., *A generalized probability density function for double-bounded random processes*, Journal of Hydrology, 46, 79–88, 1980.

[4] Kao, J.H., *Computer methods for estimating Weibull parameters in reliability studies*, IRE Transactions on Reliability and Quality Control, 13, 15-22, 1958.

[5] Dumonceaux, R., Antle, C.E., *Discrimination between the log-normal and the Weibull distributions*, Technometrics, 15 (4), 923-926, 1973.

[6] Balakrishnan, N., Cohen, A.C., *Order Statistics & Inference: Estimation Methods,* Elsevier, Amsterdam, The Netherlands, 2014.

[7] Alizadeh, M., Altun, E., Cordeiro, G.M., Rasekhi, M., *The odd power Cauchy family of distributions: Properties, regression models and applications*, Journal of Statistical Computation and Simulation, 88, 785–807, 2018.

[8] Elgarhy, M., *Exponentiated generalized Kumaraswamy distribution with applications*, Annals of Data Science, 5 (2), 273-292, 2018.

[9] Cordeiro, G.M., dos Santos Brito, R., *The beta power distribution*, Brazilian Journal Of Probability And Statistics, 26 (1), 88-112, 2012.

[10] Opone, F., Iwerumor, B., *A new Marshall-Olkin extended family of distributions with bounded support*, Gazi University Journal of Science, 34 (3), 899-914, 2021.

[11] Balogun, O.S., Iqbal, M.Z., Arshad, M.Z., Afify, A.Z., Oguntunde, P.E., *A new generalization of Lehmann type-II distribution: Theory, simulation, and applications to survival and failure rate data*, Scientific African, 12, e00790, 2021.

[12] Saraçoğlu, B., Tanış, C., *A new statistical distribution: cubic rank transmuted Kumaraswamy distribution and its properties*, Journal of the National Science Foundation of Sri Lanka, 46 (4), 505-518, 2018.

[13] Jamal, F., Chesneau, C., *A new family of polyno-expo-trigonometric distributions with applications*, Infinite Dimensional Analysis, Quantum Probability and Related Topics, 22 (04), 1950027, 2019.

Adıyaman University Journal of Science
https://dergipark.org.tr/en/pub/adyujsci
DergiPark AKADEMİK
ISSN 2147-1630
e-ISSN 2146-586X

Contributions to the Flora of Çelikhan District (Adıyaman)

Ömer KILIÇ[1,*], Şinasi YILDIRIMLI[2]

[1] *Adıyaman University, Faculty of Pharmacy, Department of Basic Science of Pharmacy, 02000, Adıyaman, Türkiye*
okilic@adiyaman.edu.tr, ORCID: 0000-0003-3409-1572
[2] *Hacettepe University, Faculty of Science, Department of Biology, 06000, Ankara, Türkiye*
ot@hacettepe.edu.tr, ORCID: 0000-0001-9648-7471

Received: 13.07.2022 **Accepted:** 29.09.2022 **Published:** 30.12.2022

Abstract

This study was carried out to contribute to the flora of Çelikhan District (Adıyaman). 592 plant samples were collected from the research area. As a result of the evaluation of these plants, a total of 454 taxa were identified, including 295 genera belonging to 62 families. Of these taxa, 3 of them were belong to Pteridophyta and 451 of Spermatophyta divisions. Coniferophyta and Magnoliophyta subdivisions in the Spermatophyta division contained 2 and 449 taxa, respectively. It was determined that 449 taxa were belong to Magnoliophyta subdivision, 385 were belong to Magnoliopsida and 64 were belong to Liliopsida class. It was determined that 30 taxa from the study area were endemic, and the endemism rate was found to be 6.6%. The distribution of taxa according to phytogeographic regions were as follows: Anatolian-Turan 158 (34.8%), Mediterranean 34 (7.5%), Euro-Siberian 33 (7.1%), multi-regional and unknown phytogeographical regions 229 (50.4%). The first five family according to the number of taxa were; Asteraceae 42 (9.2%), Fabaceae 37 (8.1%), Brassicaceae 36 (7.9%), Lamiaceae 35 (7.7%), Poaceae 31 (6.8%). The first five genera according to the number of taxa were; *Astragalus* 9, *Silene* 8, *Salvia* 7, *Trifolium* 6 and *Vicia* 6. Within the scope of the study, a new and endemic onion species was discovered, named Adıyaman and this species was introduced to the literature as *Allium adiyamanense* Yıld. & Kılıç.

* Corresponding Author DOI: 10.37094/adyujsci.1143607

Keywords: Plant; Flora; Çelikhan; Adıyaman; Turkey

Çelikhan İlçesi (Adıyaman) Florasına Katkılar

Öz

Bu çalışma, Çelikhan İlçesi (Adıyaman) ve yakın çevresinin florasına katkı sunmak amacıyla yapıldı. Araştırma alanından 592 bitki örneği toplandı. Bu bitkilerin değerlendirilmesi sonucunda toplamda 62 familyaya ait 295 cins olmak üzere toplam 454 takson tespit edildi. Bu taksonlardan 3'ü Pteridophyta ve 451'i Spermatophyta bölümlerine aittir. Spermatophyta bölümündeki Coniferophyta ve Magnoliophyta alt bölümleri sırasıyla 2 ve 449 takson içermekte. Magnoliophyta alt bölümüne ait 449 taksonun 385'nin Magnoliopsida, 64'nün Liliopsida sınıfına ait olduğu belirlendi. Çalışma alanından 30 taksonun endemik olduğu belirlenerek endemizm oranı %6.6 olarak tespit edildi. Taksonların fitocoğrafik bölgelere göre dağılımı şöyledir: Anadolu-Turan 158 (%34.8), Akdeniz 34 (%7.5), Avrupa-Sibirya 33 (%7.1), çok bölgeli ile bilinmeyen fitocoğrafik bölgeler 229 (%50.4). Takson sayısına göre ilk beş familya; Asteraceae 42 (%9.2), Fabaceae 37 (%8.1), Brassicaceae 36 (%7.9), Lamiaceae 35 (%7.7), Poaceae 31 (%6.8). Takson sayısına göre ilk beş cins; *Astragalus* 9, *Silene* 8, *Salvia* 7, *Trifolium* 6, *Vicia* 6. Çalışma kapsamında yeni ve endemik bir soğan türü keşfedilip Adıyaman ismi verilerek *Allium adiyamanense* Yıld. & Kılıç olarak literatüre kazandırıldı.

Anahtar Kelimeler: Bitki; Flora; Çelikhan; Adıyaman; Türkiye.

1. Introduction

Turkey is rich in plant diversity. More than 13.000 plant taxa have natural distribution in Turkey. Some of the reasons of Turkey's plant diversity can be listed as follows; Turkey includes three phytogeographic (Europe-Siberian, Mediterranean, Anatolian-Turanian) regions, geographical location, its topography, habitat diversity, being in the transition zone between Europe and Asia, geomorphological structure, different edaphic factors and ecological characteristics [1]. The research area is in the Anatolian-Turan phytogeographic region. The vegetation of the study area and its surroundings mostly depends on the topographic structure and ecological characteristics of the region. Although the continental climate type is generally seen in Adıyaman, the features of the Mediterranean climate are also encountered in some parts of the province. As a result of the field studies and observations, there are three dominant vegetation types in the project area and its near surroundings. These are; degraded forest-bush vegetation, steppe vegetation and aquatic-humid area vegetation.

The new species, *Aethionema adiyamanense* Yıld. & Kılıç, *Pimpinella adiyamanensis* Yıld. & Kılıç, *Allium adiyamanense* Yıld. & Kılıç [2-3], which were discovered in recent years; are also indicators that Adıyaman and its surroundings have an important potential in terms of plant diversity and richness. It is expected that the data obtained from this study will contribute to the relevant fields and shed light on them.

With this study, it is aimed to contribute the flora of Çelikhan (Adıyaman) district and to enrich Adıyaman University Pharmacy Faculty Herbarium.

2. Material and Methods

The research materials consist of plant samples that were collected with periodic field studies in the vegetation at periods of 2019-2022. Plant materials in the area were collected in accordance with the herbarium collection techniques and in a way to include the organs necessary for identification. The necessary information of these samples was recorded, and identification of plant materials were done by project member taxonomists Prof. Dr. Ömer Kılıç and Prof. Dr. Şinasi Yıldırımlı with the "Flora of Turkey and the East Aegean Islands" books [4] and with the help of a stereomicroscope. Some of the specimens were turned into herbarium specimens and kept in Adıyaman University Pharmacy Faculty Herbarium. The biological types of taxa were detected according to Raunkiaer [5]. IUCN (2012, 2013, 2021) sources were used to determine the hazard categories of endemic taxa [6-8]. The climate characteristics of the research area was evaluated using the data of the relevant meteorology station. The climate diagram was drawn according to the Gaussen (1955) method [9]. Climate type and bioclimatic layer were calculated and interpreted according to the Emberger method [10].

3. General Properties of Research Area

The research area is located in the C7 square according to Davis's grid system (Fig. 1). The main settlements in and around the research area are; Yeşilyayla, Yoğutlu, Köseuşağı, Aksu, Deveboynu, Yedioluk, Kozan, Koçali, Ormaniçi, Gökçay, Bulam, Recep, Korucak, Doğanlı, Şemikan, Karaçayır, Mutluca, Konakdere, Çatalağaç, Şahverdi, Kuyucak, Derinsu, Pınarbaşı, Kavak Mustafabeyli, Safe, Karadere, Rezip villages and their hamlets. The altitude of the research area varies between 1000-2000 m. The location map of the research area is shown in Fig. 2.

Adıyaman, is located in the southeast of Turkey, south of the Upper Euphrates Section of the Eastern Anatolia Region and north of the Middle Euphrates Section of the South-eastern Anatolia Region. Çelikhan, located between Malatya and Adıyaman cities, was established among the high mountains, which are the continuation of the Southeast Taurus Mountains. The

most important streams are Bulam and Abdulharap streams. Çat Dam is located on Abdulharap Stream. The altitude of the Çelikhan centre is 1387 m. There is Bozdağ Mountain (2.250 m) in the west, Bezar Mountain (1.900 m) in the south, Akdağ Mountain (2.506 m) in the east and Beydağ Mountain (2.544 m) in the north of Çelikhan. In the study area, there are different habitats such as steppe, bush, forest, rocky area, wetland, meadow areas, and the vegetation is shaped according to these habitats, in addition to ecological and geomorphological characteristics of the research area. In the study area, plant taxa belonging to the steppe formation were dominant.

In order to determine and interpret the climatic characteristics of the research area, the last ten years meteorological data of the Çelikhan district were used. Climate data are shown in Table 1 and Table 2, and the climate diagram is shown in Fig. 3.

Table 1: Climatic data of Çelikhan for the years 2012-2021

	Jan	Feb	Mar	Apr	May	Jun	July	Aug	Sept	Oct	Nov	Dec	Yearly Average
Temp (°C)	0.8	2.5	6.07	11.1	15.4	20.7	25.4	26.2	21.2	14.4	7.3	1.9	12.7
Min. Temp. (°C)	-12.1	-8.1	-4.5	0.3	5.2	9.6	11.3	12.1	7.1	5.53	-1.5	-8.2	1.4
Max. Temp. (°C)	9.1	14.6	17.9	23.9	28.01	33.3	36.1	36.5	33.7	24.6	19.0	11.2	24.0
Monthly relative humidity (mm)	75.4	70.4	64.4	56.1	57.0	40.3	29.3	29.6	36.3	51.2	63.0	74.2	47.9
Monthly precipitation (mm)	134.9	75.2	102.5	59.4	73.0	14.5	0.6	3.6	20.5	49.4	61.0	49.0	53.6

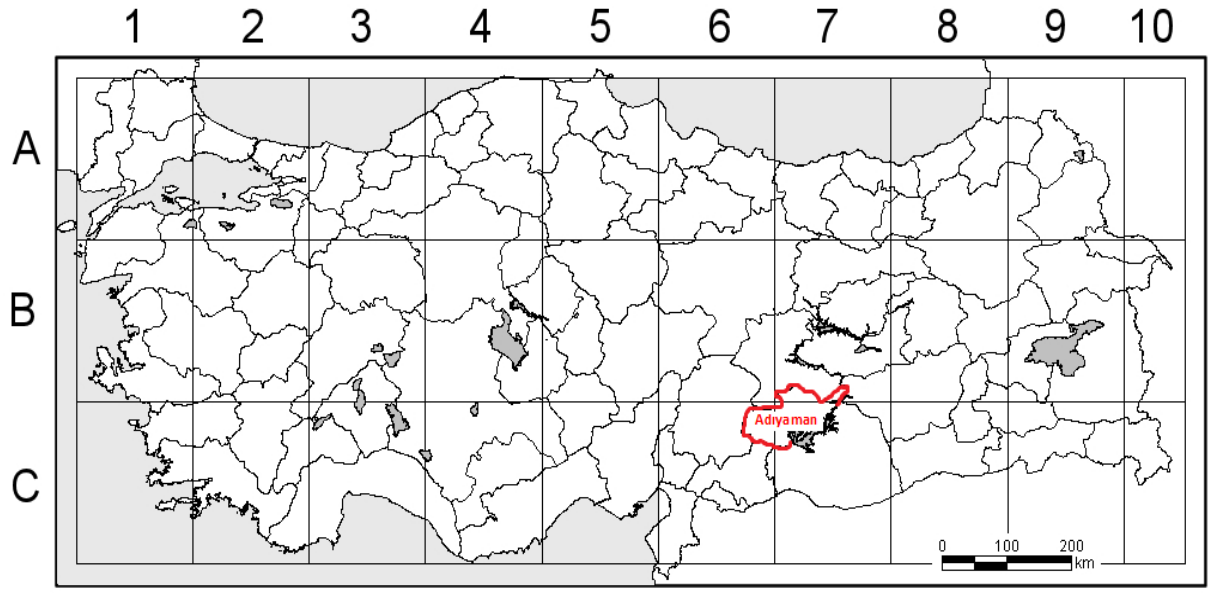

Figure 1: The location of Adıyaman according to the grid system

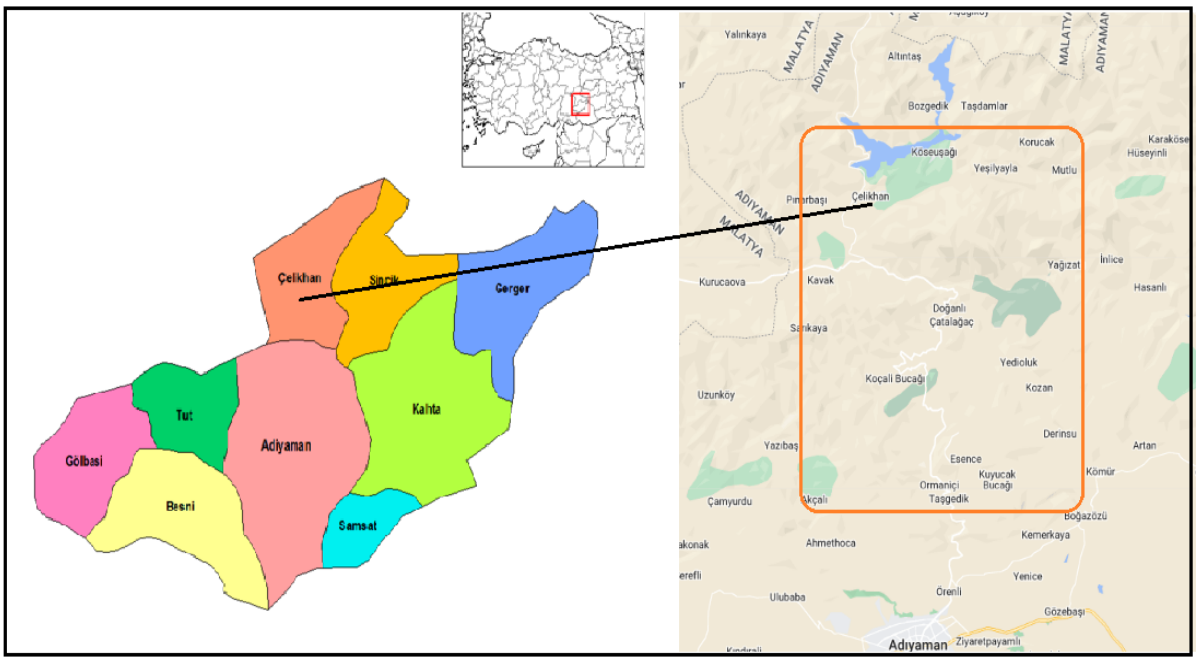

Figure 2: Location map of the research area

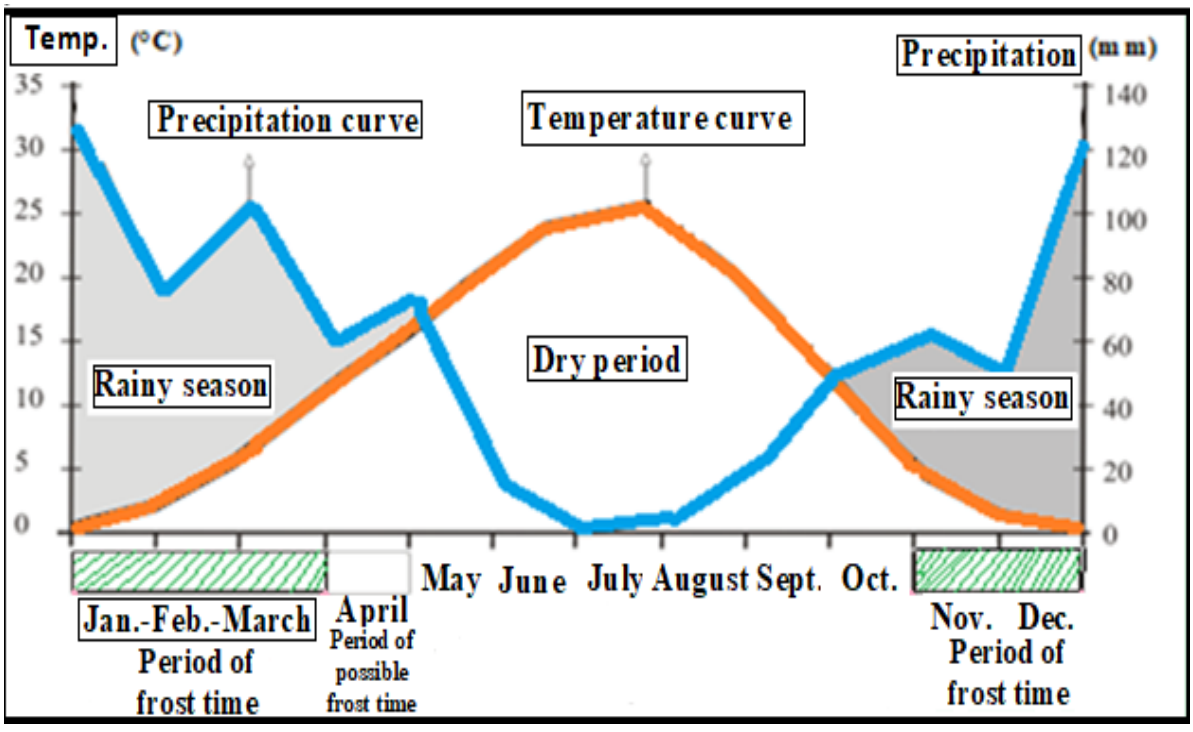

Figure 3: Climate diagram of Çelikhan

Table 2: Seasonal precipitation (mm) data of Çelikhan

Dec	Jan	Feb	March	Apr	May	June	July	August	Sept	Oct	Nov	Yearly
48.9	133.8	75.1	101.5	59.3	73.0	14.2	0.6	3.5	20.5	49.2	61.1	Average
	257.8			233.8			18.3			130.8		640.7

The highest average rainfall in Çelikhan was 134.9 mm in January. It is seen that the average relative humidity rate is the highest in January with a rate of 75.4%. Due to reasons such as different geomorphological and ecological characteristics of the Çelikhan district and its immediate surroundings, due to the roughness and mountainousness, the winter season is harsh in this district and therefore the possible frost event lasts for 4 months during the year. According to the climatic data of Çelikhan station, the average annual precipitation is 640.7 mm, and it is seen that the season with the highest average annual precipitation is winter (Table 2).

When Emberger's drought index (S = PE / M) formula is calculated using the climatic data of Çelikhan, the "S" value is 0.5 and *semi-arid mediterranean climate type* is observed in the research area [11]. When the seasonal distribution of precipitation in Çelikhan is examined (Table 2), it is seen that the most precipitation is in the winter season. After the winter season, the seasons with the highest precipitation are spring (S), autumn (A) and summer (S), respectively. So, the precipitation regime of research area is ranking winter, spring, autumn, summer; forming the *first type of the eastern mediterranean precipitation regime* [11].

4. Results

As a result of the evaluation of the collected plants, a total of 454 taxa were identified. It was determined that 30 taxa from the study area were endemic. The distribution of taxa according to phytogeographic regions was as follows: Anatolia-Turan 158, Mediterranean 34, Euro-Siberia 33, multi-regional and unknown phytogeographic regions 229. The first five families according to the number of taxa; Compositae 42, Leguminosae 37, Cruciferae 36, Labiatae 35, Graminea 31. The first five genera according to the number of taxa; *Astragalus* 9, *Silene* 8, *Salvia* 7, *Trifolium* 6, *Vicia* 6. *Allium adiyamanense* Yıld. & Kılıç was identified as a new and endemic species by the Project members. Photographs of some of the detected taxa and some images from the research area were given as supplementary material.

The localities, habitats and altitudes where the plants are collected are shown as codes in the list below and the locality and habitats of the taxa are indicated by using these codes in the plant list.

1. Çelikhan road right sections 8-10. km slopes, right and left of the road, stony areas, 1350-1400 m.

2. Yeşilyayla village surroundings, steppe areas, 1700-1800 m.

3. Akdağ northern slopes, steppe-stony areas, 1650-1750 m.

4. Northern parts of Şerefhan village, humid areas, 1400-1500 m.

5. Around Doğanlı village, degraded forest clearing, 1400-1500 m.

6. Eastern parts of Şemikan village, steppe, 1100-1200 m.

7. Mountains, slopes, steppe areas throughout Karaçayır village, 1300-1400 m.

8. Akdag, on the southwest slopes of the vineyards and around the summit, 1400-1500 m.

9. Eastern and western parts of Mutluca village, steppe areas, 1350-1450 m.

10. Southern and northern parts of Doğanlı village, steppe, humid areas, 1250-1350 m.

11. Kuyucak village surroundings, moist-stony habitats, 950-1050 m.

12. Çelikhan road, right sections, roadside, slopes, steppe stony areas, 1300-1400 m.

13. Konakdere village surroundings, forest clearings and steppe, 1300-1400 m.

14. Çatalağaç village entrance, roadsides, 1300-1400 m.

15. Northern parts of Şahverdi village plateau, humid areas, 1250-1350 m.

16. Sirinsu fountain surroundings, slopes, stream sides, 1200-1300 m.

17. Mustafabeyli village surroundings, slopes, 1250-1350 m.

18. Şıhment area, northern slopes of Akdağ, around the fountain, 1850-1950 m.

19. Different habitats around the Güvenli village, 1300-1450 m.

20. Southern parts of Karadere village, slopes, 1400-1500 m.

21. Rezip village surroundings, steppe, 1000-1100 m.

22. Areas of Eti Bakır Krom business, humid, steppe regions, 1350-1500 m.

23. Yeşilyayla village surroundings, humid areas, 1700-1800 m.

24. Celikhan road 25-30 km, right and left of the road, slopes, 1300-1400 m.

25. Southern parts of Ormaniçi village, slopes, 1350-1450 m.

26. Eastern parts of Gökçay village, steppe-stony areas, 1400-1500 m.

27. Bulam village entrance, roadsides, 1250-1400 m.

28. Korucak village surroundings, steppe areas, 1350-1450 m.

29. Çelikhan road 35-40. km, right and left slopes of the road, 1350-1500 m.

30. Çelikhan, Başpınar neighborhood upper parts, 1500-1600 m.

31. Akdag, northern slopes, around Barziv, 1800-1900 m.

32. Eskiköy hamlet, stony and steppe areas at the upper parts of the mine, 1500-1550 m.

33. Çelikhan road left-right sections 45-50 km, slopes, 1400-1500 m.

34. Southern parts of Koçali village, steppe, 1150-1200 m.

35. Steppe south of Yoğutlu village, 1350-1500 m.

36. Aksu village, Çığdere locality, 900-1000 m.

37. Deveboynu village surroundings, steppe areas, 1250-1400 m.

38. Area around Recep village, moist habitats, 1300-1400 m.

39. From Adıyaman to Çelikhan, on the 55-60 th km of the road, right-left sections, slope, 1100-1200 m.

40. Between Çelikhan and Yeşilyurt, 15-20. km, right and left of road, stony slopes, 1350-1450 m.

41. Steppe slopes between Köseuşağı and Yeşilyayla villages, 1650-1750 m.

42. Between Koçali and Adıyaman, 10 km after Koçali, Ouercetum, sandy hills, 1300-1400 m.

43. Between Yesilyurt-Çelikhan, slopes, rocky and stony habitats, 1650-1865 m.

44. Humid areas between Yedioluk and Kozan villages, 1150-1250 m.

45. Kuyucak village surroundings, steppe habitats, 950-1050 m.

46. Between Kavak and Pınarbaşı villages, steppe, 1300-1400 m.

47. Between Koçali and Çelikhan, watery valley, oak (*Quercus brandii*) forest, 1060-1160m.

48. Derinsu village surroundings, moist habitats, 1100-1200 m.

49. Between Koçali and Çelikhan, Doğanlı village, Meydan hill, 1200-1300 m.

50. From Çelikhan to Akdağ, forest areas, 1600-1700 m.

4.1. Plant List

Abbreviations used in plant list are as follows; Akd.: Mediterranean; Av.-Sib.: Euro-Siberian; An.-Tur.: Anadolu-Turan; End.: Endemic; ÖK: Ömer Kılıç; ŞY: Şinasi Yıldırımlı, Fa: fanerophyte; Hk: hemicryptophyte; Ka: kamefit; Cr: cryptophyte; T: therophyte; EN: endangered; VU: vulnerable; LC: least concern; NT: near threatened.

PTERIDOPHYTA

DENNSTAEDTIACEAE

Pteridum aquilinum (L.) Kuhn, 7051, 02.07.2020, Hk.

ADIANTACEAE

Adiantum capillus-veneris L., 36, 18.06.2020, ÖK 6992. Hk.

EQUISETACEAE

Equisetum ramosissimum Desf., 10, 20.05.2021, ÖK 7112. Kr.

ATHYRIACEAE

Cystopteris fragilis (L.) Bernh., 4, 12.05.2022, ÖK 7351. Hk.

SPERMATOPHYTA

GYMNOSPERMAE

CUPRESSACEAE

Juniperus oxycedrus L., 8, 14.06.2021, ÖK 7195. Fa.

PINACEAE

Cedrus libani A.Rich var. *libani,* 2, 25.05.2022, ÖK 7352. Fa.

Picea orientalis (L.) Link, 30, 10.06.2021, ÖK 7196. Fa.

Pinus nigra Aiton. subsp. *pallasiana* (Lamb.) Holmboe, 30, 15.06.2021, ÖK 7197. Fa.

EPHEDRACEAE

Ephedra major Host, 16, 26.05.2021, ÖK 7113. Ka.

ANGIOSPERMAE

RANUNCULACEAE

Caltha polypetala Hochst. ex Lorent, 9, 10.06.2020, ÖK 7047. Hk.

Nigella nigellastrum (L.) Wilk., 19, 10.06.2020, ÖK 7050. Hk.

Delphinium peregrinum L., 1, 16.06.2021, ÖK 7198. Hk.

Consolida orientalis (Gay.) Schröd., 2, 15.04.2022, ÖK 7300. T.

Clematis flammula L., 3, 02.06.2020, ÖK 7042. Hk.

Adonis aestivalis L. subsp. *aestivalis*, 4, 20.05.2021, ÖK 7114. T.

Ranunculus cuneatus Boiss., 13, 12.06.2022, ÖK 7401. Hk.

Ranunculus damascenus Boiss. & Gaill., 1, 23.06.2022, ÖK 7442. An.-Tur. Kr.

Ceratocephalus falcatus (L.) Pers., 2, 12.06.2020, ÖK 6994. T.

Thalictrum minus L. var. *minus* Boiss., 5, 16.06.2020, ÖK 6995. Hk.

Anemone coronaria L., 6, 01.06.2020, ÖK 6990. Kr.

BERBERIDACEAE

Bongardia chrysogonum (L.) Griseb., 3, 17.06.2020, ÖK 6996. An.-Tur. Hk.

Leontice leontopetalum L. subsp. *leontopetalum* 4, 17.06.2020, ÖK 6997. Hk.

PAPAVERACEAE

Glaucium corniculatum (L.)Rud.subsp.*refractum* (Nàb.)Cullen, 7,16.06.2021,ÖK 7199.An.-Tur. Hk.

Roemeria hybrida (L.) DC. subsp. *hybrida,* 8, 16.05.2020, ÖK 6940. T.

Papaver rhoeas L., 9, 14.05.2020, ÖK 6941. Hk.

Papaver clavatum Boiss., 31, 04.05.2021, ÖK 7115. Hk. End.

Hypecoum imberbe Sibth. & Sm., 11, 16.04.2021, ÖK 7101. T.

Corydalis haussknechtii Liden, 12, 24.04.2022, ÖK 7301. Kr.

Fumaria officinalis L., 13, 16.05.2020, ÖK 6942. T.

BRASSICACEAE

Brassica deflexa Boiss, 14, 21.05.2021, ÖK 7116. T. An.-Tur.

Sinapis arvensis L. subsp. *arvensis*, 15, 18.04.2022, ÖK 7302. T.

Conringia orientalis (L.) Andrz., 16, 01.05.2020, ÖK 6943. T.

Cardaria draba (L.) Desv. subsp. *draba,* 17, 04.05.2021, ÖK 7117. Hk.

Coluteocarpus vesicaria (L.) Holmboe subsp.*vesicaria*, 18,14.05.2021, ÖK 7118. An.-Tur. Hk.

Aethionema adiyamanense Yıld. & Kılıç, 47, 18.06.2019, ŞY 44198. An.-Tur. Hk. End. New species. NT.

Aethionema arabicum (L.) Andrz. ex DC., 38, 20.05.2020, ÖK 6944. T.

Aethionema schistosum Boiss. & Kotschy, 42, 20.05.2020, ŞY 30793.

Aethionema membranaceum (Desf.) DC. 40, 24.11.2019, ŞY 43178

Erysimum smyrnaeum Boiss. & Balansae, 40, 24.11.2019, ŞY 43179.

Fibigia clypeata (L.) Medicus 40, 23.05.2017, ŞY 43180.

Fibigia eriocarpa (DC.) Boiss. 40, 23.05.2017, ŞY 43181.

Thlaspi arvense L., 32, 04.05.2020, ÖK 6945. T.

Capsella bursa-pastoris (L.) Medik., 13, 20.03.2020, ÖK 6899. T.

Alyssum praecox Boiss. et Bal. var. *praecox*, 15, 20.04.2021, ÖK 7102. End. LC. Ka.

Alyssum murale Waldst. & Kit. var. *murale*, 16, 01.05.2020, ÖK 6946. T.

Draba nemorosa L., 17, 14.05.2020, ÖK 6947. T.

Arabis deflexa Boiss., 18, 15.03.2020, ÖK 6890. Akd. Hk.

Barbarea auriculata Hausskn. ex Bornm. var. *auriculata*, 19, 20.04.2020, ÖK 6936. End. Hk.

Isatis candolleana Boiss. 20, 24.04.2022. ÖK 7303. End. Hk. An.-Tur.

Cardamine uliginosa Bieb., 21, 20.05.2020, ÖK 6948. Hk.

Drabopsis verna K. Koch, 22, 01.05.2021, ÖK 7119. An.-Tur. T.

Hesperis bicuspidata (Willd.) Poir., 23, 16.04.2020, ÖK 6937. Hk.

Erysimum eginense Hausskn. ex Bornm., 24, 20.03.2020, ÖK 6895. End. Hk.

Alliaria petiolata (M. Bieb.) Cavara & Grande, 25, 27.03.2020, ÖK 6898. T.

Sisymbrium altissimum L., 26, 21.06.2020, ÖK 6999. T.

Descuraina sophia (L.) Webb ex Prantl, 27, 24.05.2021, ÖK 7120. T.

RESEDACEAE

Reseda armena Boiss. var. *armena*, 28, 06.06.2021, ÖK 7210. End. An.-Tur. Hk.

CISTACEAE

Helianthemum ledifolium (L.) Mill. var. *ledifolium*, 29, 21.06.2020, ÖK 7000. Hk.

VIOLACEAE

Viola odorata L., 30, 20.03.2020, ÖK 6896. T.

Viola parvula Tineo, 31, 20.04.2021, ÖK 7103. T.

POLYGALACEAE

Polygala supina Schreb., 32, 21.06.2020, ÖK 7001. Hk.

PORTULACACEAE

Portulaca oleracea L., 33, 02.05.2020, ÖK 6949. T.

CARYOPHYLLACEAE

Arenaria macrosephala Boiss., 34, 04.05.2022, ÖK 7350. End. LC. Hk.

Minuartia hybrida (Vill.) Sch. subsp. *hybrida*, 35, 01.05.2020, ÖK 6950. Akd. T.

Stellaria media (L.) Vill. subsp. *media*, 36, 20.03.2022, ÖK 7295. T.

Cerastium longifolium Willd., 37, 27.04.2020, ÖK 6922. T.

Holosteum umbellatum L. var. *umbellatum*, 38, 20.04.2022, ŞY 44418. T.

Sagina procumbens L., 39, 01.05.2021, ÖK 7121. Hk.

Dianthus crinutus Sm. var. *crinutus*, 40, 22.06.2020, ÖK 7002. Hk.

Velezia rigida L., 7052, 13.07.2020, ŞY 44217. T.

Saponaria prostrata Willd. subsp. *anatolica* Hedge, 2, 16.06.2021, ÖK 7211. End. An.-Tur. T.

Gysophila aucheri Boiss. 3, 02.06.2020, ÖK 7003. End. VU. An.-Tur. Hk.

Vaccaria pyramidata Medik.var.*grandiflora* (Fisch. ex DC.)Cullen, 4, 14.06.20,ÖK 7004.An-Tur. T.

Silene spergulifolia (Desf.) M. Bieb., 5, 16.06.2020, AD 7005. An.-Tur. Hk.

Silene ampullata Boiss., 6, 20.05.2021, ÖK 7122. An.-Tur. Hk.

Silene vulgaris (Moench) Garcke var. *vulgaris*, 7, 18.06.2020, ÖK 7006. Hk.

Silene compacta Fisch., 8, 30.05.2020, ÖK 6951. Hk.

Agrostemma githago L., 9, 11.06.2021, ÖK 7212. T.

ILLECEBRACEAE

Herniaria incana Lam., 10, 21.04.2020, ÖK 6923. Hk.

Scleranthus annuus L. subsp. *annuus*, 11, 16.06.2021, ÖK 7213. T.

Paronychia kurdica Boiss. subsp. *kurdica* var. *kurdica*, 12, 01.05.2020, ÖK 6952. Hk.

POLYGONACEAE

Polygonum cognatum Meisn., 13, 16.05.2020, ÖK 6953. Hk.

Polygonum arenastrum Boreau, 14, 23.06.2020, ÖK 7007. T.

Polygonum lapathifolium L., 15, 11.05.2020, ÖK 6954. T.

Rumex acetosella L. 16, 16.05.2021, ÖK 7123. Hk.

Rumex scutatus L. 17, 01.06.2021, ÖK 7214. Hk.

Rheum ribes L., 42, ŞY 30802, 16.04.2016. Hk.

Rheum telianum İlçim, 3, 10.06.2022, ÖK 7430. Hk. End. NT.

CHENOPODIACEAE

Chenopodium album L. subsp. *album* var. *album*, 18, 19.06.2020, ÖK 7008. T.

Chenopodium foliosum (Moench) Asch., 19, 20.04.2020, ÖK 6924. T.

AMARANTHACEAE

Amaranthus albus L., 20, 11.06.2021, ÖK 7215. T.

TAMARICACEAE

Tamarix tetrandra Pallas ex M. Bieb., 22, 16.05.2021, ÖK 7124. Fa.

HYPERICACEAE

Hypericum scabrum L., 21, 20.05.2020, ÖK 6955. An.-Tur. Ka.

Hypericum perforatum L.,23, 11.06.2021, ÖK 7216. Hk.

MALVACEAE

Malva neglecta Wallr., 24, 21.04.2020, ÖK 6925. Hk.

Alcea pallida Waldst. & Kit., 25, 01.06.2021, ÖK 7217. Hk.

Hibiscus trionum L., 26, 18.05.2020, ÖK 6956. T.

LINACEAE

Linum nodiflorum L., 27, 20.06.2020, ÖK 7009. Akd. Hk.

GERANIACEAE

Geranium tuberosum L. subsp. *tuberosum*, 28, 25.03.2022, ÖK 7292. An.-Tur. Kr.

Geranium stepporum P.H. Davis, 29, 25.04.2022, ÖK 7304. An.-Tur. Kr.

ZYGOPHYLLACEAE

Tribulus terrestris L., 30, 26.05.2020, ÖK 6957. Hk.

RUTACEAE

Haplophyllum armenum Spach, 31, 19.06.2020, ÖK 7010. End. Ka

RHAMNACEAE

Paliurus spina-christi Mill., 32, 20.06.2021, ÖK 7218. Fa.

FABACEAE

Colutea cilicica Boiss. & Balansa, 33, 20.05.2020, ÖK 6958. Fa.

Astragalus gummifer Labill., 34, 22.06.2020, ÖK 7011. An.-Tur. Ka.

Astragalus bicolor Lam., 35, 14.06.2020, ÖK 7012. End. An.-Tur. Ka.

Astragalus declinatus Wild, 36, 23.06.2020, ÖK 7013. An.-Tur. Ka.

Astragalus compactus Lam., 37, 21.06.2021, ÖK 7219. End. An.-Tur. Ka.

Vicia cracca L. subsp. *stenophylla* Vel., 38, 23.06.2020, ÖK 3806. Hk.

Vicia ervilia (L.) Willd., 40, 23.04.2020, ÖK 6926. Akd. T.

Vicia cuspidata Boiss., 39, 23.06.2021, ÖK 7220. Akd. T.

Vicia tetrasperma (L.) Schreb., 13, 23.06.2021, ÖK 7215. T.

Lathyrus incospicus L., 4, 23.05.2020, ÖK 6959. Hk.

Pisum sativum L. subsp. *elatius* var. *pumilio*, 16, 11.03.2020, ÖK 6889. Akd. T.

Trifolium campestre Schreb., 32, 18.05.2020, ÖK 6960. Hk.

Trifolium pratense L. var. *pratense*, 20, 18.05.2021, ÖK 7125. T.

Trifolium arvense L. var. *arvense*, 25, 23.06.2020, ÖK 7014. T.

Trifolium angustifolium L. var. *intermedium* (Guss.) Gib. & Belli, 26, 23.06.2020, ÖK 7015. T.

Trifolium purpureum L. var. *purpureum*, 27, 21.06.2020, ÖK 7016. T. Det: ŞY.

Trifolium repens L. var. *repens*, 15, 20.05.2020, ÖK 6961. T

Melilotus officinalis (L.) Desr., 6, 26.06.2020, ÖK 7017. Hk.

Melilotus alba Desr., 26, 16.06.2021, ÖK 7222. Hk.

Trigonella brachycarpa (Fisch.) Moris, 28, 23.06.2021, ÖK 7223. An.-Tur. Hk.

Medicago sativa L. subsp. *sativa*, 38, 16.05.2020, AD 3711. Hk.

Medicago rigidula (L.) All. var. *cinerascens* (Jord.) Rouy, 29, 13.06.2020, ÖK 7018. T.

Medicago radiata L., 40, ŞY 44224, 13.07.2018. T.

Lotus gebelia Vent. var. *gebelia*, 5, 25.04.2020, ÖK 6927. Hk.

Coronilla varia L. subsp. *varia*, 24, 20.05.2021, ÖK 7126. Hk.

Onobrychis caput-galli (L.) Lam., 19, 20.05.2020, ÖK 6962. Akd. Hk.

Cicer anatolicum Alef., 22, 10.06.2022, ÖK 7411. Hk

Trigonella kotschyi Fenzl, 24, 04.06.2021, ÖK 7224. End. An.-Tur. T.

Robinia pseudoacacia L., 22, 17.06.2020, ÖK 7019. Fa.

Ebenus haussknechtii, 31, 17.06.2021, ÖK 7225. End. Hk.

Sophora alopecuroides L. var. *alopecuroides,* 18, 04.06.2020, ÖK 7020. Kr.

ROSACEAE

Filipendula vulgaris Moench, 33, 22.06.2020, ÖK 7021. Av.-Sib. Hk.

Rubus sanctus Schreb., 36*,* 11.06.2020, ÖK 7022. Fa.

Potentilla recta L., 36, 16.06.2021, ÖK 7226. Hk.

Potentilla reptans L., 30, 23.06.2020, ÖK 7023. Hk.

Sanguisorba muricata Franch subsp. *muricata*, 36, 07.05.2020, ŞY 3789. Hk

Geum urbanum L., 1, 23.06.2020, ÖK 7024. Av.-Sib. Kr.

Agrimonia eupatoria L., 2, 13.06.2021, ÖK 7227. Hk.

Rosa canina L., 23, 21.06.2020, ÖK 7025. Fa.

Crataegus monogyna Jacq. subsp. *monogyna*, 37, 16.06.2020, ÖK 7026. Fa.

Crataegus meyeri Pojark, 18, 21.06.2021, ÖK 7228. An.-Tur. Fa.

LYTHRACEAE

Lythrum salicaria L., 23, 02.06.2022, ÖK 7407. Av.-Sib. Hk.

ONAGRACEAE

Epilobium minutiflorum Hausskn., 15, 11.06.2021, ÖK 7248. An.-Tur. Hk.

CRASSULACEAE

Rosularia radiciflora Boriss. subsp. *radiciflora,* 29, 16.05.2021, ÖK 7127. An.-Tur. Hk.

Umbilicus erectus DC., 12, 21.06.2022, ÖK 7463. Kr.

Sedum sempervivoides Bieb., 32, 23.06.2020, ÖK 7038. Hk.

APIACEAE

Grammosciadium platycarpum Boiss. & Hausskn., 40, ŞY 44179. An.-Tur. Hk.

Eryngium campestre L. var. *virens* Link, 2, 16.05.2020, ÖK 7027. Hk.

Chaerophyllum crinitum Boiss., 3, 02.06.2021, ÖK 7229. An.-Tur. Kr.

Anthriscus cerefolium (L.) Hoffm., 4, 13.06.2022, ÖK 7437. Hk.

Scandix pecten-veneris L., 5, 13.06.2021, ÖK 7230. T.

Bifora radians M.Bieb., 6, 23.05.2020, ÖK 6964. T.

Pimpinella adiyamanensis Yıld. & Kılıç.,34,25.04.2020, ŞY 44185.An.-Tur. Hk. End. NT.

Lecokia cretica (Lam.) DC., 24, 27.04.2020, ŞY 30787. Kr.

Stenotaenia macrocarpa Freyn & Sint., 7, 14.06.2020, ÖK 7028. End. T.

Bupleurum rotundifolium L., 8, 23.05.2020, ÖK 6965. T.

Falcaria vulgaris Bernh., 9, 23.06.2021, ÖK 7231. Hk.

Ferula orientalis L., 10, 10.05.2020, ÖK 6960. An.-Tur. Hk.

Malabaila dasyantha (K.Koch) Grossh., 11, 18.05.2020, ÖK 6966. An.-Tur. Hk.

Heracleum persicum Desf., 15, 02.06.2021, ÖK 7232. An.-Tur. Hk.

Torilis leptocarpa (Hochst.) Towsend, 12, 02.06.2021, ÖK 7233. An.-Tur. Hk.

Zosima absinthifolia (Vent.) Link, 13, 14.06.2020, ÖK 7029. Kr.

Astrodaucus orientalis (L.) Drude, 14, 16.06.2021, ÖK 7234. An.-Tur. T.

Caucalis platycarpos L., 16, 01.06.2020, ÖK 7030. T.

Artedia squamata L., 17, 21.06.2021, ÖK 7235. T.

Asperula arvensis L., 18, 11.06.2020, ÖK 7031. Akd. T.

Galium verum L. subsp. *verum*, 19, 16.06.2020, ÖK 7032. Av.-Sib. Ka.

Galium humifusum M. Bieb., 20, 23.06.2021, ÖK 7236. Hk.

Callipeltis cucullaria (L.) Steven, 21, 23.05.2020, ÖK 6967. An.-Tur. T.

Cruciata articulata (L.) Ehrend., 22, 25.05.2021, ÖK 7128. An.-Tur. Hk.

VALERIANACEAE

Valeriana sisymbriifolia Vahl., 23, 14.05.2020, ÖK 6968. An.-Tur. Hk.

Valerianella pumila (L.) DC., 24, 21.06.2021, ÖK 7237. Hk.

DIPSACACEAE

Cephalaria hirsuta Stapf, 25, 11.06.2020, ÖK 7033. An.-Tur. Hk.

Scabiosa persica Boiss., 26, 16.05.2020, ÖK 6969. An.-Tur. T.

Scabiosa rotata M. Bieb., 27, 14.05.2021, ÖK 7129. An.-Tur. T.

Pterocephalus plumosus (L.) Coult., 28, 23.06.2020, ŞY 44220. Hk.

ASTERACEAE

Xanthium spinosum L., 29, 23.06.2020, ÖK 7034. T.

Xanthium strumarium L. subsp. *strumarium*, 30, 16.06.2021, ÖK 7259. T.

Inula oculus-christi L., 36, 21.06.2020, ÖK 7035. Av.-Sib. Kr.

Helichrysum plicatum DC. subsp. *plicatum*, 31, 01.06.2020, ÖK 7036. Ka.

Conyza canedensis (L.) Cronquist, 32, 16.06.2020, ÖK 7037. T.

Bellis perennis L., 36, 18.05.2021, ÖK 7130. Av.-Sib. Hk.

Senecio vernalis Waldst. & Kit., 37, 16.06.2020, ÖK 7038. T.

Tussilago farfara L., 38, 27.03.2020, ÖK 6859. Av.-Sib. Hk.

Anthemis tinctoria L. var. *tinctoria*, 39, 21.06.2020, ÖK 7039. Hk.

Anthemis coelopoda Boiss. var. *coelopoda*, 40, 14.06.2020, ÖK 7040. Hk.

Achillea vermicularis Trin., 34, 13.06.2020, ÖK 7041. An.-Tur. Hk.

Achillea biebersteinii Afan., 21, 18.05.2020, ÖK 6970. An.-Tur. Hk.

Achillea millefolium L. subsp. *pannonica* (Scheele) Hayek, 4, 31.06.2021,ÖK 7238. Av.-Sib. Hk.

Tanacetum densum (Lab.) subsp. *amani* Heywood, 26, 13.06.2021, ÖK 7239. End. Hk.

Tanacetum abrotenifolium (L.) Druce, 16, 13.06.2020, ÖK 7042. An.-Tur. Hk.

Gundelia tournefortii L. var. *armata* Freyn & Sint., 27, 20.05.2020, ÖK 6971. An.-Tur. Hk.

Gundelia komagenensis Fırat, 42, ÖK 7053, 13.07.2020. An.-Tur. Hk. End.

Arctium minus (Hill) Bernh. subsp. *pubens* (Bab.) Arènes, 28,14.06.2020,ÖK 7043. Av.-Sib. Hk.

Onopordum carduchorum Bornm. & Beauverd, 28, 21.06.2021, ÖK 7240. An.-Tur. Hk.

Cirsium amani Post., 29, 13.06.2020, ÖK 7045. Hk.

Cirsium macrobotrys (C.Koch) Boiss. 30, 29.06.2021, ÖK 7241. Hk.

Picnomon acarna (L.) Cass., 31, 13.06.2020, ÖK 7046. Akd. T.

Carduus nutans L. subsp. *nutans*, 28, 13.07.2020, ÖK 7054. Hk.

Carduus pycnocephalus L. subsp. *breviphyllarius* Davis, 29, 25.04.2022, ÖK 7305. Hk.

Centaurea solstitialis L. subsp. *solstitialis*, 30, 16.05.2022, ÖK 7353. T.

Centaurea iberica Trev. ex Spreng., 31, 16.05.2020, ÖK 6972. Hk.

Centaurea depressa M. Bieb., 32, 21.06.2020, ÖK 7047. T.

Crupina crupinastrum (Moris.) Vis., 40, 18.05.2021, ÖK 4135. T.

Crupina vulgaris Cass. 47, ŞY 44187, 13.07.2018. T.

Cnicus benedictus L. var. *benedictus*, 36, 13.06.2020, ŞY 44191. T.

Xeranthemum annuum L., 34, 14.06.2020, ÖK 7048. T.

Chardinia orientalis (L.) Kuntze, 35, 21.06.2020, ŞY43169. An.-Tur. T.

Echinops orientalis Trautv., 37, 13.06.2020, ÖK 7049. An.-Tur. Hk.

Klasea oligocephala (DC.) Greuter & Wagenitz, 42, Ş.Y 30789. An.-Tur. Hk.

Scorzonera suberosa K.Koch subsp. *suberosa*, 39, 24.05.2021, ÖK 7131. An.-Tur. Hk.

Scorzonera phaeopappa Boiss., 40, 28.11.2020*,* ŞY 43170. An.-Tur. Hk.

Scorzonera mollis M.Bieb. subsp. *mollis*, 43, ŞY 43171. 28.11.2020. An.-Tur. Hk.

Tragopogon aureus Boiss., 40, 13.06.2021, ÖK 7242. An.-Tur. Hk.

Leontodon asperrimus (Willd.) J. Ball., 27, 20.05.2021, ÖK 7132. An.-Tur. Hk.

Picris kotschyi Boiss., 28, 21.06.2020, ÖK 7050. Hk.

Pilosella cymosa (L.) C.H. & F.H. Schultz, 28, 13.06.2020, ÖK 7051. Av.-Sib. Hk.

Taraxacum crepidiforme DC. subsp. *crepidiforme*, 35, 14.06.2021, ÖK 7243. An.-Tur. Hk.

Crepis sancta (L.) Babc., 11, 13.06.2020, ÖK 7052. T.

Crepis foetida L. subsp. *foetida*, 12, 18.04.2021, ÖK 7104. T.

CAMPANULACEAE

Campanula involucrata Aucher ex A.DC., 9, 18.04.2021, ÖK 7105. An.-Tur. Hk.

Asyneuma amplexicaule (Willd.) Hand.-Mazz. subsp. *amplexicaule* var. *angustifolium* (Boiss.) Bornm., 24, 24.06.2020, ÖK 7085. An.-Tur. Hk.

Legousia pentagonia (L.) Thellung, 13, 14.04.2021, ÖK 7105. Akd. T.

ASCLEPIDIACEAE

Vincetoxicum canescens (Willd.) Decne. subsp. *canescens*, 24, 16.06.2020, ÖK 7053. Kr.

GENTIANACEAE

Centaurium erythraea Rafn. subsp. *turcicum* (Velen.) Melderis, 28, 03.06.2021, ÖK 7285. T.

Gentiana olivieri Griseb., 16, 14.05.2020, ÖK 6972. T.

CONVOLVULACEAE

Convolvulus galaticus Rostan ex Choisy, 32, 14.06.2020, ÖK 7054. End. An.-Tur. Hk.

CUSCUTACEAE

Cuscuta brevistyla A. Braun., 18, 16.06.2022, ÖK 7440. T.

BORAGINACEAE

Heliotropium circinatum Griseb., 28, 16.05.2020, ÖK 6974. An.-Tur. T.

Heliotropium europaeum L., 14, 14.06.2020, ÖK 7055. Akd. T.

Rochelia disperma (L. f.) K. Koch var. *disperma*, 21, 31.06.2021, ÖK 7244. T.

Asperugo procumbens L. 40, 24.05.2021, ÖK 7133. Av.-Sib. T.

Myosotis heteropoda Trautv., 2, 16.05.2022, ÖK 7354. An.-Tur. T.

Paracaryum racemosum (Schreb.)Brit var.*racemosum*, 29, 14.05.20,ÖK 6974. End.An.-Tur. Hk. LC.

Buglossoides arvensis (L.) I.M. Johnst., 17, 24.04.2020, ÖK 6928. T.

Echium glomeratum Poir., 29, 16.05.2020, ÖK 6975. Akd. Hk.

Echium italicum L., 27, 23.05.2022, ÖK 7355. Akd. Hk.

Moltkia coerulea (Willd.) Lehm., 24, 13.06.2020, ÖK 7056. An.-Tur. Hk.

Onosma sericeum Willd., 29, 23.05.2022, ÖK 7356. An.-Tur. Hk.

Onosma albo-roseum Fisch.& C.A.Mey. subsp. *albo-roseum* var. *albo-roseum*, 17, 13.06.2020, ÖK 7057. An.-Tur. Hk.

Rindera caestiposa (A. DC.) Bunge, 18, 14.06.2021, ÖK 7245. An.-Tur. Hk

Cerinthe minor L. subsp. *auriculata* (Ten.) Domac, 8, 21.06.2020, AD 3815. Av.-Sib. Hk.

Brunnera orientalis (Schenk.) John., 39, 13.06.2020, ÖK 7058. Hk.

Anchusa azurea Mill. var. *azurea*, 38, 16.05.2020, ÖK 6976. Hk.

Anchusa strigosa Labill., 37, 13.05.2022, ÖK 7357. Hk.

Nonea melanocarpa Boiss., 15, 18.05.2022, ÖK 7358. An.-Tur. T.

Nonea caspica (Willd.) G. Don, 27, 18.05.2021, ÖK 7134. T.

Alkanna tinctoria (L.) Tausch subsp. *tinctoria*, 36, 16.05.2022, ÖK 7359. Akd. Hk.

Solenanthus stamineus (Desf.) Wettst., 35, 16.05.2021, ÖK 7135. Hk.

SOLANACEAE

Solanum nigrum L. subsp. *nigrum*, 33, 11.06.2020, ÖK 7059. T.

Hyoscyamus niger L., 34, 24.05.2022, ÖK 7360. Hk.

SCROPHULARIACEAE

Verbascum diversifolium Hochst., 32, 21.06.2021, ÖK 7246. End. An.-Tur. Hk.

Verbascum lasianthum Boiss. ex Benth., 31, 13.06.2021, ÖK 7230. Hk.

Scrophularia scopolii (Hoppe ex) Pers. var. *scopolii*, 30, 21.05.2022, ÖK 7361. Hk.

Scrophularia rimarum Bornm., 28, 16.04.2021, ÖK 7107. Ka.

Linaria grandiflora Desf., 27, 13.06.2020, ÖK 7060. An.-Tur. Hk.

Veronica bozakmanii M.A. Fisch., 26, 18.04.2020, ÖK 6930. An.-Tur. T.

Veronica orientalis Mill. subsp. *orientalis*, 25, 13.06.2021, ÖK 7258. Ka.

Veronica bornmuellerii Hausskn., 24, 18.04.2021, ÖK 7108. An.-Tur. T.

Bungea trifida (Vahl) C.A.Mey., 22, 18.05.2020, ÖK 6977. An.-Tur. Hk.

OROBANCHACEAE

Orobanchae aegyptica Pers., 21, 03.06.2021, ÖK 4222. T.

ACANTHACEAE

Acanthus dioscoridis L. var. *dioscoridis*, 20, 14.06.2020, ÖK 7061. An.-Tur. Hk.

GLOBULARIACEAE

Globularia trichosantha Fisch. & C.A. Mey. subsp. *trichosantha*, 15, 16.05.2021, ÖK 4147. Hk.

LAMIACEAE

Ajuga chamaepitys (L.) Schreb. subsp. *chia* (Schreb.) Arcang.var.*chia*, 19,18.05.2022, ÖK 7362. Hk.

Teucrium parviflorum Schreb., 18, 14.05.2020, ÖK 6978. An.-Tur. Hk.

Teucrium chamaedrys (Celàk.) Rech. fil. subsp. *sinuatum*, 17, 30.05.2020, ÖK 6979. An.-Tur. Ka.

Teucrium polium L., 16, 14.05.2021, ÖK 7137. Hk.

Scutellaria orientalis L. subsp. *bicolor* (Hochst.)J.R. Edm.,17,01.06.2021,ÖK 7228.End.An-Tur. Ka.

Phlomis leucophracta P.H. Davis & Hub.-Mor., 16, 23.06.2021, ÖK 7246. Hk.

Lamium amplexicaule L. subsp. *amplexicaule*, 15, 14.04.2020, ÖK 6931. Hk.

Lamium macrodon Boiss. & A. Huet., 34, 18.04.2022, ÖK 7306. An.-Tur. T.

Marrubium astracanicum Jacq. subsp. *astracanicum*, 14, 14.05.2022, ÖK 7363. Hk.

Sideritis montana L. subsp. *montana*, 13, 14.04.2022, ÖK 7307. Akd. T.

Stachys lavandulifolia Vahl var. *brachydon* Boiss., 12, 14.05.2020, ÖK 6980. An.-Tur. Ka.

Stachys atherocalyx K. Koch, 11, 03.06.2020, ÖK 7039. Av.-Sib. T.

Stachys rupestris Montbret et Aucher ex Benth., 27, 03.06.2020, ÖK 7040. An.-Tur. Hk.

Nepeta transcaucasica Grossh., 27, 16.05.2020, ÖK 6981. An.-Tur. Hk.

Lallemantia peltata Fisch. & C.A. Mey., 10, 18.04.2021, ÖK 7111. An.-Tur. T.

Prunella vulgaris L., 4, 21.05.2022, ÖK 7364. Av.-Sib. Hk.

Origanum vulgare L. subsp. *gracile* (K.Koch) Letswaart, 9, 14.06.2020, ÖK 7062. An.-Tur. Hk.

Satureja hortensis L., 8, 01.05.2020, ÖK 6982. Hk.

Thymus pubescens Boiss. & Kotschy ex Čelak var. *pubescens*, 7, 23.06.2020, ÖK 7063. An.-Tur. Ka.

Thymus kotschyanus Boiss. & Hohen. var. *kotschyanus*, 6, 30.05.2020, ÖK 6983. An.-Tur. Ka.

Mentha longifolia (L.) Huds. subsp. *longifolia*, 4, 01.06.2022, ÖK 7435. Av.-Sib. Hk.

Ziziphora capitata L., 5, 14.05.2022, ÖK 7360. An.-Tur. T.

Salvia verticillata L. subsp. *verticillata,* 3, 14.06.2020, ÖK 7064. Hk.

Salvia trichoclada Benth., 2, 24.06.2021, ÖK 7247. An.-Tur. Hk.

Salvia multicaulis Vahl., 1, 21.05.2022, ÖK 7365. An.-Tur. Hk.

Salvia microstegia Boiss. & Bal., 14, 23.06.2020, ÖK 7065. An.-Tur. Hk.

Salvia virgata Jacq., 10, 14.05.2022, ÖK 7366. An.-Tur. Hk.

PLUMBAGINACEAE

Acantholimon acerosum (Willd.) Boiss. var. *acerosum*, 31, 21.06.2021, ÖK 7248. LC. An.-Tur. Ka.

PLANTAGINACEAE

Plantago lanceolata L., 36, 18.05.2020, ÖK 6984. Hk.

ELAEAGNACEAE

Elaeagnus angustifolia L., 22, 18.05.2020, ÖK 6985. Fa.

ARISTOLOCHIACEAE

Aristolochia maurorum L., 26, 23.06.2021, ÖK 7249. An.-Tur. Hk.

EUPHORBIACEAE

Euphorbia chamaesyce L., 17, 14.06.2020, ÖK 7066. T.

Euphorbia falcata L. subsp. *falcata* var. *falcata*, 15, 23.06.2020, ÖK 7067. T.

Euphorbia denticulata Lam., 10, 01.05.2020, ÖK 6986. An.-Tur. Hk.

URTICACEAE

Urtica dioica L., 36, 16.05.2020, ÖK 6987. Av.-Sib. Hk.

ULMACEAE

Celtis tournefortii Lam. 22, 23.06.2021, ÖK 7250. Ka.

FAGACEAE

Quercus libani Olivier, 1, 14.06.2020, ÖK 7068. An.-Tur. Fa.

Quercus coccifera L. 1, 14.06.2020, ÖK 7069. An.-Tur. Fa.

Quercus brantii Lindley, 47, ŞY 44227 13.07.2018. An.-Tur. Fa.

SALICACEAE

Salix alba L., 36, 21.06.2020, ÖK 7070. Av.-Sib. Fa.

Populus alba L., 16, 22.05.2022, ÖK 7367. Av.-Sib. Fa.

LILIOPSIDA (MONOCOTYLEDON)

LILIACEAE

Allium adiyamanense Yıld. & Kılıç, 47, 03.08.2019, ŞY 44252. Kr. End. NT.

Allium atroviolaceum Boiss., 26, 23.06.2020, ÖK 7071. Kr.

Allium scorodoprasum L. subsp. *rotundum* (L.) Stearn, 40, 21.06.2021, ÖK 7251. Akd. Kr.

Allium chrysantherum Boiss. & Reut., 42, 23.05.2017. ŞY 43208. Kr.

Eremurus spectabilis M. Bieb., 31, 16.05.2020, ÖK 6988. An.-Tur. Kr.

Scilla siberica Haw. subsp. *armena* (Grossh.) Mordak, 18, 25.04.2022, ÖK 7310. An.-Tur. Kr.

Puschkinia scilloides Adams var. *libanotica* (Zucc.) Boiss., 15,18.04.2020, ÖK 6932.An.-Tur. Kr.

Ornithogalum oligophyllum E.D. Clarke, 15, 15.04.2020, ÖK 6933. Kr.

Ornithogalum narbonense L. 38, 04.05.2022, ŞY 4506. Akd. Kr.

Ornithogalum yesilyurtense Yıld. & Kılıç, ŞY 45168. An.-Tur. Kr. End.

Muscari neglectum Guss., 19, 15.04.2022, ÖK 7308. Kr.

Muscari comosum (L.) Mill., 20, 16.04.2020, ŞY44253. An.-Tur. Kr.

Bellevaila pycnantha (K. Koch) Losinsk., 11, 16.04.2020, ÖK 6934. An.-Tur. Kr.

Bellevaila fominii Woronow, 38, 21.04.2022, ÖK 7309. An.-Tur. Kr.

Fritillaria latifolia Willd., 8, 01.05.2020, ÖK 6989. Akd. Kr.

Tulipa armena Boiss. var. *armena*, 40, 14.05.2021, ÖK 7138. An.-Tur. Kr.

Gagea taurica Stev., 16, 15.03.2022, ÖK 7295. An.-Tur. Kr.

Gagea villosa subsp. *villosa* var. *villosa*, 24, 25.03.2022, ÖK 7315. Akd. Kr.

Colchicum szovitsii Fisch. & C.A.Mey., 34, 15.04.2021, ÖK 7110. An.-Tur. Kr.

Merendera sobolifera C.A. Mey., 15, 25.03.2020, ÖK 3550. An.-Tur. Kr.

AMARYLLIDACEAE

Ixiolirion tataricum (Pall.) Herb. subsp. *montanum* (Labill.) Takht., 19, 24.05.2022, ÖK 7362. An.-Tur. Kr.

IRIDACEAE

Iris reticulata M. Bieb. var. *reticulata*, 12, 01.05.2020, ÖK 6768, ÖK 3779. Kr.

Iris persica L., 34, 11.04.2020, ÖK 6935. An.-Tur. Kr.

Crocus kotschyanus K. Koch subsp. *kotschyanus,* 38, 30.05.2022, ÖK 7368. Kr.

Gladiolus atroviolaceus Boiss., 47, ŞY 43210, 24.03.2018. Kr.

Gladiolus kotschyanus Boiss. 47, 24.05.2017, ŞY 43307. An.-Tur. Kr.

ORCHIDACEAE

Orchis mascula (L.) L. subsp. *pinetorum* (Boiss. & Kotschy) G.Camus, 47, 06.12.2018. ŞY 43213.

Orchis coriophora L., 23, 01.06.2020, ÖK 7047. Kr.

Ophrys reinholdii Spruner ex Fleischm. 28, 24.05.2022, ŞY 7369. Kr.

Dactylorhiza romana (Seb.) Soó subsp. *romana,* 47, ŞY 30805. Kr.

TYPHACEAE

Typha latifolia L., 16, 16.05.2022, ÖK 7382. Hk.

JUNCACEAE

Juncus inflexus L., 36, 01.06.2022, ÖK 7404. Hk.

Luzula pseudosudetica V. Krecz., 16, 02.06.2020, ÖK 7047. Öksin Elementi. Hk.

CYPERACEAE

Cyperus fuscus L., 22, 14.06.2022, ÖK 7439. Av.-Sib. Hk.

Scirpoides holoschoenus (L.) Sojak, 22, 11.05.2022, ÖK 7380. Hk.

Carex melanostachya Bieb. ex Willd.,22, 14.06.2020, ÖK 7072. Hk.

Carex distans L., 22, 11.05.2020, ÖK 6990. Av.-Sib. Hk.

POACEAE

Trisetum rigidum (Bieb.) Roemer & Schultes, 37, 21.06.2020, ÖK 7073. An.-Tur.

Elymus repens (L.) Gould subsp. *repens*, 19, 23.06.2021, ÖK 7252. An.-Tur. Hk.

Aegilops umbellulata Zhuk. subsp. *umbellulata*, 11, 14.06.2020, ÖK 7074. An.-Tur. T.

Secale ciliatoglume (Boiss.) Grossh., 6, 11.06.2020, ÖK 7075. An.-Tur. Ka.

Hordeum bulbosum L., 37, 21.06.2021, ÖK 7253. Kr.

Hordeum violaceum Boiss. & A. Huet, 24, 13.06.2020, ÖK 7042. An.-Tur. Hk.

Taeniatherum caput-medusae (L.) Nevski subsp. *crinitum* (Schreb.) Melderis, 12, 14.06.2020, ÖK 7076. An.-Tur. T.

Bromus sterilis L., 20, 23.06.2021, ÖK 7254. T.

Avena sterilis L. subsp. *sterilis*, 17, 21.06.2021, ÖK 7250. T.

Arrhenatherum kotschyii Boiss., 31, 23.06.2020, ÖK 7255. An.-Tur. Hk.

Koeleria cristata (L.) Pers., 17, 14.06.7221, ÖK 4209. Hk.

Calamagrostis pseudophrogmites (Haller f.) Koeler, 32, 03.06.2021, ÖK 7195. Av.-Sib. Hk.

Apera intermedia Hack., 15, 23.06.2020, ÖK 7078. An.-Tur. T.

Nardus stricta L., 24, 23.06.2020, ÖK 7079. Av.-Sib. Hk.

Phleum exaratum Hochst. ex Griseb. subsp. *exaratum*, 23, 03.06.2022, ÖK 7399. T.

Agrostis gigantea Roth., 23, 24.06.2020, ÖK 7080. Av.-Sib. Hk.

Vulpia myuros (L.) C.C. Gmelin, 34, 24.06.2020, ÖK 7081. T.

Psilurus incurvus (Govan) Schinz & Thell., 37, 14.06.2020, ÖK 7082. T.

Poa bulbosa L. var. *vivipara*, 2, 14.06.2020, ÖK 7083.

Catabrosa aquatica (L.) P. Beauv., 3, 15.06.2020, ÖK 7084. Hk.

Dactylis glomerata L. subsp. *glomerata*, 25, 14.06.2020, ÖK 7085. Hk.

Briza humilis M. Bieb., 4, 14.06.2021, ÖK 7259. T.

Melica persica Kunth subsp. *persica*, 5, 04.06.2021, ÖK 7106. An.-Tur. Hk.

Stipa ehrenbergiana Trin. & Rupr., 8, 02.06.2020, ÖK 7045. An.-Tur. Hk.

Phragmites australis (Cav.) Trin. ex Steud., 12, 24.06.2020, ÖK 7086. Av.-Sib. Hk.

Cynodon dactylon (L.) Pers. var. *villosus* Regel, 26, 31.06.2020, ÖK 7087. Hk.

Setaria verticillata (L.) P. Beauv. var. *verticillata*, 12, 24.06.2021, ÖK 7256. T.

Lolium perenne L., 19, 24.05.2021, ÖK 7140. Av.-Sib. Hk.

5. Discussion

This study was carried out to contribute the flora of Çelikhan District (Adıyaman). Within the scope of the study, 592 plant samples were collected by visiting the research area during the vegetation periods of 2019-2022. As a result of the evaluation of these plants, a total of 454 taxa,

295 genera belonging to 62 families, were identified. Between those, it was determined that 30 taxa from the study area were endemic. According to the number of taxa, the first families emerged as Asteraceae, Legumimosae, Brassicaceae, Lamiaceae, Poaceae. The first five genera according to the number of taxa were *Astragalus, Silene, Salvia, Trifolium* and *Vicia* respectively. The new species named *Aethionema adiyamanense* Yıld. & Kılıç, *Pimpinella adiyamanensis* Kılıç & Yıld., *Rheum telianum* İlçim, *Gundelia komagensis* Fırat, which have been introduced to the scientific world in Adıyaman in recent years, were collected again from the study area. Although the order of families containing the most taxa in our country does not change in short periods; the current order is as follows; Asteraceae, Fabaceae, Brassicaceae, Poaceae, Lamiaceae, Caryophyllaceae, Apiaceae, Scrophulariaceae. The order of the five families containing the most taxa in research area is Asteraceae, Fabaceae, Brassicaceae, Lamiaceae, Poaceae, and the first three of the families containing the most taxa in the Flora of Turkey are the same and similar to other orders. The order of Lamiaceae and Poaceae families has changed. The families in the first place in terms of the number of taxa in our research area reflect the general characteristics of the Eastern Anatolian Flora, except for their order. The ranking of the first five families in the floristic studies carried out in areas close to our area is given in Table 3.

Table 3: Distribution of the first five families containing the most taxa according to studies

Research No and Title	**First Five Family According to Number of Taxa**
1. Contributions to the Flora of Çelikhan District (Adıyaman)	Asteraceae 42, Fabaceae 37, Brassicaceae 36, Lamiaceae 35, Poaceae 31
2. Flora and vegetation of Adıyaman Unv. Campus [15]	Poaceae 33, Asteraceae 32, Fabaceae 31, Brassicaceae 26, Lamiaceae 15
3. Flora of Akdağ (Çelikhan-Adıyaman) [17]	Asteraceae 75, Fabaceae 66, Brassicaceae 45, Caryophyllaceae 43, Lamiaceae 42
4. Flora of Ali Mountain ve Ziyaret Hill (Adıyaman) [14]	Asteraceae 47, Fabaceae 39, Poaceae 36, Lamiaceae 31, Brassicaceae 21
5. Flora of Atatürk Dam Basin of Şanlıurfa Part [16]	Fabaceae 49, Asteraceae 49, Poaceae 21, Brassicaceace 20, Lamiaceae 17
6. Flora and Vegetation of Gazihan Dede (Adıyaman) Promenade Area [13]	Asteraceae 43, Fabaceae 27, Lamiaceae 27, Poaceae 20, Apiaceae 17
7. Contributions of Nemrut Mountain (Adıyaman) Flora [12]	Asteraceae 35, Lamiaceae 25, Poaceae 23, Brassicaceae 19, Fabaceae 18

In our research area, the richest family in terms of number of taxa is Asteraceae with 42 taxa. Asteraceae family is the first family with the highest number of taxa in the Flora of Turkey. As seen in our research and studies in nearby areas, Asteraceae is the richest family in terms of taxa number, except for the 2nd and 5th studies (Table 3). The majority of Asteraceae taxa are cosmopolitan in nature, and the reasons such as their members' adaptation to different habitats, has wide ecological tolerance and their ability to spread easily with their pappus are among the

most important factors that cause this family to contain the most taxa in Turkey. The second family containing the most taxa in our research area is Fabaceae with 37 taxa (Table 3). Research area reflects the characteristics of the Iran-Turanian phytogeographic region and the abundance of habitats suitable for Leguminosae taxa have caused Leguminosae members to be in the second place in terms of the number of taxa. As can be seen in Table 3, Fabaceae is in the second place in terms of taxon content in studies 3, 4 and 6. Brassicaceae family has 36 taxa in the research area. Most of Brassicaceae taxa are cosmopolitan and in the therophyte life form, and most of Brassicaceae members have a high adaptability to harsh climatic conditions. As seen in Table 3, Cruciferae family is in the first place in terms of taxon content. The fourth largest family in terms of the number of taxa in research area is the Lamiaceae family with 35 taxa (Table 3). As seen in Table 3, Labiatae family is among the first five families in terms of taxon content in all studies. In our research area, Poaceae family is in the fifth place with 31 taxa. Most of the Graminea members are cosmopolitan and their habitats are generally steppe areas, open meadows, pasture areas and sandy areas; have caused an increase in the grassy taxa in our research area (Table 3). The five genera richest in terms of taxa number in our research area are *Astragalus 9, Silene 8, Salvia 7, Trifolium 6, Vicia 6*, and the taxa numbers of the first five genera in the areas close to our research area are shown in Table 4.

Table 4: Distribution of the first five genera containing the most taxa according to studies

Research No and Title	**First Five Genus According to Number of Taxa**
1. Contributions to the Flora of Çelikhan District (Adıyaman)	*Astragalus* 9, *Silene* 8, *Salvia* 7, *Trifolium* 6, *Vicia* 6
2. Flora and Vegetation of Adıyaman Unv. Campus [15]	*Trifolium* 5, *Bromus* 5, *Allium* 4, *Euphorbia* 4, *Lamium* 3
3. Flora of Akdağ (Çelikhan-Adıyaman) [17]	*Astragalus* 21, *Silene* 13, *Veronica* 10, *Allium*/ *Galium* 9, *Ranunculus/Asperula/Trifolium /Minuartia/Geranium/ Erysimum* 8
4. Flora of Ali Mountain ve Ziyaret Hill (Adıyaman) [14]	*Allium/Convolvulus/Trifolium* 7, *Bromus/Galium 6*
5. Flora of Atatürk Dam Basin of Şanlıurfa Part [16]	*Trifolium* 10, *Vicia* 7, *Astragalus* 6, *Centaurea* 5, *Bromus* 5
6. Flora and Vegetation of Gazihan Dede (Adıyaman) Promenade Area [13]	*Inula* 8, *Euphorbia* 7, *Scabiosa* 6, *Hypericum* 5, *Convolvulus* 4
7. Contributions of Nemrut Mountain (Adıyaman) Flora [12]	*Astragalus* 9, *Alyssum* 7, *Silene* 7, *Allium* 6, *Centaurea* 6

The reasons such as the high adaptation characteristics of *Astragalus, Silene, Salvia, Trifolium, Vicia* members to the habitats and their adoption of the living conditions brought about by the climatic characteristics of the Anatolian-Turanian phytogeographic region are among the factors that cause these genus members to be seen at a high rate in our area. Table 4 shows the first five genera rankings in terms of the number of taxa in the study area and the first five genera

rankings determined as a result of floristic studies in nearby regions. In the studies we compared in terms of taxon content at family and genus level, there are some differences in the ordering of families and genera, which can be explained by reasons such as the habitat demands of plants, differences in the ecological characteristics of the areas, biotic-abiotic conditions of the environment, and differences in working method and time. In terms of taxon content, *Astragalus* is in the first five genera in most of the studies in Table 4, and the predominance of steppe habitats in and around the area is one of the most important factors causing this situation.

The ratios of phytogeographic region members determined as a result of floristic research in our research area and nearby areas are shown in Table 5.

Table 5: Distribution rates of taxa in the study area and nearby areas in phytogeographic regions

Research No and Title	**Phytogeographic Regions**
1. Contributions to the Flora of Çelikhan District (Adıyaman)	Anatolia-Turanian 158, Mediterrian 34 Europe-Siberia 33
2.Flora and Vegetation of Adıyaman Unv. Campus [15]	Anatolia-Turanian 45, Mediterrian 16 Europe-Siberia 89
3.Flora of Akdağ (Çelikhan-Adıyaman) [17]	Anatolia-Turanian 220, Mediterrian 64 Europe-Siberia 29
4.Flora of Ali Mountain ve Ziyaret Hill (Adıyaman) [14]	Anatolia-Turanian 97, Mediterrian 59 Europe-Siberia 19
5. Flora of Atatürk Dam Basin of Şanlıurfa Part [16]	Anatolia-Turanian 79, Mediterrian 38 Europe-Siberia 12
6.Flora and Vegetation of Gazihan Dede (Adıyaman) Promenade Area [13]	Anatolia-Turanian 87, Mediterrian 39 Europe-Siberia 17
7.Contributions of Nemrut Mountain (Adıyaman) Flora [12]	Anatolia-Turanian 101, Mediterrian 26 Europe-Siberia 2

There are 158 taxa belonging to the Anatolian-Turanian phytogeographic region in the research area. In the Anatolian-Turan phytogeographic region, the continental climate with hot and dry summers and cold and rainy winters is dominant. As seen in Table 5, taxa belonging to the Anatolian-Turanian phytogeographic region are in the first place in all areas. Mediterranean phytogeographic region taxa are in the second rank in terms of the number of taxa in our area (Table 5), this is the case in which the continental climate is dominant in the research area, microclimatic features are seen in some regions, it includes transitional regions with continental and Mediterranean climate characteristics, temperate and summer drought, which is typical of the Mediterranean climate. It can be attributed to the fact that the habitats that it has an impact on are more in the research area. In the Euro-Siberian phytogeographic region, humid, cool and semi-

temperate climate characteristics are dominant, the ecological demands of the members of this phytogeographic region are mostly wet, less hot, humid and shaded habitats. All of the research areas seen in Table 3 are located in the Anatolian-Turanian phytogeographic region. Therefore, it is normal for Anatolian-Turan elements to take the first place in terms of taxa number in all studies. There are similarities in the distribution ratios of taxa in the research area and areas close to the research area according to the plant geography regions, and the differences in the ratios can be caused by the geological, geomorphological, topographic, ecological characteristics of the study areas, the climatic differences in the years studied and the differences in the field studies.

In the research area, it was determined that 30 taxa were endemic (Table 6). Hazard categories are of endemic taxa are showed in the plant list at the end of the plant taxa.

Table 6: Number of taxa and endemic taxa of research areas

Research No and Title	Number of Taxa	Number of Endemic Taxa
1. Contributions to the Flora of Çelikhan District (Adıyaman)	454	30
2. Flora and Vegetation of Adıyaman Unv. Campus [15]	322	6
3. Flora of Akdağ (Çelikhan-Adıyaman) [17]	677	97
4. Flora of Ali Mountain ve Ziyaret Hill (Adıyaman) [14]	428	19
5. Flora of Atatürk Dam Basin of Şanlıurfa Part [16]	291	9
6. Flora and Vegetation of Gazihan Dede (Adıyaman) Promenade Area [13]	297	13
7. Contributions of Nemrut Mountain (Adıyaman) Flora [12]	250	43

As a result, it is expected that the data obtained from this study will shed light on and supports floristic studies both in Adıyaman and Turkey.

Acknowledgements

This study was supported by Adıyaman University Scientific Research Projects Unit under project number ECZFMAP/2019-0004.

References

[1] Ekim, T., Damarlı Bitkiler in Güner A., Ekim T., *Resimli Türkiye Florası*, Flora Araştırmaları Derneği/Türkiye İş Bankası Kültür Yayınları, İstanbul, 2014.

[2] Kılıç, Ö., Yıldırımlı, Ş., *A New Species, Allium adiyamanense* (*Amaryllidaceae*/ *Alliaceae*/ *Liliaceae*) From Turkey, Ot Sistematik Botanik Dergisi, 26(1), 33-39, 2019.

[3] Yıldırımlı, Ş., Kılıç Ö., *Three new species of Apiaceae Family from Turkey, Bunium sancakense, Pimpinella adiyamanensis, Trigonosciadium solhanense,* Ot Sistematik Botanik Dergisi, 26(1), 41-52, 2019.

[4] Davis, P.H., *Flora of Turkey and the East Aegean Islands*, Edinburgh University Press., volumes 1-9, 1965-1988.

[5] Raunkiaer, C., *The life forms of plants and statistical plant geography,* Oxford, Clarendon Press, 1934.

[6] IUCN., *Guidelines for Application of IUCN Red List Criteria at Regional and National Levels*: Version 4.0. IUCN, Gland, Switzerland and Cambridge, UK, 2012.

[7] IUCN., *Red list categories: Version 3.1.* Prepared by the IUCN Species Survival Commission. Gland", Switzerland and Cambridge, 2013.

[8] IUCN., *Green Status of Species: A global standard for measuring species recovery and assessing conservation impact.* Version 2.0. Gland, Switzerland, 2021.

[9] Gaussen, H., *Determination des Climats par la Methode des Courbes Ambrothermiques*, Comptes Rendus Hebdomadaires Des Seances De L Academie Des Sciences, 240(6), 642-643, 1955.

[10] Emberger, L*., Sur une Formule Climatique et ses Applications en Botanique*, Comptes rendus de l'Académie des Sciences, 191, 389-390, 1930.

[11] Akman, Y., *İklim ve Biyoiklim*. Palme Yayınları Mühendislik Serisi, Ankara. 304, 1990.

[12] Tel, A.Z., *Contributions to the flora of Nemrut Mountain (Adıyaman/Turkey*), Biological Diversity and Conservation, 2, 1, 36-60, 2009.

[13] Ortaç, Z., Tel, Z., *Gazihan Dede Mesire Alanı (Adıyaman-Türkiye) florası*. Türler ve Habitatlar, 2, 1, 33-53, 2021.

[14] Tel, A.Z. & Şahin, M.S., *A Research on the Floristic Composition of the Vegetation Types of Ali Mountain and Ziyaret Hill (Adiyaman/Turkey)*. ADYÜTAYAM 4 (1),1-19, 2016.

[15] Koç, S., *Adıyaman Üniversitesi Kampüsünün Flora ve vejetasyonu,* Yüksek lisans tezi, Adıyaman Üniversitesi, 2019.

[16] Çetiner, M., *Atatürk Baraj Gölü Havzası'nın Şanlıurfa Bölümü Florası*, Yüksek lisans tezi, Adıyaman Üniversitesi, 2020.

[17] Avcı, H., *Akdağ (Çelikhan) Florası,* Yüksek lisans tezi, İnönü Üniversitesi, 2019.

SUPPLEMENTARY INFORMATION FILE

Adıyaman University Journal of Science
https://dergipark.org.tr/en/pub/adyujsci
DergiPark AKADEMİK
ISSN 2147-1630
e-ISSN 2146-586X

Contributions to the Flora of Çelikhan District (Adıyaman)

Ömer KILIÇ[1*], Şinasi YILDIRIMLI[2]

[1]*Adıyaman University, Faculty of Pharmacy, Department of Basic Science of Pharmacy, 02000, Adıyaman, Türkiye.*
okilic@adiyaman.edu.tr, ORCID: 0000-0003-3409-1572
[2]*Hacettepe University, Faculty of Science, Department of Biology, 06000, Ankara, Türkiye*
ot@hacettepe.edu.tr, ORCID: 0000-0001-9648-7471

Captions

Figure SI-1. Some plant taxa and habitats in the research area

* Corresponding Author
DOI: 10.37094/adyujsci.1143607

SUPPLEMENTARY INFORMATION FILE

Gundelia komagenensis

Fibigia macrocarpa

Melica persica subsp *persica*

Stony steppe habitat

Steppe habitat

Wetland-moisty habitat

Morina persica subsp. *decussatifolia*

Papaver rhoeas

Rocky-garigue habitat

Herbarium samples

Project researcher Prof.Dr.Şinasi Yıldırımlı

Steppe-stony habitat

Forested area and rocky habitat

Project manager Prof.Dr.Ömer Kılıç

Wetland habitat

Aethionema apetalum

Acanthus dioscoridis var. *dioscoridis*

Centaurea urvillei subsp *hayekiana*

Acantholimon calvertii

Damaged foresty, steppe and Rocky habitat

Aethionema adiyamanense

SUPPLEMENTARY INFORMATION FILE

Ajuga chamaepitys subsp. chia var. chia

Alcea dissecta

Achillea vermicularis

Carex distans

Centaurea iberica

Ceratocephala falcata

Cuscuta brevistyla

Chenopodium foliosum

Dianthus lactiflorus

Fumaria parviflora

Geranium stepporum

Hypericum perforatum

Juniperus oxycedrus subsp. *oxycedrus*

Crataegus monogyna subsp. *monogyna*

Platanus orientalis

Quercus libani

Rosa canina

Rubus sanctus

Cichorium intybus

Mellilotus officinalis

Teucrium polium

SUPPLEMENTARY INFORMATION FILE

Senecio vernalis

Marrubium astracanicum subsp. astracanicum

Ixilorion tataricum subsp *montanum*

Forest, open area habitat

Scutellaria orientalis subsp. *orientalis*

Centaurea virgata

Buglossoides arvensis

Anarrhinum orientale

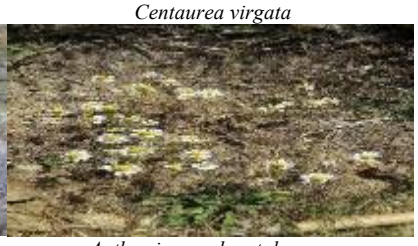

Anthemis pseudocotula

Onosma sericeum

Scabiosa rotata

Ziziphora capitata

Cnicus benedictus var. *benedictus*

Centaurea solstitialis subsp. *solstitialis*

Crupina crupinastrum

Salvia multicaulis

Fibigia ericarpa

Rumex acetosella

Silene vulgaris

Galium mite

Plantago lanceolata

Malva neglecta

Equisetum arvense var. *arvense*

Stony habitat

Phragmites australis

Nasturtium officinale

Stachys rupestris

Iris persica

Marrubium astracanicum subsp. astracanicum

Legousia falcata

Buglossoides arvensis

Anarrhinum orientale

Anthemis pseudocotula

Marrubium globosum

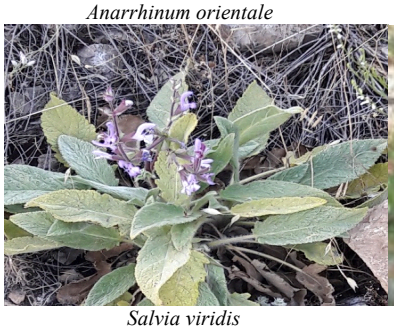

Salvia viridis

Tamarix smyrnensis

Muscari comosum

Allium flavum subsp. *flavum*

Gagea taurica

Figure SI-1: Some plant taxa and habitats in the research area

Adıyaman University Journal of Science
https://dergipark.org.tr/en/pub/adyujsci
DergiPark AKADEMİK
ISSN 2147-1630
e-ISSN 2146-586X

Determination of Some Elements in Canned and Frozen Vegetables Sold in Balıkesir (Türkiye) Markets and Nutritional Assessment

Feyzullah TOKAY*

Balıkesir University, Faculty of Science and Arts, Chemistry Department, Balıkesir, Türkiye
feyzullahtokay@balikesir.edu.tr, ORCID: 0000-0002-8894-1918

Received: 29.09.2022 **Accepted:** 02.11.2022 **Published:** 30.12.2022

Abstract

In this work, determination of some elements including Pb, Ni, Ba, Fe, Zn, Mg, Mn, Al, Cu, Mo, Ca, B, Cr, Cd, V and Co was carried out in some canned and frozen vegetable samples sold in Balıkesir, Türkiye. The study covered randomly chosen 13 canned and frozen samples such as green peas, okra, shell bean, sweet corn, green beans, garniture and tomato paste. Mineralization of the samples was achieved using microwave assisted wet digestion in closed vessels. The element contents were determined using ICP OES. The element contents were between 0.16-1.86 mg kg^{-1} for Ni; 0.33-5.02 mg kg^{-1} for Ba; 4.20-32.22 mg kg^{-1} for Fe; 1.65-14.64 mg kg^{-1} for Zn; 124.83-1016.79 mg kg^{-1} for Mg; 0.87-4.99 mg kg^{-1} for Mn; 0.32-1.74 mg kg^{-1} for Al; 0.78-14.97 mg kg^{-1} for Cu; 0.38-4.24 mg kg^{-1} for Mo; 42.60-1607.40 mg kg^{-1} for Ca and 0.96-7.56 mg kg^{-1} for B. Additionally, Pb was determined in only frozen green peas as 1.3±0.1 mg kg^{-1}. In general, the highest element contents were found in frozen samples. In terms of nutritional assessment, estimated daily intakes of the elements were compared with recommended dietary allowances (RDA), nutrition reference values (TFC) and daily tolerable upper intake levels (UL) which were established by World Health Organization, Turkish Food Codex and Institute of Medicine, respectively. The results showed that the element contents of the analysed samples did not exceeded the permissible limits set by various health organizations. It is

* Corresponding Author DOI: 10.37094/adyujsci.1181786

concluded that the contamination of these products may be an important threatening for public health. Therefore, monitoring of these samples should be a vital strategy for food industry.

Keywords: Canned food; Frozen food; ICP OES; Metal determination; Nutritional assessment.

Balıkesir (Türkiye) Marketlerinde Satılan Konserve ve Dondurulmuş Sebzelerde Bazı Elementlerin Tayini ve Beslenme Açısından Değerlendirilmesi

Öz

Bu çalışmada, Balıkesir Türkiye'de marketlerde satılan bazı konserve ve dondurulmuş sebze örneklerinde Pb, Ni, Ba, Fe, Zn, Mg, Mn, Al, Cu, Mo, Ca, B, Cr, Cd, V ve Co gibi elementlerin tayini yapılmıştır. Çalışma, bezelye, bamya, barbunya, tatlı mısır, yeşil fasulye, garnitür ve salça gibi rastgele seçilmiş 13 konserve ve dondurulmuş örneği kapsamaktadır. Numunelerin çözünürleştirilmesi, kapalı kaplarda mikrodalga destekli yaş yakma kullanılarak gerçekleştirilmiştir. Numunelerin element içerikleri ICP OES kullanılarak belirlenmiştir. Buna göre numunelerdeki element içeriklerinin Ni için 0,16-1,86 mg kg^{-1}; Ba için 0,33-5,02 mg kg^{-1}; Fe için 4,20-32,22 mg kg^{-1}; Zn için 1,65-14,64 mg kg^{-1}; Mg için 124,83-1016,79 mg kg^{-1}; Mn için 0,87-4,99 mg kg^{-1}; Al için 0,32-1,74 mg kg^{-1}; Cu için 0,78-14,97 mg kg^{-1}; Mo için 0,38-4,24 mg kg^{-1}; Ca için 42,60-1607,40 mg kg^{-1} ve B için 0,96-7,56 mg kg^{-1} aralığında olduğu tespit edilmiştir. Ayrıca, Pb elementi sadece donmuş bezelye numunesinde 1,3±0,1 mg kg^{-1} olarak belirlenmiştir. Genel olarak, donmuş örneklerde element içeriklerinin en yüksek olduğu gözlenmiştir. Beslenme açısından değerlendirildiğinde, elementlerin tahmini günlük alımları, Dünya Sağlık Örgütü, Türk Gıda Kodeksi ve İlaç Enstitüsü tarafından belirlenen, sırasıyla, tüketilmesi tavsiye edilen günlük miktar (RDA), beslenme referans değerleri (TFC) ve günlük tolere edilebilir üst alım seviyeleri (UL) ile karşılaştırılmıştır. Sonuçlar, analiz edilen numunelerin element içeriklerinin, çeşitli sağlık kuruluşları tarafından belirlenen sınırları aşmadığını göstermiştir. Bu ürünlerin potansiyel kirliliği halk sağlığı için önemli bir tehdit olabileceği sonucuna varılmıştır. Bu nedenle, bu örneklere ait kimyasal analiz sonuçlarının izlenmesi gıda endüstrisi için hayati bir stratejidir.

Anahtar Kelimeler: Konserve gıda; Dondurulmuş gıda; ICP OES; Metal tayini; Beslenme değerlendirilmesi.

1. Introduction

Considering the changing living conditions and busy working schedules of the human, nowadays, processed foods including canned, packaged or frozen, have growing interest. These food types such as vegetables, fruits, meat and drink are highly consumed in daily life [1-5]. So,

they are important sources of carbohydrates, proteins, fibres, vitamins, minerals and trace elements. Assuming the high consumption amounts of these foods, production conditions and packaging materials, exposure possibility of human to contaminants especially to heavy metals may occur more likely. Soil may be considered as the primary responsible for the metal content of the vegetables [6]. However, other sources including industrial emissions, release of wastes, using of herbicides, fertilizers and insecticides affect the trace element levels. Due to growing industry, pollution level of the foods is constantly increasing. Additionally, due to globalization and trade, the rate of spread of this pollution is also increasing especially by foodstuff. Additionally, migration of the elements from packaging material through the food is another problem on contamination [7-9].

In this perspective, monitoring the quality and safety of food are the most important problems for the producers. Moreover, as it is important for human health, determination of the contaminants including inorganic, organic and organometallic species in the food is a challenge for the analysts [10]. Although some of the trace elements taken with diet are essential, their high concentration may be toxic at high levels and may led to chronic health disorders. Consideringly, determination of the elements in the food samples is quite important to elicit the element profiles and amount that consumers are exposed to. Various techniques have been used for determination of the elements including flame atomic absorption spectrometry (FAAS) [11], graphite furnace atomic absorption spectrometry (GFAAS) [12], inductively coupled plasma optic emission spectrometry (ICP OES) [13] and mass spectrometry (ICP MS) [3, 4] and polarography and voltammetry [14]. Among these techniques, ICP OES offers wide dynamic linear range.

Various sample preparation protocols have been utilized prior to element detection for food samples. Liquid-liquid extraction, dry ashing, open vessel wet digestion and closed vessel wet digestion are some of the most commonly used sample preparation procedures for various samples including edible oils, milk, food additives, dairy products, frozen and canned foods [15-19]. Closed vessel wet digestion is one of the most effective matrix-destructive way among abovementioned sample preparation procedures. Digestion of the sample is carried out in a closed vessel under high pressure and temperature and closed system preserve the sample from contamination and/or loss of analytes.

The main objectives of the proposed study were (*i*) determination of Pb, Ni, Ba, Fe, Zn, Mg, Mn, Al, Cu, Mo, Ca, B, Cr, Cd, V and Co in canned and frozen food samples (green peas, okra, shell bean, sweet corn, green beans, garniture and tomato paste) from Balıkesir, Türkiye, (*ii*) to compare the obtained results via estimated daily intake (EDI) with recommended daily

allowances (RDA), nutrition reference values of Turkish Food Codex and daily tolerable upper intake levels, (*iii*) to compare the results with those reported in literature.

2. Materials and Methods

2.1. Chemicals

All reagents were of analytical grade and used without any purification. All glass and plastic laboratory equipments were cleaned by soaking in 10% (v/v) HNO_3, rinsed with deionized water and dried in a dust free environment. The deionized water that used throughout the experiments was obtained from reversed osmosis water purification system. The concentrated HNO_3 and HCl were purchased from Merck (Darmstadt, Germany). ICP multi element stock standard solution for Pb, Ni, Ba, Fe, Zn, Mg, Mn, Al, Cu, Mo, Ca, B, Cr, Cd, V and Co (1000 mg L^{-1}) was obtained from Merck, Darmstadt, Germany. The external standard calibration method was used for construction of calibration curves in a working range 0.01-5.00 mg L^{-1} with 3% HNO_3 ($r^2 \geq 0.995$). The digestion procedure was validated using a certificated reference material NIST-1549a whole milk powder (CRM) purchased from National Institute for Standards and Technology (NIST), Gaithersburg, MD, USA.

2.2. Instrumentation

An axially viewed Perkin Elmer Optima 3100 XL inductively coupled plasma optic emission spectrometer was utilized for determination of the target analytes in food samples. The working conditions of the ICP OES were tabulated in Table 1. CEM Mars 5 (Matthews, NC, USA) microwave oven system equipped with pressure and temperature controlled closed vessels was used for wet digestion of the food samples. The mass of the samples were weighed with Precisa XB 220A analytical laboratory balance.

Table 1: Working conditions for ICP OES

Polychromator	Echelle based polychromator, UV region (167-403 nm)
Recalibration system	Hg lamp
Detector	Segmented array charge coupled device detector
RF jenerator	40 MHz, free running, 750-1000 Watts
Nebulizer	Cross flow
Plasma gas flow	15 L min^{-1}
Auxiliary gas flow	0.5 L min^{-1}
Nebulization gas flow	0.5 L min^{-1}
Sample flow rate	1.5 mL min^{-1}
Wavelengths (nm)	220.349 for Pb; 231.604 for Ni; 233.527 for Ba; 238.204 for Fe; 206.200 for Zn; 285.213 for Mg; 257.610 for Mn; 308.215 for Al; 327.393 for Cu; 202.031 for Mo; 317.933 for Ca; 249.667 for B; 267.716 for Cr; 228.802 for Cd; 290.880 for V; 228.616 for Co

2.3. Sample collection

Various retail samples of canned or frozen food including green peas, okra, shell bean, sweet corn, green beans, garniture and tomato paste of randomly chosen different brands were obtained from local supermarkets of Balıkesir, Türkiye. The purchased products were within the expiry date declared on the respective packages. All the samples were transported to research laboratory and kept in their original packages to avoid contamination. Frozen and canned food samples were kept at -18°C and +4°C, respectively, up to analysis.

2.4. Preparation of the samples

All the samples were prepared in the same way for chemical analysis. Initially, each sample was removed from storage conditions and reached to room temperature. The samples were homogenized using a food blender with stainless steel cutters. In the next step, the homogenized samples were accurately weighted (about 1.0 g) in Teflon liners of microwave oven system. Then, 5 mL of concentrated HNO_3 was added on the samples and covered with watch glass to allow pre-digestion in a fume hood by standing overnight. After that, the vessels were closed and subjected to temperature controlled program (ramp up to 180 °C and 185 psi in 25 min with 600 W and hold for 10 min). Finally, the digested samples were cooled to room temperature, transferred to a volumetric flask and diluted up to 25 mL. For each sample three independent experiments were performed in addition to blank samples. The digested samples were analysed by ICP OES.

2.5. Analysis of standard reference material

The analysis of CRM (NIST-1549a whole milk powder) was used in order to verify the digestion procedure and to assess the degree of the contamination at any stage of sample treatment. The digestion of the CRM was performed in triplicate according to the same procedure that was described above.

3. Results and Discussion

Determination of the analytes including Pb, Ni, Ba, Fe, Zn, Mg, Mn, Al, Cu, Mo, Ca, B, Cr, Cd, V and Co in green peas, okra, shell bean, sweet corn, green beans, garniture and tomato paste samples was achieved using ICP OES. Cr, Cd, V and Co contents of all samples were found below detection limits (LOD). The LOD values ($3s_b/m$) were 109.65 µg kg^{-1} for Pb; 117.49 µg kg^{-1} for Ni; 80.69 µg kg^{-1} for Ba; 280.19 µg kg^{-1} for Fe; 147.58 µg kg^{-1} for Zn; 263.90 µg kg^{-1} for Mg; 182.96 µg kg^{-1} for Mn; 231.69 µg kg^{-1} for Al; 536.02 µg kg^{-1} for Cu; 109.02 µg kg^{-1} for Mo;

723.88 µg kg^{-1} for Ca; 218.55 µg kg^{-1} for B; 79.98 µg kg^{-1} for Cr; 52.41 µg kg^{-1} for Cd; 64.07 µg kg^{-1} for V and 135.47 µg kg^{-1} for Co for the applied method.

The CRM NIST-1549a whole milk powder was analysed to show the efficiency of the digestion procedure and accuracy of the analysis. The analysis results of CRM were tabulated in Table 2 for the analytes Ba, Ca, Fe, Cu, Mg and Zn. The recovery values which were obtained between 93.6%-107.8%, proved that there is no contamination or loss of analyte during the digestion procedure. Additionally, according to Student's *t* test, the differences between the experimental results ($\bar{x}$) and certified values (µ) were statistically insignificant at the 95% significance level.

Table 2: Analysis results and statistical evaluation for certified reference material (N=3)

Element	Certified Value (mg kg^{-1})	Experimental Value (mg kg^{-1})	Recovery (%)	$\lvert x-\mu \rvert$	$\frac{ts}{\sqrt{N}}$
Ba	0.566±0.039	0.56±0.01	99.2	0.005	0.030
Ca	8810±240	8514.06±491.95	96.6	295.94	1221.31
Fe	1.85±0.73	1.99±0.36	107.8	0.14	0.88
Cu	0.638±0.049	0.60±0.03	93.6	0.04	0.09
Mg	892±62	881.94±21.65	98.9	10.06	53.74
Zn	33.8±2.3	36.06±2.07	106.7	2.26	5.14

3.1. Concentration of target analytes in samples

The results of the analyte contents for the samples, green peas, okra, shell bean, sweet corn, green beans, garniture and tomato paste were tabulated in Table 3. The amounts of the analytes were reported as mg kg^{-1} for each sample in wet weight basis.

The concentrations of the examined analytes were between 0.16-1.86 mg kg^{-1} for Ni; 0.33-5.02 mg kg^{-1} for Ba; 4.20-32.22 mg kg^{-1} for Fe; 1.65-14.64 mg kg^{-1} for Zn; 124.83-1016.79 mg kg^{-1} for Mg; 0.87-4.99 mg kg^{-1} for Mn; 0.32-1.74 mg kg^{-1} for Al; 0.78-14.97 mg kg^{-1} for Cu; 0.38-4.24 mg kg^{-1} for Mo; 42.60-1607.40 mg kg^{-1} for Ca and 0.96-7.56 mg kg^{-1} for B for investigated samples. In terms of Pb, the concentrations were below detection limits for all samples excluding frozen green peas. The concentration of Pb was 1.34±0.10 mg kg^{-1} in frozen green peas. Ca and Mg levels were the highest for all samples among investigated analytes. In terms of concentrations, these analytes were followed by Fe for all samples except frozen sweet corn and jarred tomato paste. Additionally, excluding the samples frozen green peas, frozen shell bean and canned green beans, Ni concentrations were found to be the lowest in the samples. The variation

in analyte concentration of the investigated samples may be attributed to numerous factors including the region where the vegetable grown, source of food, type of food processing, type of packaging and possible corrosion of can.

The highest and the lowest concentrations of Ni were found in frozen green peas (1.86±0.06 mg kg^{-1}) and canned sweet corn (0.150±0.003 mg kg^{-1}). On the other hand, Ni content of sample 13 (canned green peas) was found to be below detection limit. The obtained data showed that our findings for Ni were lower than the results reported in literature [10, 19]. Additionally, the results were found comparable with the report from Türkiye and India [1, 8].

In terms of Fe, the concentrations were between 4.53-18.84 mg kg^{-1} in canned foods and 4.20-32.22 mg kg^{-1} in frozen food samples. The lowest Fe content was detected for frozen sweet corn (4.20±0.36) sample and the highest level was detected for frozen shell bean (32.22±1.10). Generally, it may be concluded here that Fe levels of canned food samples were lower than the frozen food samples for investigated samples. Comparing the data, the results were found almost similar to that found in Lebanon [7], India [8], Iran [11] and Ghana [21] for various canned or frozen food samples, but lower than the data obtained by Tuzen and Soylak [1].

Considering Zn which is a nutritionally essential element and deficiency may lead some disorders, the concentrations were between 1.65-14.64 mg kg^{-1}. The lowest and highest concentrations of Zn were found in canned green beans (1.65±0.14) and frozen shell bean (14.64±1.08), respectively. Additionally, similar to judgment for Fe above, levels of Zn in canned food samples were lower than the frozen food samples for investigated samples. These values were found similar and/or comparable to those reported by [6, 7, 19, 20], but were extremely lower obtained by Ahmadi and Ziarati [11] and Tuzen and Soylak [1].

The concentrations of Mn were ranged from 0.87±0.09 mg kg^{-1} (tomato paste) to 4.99±0.28 mg kg^{-1} (frozen shell bean). Considering the analyzed sample types as frozen and canned, the levels of Mn did not show a clear trend to differentiate. The results were in good agreement with [8] and [21]. On the other hand, previous finding from Türkiye [1] is about five times that observed for the counterpart assortments in this study.

Mean concentrations of Al of the investigated samples were varied between 0.32(±0.02)-1.74(±0.74) mg kg^{-1}. Besides that Al contents were below detection limit for sweet corn samples both for canned and frozen. The decreasing order of Al contents of the samples were frozen green peas>frozen green beans>canned shell bean>canned green peas>canned okra>frozen shell bean>tomato paste(jarred)>tomato paste(tin can)>frozen okra=frozen garniture>canned green beans. Reports showed the levels of Al for tomato 9.8±4.2 mg kg^{-1} [8], for vegetables and legumes 0.74±0.49-1.63±0.80 mg kg^{-1} [7], for corn, pea, tomato and bean 1.27±0.10-1.73±0.12 mg kg^{-1} [1]. The obtained results were found comparable with the literature excepting assortments consumed in India [7].

Cu concentrations of the samples present in this study were varied from 0.78±0.04 mg kg^{-1} to 14.97±0.14 mg kg^{-1}. The concentrations of the analyte showed similar trend for green peas, okra, shell bean, sweet corn and green beans samples in each varieties. Conversely, Cu concentrations of tomato samples were different about fifteen times. Values of Cu were 0.91±0.07-2.62±0.27 mg kg^{-1} [22], 0.89±0.02-0.91±0.02 mg kg^{-1} [20], 0.8±0.4-1.3±0.3 mg kg^{-1} [8], 1.28±0.81-2.14±1.35 mg kg^{-1} [7], 6.22±1.23-8.03±2.76 mg kg^{-1} [11], 2.94±0.24-7.77±0.57 mg kg^{-1} [1]. The reported values found comparable with the results present in this study except the jarred tomato paste sample (14.97±0.14 mg kg^{-1}).

To the best of our knowledge, determination of the analytes Ba, Mo and B were firstly presented in this study for the mentioned sample types. The obtained results were between 0.33±0.01-5.02±0.16 mg kg^{-1}; 0.384±0.005-4.24±0.31 mg kg^{-1} and 0.96±0.08-7.56±1.45 mg kg^{-1} for Ba, Mo and B, respectively. In regard of analyzed sweet corn samples all these elements were below detection limits. Additionally, Mo contents of canned and frozen okra, frozen green beans and tomato paste samples were below detection limits. The similar results were also found for canned shell bean and canned green beans in the case of B.

Considering Mg levels of the samples, the concentrations were varied from 124.83±4.31 mg kg^{-1} (tomato paste, tin can) to 1016.79±21.20 mg kg^{-1} (frozen okra). The obtained results showed that Mg levels of frozen samples were relatively higher than the canned samples. In the case of Ca, the mean concentrations were between 42.60±1.43-1607.40±84.62 mg kg^{-1}.The highest and lowest levels of Ca were quantified for frozen

okra and canned sweet corn, respectively. The existing tendency of the analyte was showed similarity with Mg which were relatively high in frozen samples. However, it should be noted that these findings were found to be lower than the values obtained in Iran [11] both for Mg and Ca.

Table 3: Analysis results of canned and frozen vegetables (N=3)

Sample No	Sample	Element (mg kg^{-1})											
		Pb	Ni	Ba	Fe	Zn	Mg	Mn	Al	Cu	Mo	Ca	B
1	Frozen Green Peas	1.3±0.1	1.86±0.06	0.90±0.02	21.00±1.87	8.28±0.24	444.55±15.21	4.29±0.18	1.74±0.74	5.31±0.30	0.97±0.03	425.70±10.73	7.56±1.45
2	Canned Okra (Tin Can)	nd	0.19±0.01	5.02±0.16	12.93±0.46	3.41±0.05	298.63±12.64	1.22±0.05	0.97±0.08	1.92±0.12	nd	931.02±60.34	3.90±0.20
3	Frozen Shell Bean	nd	0.54±0.04	0.41±0.02	32.22±1.10	14.64±1.08	791.19±71.29	4.99±0.28	0.72±0.07	6.44±0.40	4.24±0.31	435.17±45.84	6.78±0.26
4	Canned Sweet Corn (Tin Can)	nd	0.150±0.003	nd	4.53±0.61	4.51±0.13	175.62±1.09	1.10±12.22	nd	0.84±0.08	nd	42.60±1.43	nd
5	Frozen Sweet Corn	nd	0.252±0.001	nd	4.20±0.36	4.58±0.29	275.58±25.90	1.24±0.21	nd	1.00±0.05	nd	85.15±3.02	nd
6	Canned Shell Bean (Tin Can)	nd	0.21±0.01	0.34±0.01	18.84±1.17	7.00±0.44	228.26±2.26	2.43±0.15	1.18±0.10	4.16±0.02	2.70±0.25	474.74±24.56	nd
7	Frozen Green Beans	nd	0.204±0.004	0.48±0.03	10.38±1.45	2.29±0.07	209.02±9.32	1.79±0.09	1.34±0.03	0.98±0.10	nd	540.62±20.40	1.20±0.02
8	Canned Green Peas (Tin Can)	nd	0.33±0.01	2.25±0.04	12.49±0.22	7.07±0.36	281.58±6.31	3.02±0.08	1.03±0.08	2.89±0.14	1.18±0.08	449.34±13.56	2.78±0.63
9	Frozen Okra	nd	0.33±0.02	2.02±0.11	5.89±0.04	8.40±0.32	1016.79±21.20	2.92±0.14	0.63±0.06	2.08±0.13	nd	1607.40±84.62	4.39±0.42
10	Frozen Garniture	nd	0.32±0.03	0.77±0.04	8.40±0.06	7.12±0.37	287.91±4.81	2.22±0.19	0.63±0.06	2.30±0.09	0.81±0.04	301.24±8.37	1.64±0.10
11	Tomato Paste (Tin Can)	nd	0.16±0.01	0.33±0.01	10.22±0.99	1.75±0.14	124.83±4.31	0.87±0.09	0.67±0.05	0.92±0.04	nd	174.74±0.55	0.96±0.08
12	Tomato Paste (Jarred)	nd	0.198±0.001	0.34±0.01	5.78±0.44	2.01±0.09	193.74±2.53	1.44±0.04	0.69±0.07	14.97±0.14	nd	172.69±9.48	1.17±0.03
13	Canned Green Beans (Tin Can)	nd	nd	0.38±0.01	15.32±0.93	1.65±0.14	153.53±5.05	0.99±0.02	0.32±0.02	0.78±0.04	0.384±0.005	350.45±16.98	nd

3.2. Nutrition reference values

Daily contribution of Fe, Zn, Mg, Mn, Cu, Mo and Ca to dietary intake were calculated from the total amounts of the analytes using consumed portions to find out the nutritional value of the investigated samples (Table 4). According to Turkish Food Codex, the consumed portion of the vegetables was assumed as 150 g. The calculated estimated daily intake (EDI) values of certain analytes were appraised by benchmarking of recommended dietary allowances (RDA) established by World Health Organization, nutrition reference values (TFC) established by Turkish Food Codex and daily tolerable upper intake levels (UL) established by Institute of Medicine. Considering the highest amounts of the analytes in the examined samples, the EDI values were in decreasing order as follow: Ca>Mg>Fe>Cu=Zn>Mn>Mo. On the other hand, considering to EDIs to RDA and/or TFC, generally, the highest contribution range was provided by Mo element for all samples. Typically, contribution to RDA values showed increasing order as follow: Mn<Zn<Ca<Fe<Mg<Cu<Mo. Similar to RDA, the contribution of analytes were lined up in increasing order as follow for TFC: Zn<Ca<Fe<Mn<Mg<Cu<Mo. In terms of upper intake levels, the calculated estimated daily intakes of Zn, Mg, Cu, Mo and Ca were below daily tolerable upper intake levels (UL) defined by Institute of Medicine for adults. Additionally, due to the absence of a UL for Fe, Mn and Ni, it was not able to evaluate the EDIs for tenability. Finally, under normal conditions, it can be seen that daily consumption of the analyzed samples will not cause any harmful impact on health.

Table 4: Nutritional assessment for the analysed samples

Analyte	Detected Analyte Concentration Range[1] (mg kg^{-1})	EDI[2] (mg day^{-1})	Contribution to RDA[3, 5] (%)	Contribution to TFC[4, 5] (%)	Daily Tolerable Upper Intake Levels (UL)
Fe	4.20-32.22	0.6-4.8	4-32 (F) 6-48 (M)	4-34	Not established
Zn	1.65-14.64	0.2-2.2	2-18 (F), 1-15 (M)	2-22	25 mg
Mg	124.83-1016.79	18.9-152.5	7-54 (F), 5-44 (M)	5-41	2500 mg
Mn	0.87-4.99	0.1-0.7	2-14 (F/M)	5-35	Not established
Cu	0.78-14.97	0.1-2.2	3-73 (F/M)	10-220	5 mg
Mo	0.38-4.24	0.06-0.64	24-256 (F/M)	120-1280	0.6 mg
Ca	42.60-1607.40	6.4-241.1	0.5-20.1 (F/M)	0.8-30.1	2500 mg
Ni	0.16-1.86	0.02-0.28	-	-	Not established

[1] Analyte concentration ranges were extracted from Table 3 which indicates detected minimum and maximum levels, respectively.

[2] Estimated daily intake (EDI) was calculated by the equation; $EDI = \frac{Total\ element\ content\ of\ sample \times Consumed\ Food\ Amount}{Day}$

Consumed Food portion was assumed as 150 g per adult according to Turkish Food Codex

[3] Recommended Daily Allowance (RDA); for female (F), for male (M): Fe 15 mg (F), 10 mg (M); Zn 12 mg (F), 15 mg (M); Mg 280 mg (F), 350 mg (M); Ca 1200 mg (F/M); Mn 5 mg(F/M); Cu 3 mg (F/M); Mo 250 µg (F/M)

[4] Turkish Food Codex (TFC) Nutrition Reference Values for adult: Fe 14 mg; Zn 10 mg; Mg 375 mg; Ca 800 mg; Mn 2 mg; Cu 1 mg; Mo 50 µg

[5] Contribution percentages were calculated according to lowest and highest EDI values, respectively.

4. Conclusion

In this study, determination of some elements including Pb, Ni, Ba, Fe, Zn, Mg, Mn, Al, Cu, Mo, Ca, B, Cr, Cd, V and Co was carried out in canned or frozen food samples such as green peas, okra, shell bean, sweet corn, green beans, garniture and tomato paste sold in local markets of Balıkesir. Additionally, the results of Ba, Mo and B were firstly reported for those sample types. Quantification of the analytes was achieved using ICP OES after decomposition of the samples by microwave digestion. The obtained results showed that the analytes Cr, Cd, V and Co were below detection limits for all samples. Generally, comparing to frozen samples, the analyte levels of canned food samples were recorded lower. It can be concluded that all samples that were analyzed in this study were within international maximum permissible limits. Therefore, it can be concluded that the consumers have no potential risk through consuming those products. Nevertheless, the number of the analyzed samples may be found limited for a general judgment. However, this study may be assessed as a precursor work and in future, sample types and numbers may be expanded. As a conclusion, comprehensively and periodically monitoring of elements in such samples is imperative to safeguard the health of the public.

References

[1] Tuzen, M., Soylak, M., *Evaluation of trace element contents in canned foods marketed from Turkey*, Food Chemistry, 102 (4), 1089-1095, 2007.

[2] Dallatu, Y.A., Abechi, S.E., Abba, H., Mohammed, U.S., Ona, E.C., *Level of heavy metals in fresh and canned foods consumed in North Central Nigeria*, Scholarly Journal of Agricultural Science, 3 (6), 210-213, 2013.

[3] Kowalska, G., Pankiewicz, U., Kowalski, R., *Determination of the Level of Selected Elements in Canned Meat and Fish and Risk Assessment for Consumer Health*, Journal of Analytical Methods in Chemistry, 2020 (2148794), 1-13, 2020.

[4] Bağdat, S., Özkan, M.H., Tokay, F., Güçer, Ş., *A Novel and Validated Chemical-Enzymatic Strontium Fractionation Method for Wheat Flour from Celestite Mining Area: the First Approach for Sequential Fractionation*, Food Analytical Methods, 12 (2), 313-321, 2019.

[5] Bağdat Yaşar, S, Köse Baran, E., Tokay, F., *Element Fractionation Analysis for Milk in Its Real Matrix by Inductively Coupled Plasma Optical Emission Spectrometry*, Spectroscopy Letters, 46 (2), 100-108, 2013.

[6] Bağdat Yaşar, S., Güçer, Ş., *Fractionation analysis of magnesium in olive products by atomic absorption spectrometry*, Analytica Chimica Acta, 505 (1), 43-49, 2004.

[7] Korfalı, S.I., Hamdan, W.A., *Essential and Toxic Metals in Lebanese marketed canned food : Impact of metal cans*, Journal of Food research, 2 (1), 19-30, 2013.

[8] Basha, A.M., Yasovardhan, N., Satyanarayana, S.V., Reddy, G.V.S., Kumar, A.V., *Trace metals in vegetables and fruits cultivated around the surroundings of Tummalapalle uranium mining site, Andhra Pradesh, India*, Toxicology Reports, 1, 505-512, 2014.

[9] Ojezele, O.J., Okparaocha, F.J., Oyeleke, P.O., Agboola, H.I., *Quantification of Some Metals in Commonly Consumed Canned Foods in South-west Nigeria: Probable Pointer to Metal Toxicity*, Journal of Applied Sciences and Environmental Management, 25 (8), 1519-1525, 2021.

[10] Tokay, F., Bağdat, S., *Determination of Iron and Copper in Edible Oils by Flame Atomic Absorption Spectrometry After Liquid-Liquid Extraction*, Journal of the American Oil Chemists' Society, 92 (3), 317-322, 2015

[11] Ahmadi, A., Ziarati, P., *Chemical composition profile of canned and frozen sweet corn (zea mays L.) in Iran*, Oriental Journal of chemistry, 31 (2), 1065-1070, 2015.

[12] Rusin, M., Domagalska, J., Rogala, D., Razzaghi, M., Szymala, I., *Concentration of cadmium and lead in vegetables and fruits*, Scientific Reports, 11, 1-10, 2021.

[13] Tokay, F., Bağdat, S., *A novel and simple approach to element fractionation analysis: Single step fractionation of milk*, Food Chemistry, 379 (32162), 1-10, 2022.

[14] Palisoc, S.T., Bentulan, J.M.O., Natividad, M.T., *Determination of trace heavy metals in canned food using Graphene/AuNPs/$[Ru(NH_3)_6]^{3+}$/Nafion modified glassy carbon electrodes*, Journal of Food Measurement and Characterization, 13 (1), 169-176, 2019.

[15] Bağdat Yaşar, S, Köse Baran, E., Tokay, F., *Element fractionation analysis for infant formula and food additives by inductively coupled plasma optical emission spectrometry*, International Journal of Food Science and Technology, 49 (2), 392-398, 2014.

[16] Tokay, F., Köse Baran, E., Bağdat, S., *Assessment of Element Partitioning in Dairy Products: Application of Three Stage Sequential Fractionation Scheme and Metal Determination by ICP-OES*, Current Nutrition and Food Science, 14 (3), 264-271, 2018.

[17] Fiamegos, Y., Vahcic, M., Emteborg, H., Snell, J., Raber, G., Cordeiro, F., Robouch, P., de la Calle, B., *Determination of toxic trace elements in canned vegetables. The importance of sample preparation*, Trends in Analytical Chemistry, 85 (Part B), 57-66, 2016.

[18] Sobhanardakani, S., Hosseini, S.V., Tayebi, L., *Heavy Metals Contamination of canned fish and related implication in Iran*, Turkish Journal of Fisheries and Aquatic Sciences, 18 (8), 951-957, 2018.

[19] Köse Baran, E., Bağdat, S., *Spectrometric Determination of Copper in Edible Oil Based on the Extraction with N,N'-bis(5-methoxy-salicylidene)-2-hydroxy-1,3-propanediamine*, Food Science and Technology Research, 19 (4), 647-653, 2013.

[20] Massadeh, A.M., Al-Massaedh, A.T., *Determination of heavy metals in canned fruits and vegetables sold in Jordan market*, Environmental Science and Pollution Research, 25 (2), 1914-1920, 2018.

[21] Boadi, N., Mensah, J., Twumasi, S., Badu, M., Osei, I., *Levels of selected heavy metals in canned tomato paste sold in Ghana*, Food Additives and Contaminants: Part B, 5 (1), 50-54, 2012.

[22] Al Zabadi, H., Sayeh, G., Jodeh, S., *Environmental exposure assessment of cadmium, lead, copper and zinc in different Palestinian canned foods*, Agricultural & Food Security, 7 (50), 1-7, 2018.

Adıyaman University Journal of Science
https://dergipark.org.tr/en/pub/adyujsci
DergiPark AKADEMİK
ISSN 2147-1630
e-ISSN 2146-586X

Redescription of *Penicillicaris pectinimana* (Car, 1884) (Copepoda, Harpacticoida, Parastenheliidae)

Seher KURU[1,*], Süphan KARAYTUĞ[2]

[1]*Mersin University, Advanced Technology Education Research and Application Center, 33343, Mersin, Türkiye*
seherkuru33@gmail.com, ORCID: 0000-0001-8534-5486
[2]*Mersin University, Faculty of Sciences, Department of Biology, 33343, Mersin, Türkiye*
suphankaraytug@gmail.com, ORCID: 0000-0001-8980-4133

Received: 09.09.2022 **Accepted:** 11.11.2022 **Published:** 30.12.2022

Abstract

The main aim of this study is to conduct a taxonomic revision of *Penicillicaris pectinimana* living in the mediolittoral zone of Türkiye. Therefore, numerous specimens of both sexes collected from Mediterranean (25 localities), Aegean (9 localities) and the Black Sea (10 localities) coasts were morphologically reexamined in detail for the first time with the aid of light and scanning electron microscopes. Hundreds of individuals belonging to *Penicillicaris pectinimana* populations collected from different localities were comparatively analysed in terms of inter/intra population variability. In the light of the data obtained in this study, it was revealed that *Penicillicaris pectinimana* has very wide distribution on the coasts of Turkey and it is found in all localities examined. All possible morphological details of both sexes of *Penicillicaris pectinimana* were redescribed for the first time in detail since it was described in 1884.

Keywords: *Parastenhelia*; Taxonomy; Meiofauna; Revision.

* Corresponding Author DOI: 10.37094/adyujsci.1172195

Penicillicaris pectinimana (Car, 1884) (Copepoda, Harpacticoida, Parastenheliidae) Redeskripsiyonu

Öz

Bu çalışmanın temel amacı Türkiye'nin mediolittoral bölgesinde yaşayan *Penicillicaris pectinimana* türünün taksonomik revizyonunu yapmaktır. Bu yüzden Akdeniz (25 lokalite), Ege (9 lokalite) ve Karadeniz (10 lokalite) sahillerinden toplanmış çok sayıda her iki eşeye ait örnek ışık ve taramalı elektron mikroskopları yardımıyla morfolojik olarak yeniden ilk defa detaylı olarak incelendi. Farklı lokalitelerden toplanmış *Penicillicaris pectinimana* populasyonları populasyon içi ve populasyonlar arası varyasyon açısından karşılaştırmalı olarak analiz edildi. Elde edilen veriler ışığında, *Penicillicaris pectinimana* türünün Türkiye sahillerinde geniş bir yayılışa sahip olduğu ortaya konuldu. *P. pectinimana* türünün tanımlandığı 1884 yılından bu yana ilk kez her iki eşeyinin olası tüm morfolojik ayrıntıları yeniden tanımlandı.

Anahtar Kelimeler: *Parastenhelia*; Taksonomi; Mayofauna; Revizyon.

1. Introduction

The members of family Parastenheliidae are essentially marine, benthic, and mostly inhabit the intertidal zone and also prefer phytal habitats [1]. Taxonomic history of the family had long been very complicated. When Thompson and A. Scott [2] built the genus *Parastenhelia*, they placed it within family Harpacticidae. Later, many authors placed the genus in many other families, respectively, Canthocamptidae [3, 4], Diosaccidae [5], Thalestridae [6]. Then Lang [1] established Parastenheliidae family and assigned *Parastenhelia* as the type genus. Willen [7] transferred the genus *Karllangia* Noodt, 1964 from Ameiridae to Parastenheliidae. Then Gee [8] stated that *Parastenhelia anglica* Norman & T. Scott, 1905 and *Karllangia tertia* Kunz, 1975 are morphologically closely related and he established the genus *Foweya* for these two species. Huys and Mu [9] revalidated *Thalestrella* Monard, 1935 and retrieved it from the synonym list of *Parastenhelia* and they accepted *Karllangia* synonym of *Thalestrella*. Very recently, a pioneering familial review conducted by Huys and Mu [2] who critically evaluated all previous literature, and they determined 10 valid genera and about 30 valid species. In this study, taxonomic identification of extensive materials collected from the mediolittoral zone of Turkish coasts which were previously labelled as *P. spinosa* sensu lato were re-examined and revised according to recent literature [1]. According to Huys and Mu [9], all materials examined in this study actually belonged to *Penicillicaris pectinimana* which has not been recorded since its original description [10]. Here, a redescription of *P. pectinimana* is

made in order to provide a basis for the future comparisons of the species from the other localities.

2. Materials and Methods

Examined specimens were obtained from the harpacticoid collection of zoology department of Mersin University. All materials were collected from phytal habitats along the mediolittoral zone of Turkish coasts (Fig. 1). Dissection and preparation of the specimens were made as described in Kuru and Karaytuğ [11]. Huys et al. [12] were followed for descriptive terminology, abbreviations used in text and figures. Scale bars in all illustrations were in µm. Kaymak and Karaytuğ [13] were followed for examined specimens with Scanning Electron Microscopy (SEM).

Figure 1: Distribution of *Penicillicaris pectinimana* (Car, 1884) based on the examined materials along the Turkish coasts

3. Results and Discussion

3.1. Redescription of *Penicillicaris pectinimana* (Car, 1884)

Systematics: Order Harpacticoida Sars, 1903

Family Parastenheliidae Lang, 1936

Genus *Penicillicaris* Huys and Mu, 2021

Penicillicaris pectinimana (Car, 1884); (Figs. 2-15)

Material Examined: St1, 53♀♀, 15♂♂, 24/11/2007 (N 36° 08.315'; E 35° 54.598'); St2, 32♀♀, 19♂♂, 24/11/2007 (N 36° 14.008'; E 35° 50.220'); St3, 9♀♀, 2 ♂♂, 07/04/2007 (N 36° 32.089'; E 36° 02.485'); St4, 53 ♀♀, 8 ♂♂, 25/11/2007 (N 36° 53.409'; E 35° 56.775'); St5, 25♀♀, 5♂♂, 25/11/2007 (N 36° 51.329'; E 35° 54.389'); St6, 3♂♂, 24/11/2007 (N 36° 15.344'; E 35° 49.028');St7, 7♀♀, 3♂♂,24/11/2007 (N 36° 17.204'; E 35° 47.325'); St8, 53 ♀♀, 11 ♂♂,25/11/2007 (N 36° 46.133'; E 35° 46.553'); St9, 3♀♀, 25/11/2007 (N 36° 33.937'; E 35° 19.600'); St10, 2♀♀, 3♂♂, 26/11/2007 (N 36° 30.009'; E 34° 11.322'); St11, 13♀♀, 26/11/2007 (N 36° 27.473'; E 34° 08.647');St13, 1♂, 10/04/2007 (N 36° 27.570'; E 34° 07.984'); St14, 43♀♀, 11♂♂, 23/09/2011 (N 36°25'9"; E 34°5'30"); St15, 3♀♀, 6♂♂, 27/11/2007 (N 36° 17.829'; E 33° 50.863'); St16, 1♀, 27/11/2007 (N 36° 17.094'); E 33° 49.928'; St17, 1♀, 27/11/2007 (N 36° 16.264'; E 33° 48.842'); St18, 13♀♀, 6♂♂, 27/11/2007 (N 36° 11.453'; E 33° 39.363'); St19, 14♀♀, 4♂♂, 28/11/ 2007 (N 36° 09.315'; E 33° 26.548'); St20, 18♀♀, 7♂♂, 29/11/2007 (N 36° 05.167'; E 32° 54.354'); St21, 19♀♀, 5♂♂, 14/07/2007 (N 36° 01.959'; E 32° 48.749');St22, 6♀♀, 2♂♂, 29/11/2007 (N 36° 32.066'; E 32° 02.028'); St23, 6♀♀, 1♂, 01/12/2007 (N 36° 16.467'; E 30° 24.543');St24, 39♀♀, 10♂♂, 01/12/2007 (N 36° 16,743'; E 30° 08.392'); St25, 6♀♀, 4♂♂,01/12/2007 (N 36° 12.395'; E 29° 36.087');St26, 1♀, 10/08/2002 (N 41° 37.569'; E 28° 06.207'); St27, 1♀, 07/07/2001 (N 41° 06.875'; E 30° 41.060'); St28, 7♀♀, 4♂♂, 14/09/2002 (N 41° 50.847'; E 32° 45.177'); St29, 4♀♀, 1♂, 13/09/2002 (N 41° 57.133'; E 34° 23.516'); St30, 1♀, 1♂, 11/09/2002 (N 41° 06.806'; E 37° 43.037');St31, 2♀♀, 2♂♂, 10/09/2002 (N 41° 00.249'; E 38° 48.473'); St32, 1♀, 10/09/2002 (N 41° 05.677'; E 39° 23.718'); St33, 1♀, 1♂, 10/09/2002 (N 41° 03.152'; E 39° 32.227'); St34, 2♀♀, 1♂, 09/09/2002 (N 41° 01.039'; E 40° 22.165'); St35, 6♀♀, 1♂,08/09/2002 (N 41° 26.431'; E 41° 27.282'); St36, 2♀♀, 4♂♂, 17/05/2012 (N 36° 33.312'; E 29° 03.378'); St37, 1♀, 16/04/2007 (N 36°43.592"; E 28°07.810");St38, 4♀♀, 4♂♂, 15/04/2007 (N 36°41.131"; E 27°22.429"); St39, 20♀♀, 11♂♂, 24/05/2012 (N 38°40.153"; E 26°26.008"); St40, 1♀, 1♂, 24/05/2012 (N 38°37.168"; E 26°21.280"); St41, 1♀, 1♂, 24/05/2012 (N 38°20.500"; E 26°27.018"); St42, 9♀♀, 5♂♂, 24/05/2012 (N 38°17.065"; E 26°15.053"); St43, 5♀♀, 3♂♂, 12/07/2001 (N 39°31.603"; E 26°69.143"); St44, 1♀, 23/06/2002 (N 39°37.014"; E 26°62.193").

Redescription of female. The description based on a female from St. 19. Body semicylindrical in dorsal view, broadest at posterior margin of cephalothorax, tapering posteriorly, without clear distinction between urosome and prosome (Fig. 2). Total body length from tip of rostrum to posterior margin of caudal rami 428 μm. All somites except penultimate somite with pores and sensillae as figured. Rostrum (Fig. 4A) elongated, reaching to half of second antennulary segment and defined at base; triangular with pointed tip; bears a pore and a pair of subapical sensilla. Cephalothorax and P2–P4 pedigerous somites with plain hyaline

frills; urosomites with incised frills around posterior margin (Fig. 3A). Somites bearing P2-P4 with dorsal transverse rows of minute spinules. Somite bearing P5, genital double-somite, second abdominal somite and third abdominal somite with row of spinules around dorsal and dorsolateral posterior margin extending ventrally and laterally. Genital double-somite also with dorsal spinule row midway extending laterally (Fig. 2). Ventral and lateral posterior margin of anal somite and both sides of anal operculum with spinules as figured (Fig. 3E). Semi-circular anal operculum (Fig. 2B) without ornamentation. Long, fine, hair-like extensions around anal frill.

Caudal rami (Figs. 2, 8A) about as long as broad, with transverse spinule row as figured; pore present on dorsal and ventral surfaces; with seven setae. Seta I located ventrally near outer margin; naked and minute; seta II located anterolaterally, naked; seta III relatively long, slender and naked, located at outer distal corner; seta IV located terminally near outer corner, long and bipinnate, bases slightly swollen, with a fracture plane, seta V about two times longer than seta IV, markedly swollen at base, with a fracture plane; seta VI originates from inner subdistal corner, naked and long; seta VII arising from dorsal surface, triarticulated at base.

Antennule (Fig. 4A) 8-segmented; all segments without spinule ornamentation; all setae naked; with aesthetasc on segments 4 and 8; apical acrothek consisting of aesthetasc and two setae. Armature formula as follows: 1-[1], 2-[10], 3-[6], 4–[2 + (1 + ae)], 5–[2], 6-[2], 7-[4], 8-[5 + acrothek].

Antenna (Fig. 4B). Allobasis formed by complete fusion of basis and proximal endopodal segment; abexopodal margin with two rows of spinules and with one spinulose seta, inner margin with two spinules near the base of exopod. Endopod bears scarce spinules laterally at outer margin; bears a small seta and two well developed penicillate spines at lateral margin; four geniculate setae which the longest fused at base to a naked seta, one strong unipinnate spine, one large penicillate spine (penicillate spines showed with arrows in Fig. 3F). Exopod 2-segmented; first segment bears two setae; second segment bears five setae: lateral two setae unipinnate, apical margin with a well-developed unipinnate seta and two naked slender setae (Fig. 3C).

Mandible (Fig. 5A). Coxal gnathobase well developed, with few spinules on surface as figured, cutting edge complex with various multicuspidate teeth, bears a well-developed tooth located at ventral corner, bears a unipinnate short seta at dorsal corner. Basis elongated, bears two plumose setae and one naked seta near inner distal corner and with a spinule row on both posterior and anterior surfaces. Endopod 1-segmented and armatured with two setae laterally

and four setae terminally which of two fused at base. Exopod 1-segmented, small and squarish, with one naked setae and two plumose seta.

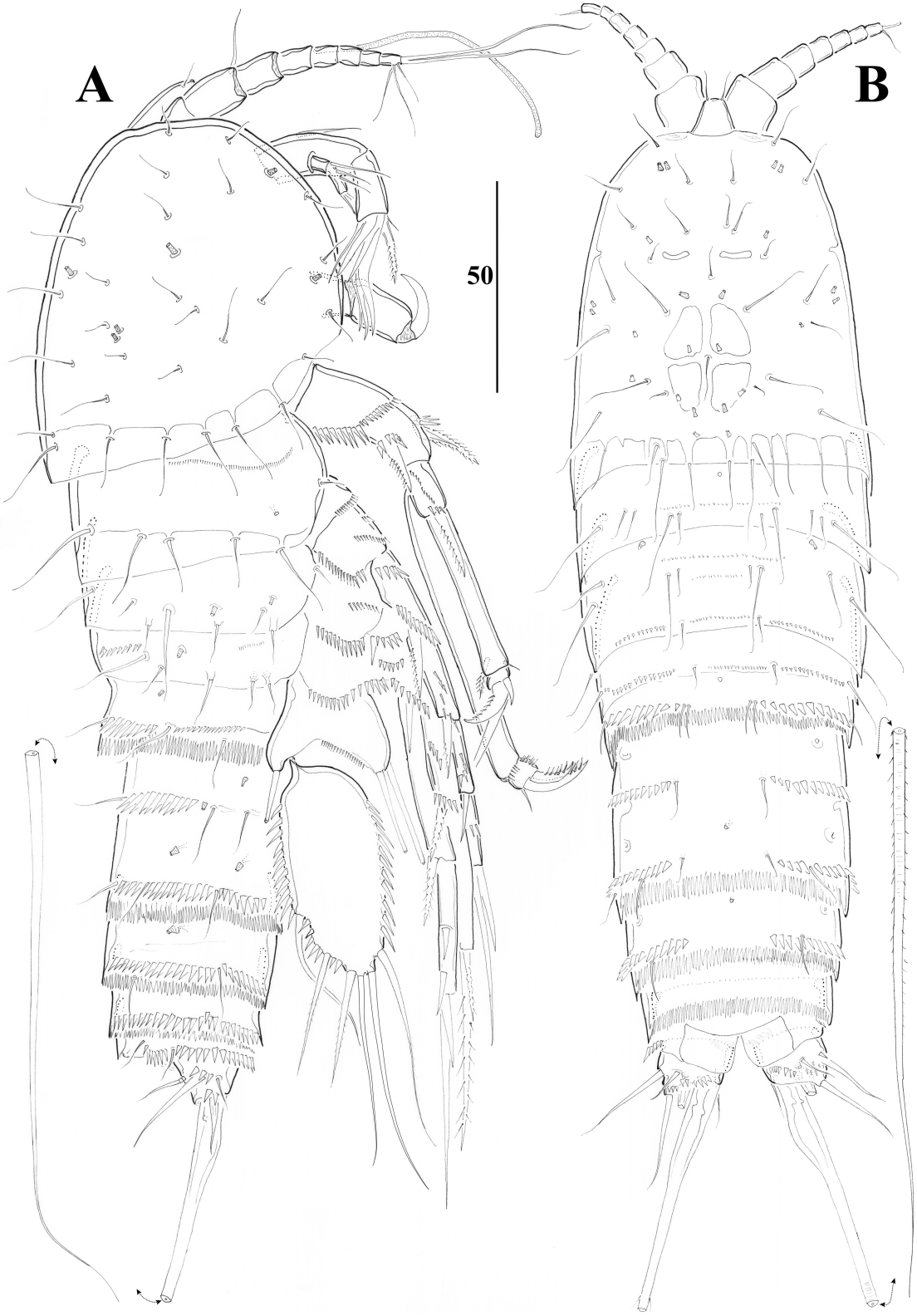

Figure 2: *Penicillicaris pectinimana* (Car, 1884), ♀, A, lateral habitus; B, dorsal habitus

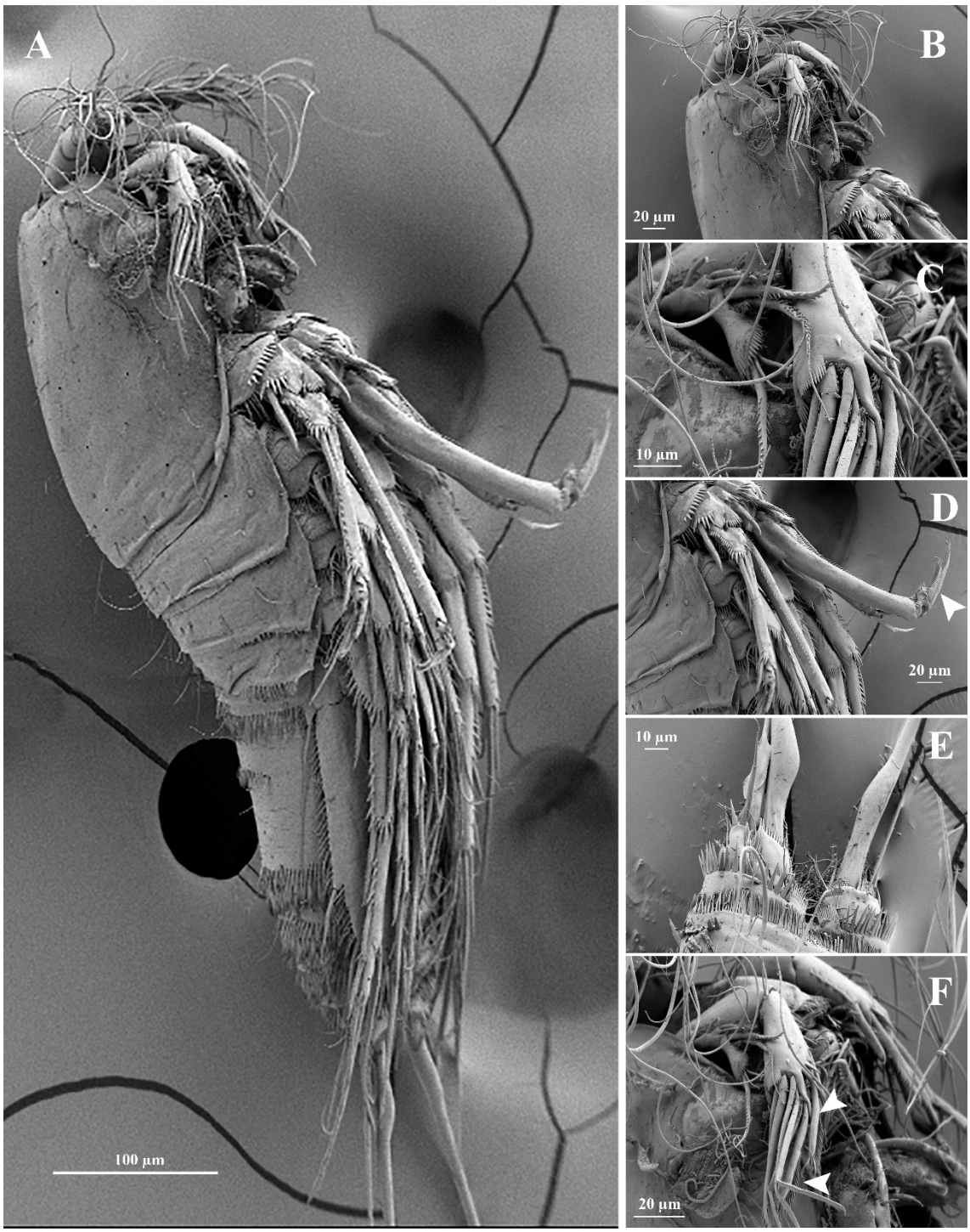

Figure 3: *Penicillicaris pectinimana* (Car, 1884), ♀, A, habitus lateral; B, cephalothorax; C, A2; D, P1; E, caudal rami; F, A2 distal endopod segment (SEM)

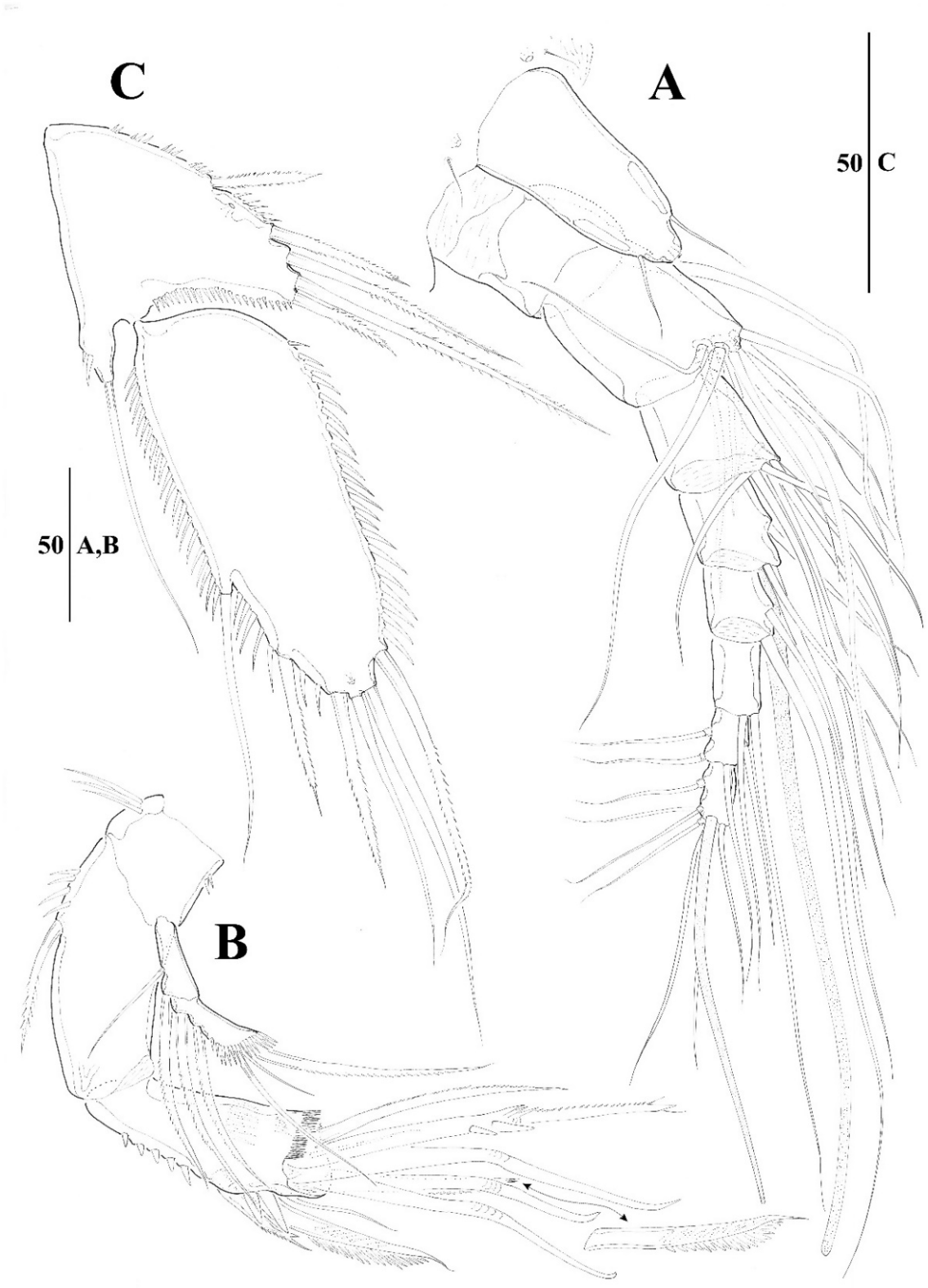

Figure 4: *Penicillicaris pectinimana* (Car, 1884), ♀, A, A1 and rostrum; B, A2; C, P5

Maxillule (Fig. 5B). Arthrite of praecoxa with two long setae on anterior surface and with seven spiniform elements around distal margin and two short elements near inner margin. Coxal endite consists of five setae around distal margin; coxal epipodite represented by a seta. Basis with five setae located around distal margin; rami fused partially to basis, endopod one-segmented, with one naked seta and one plumose seta; 1-segmented exopod with four naked setae.

Maxilla (Fig. 5C). Coxa with several rows of spinules as figured with three endites, proximal endite bilobate with one unipinnate seta and one plumose seta on inner protrusion and two naked setae on outer protrusion; middle endite with two setae, outer endite with three setae; endite of allobasis drawn out into strong, unipinnate spine and with two setae; endopod 1-segmented and well developed with three naked setae.

Maxilliped (Fig. 5D). Syncoxa with three spinule rows and one pinnate seta and one plumose seta on distal margin. Basis with complex row of spinules as figured, with two medial naked setae. Endopod reduced to a strong claw bearing three accessory setae proximally and with teeth along distal inner margin.

P1 (Fig. 6A). Praecoxa small and triangular, with a spinule row along distal margin. Intercoxal sclerite small and unornamented. Coxa with spinule rows along outer margin and medial part of distal margin, and small spinule row on anterior surface as figured (Fig. 3B); a pore located on anterior surface. Basis with two spines, inner spine unipinnate and outer spine bipinnate (spines with flagellated tips); with spinule rows near the base of outer spine, around base of endopod and along inner margin. Exopod with three subequal segments, first segment bears spinule row on outer distal corner and along outer margin and with unipinnate flagellated spine; second segment with spinule row along outer margin and with flagellated spine at outer distal corner; third segment with two penicillate spines, one geniculate seta and one non-geniculate seta and anterolateral edge with a spinule row. Prehensile endopod 2-segmented; proximal segment much longer than exopod, outer lateral margin with spinule row and a short, plumose seta arising from proximal third of the segment; distal segment small, ornamented with few spinules, armatured with a minute seta at inner margin and two slightly curved, penicillate spines apically (penicillate spines showed with arrows in Fig. 3D).

P2-P4 (Figs. 6B, 7). Triangular praecoxa, bears a spinule row along distal margin. Coxa with two transverse spinule rows and a pore on anterior surface. Basis rectangular, bears a spinule row near proximal inner corner, fine spinular row located distally between insertions of rami, and scarce spinules near the base of outer seta with a pore on outer distal corner near the

base of outer seta, outer basal seta naked in P3-P4 (outer basal seta bipinnate spine with flagellated tip on P2). Rami 3-segmented, slender; endopods reaching distal segment of exopods. All segments with large spinule rows along outer lateral margin. P2-P3 enp-1 with small unipinnate inner seta (well developed on P4 enp-1); P2-P4 enp-2 with one unipinnate seta. P2 enp-3 with one inner plumose seta, two distal plumose seta and one pinnate seta on outer margin. P3-P4 enp-3 with two inner plumose setae (the inner proximal seta is unipinnate on P3 enp-3), two distal plumose setae and one outer pinnate seta. P2-P3 exp-1 with small and naked inner seta, P4 exp-1 without inner seta. P2 exp-3 inner side with one plumose seta, P3 exp-3 inner side with two plumose setae and one small naked seta, P4 inner side exp-3 one plumose, one unipinnate and one small naked seta; distal margin of P2-P4 exp-3 with one plumose seta and one semispinulose seta; outer margin of P2-P4 exp-3 with three pinnate spines. Armature formulae of swimming legs are as follows:

	Exopod	**Endopod**
P1	0.1.022	1.111
P2	1.1.123	1.1.121
P3	1.1.323	1.1.221 ♂ 1.1.02+apophysis
P4	0.1.323	1.1.221 ♂ 1.1.021

P5 (Fig. 4C). Rami separate, baseoendopods not fused medially. Endopodal lobe small extending only to the base of exopod, trapezoid; with five bipinnate setae and few spinules around base of outer basal seta; with a pore between proximal two setae; with spinules along the inner margin and distal margin. Exopod about twice longer than maximum width; very narrow basal portion of exopod articulates; with row of spinules along inner and outer margins; bears six setae: two bipinnate setae and one naked seta along outer margin, two naked setae apically, and one long, bipinnate inner seta.

P6 (Fig. 8A) cover genital aperture, bears three setae: two short and naked inner setae and one long plumose outer seta.

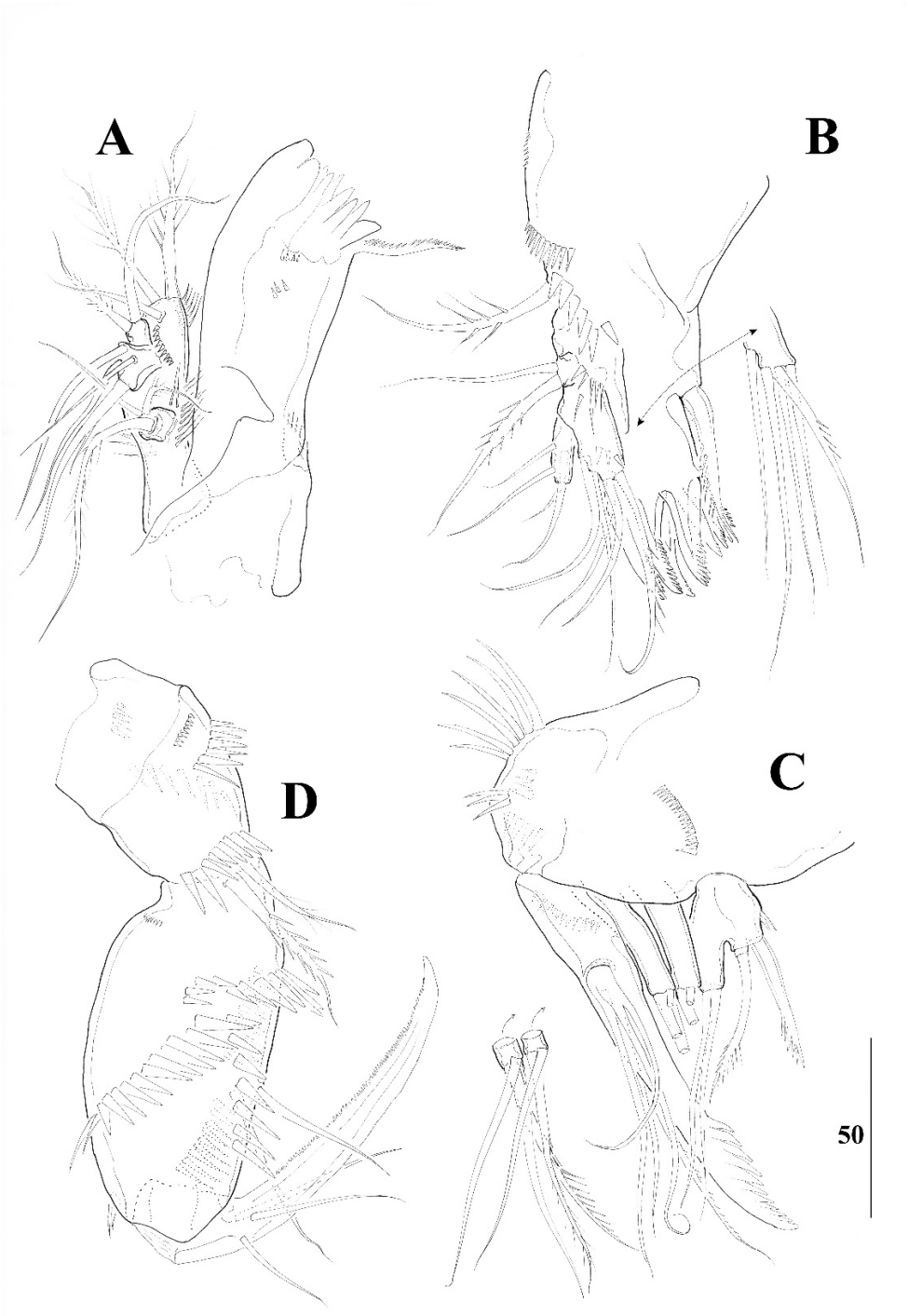

Figure 5: *Penicillicaris pectinimana* (Car, 1884), ♀, A, mandible; B, maxillule; C, maxilla; D, maxilliped

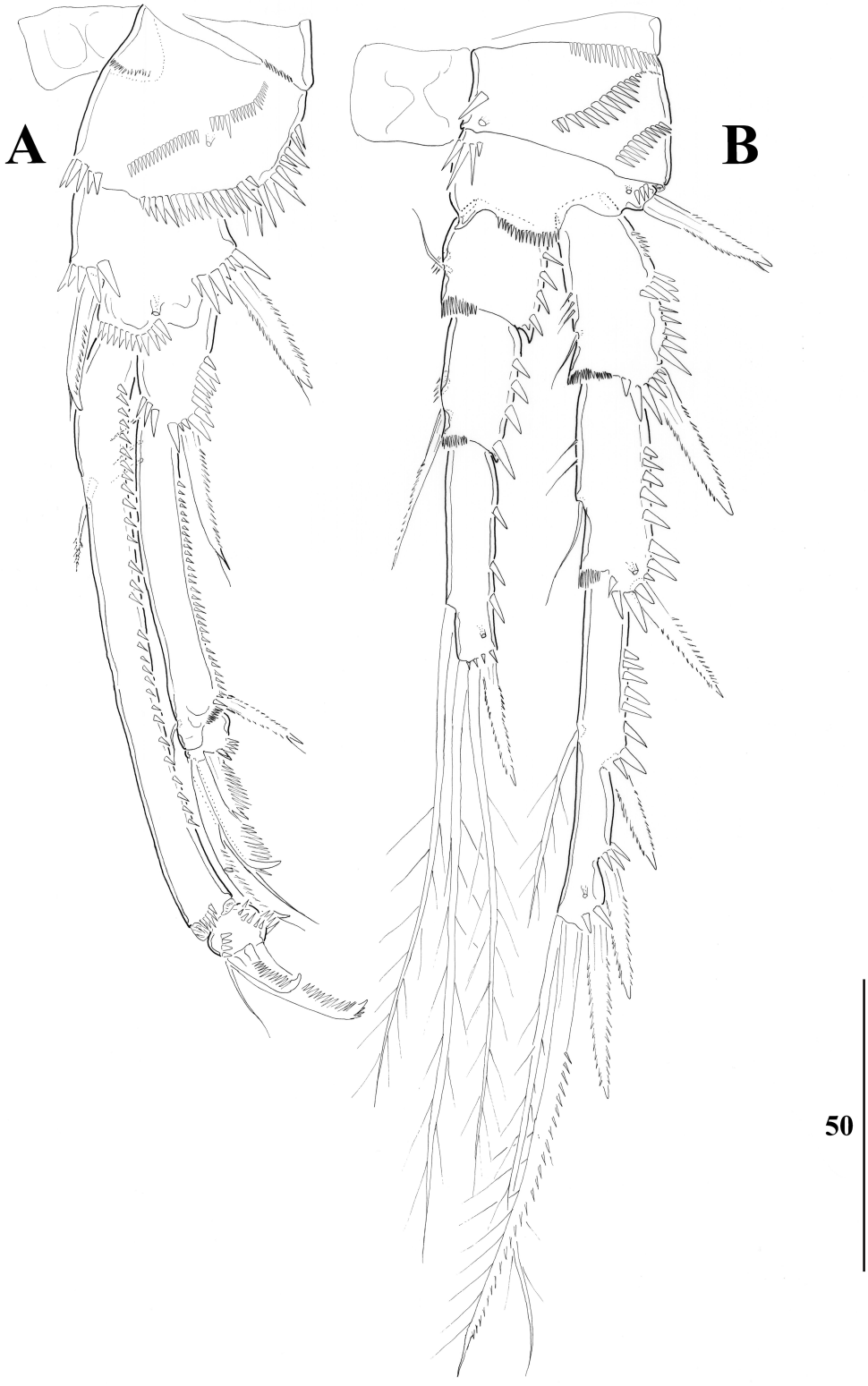

Figure 6: *Penicillicaris pectinimana* (Car, 1884), ♀, A, P1; B, P2

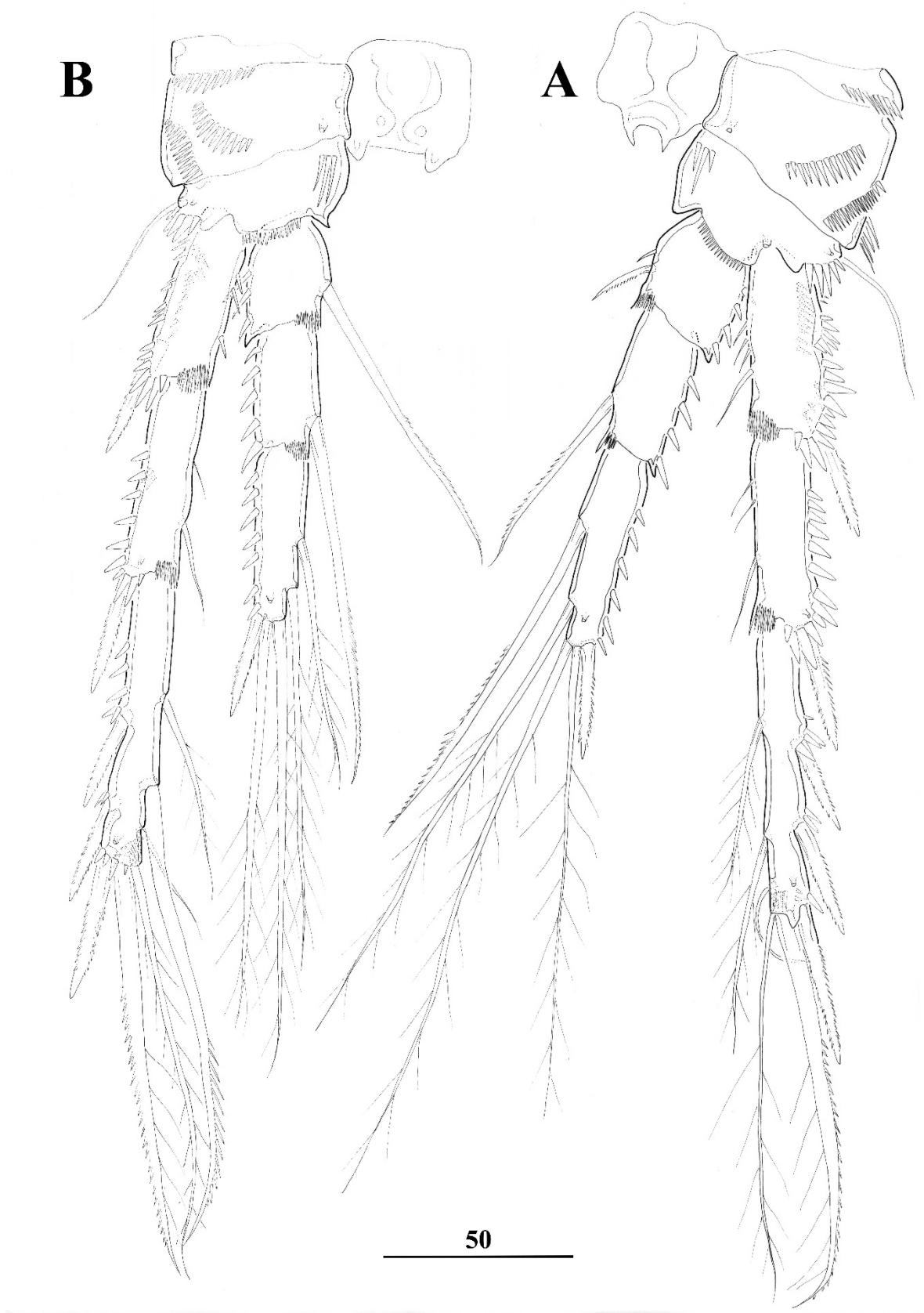

Figure 7: *Penicillicaris pectinimana* (Car, 1884), ♀, A, P3; B, P4

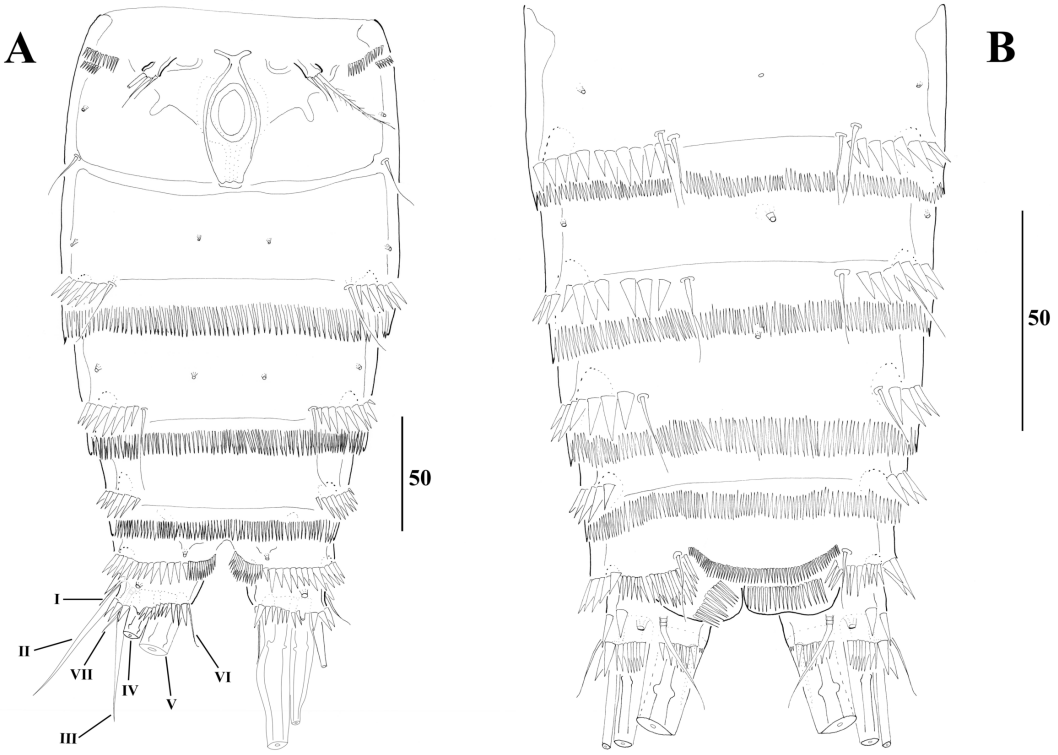

Figure 8: *Penicillicaris pectinimana* (Car, 1884), A, ♀, urosome ventral; B, ♂, urosome dorsal

Description of male. The description based on a male from St. 19. Body slightly smaller than female (Figs. 9, 10), length 362 µm. Sexual dimorphism observed in antennule, urosomal segments, length of some spinule rows P1, P2–P4 endopods, P5, P6 and caudal setae IV-V. Genital and first abdominal somites not fused (Fig. 8B). Ornamentation of urosome somites except for transverse continuous spinule row on ventral surfaces of second and third abdominal somites very similar to female (Fig. 15B). Caudal rami setae IV and V not swollen at base.

Antennule (Fig. 11) indistinctly 10-segmented, haplocer; geniculation positioned between segments 6-7 with four segments distal to it (Fig. 12C); aesthetasc on segments 5 and 10; all setae naked; thorn-liked six modified elements on segment 6 (showed with arrow on Fig. 12A-B) and bud-like two elements on segment 7 (showed with arrow on Fig. 12D). Armature formula as follows: 1-[1], 2-[10], 3-[4], 4-[4], 5-[5+ 1 plumose spine + (1 + ae)], 6-[2 +6 modified spines], 7-[1 + 2 modified spines], 8-[1], 9-[4], 10-[6 + acrothek].

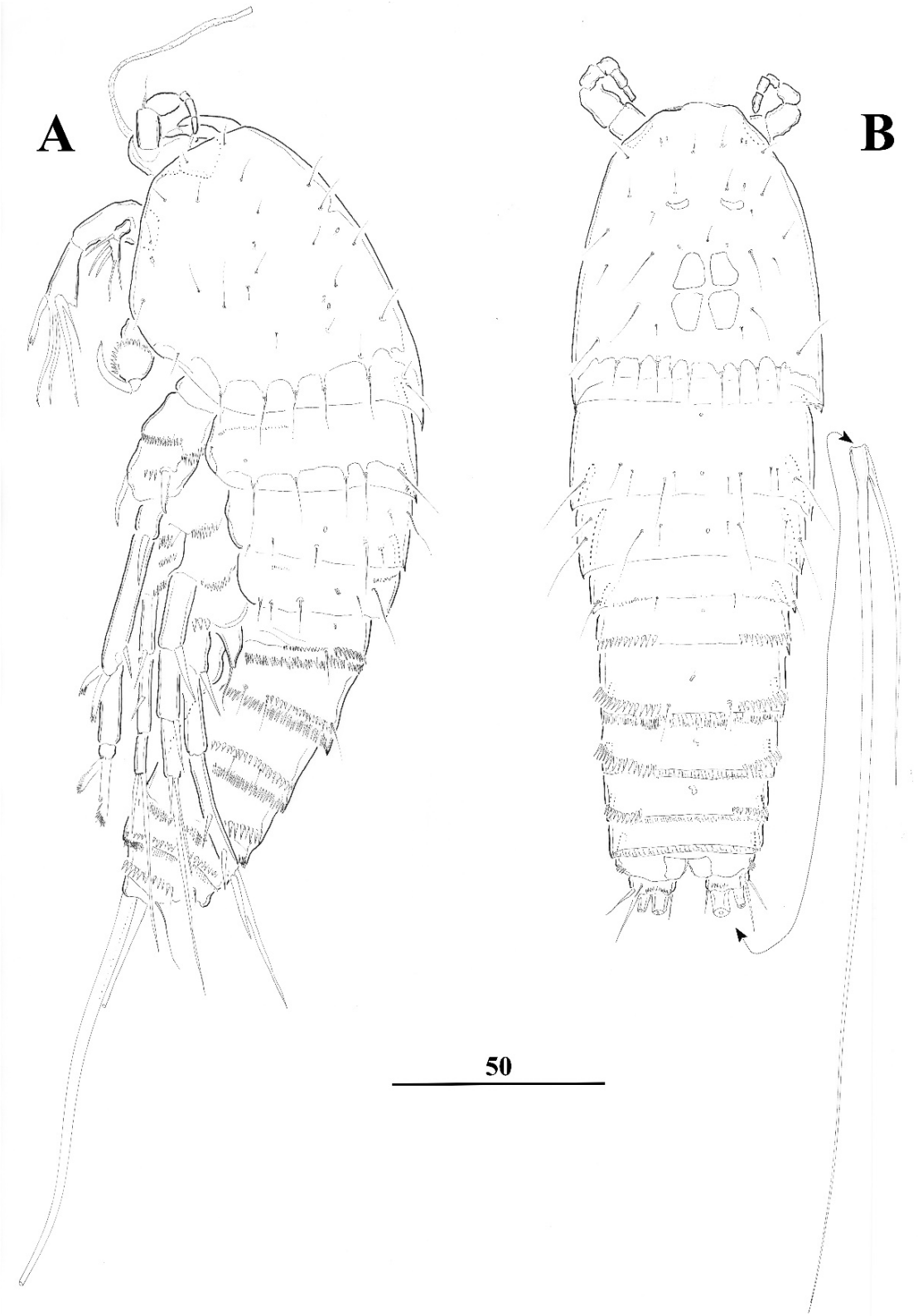

Figure 9: *Penicillicaris pectinimana* (Car, 1884), ♂, A, lateral habitus; B, dorsal habitus

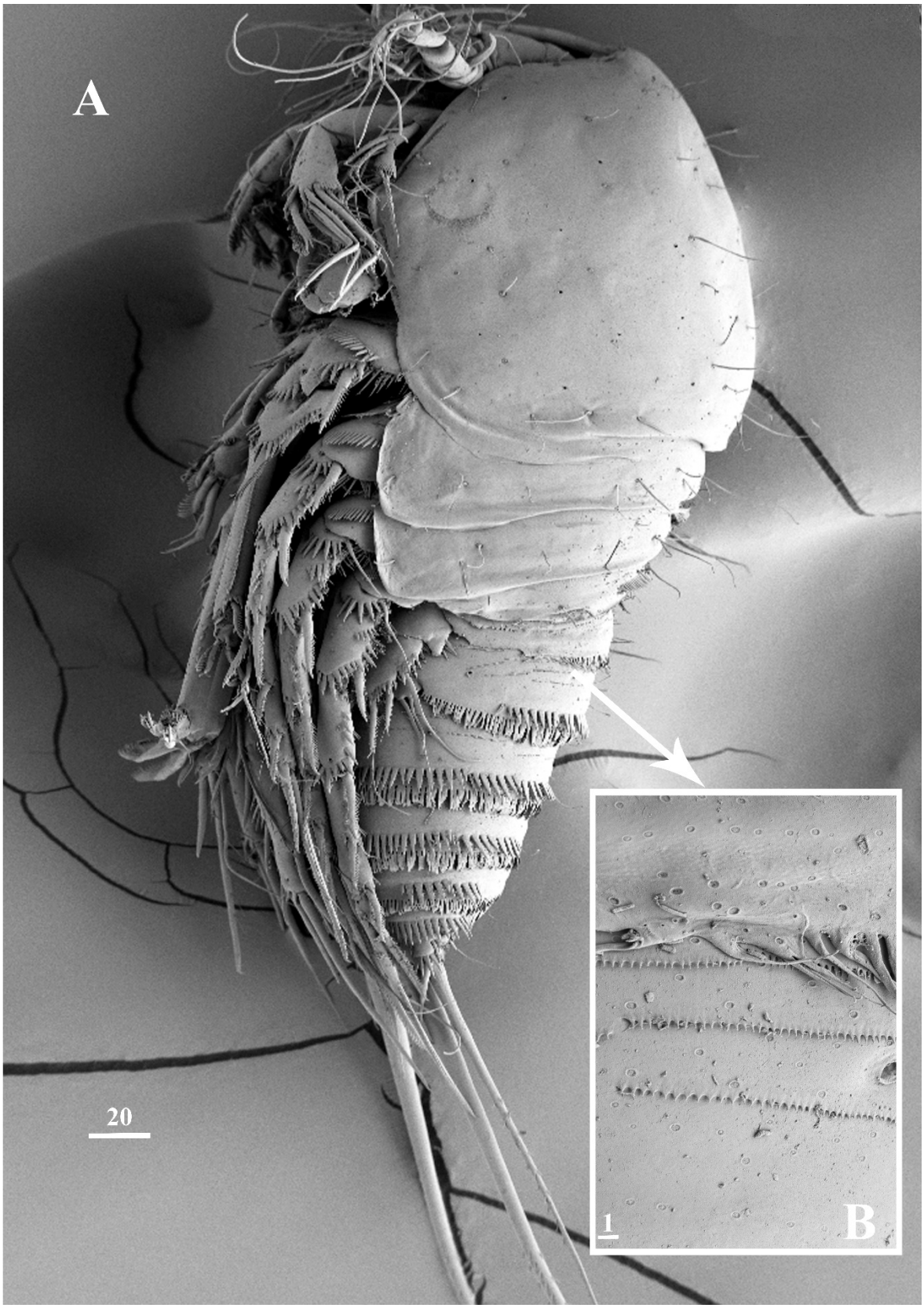

Figure 10: *Penicillicaris pectinimana* (Car, 1884), ♂, A, lateral habitus; B, hyaline frill and surface ornamentation of somite 5 (SEM)

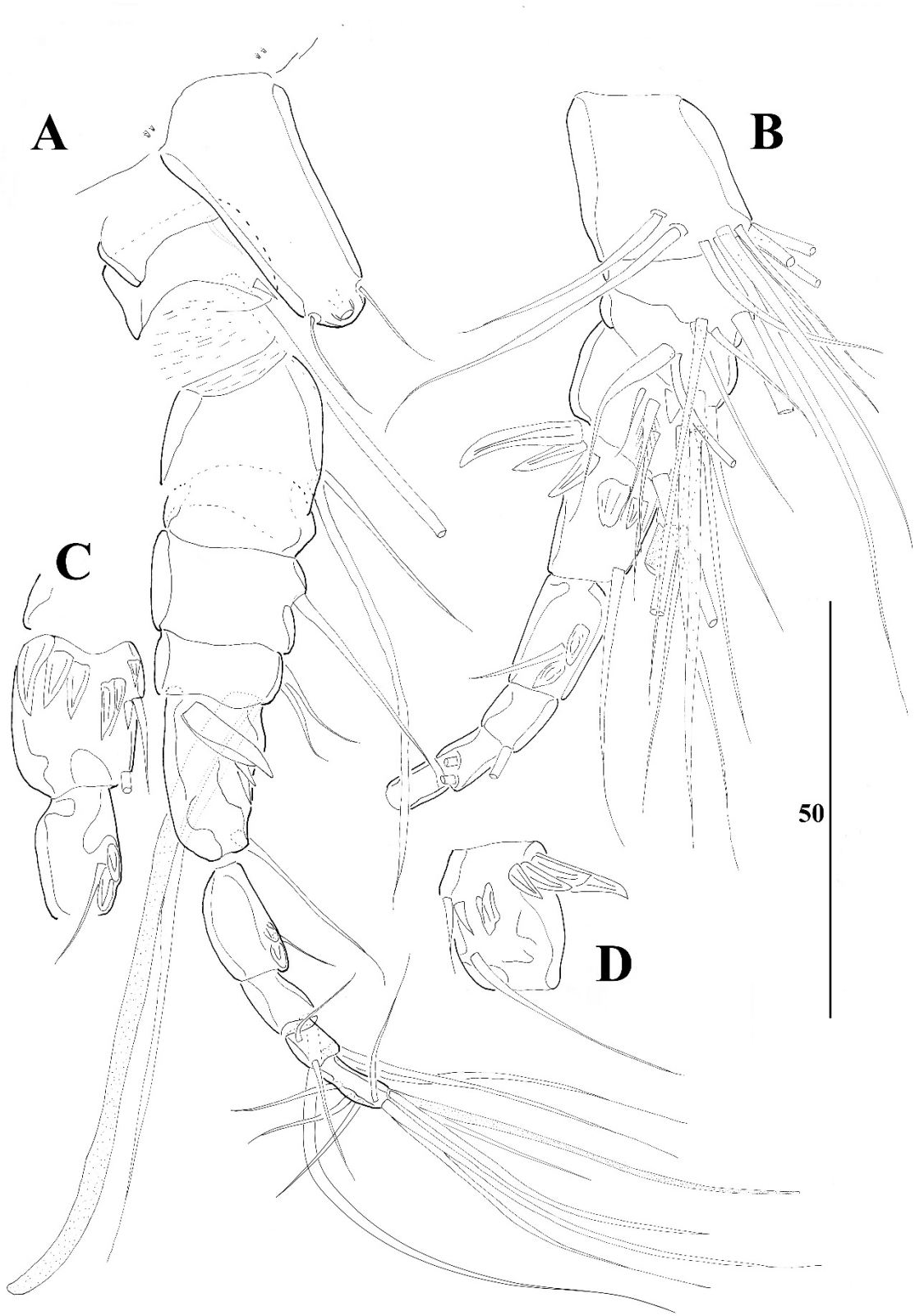

Figure 11: *Penicillicaris pectinimana* (Car, 1884), ♂, A, anterior of A1 and rostrum; B, posterior of A1; C, sixth and seventh segment of A1; D, sixth segment of A1

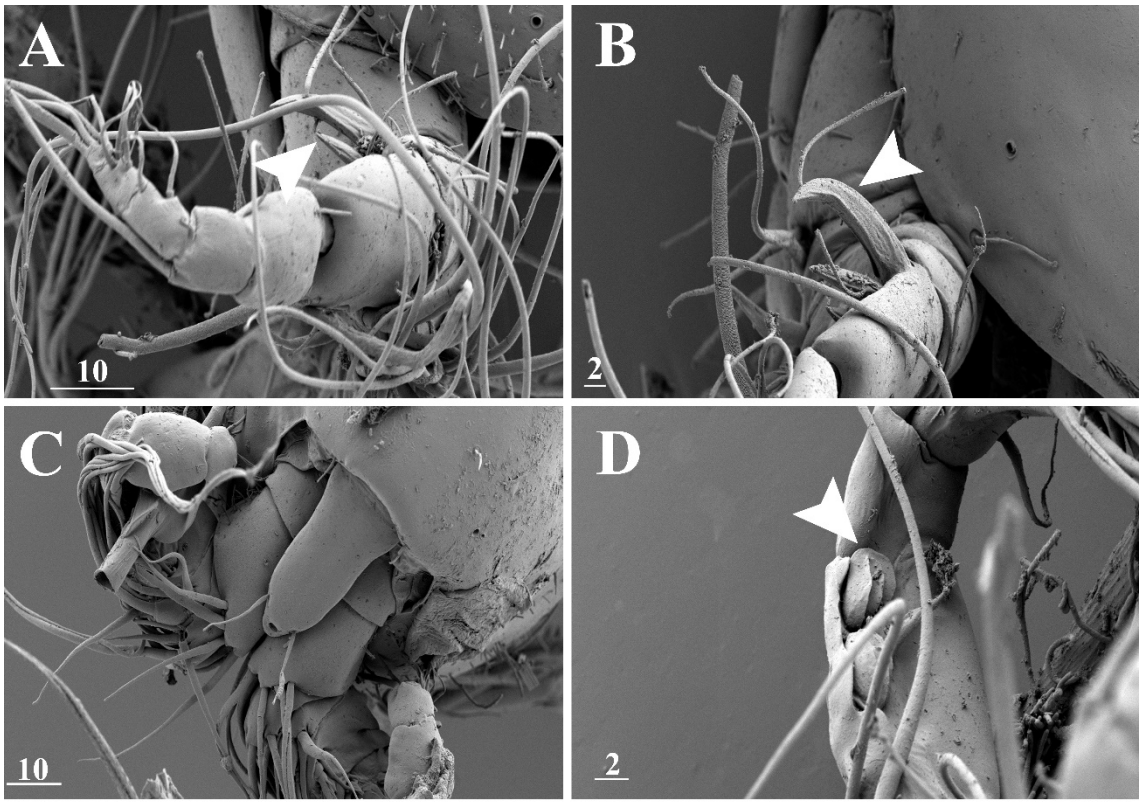

Figure 12: *Penicillicaris pectinimana* (Car, 1884), ♂, A, B, modified spine of A1 sixth segment; C, anterior of A1 and rostrum; D, modified spine of A1 seventh segment (SEM)

P1 (Fig. 13A, B). Similar with female except for precoxal spinule row and basis proximal inner margin spinule row longer than female.

P2 (Fig. 13C). Exopod as in female. Inner seta on enp-3 shorter.

P3 (Fig. 14A, B). Exopod as in female. Enp-3 shorter than that of female, with two plumose setae and apophysis.

P4 (Fig.14C). First inner seta on exp-3 relatively shorter than that of female. Enp-3 without inner seta.

P5 (Fig. 15A). Baseoendopods medially fused forming deeply incised transverse plate. Endopodal lobe with two pores and with spinule rows on distal and outer margins; outer basal seta naked and arising from short setophore, inner lobe with two bipinnate setae at distal margin. Exopod 1-segmented with spinule row along outer margin and with seven setae; proximal outer seta long and naked, the other outer lateral setae bipinnate, one of the distal setae long and naked the other distal seta bipinnate, one of inner seta naked and the other one bipinnate.

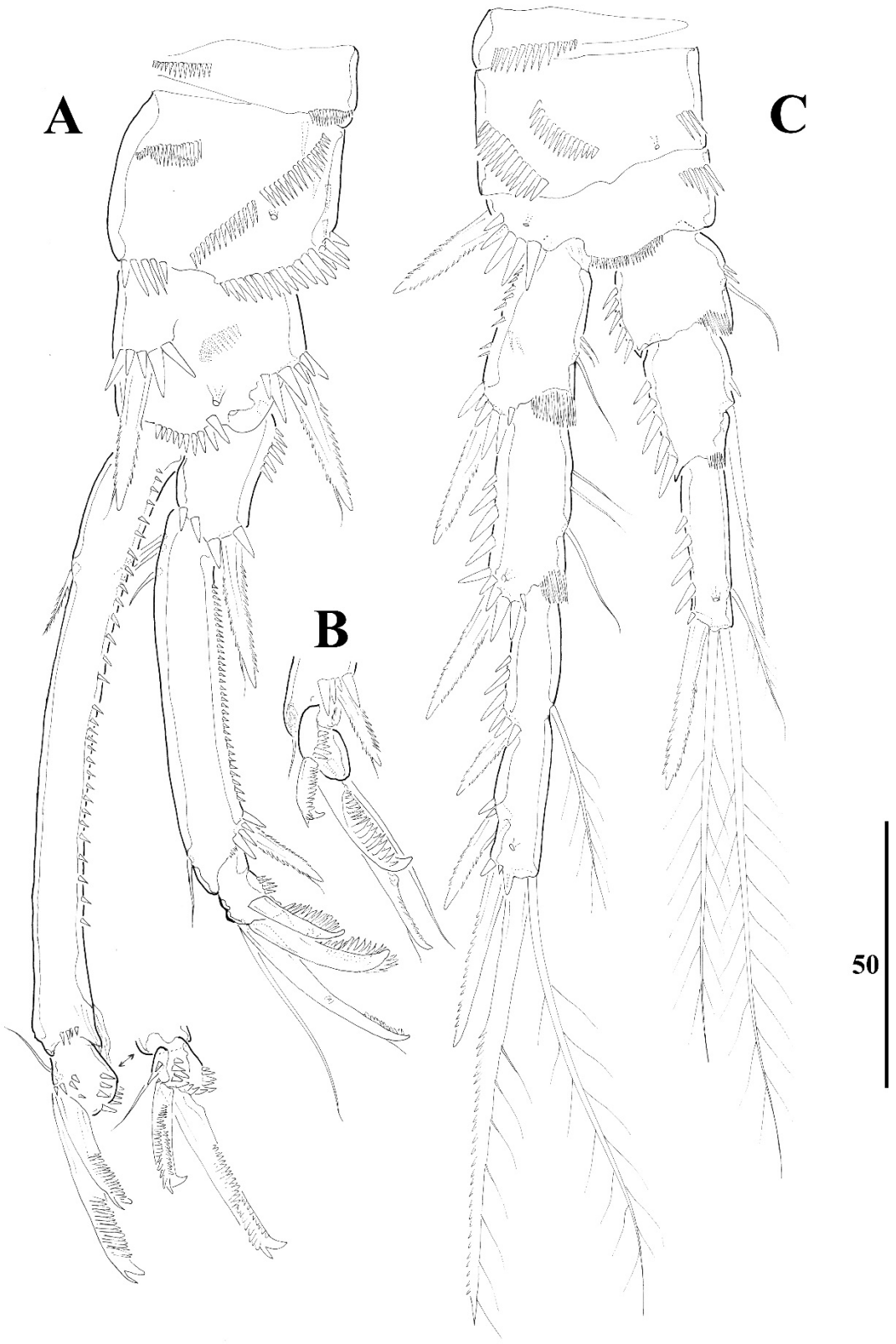

Figure 13: *Penicillicaris pectinimana* (Car, 1884), ♂, A, P1; B, distal segment of P1 exopod; C, P2

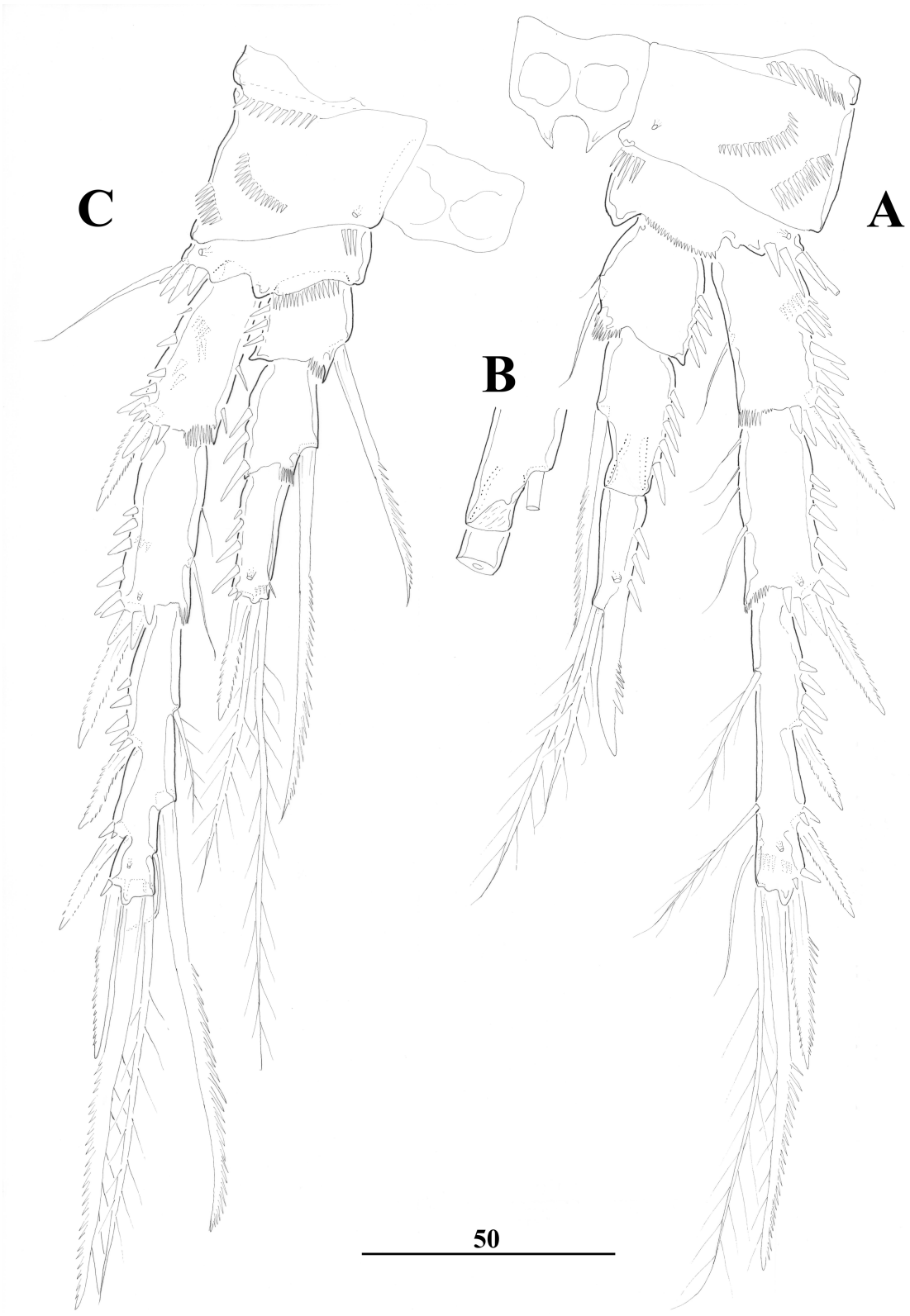

Figure 14: *Penicillicaris pectinimana* (Car, 1884), ♂, A, P3; B, second and third segment of P3 endopod; C, P4

P6 (Fig. 15B) reduced to a small plate on each side, covers genital aperture. Bears two naked setae and one bipinnate seta, middle seta nearly two times longer than other two setae.

Figure 15: *Penicillicaris pectinimana* (Car, 1884), ♂, A, P5; B, ventral of abdomen and P6

Variability. One male from St3 had three setae on P2 enp-3. A female from St. 41 had seven setae on one side of P5 exp but six on other side of P5 exp. A female from St. 69 had seven setae on one pair of P4 exp-3. Males from St. 26, St. 49, St. 72 and all materials from the Black Sea coast had four setae on P4 enp-3. A female from St. 53 had four setae on P5 baseoendopod and a male had no inner seta on P3 enp-3.

The present specimens clearly belong the genus *Penicillicaris* according to the following characters i) female P3-P4 enp-2 with inner seta, ii) P1 exopodal segments subequal in length (second segment markedly longer than the first and the third), iii) penicillate elements on distal endopod segment of antenna, iv) penicillate spine on P1 exp-3 and enp-2, v) ♂ P3 enp with apophysis [9]. The specimens morphologically most closely related to *P. pectinimana* (see Table 1) which was originally described as *Thalestris pectinimana* by Car [10] from a single female specimen collected from the vicinity of Trieste, north-eastern Italy. Huys and Mu [9] removed the species from the synonymy of *Parastenhelia spinosa* and transferred it to the newly erected genus *Penicillicaris*. Only female habitus in lateral view, antennule, antenna, maxilliped, P1 rami distal segments and P5 were illustrated in the original description of *P. pectinimana.* The morphological comparisons of the materials of this study with the original description of *P. pectinimana* by Car [10] has revealed that the only significant difference is that P5 exopod with six setae, seven in the original description. Unfortunately, the standards of Car's (1884) illustrations do not allow making further meaningful comparisons. On the other hand, Huys and Mu [9] refereed Monard's [14] report of *Microthalestris forficula* (Claus, 1863) from Banyuls-sur-Mer and Bodin's [15] report of *Parastenhelia spinosa* (Fischer, 1860) f. *penicillata* from Marseille conspecific with *P. pectinimana*. The materials examined in this study differ from above mentioned reports in the character of P4 exp-3 with eight setae instead of seven setae, but P4 exp-3 distal inner seta is very thin which can easily be overlooked. *P. penicillata* Willey, 1935 which described from Bermuda is the only species within the genus that has P4 exopod-3 with 8 setae, Willey [17] stated that distal two segments of ♀ P2-P3 endopod are frequently poorly separated in *P. penicillate* sensu Willey, 1935 [17], but P2-P3 endopod segments of the specimens examined are clearly separated. Taking into account the above-mentioned characters and considering that Willey's [17] population is located in very distant location, it can be speculated that Willey's [17] population may represent different morphological species. The redescription of both sexes of *P. pectinimana* from a wide range of localities along the Turkish coast can provide a basis for the future taxonomic studies on the species. On the other hand, considering the wide habitat range of species in Turkish water may be the indication of cryptic speciation among *P. pectinimana* populations. Therefore, a

molecular study within and between the populations of *P. pectinimana* based on freshly collected specimens may provide interesting results about the species delimitations.

Table 1: Differences between species of the genus *Penicillicaris*.

	P. maldivensis	***P. penicillata***	***P. sewelli***	***P. pectinimana***
Reference	Sewell [16]	Willey [17]; Huys and Mu [9]	Sewell [16]; Vervoort [18]	Car [10]; Monard[14]; Bodin[15]; present study
Location	Maldive archipelago, Addu Atoll	Bermuda, Trunk Island, Harrington Sound;	Maldive archipelago, Addu Atoll; Ifaluk Atoll in the Pacific	Italy, Trieste (Adriatic); Banyuls-sur-Mer; Marseille; Türkiye
♀A1 segment number	9	8	8	8
P1 exp-3	three penicillate spine + one long non-geniculate seta	two penicillate spine + one geniculate seta + one short seta	two penicillate spine + one geniculate seta + one short seta	two penicillate spine + one geniculate seta + one short seta
P2 exp/enp	unknown	unknown	1.1.123/1.1.121	1.1.123/1.1.121
P3 exp/enp	unknown	?.?.323/ 1.321	1.1.223/1.1.121	1.1.323/1.1.221
P4 exp/enp	0.1.223/1.1.121	?.1.323/ ?.?.221	-/?.?.221	0.1.2(3)23/1.1.221
P5 benp: exp	5:6	5:6	5:6	5:6-7
♀ caudal rami setae IV-V	not swollen	swollen	swollen	swollen
♂ P3 enp	0.1.02+Apophysis	0.1.02+Apophysis	0.1.02+Apophysis	0.1.02+Apophysis
♂ P4 enp	?	1.1.021	?	1.1.021
♂ P5 benp: exp	2:7	2:7	2:7	2:7

Acknowledgements

This research which is part of master thesis of Seher KURU was funded by Mersin University Research Fund under project MEÜ BAP FBE BB (SK).

References

[1] Lang, K., *Monographie der Harpacticiden. Vols. 1–2*, 1682 pp, Håkan Ohlsson, Lund, 1948.

[2] Thompson I.C., Scott A., *Report on the Copepoda collected by Prof. Herdman at Ceylon in 1902*, Report to the Government on Celyon Pearl Oyster Fishery, Gulf of Manaar 1, 227–307,1903.

[3] Scott, T., *The Entomostraca of the Scottish National Antarctic Expedition, 1902–1904* Transactions of the Royal Society of Edinburgh, 48, 521–599, 1912.

[4] Gurney, R., *XXXIII. Report on the Crustacea-Copepoda (littoral and semiparasitic). Zoological results of the Cambridge expedition to the Suez Canal, 1924*, Transactions of the Royal Society of. London, 22, 451-577, 1927.

[5] Monard, A., *Synopsis universalis generum Harpacticoidarum*, Zoologiche Jahrbücher, Abteilung für Systematik**,** 54: 139–176, 1927.

[6] Lang, K., *Marine Harpacticiden von der Cambell-Insel und einigenanderensüdlichen Inseln*, Acta Universitatis Lundensis Series 2, 30(14): 1–56, 1934.

[7] Willen, E., *Phylogeny of the Thalestridimorpha Lang, 1944 (Crustacea, Copepoda)*, 233 pp, Cuvillier Verlag, Göttingen, ,2000.

[8] Gee, J.M., *Parastenheliidae (Copepoda: Harpacticoida) from the Isles of Scilly*, Journal of Natural History, 40(47-48), 2611-2652, 2006.

[9] Huys, R., Mu, F., *Johnwellsia, a new intertidal genus of Parastenheliidae (Copepoda, Harpacticoida) from the Taiwan Strait, China, including a review of the family and key to genera*, Zootaxa,, 5051(1), 236-318, 2021.

[10] Car, L., *Ein Beitragzur Copepoden-Fauna desadriatischen Meeres,* Archiv für Naturgeschichte, 50, 237–256, 1884.

[11] Kuru, S., Karaytuğ, S., *A new species of Parastenhelia Thompson & A. Scott, 1903 (Copepoda, Harpacticoida, Parastenheliidae) from Turkey,* Biharean Biologist, 9, 121–127, 2015.

[12] Huys, R., Gee, J.M., Moore, C.G., Hamond, R., Marine and Brackish Water Harpacticoids, Part 1. *In*: Barnes, R. S. K. & Crothers, J. H. (Eds.), *Synopses of the British Fauna (New Series)*, 352 pp, Field Studies Council, Shrewsbury, 1996.

[13] Kaymak, N.B., Karaytuğ, S., Systematics of the genus *Heterolaophonte* (Crustacea, Copepoda, Harpacticoida) with redescription of *H. uncinata* and *H. curvata*. Zootaxa, 3780, 503-533, 2014.

[14] Monard, A., *Les Harpacticoïdesmarins de Banyuls*, Archives de Zoologie expérimentale et générale, 67, 259–443, 1928.

[15] Bodin, P., *Recherches sur la systématique et la distributiondes Copépodes Harpacticoïdes des substratsmeubles des environs de Marseille*. Recueildes Travaux de la Station marined' Endoume, Facultédes Sciences de Marseille, 51(35), 107–183, 1964.

[16] Sewell, R.B.S., *Copepoda, Harpacticoida,* The John Murray Expedition 1933–1934 Scientific Reports, 7(2), 117–382, 1940.

[17] Willey, A., *Harpacticoid Copepoda from Bermuda – Part II*, Annals and Magazine of Natural History Series, 10(15), 50–100, 1935.

[18] Vervoort, W., *Free living Copepoda from Ifaluk Atoll in the Caroline Islands with notes on related species*, Bulletin of the United States National Museum, 236, 1–431, 1964.

Adıyaman University Journal of Science
https://dergipark.org.tr/en/pub/adyujsci
DergiPark AKADEMİK
ISSN 2147-1630
e-ISSN 2146-586X

An Application of Trigonometric Quintic B-Spline Collocation Method for Sawada- Kotera Equation

Hatice KARABENLİ[1,*], Alaattin ESEN[2], Nuri Murat YAĞMURLU[3]

[1]*Nuray Tuncay Kara Science and Art Center, Ministry of Education, Department of Mathematics, 27560, Gaziantep, Türkiye*
haticekarabenli@gmail.com, ORCID: 0000-0003-2201-836X
[2]*Inonu University, Faculty of Science and Literature, Department of Mathematics, 44280, Malatya, Türkiye*
alaattin.esen@inonu.edu.tr, ORCID: 0000-0002-7927-5941
[3]*Inonu University, Faculty of Science and Literature, Department of Mathematics, 44280, Malatya, Türkiye*
murat.yagmurlu@inonu.edu.tr, ORCID: 0000-0003-1593-0254

Received: 05.08.2022 **Accepted:** 26.11.2022 **Published:** 30.12.2022

Abstract

In this paper, we deal with the numerical solution of Sawada-Kotera (SK) equation classified as the type of fifth order Korteweg-de Vries (gfKdV) equation. In the first step of our study consisting of several steps, nonlinear model problem is split into the system with the coupled new equations by using the transformation $w_{xxx} = v$. In the second step, to get rid of the nonlinearity of the problem, Rubin-Graves type linearization is used. After these applications, the approximate solutions are obtained by using the trigonometric quintic B-Spline collocation method. The efficiency and accuracy of the present method is demonstrated with the tables and graphs. As it is seen in the tables given with the error norms L_2 and L_∞ for different time and space steps, the present method is more accurate for the larger element numbers and smaller time steps.

Keywords: Sawada-Kotera Equation; Collocation Finite Element Method; Trigonometric Quintic B-Spline; Rubin-Graves Type Linearization.

* Corresponding Author DOI: 10.37094/adyujsci.1156498

Sawada-Kotera Denklemi için Trigonometrik Beşli Baz Fonksiyonları Kollokasyon Yönteminin Bir Uygulaması

Öz

Bu çalışmada, beşinci dereceden Korteweg-de Vries (gfKdV) denklemlerinin türü olarak sınıflandırılan Sawada-Kotera (SK) denkleminin nümerik çözümü ele alınmaktadır. Birkaç adımdan oluşan çalışmamızın ilk adımında, lineer olmayan model problem $w_{xxx} = v$ dönüşümü kullanılarak iki yeni denklem sistemine ayrıştırılmıştır. İkinci adımda, problemin lineer olmama durumundan kurtulmak için Rubin-Graves tipi lineerleştirme kullanılmıştır. Bu uygulamalardan sonra trigonometrik beşli B-Spline kollokasyon yöntemi kullanılarak yaklaşık çözümler elde edilmiştir. Mevcut yöntemin etkinliği ve doğruluğu tablolar ve grafiklerle gösterilmiştir. Farklı zaman ve konum adımı için L_2 ve L_∞ hata normları ile verilen tablolardan görüldüğü üzere, mevcut yöntem daha büyük eleman sayıları ve daha küçük zaman adımları için yüksek doğruluktadır.

***Anahtar Kelimeler*:** Sawada- Kotera Denklemi; Kollokasyon Sonlu Eleman Yöntemi; Trigonometrik Beşli B-Spline; Rubin- Graves Tipi Lineerleştirme.

1. Introduction

Many problems in various areas of scientific and engineering fields can be expressed as partial differential equations. These equations frequently appear in the fields such as fluid dynamics, plasma physics, mathematical biology, nonlinear optics, quantum mechanics etc. One of the most important problems studied in these fields is the generalized fifth order Korteweg-de Vries (gfKdV) equation. Although there isn't a general solution corresponding to the solution of the problem, the exact solutions are available for the special cases of solitary waves [1]. The generalized fifth order Korteweg-de Vries (gfKdV) equation is modelled with the relation

$$\frac{\partial w}{\partial t} + \alpha w^2 \frac{\partial w}{\partial x} + \beta \frac{\partial w}{\partial x}\frac{\partial^2 w}{\partial x^2} + \gamma \mathrm{w} \frac{\partial^3 w}{\partial x^3} + \frac{\partial^5 w}{\partial x^5} = 0, \tag{1}$$

where α, β and γ are random real parameters and w is a differentiable function related to t time and x space variables. It should be noted here that equation (1) not only expresses the motion of the long waves in shallow water under gravity and in a one dimensional nonlinear lattice, but it is also a significant mathematical model for a chain of coupled non-linear oscillators and magneto-sound propagation in plasmas [2]. In the last few years, many researchers have studied nonlinear gfKdV equations to obtain their exact solutions and numerical solutions. When the literature is investigated, there are many studies in which analytical and numerical solutions are obtained by

using the Adomian Decomposition Method [3-6], Variational Iteration Method [7, 8], Homotopy Perturbation Method [9, 10], Laplace Decomposition Approach [11, 12] and finite difference schemes based on a predictor-corrector algorithm [13]. Since the gfKdV equation doesn't have general solution expect for special cases of solitary waves, their numerical solutions are commonly studied [3]. For the numerical solutions, Bakodah [4] generalized on appropriate polynomials for the gfKdV and implemented the new modified Adomian Decomposition Method, Kaya [5] calculated explicit and numerical solutions for a various fifth-order KdV equations, Odibat and Momani [8] used the variational iteration method by obtaining a correction functional for the differential equation and Djidjeli and the others [13] proposed two methods derived using central differences with a predictor-corrector time stepping and linearizing implicit corrector scheme. In this study, different from the existing studies for numerical solutions, we are going to use the finite element collocation method. In order to obtain better and more effective numerical results, trigonometric quintic basis functions will be used.

The model problem discussed in our study is the Sawada-Kotera [14] problem which is the special form of the gfKdV equation for the parameters $\alpha = 45, \beta = 15$ and $\gamma = 15$ is given as

$$\frac{\partial w}{\partial t} + 45w^2 \frac{\partial w}{\partial x} + 15 \frac{\partial w}{\partial x} \frac{\partial^2 w}{\partial x^2} + 15\mathrm{w} \frac{\partial^3 w}{\partial x^3} + \frac{\partial^5 w}{\partial x^5} = 0 \,, \tag{2}$$

subject to initial and boundary conditions

$$w(\pm L, t) = w_x(\pm L, t) = 0, \qquad x \in (-L, L), \quad t > 0,$$

$$w(x, 0) = f(x, k, \lambda),$$

where k and λ are constant numbers.

The organization of this study is built on the main steps given in the following sections. In section 2, the used method and its application schemes are given. In section 3, initial matrix systems are composed. The obtained numerical results are discussed in the last section 4.

2. Implementation of the Collocation Finite Element Method with Trigonometric Quintic B-Spline Basis

In this section, first of all, by using the relation $\frac{\partial^3 w}{\partial x^3} = w_{xxx} = v$, two different equations will be obtained corresponding the equation (2). The new coupled equations can be written as

$$w_{xxx} - v = 0, \tag{3}$$

$$w_t + 45w^2 w_x + 15 w_x w_{xx} + 15 w v + v_{xx} = 0. \tag{4}$$

So, we can create the scheme for equation systems (3) and (4) using the collocation finite element method based on trigonometric quintic B-spline functions. For this purpose, firstly, we consider the domain $[-L, L]$ divided uniformly into sub intervals from the x_m knots as $-L = x_0 < x_1 < x_2 < \ldots < x_m = L$ where spatial step size $\Delta x = h = x_{m+1} - x_m$, for all m, $m = -2, -1, 0, 1, \ldots, M+1, M+2$. The group of trigonometric quintic B-spline basis $\{\phi_{-2}(x), \phi_{-1}(x), \ldots, \phi_{M+1}(x), \phi_{M+2}(x)\}$ forms a basis for the solution region $[-L, L]$. In this way, the approximate solutions of functions $w(x,t)$ and $v(x,t)$ can be represented with $W_m(x,t)$ and $V_m(x,t)$. Also these approximate values can be expressed with the terms $\phi_m(x)$, $\delta_m(t), \sigma_m(t)$ as

$$W_m(x,t) = \sum_{m=-2}^{M+2} \phi_m(x)\delta_m(t), \qquad V_m(x,t) = \sum_{m=-2}^{M+2} \phi_m(x)\sigma_m(t),$$

where $\phi_m(x)$ are values of the x_m knots and $\delta_m(t)$, $\sigma_m(t)$ are time-dependent coefficients which can be found by using the boundary conditions and trigonometric quintic B-spline collocation conditions [15-17]. In our paper, we use the symbolization of W_m, V_m for the approximate solutions at the knots $x = x_m$. Numerical solutions at the knots x_m derived by using the trigonometric quintic B-splines $\phi_m(x)$ are found to be:

$$W_m = W(x_m) = a_1\delta_{m-2} + a_2\delta_{m-1} + a_3\delta_m + a_2\delta_{m+1} + a_1\delta_{m+2},$$

$$W_m' = W'(x_m) = b_1\delta_{m-2} + b_2\delta_{m-1} - b_2\delta_{m+1} - b_1\delta_{m+2},$$

$$W_m'' = W''(x_m) = c_1\delta_{m-2} + c_2\delta_{m-1} + c_3\delta_m + c_2\delta_{m+1} + c_1\delta_{m+2},$$

$$W_m''' = W'''(x_m) = d_1\delta_{m-2} + d_2\delta_{m-1} - d_2\delta_{m+1} - d_1\delta_{m+2},$$

$$V_m = V(x_m) = a_1\sigma_{m-2} + a_2\sigma_{m-1} + a_3\sigma_m + a_2\sigma_{m+1} + a_1\sigma_{m+2},$$

$$V_m' = V'(x_m) = b_1\sigma_{m-2} + b_2\sigma_{m-1} - b_2\sigma_{m+1} - b_1\sigma_{m+2},$$

$$V_m'' = V''(x_m) = c_1\sigma_{m-2} + c_2\sigma_{m-1} + c_3\sigma_m + c_2\sigma_{m+1} + c_1\sigma_{m+2},$$

where

$$a_1 = \frac{\sin^5(h/2)}{\theta},$$

$$a_2 = \frac{2\sin^5(h/2)\cos(h/2)(16\cos^2(h)/2 - 3)}{\theta},$$

$$a_3 = \frac{2\sin^5(h/2)(1 + 48\cos^4(h/2) - 16\cos^2(h)/2)}{\theta},$$

$$b_1 = -\frac{5\sin^4(h/2)\cos(h/2)}{2\theta},$$

$$b_2 = -\frac{5\sin^4\left(\frac{h}{2}\right)\cos^2\left(\frac{h}{2}\right)\left(8\cos^2\left(\frac{h}{2}\right) - 3\right)}{\theta},$$

$$c_1 = \frac{5\sin^3\left(\frac{h}{2}\right)\left(5\cos^2\left(\frac{h}{2}\right) - 1\right)}{4\theta},$$

$$c_2 = \frac{5\sin^3(h/2)\cos(h/2)(-15\cos^2(h/2) + 16\cos^4(h/2) + 3)}{2\theta},$$

$$c_3 = -\frac{5\sin^3\left(\frac{h}{2}\right)\left(16\cos^6\left(\frac{h}{2}\right) - 5\cos^2\left(\frac{h}{2}\right) + 1\right)}{2\theta},$$

$$d_1 = -\frac{5\sin^2\left(\frac{h}{2}\right)\cos\left(\frac{h}{2}\right)\left(25\cos^2\left(\frac{h}{2}\right) - 13\right)}{8\theta},$$

$$d_2 = -\frac{5\sin^2\left(\frac{h}{2}\right)\cos^2\left(\frac{h}{2}\right)\left(8\cos^4\left(\frac{h}{2}\right) - 35\cos^2\left(\frac{h}{2}\right) + 15\right)}{4\theta},$$

for $\theta = \sin(h/2)\sin(h)\sin(3h/2)\sin(2h)\sin(5h/2)$ [18].

In the collocation finite element method, a differential equation is satisfied at the collocation points. We use the Crank-Nicolson approach and forward difference approximation for equations (3) and (4) at two time levels n and $n+1$

$$w_m = \frac{w_m^{n+1} + w_m^n}{2} \text{ and } v_m = \frac{v_m^{n+1} + v_m^n}{2}, \tag{5}$$

$$\dot{w}_m = \frac{w_m^{n+1} - w_m^n}{\Delta t} \text{ and } \dot{v}_m = \frac{v_m^{n+1} - v_m^n}{\Delta t},$$

where w_m^n, v_m^n are the parameters at the time $n\Delta t$, $\Delta t = k = t_{k+1} - t_k$ is time step and $n = 0,1,\ldots,N$ and " • " demonstrates the derivative with respect to t. Before placing these equations in equations (3) and (4), we must apply the Rubin-Graves type linearization method [19] to the non-linear terms of the equation given in equation (4). By applying Rubin-Graves to the non-linear terms return the form

$$(w^2 w_x)^{n+1} = 2w^n w^{n+1} w_x^n + (w^n)^2 w_x^{n+1} - 2(w^n)^2 w_x^n,$$

$$(w_x w_{xx})^{n+1} = w_x^{n+1} w_{xx}^n + w_x^n w_{xx}^{n+1} - w_x^n w_{xx}^n\,, \tag{6}$$

$$(wv)^{n+1} = w^{n+1} v^n + w^n v^{n+1} - w^n v^n.$$

By substituting equations (5) and (6) into equations (3) and (4), we obtain the following equations

$$w_{xxx}^{n+1} - v^{n+1} = -w_{xxx}^n + v^n \tag{7}$$

$$\left(1 + 45\Delta t z_m (z_m)_x + \frac{15\Delta t}{2} g_m\right) w^{n+1} + \left(\frac{45\Delta t}{2}(z_m)^2 + \frac{15\Delta t}{2}(z_m)_{xx}\right)(w_x)^{n+1}$$

$$+ \tfrac{15\Delta t}{2}(z_m)_x (w_{xx})^{n+1} + \tfrac{15\Delta t}{2} z_m v^{n+1} + \tfrac{\Delta t}{2}(v_{xx})^{n+1} \tag{8}$$

$$= w^n + \tfrac{45\Delta t}{2}(z_m)^2 (w_x)^n - \tfrac{\Delta t}{2}(v_{xx})^n,$$

where Δt is the time step, the values $z_m = w$, $g_m = v$ and their derivatives $(z_m)_x = w_x$, $(z_m)_{xx} = w_{xx}$ approximation values are used for the purpose of the linearization of nonlinear terms in the finite element schemes at time step.

Then, by substituting the nodal values W_m, V_m and their required derivatives at the collocation points into equations (7) and (8), the following finite element schemes are obtained as

$$d_1\delta_{m-2}^{n+1} + d_2\delta_{m-1}^{n+1} - d_2\delta_{m+1}^{n+1} - d_1\delta_{m+2}^{n+1}$$

$$-a_1\sigma_{m-2}^{n+1} - a_2\sigma_{m-1}^{n+1} - a_3\sigma_m^{n+1} - a_2\sigma_{m+1}^{n+1} - a_1\sigma_{m+2}^{n+1}$$

$$= -d_1\delta_{m-2}^n - d_2\delta_{m-1}^n + d_2\delta_{m+1}^n + d_1\delta_{m+2}^n$$

$$+a_1\sigma_{m-2}^n + a_2\sigma_{m-1}^n + a_3\sigma_m^n + a_2\sigma_{m+1}^n + a_1\sigma_{m+2}^n\,, \tag{9}$$

$$\lambda_1\delta_{m-2}^{n+1} + \lambda_2\delta_{m-1}^{n+1} + \lambda_3\delta_m^{n+1} + \lambda_4\delta_{m+1}^{n+1} + \lambda_5\delta_{m+2}^{n+1}$$

$$+\mu_1\sigma_{m-2}^{n+1} + \mu_2\sigma_{m-1}^{n+1} + \mu_3\sigma_m^{n+1} + \mu_4\sigma_{m+1}^{n+1} + \mu_5\sigma_{m+2}^{n+1}$$

$$= \lambda_6\delta_{m-2}^n + \lambda_7\delta_{m-1}^n + \lambda_8\delta_m^n + \lambda_9\delta_{m+1}^n + \lambda_{10}\delta_{m+2}^{n+1}$$

$$+\mu_6\sigma_{m-2}^n + \mu_7\sigma_{m-1}^n + \mu_8\sigma_m^n + \mu_9\sigma_{m+1}^n + \mu_{10}\sigma_{m+2}^n\,, \tag{10}$$

for $m = 0,1,\ldots,M$ where the coefficients of the δ values are

$$\lambda_1 = \alpha_1 + \ 45a_1\Delta t z_m (z_m)_x + \tfrac{15a_1\Delta t}{2} g_m \ + \tfrac{45b_1\Delta t}{2}(z_m)^2 + \tfrac{15b_1\Delta t}{2}(z_m)_{xx} \ + \tfrac{15c_1\Delta t}{2}(z_m)_x\,,$$

$$\lambda_2 = \alpha_2 + \ 45a_2\Delta t z_m(z_m)_x + \frac{15a_2\Delta t}{2} g_m \ + \frac{45b_2\Delta t}{2}(z_m)^2 + \frac{15b_2\Delta t}{2}(z_m)_{xx} \ + \frac{15c_2\Delta t}{2}(z_m)_x ,$$

$$\lambda_3 = \alpha_3 + \ 45a_3\Delta t z_m(z_m)_x + \frac{15a_3\Delta t}{2} g_m \ + \frac{15c_3\Delta t}{2}(z_m)_x,$$

$$\lambda_4 = \alpha_2 + \ 45a_2\Delta t z_m(z_m)_x + \frac{15a_2\Delta t}{2} g_m \ - \frac{45b_2\Delta t}{2}(z_m)^2 - \frac{15b_2\Delta t}{2}(z_m)_{xx} \ + \frac{15c_2\Delta t}{2}(z_m)_x,$$

$$\lambda_5 = \alpha_1 + \ 45a_1\Delta t z_m(z_m)_x + \frac{15a_1\Delta t}{2} g_m \ - \frac{45b_1\Delta t}{2}(z_m)^2 - \frac{15b_1\Delta t}{2}(z_m)_{xx} \ + \frac{15c_1\Delta t}{2}(z_m)_x,$$

$$\lambda_6 = \alpha_1 + \frac{45b_1\Delta t}{2}(z_m)^2, \ \lambda_7 = \alpha_2 + \frac{45b_2\Delta t}{2}(z_m)^2, \ \lambda_8 = \alpha_3,$$

$$\lambda_9 = \alpha_2 - \frac{45b_2\Delta t}{2}(z_m)^2, \ \lambda_{10} = \alpha_1 - \frac{45b_1\Delta t}{2}(z_m)^2,$$

and the coefficients of the σ values are

$$\mu_1 = \frac{15a_1\Delta t}{2} z_m \ + \frac{c_1\Delta t}{2}, \mu_2 = \frac{15a_2\Delta t}{2} z_m \ + \frac{c_2\Delta t}{2}, \ \mu_3 = \frac{15a_3\Delta t}{2} z_m \ + \frac{c_3\Delta t}{2},$$

$$\mu_4 = \frac{15a_2\Delta t}{2} z_m \ + \frac{c_2\Delta t}{2}, \ \mu_5 = \frac{15a_1\Delta t}{2} z_m \ + \frac{c_1\Delta t}{2}, \mu_6 = -\frac{c_1\Delta t}{2},$$

$$\mu_7 = -\frac{c_2\Delta t}{2}, \ \mu_8 = -\frac{c_3\Delta t}{2}, \mu_9 = -\frac{c_2\Delta t}{2}, \mu_{10} = -\frac{c_1\Delta t}{2}.$$

The pentadiagonal matrix system (9) and (10) consists of $2M + 2$ linear equations and $2M + 10$ unknown parameters $\boldsymbol{\delta}_m = (\delta_{-2}, \delta_{-1}, \ldots, \delta_{M+1}, \delta_{M+2})^T$ and $\boldsymbol{\sigma}_m = (\sigma_{-2}, \sigma_{-1}, \ldots, \sigma_{M+1}, \sigma_{M+2})^T$. To solve this system uniquely, we must eliminate eight unknowns from this system. We can obtain these equations from the left and right boundary conditions and use them in the system to eliminate the fictitious values δ_{-2}, δ_{-1}, δ_{M+1}, δ_{M+2}, σ_{-2}, σ_{-1}, σ_{M+1}, σ_{M+2}. So, the system becomes matrix in the following form

$$A\delta_m^{n+1} = B\delta_m^n + E, \tag{11}$$

$$C\sigma_m^{n+1} = D\sigma_m^n + F, \tag{12}$$

where A, B, C and D are $(M + 1) \times (M + 1)$ pentadiagonal matrixes and E, F are $(M + 1)$ column vectors. This system can be solved by a suitable numerical method. To obtain the solution at the $(n + 1)th$ time level, we need to know the solution at the nth time level. Thinking iteratively, we should firstly know initial vectors $\boldsymbol{\delta}_m^0 = (\delta_0^0, \delta_1^0 \ldots, \delta_M^0)^T$ and $\boldsymbol{\sigma}_m^0 = (\sigma_0^0, \sigma_1^0 \ldots, \sigma_M^0)^T$ for initializing the iterative solution.

3. Initial Vector

To start time evaluation of the approximate solution firstly, we must determine the initial vectors $\boldsymbol{\delta}_m^0$ and $\boldsymbol{\sigma}_m^0$. For this aim, the initial conditions

$$a_1\delta_{m-2}^0 + a_2\delta_{m-1}^0 + a_3\delta_m^0 + a_2\delta_{m+1}^0 + a_1\delta_{m+2}^0 = W(x_m, 0),$$

$$a_1\sigma_{m-2}^0 + a_2\sigma_{m-1}^0 + a_3\sigma_m^0 + a_2\sigma_{m+1}^0 + a_1\sigma_{m+2}^0 = V(x_m, 0),$$

are used at the initial time t_0 for $m = 0,1,\dots,M$. To attain a solvable system, we need to remove the fictitious eight parameters δ_{-2}, δ_{-1}, δ_{M+1}, δ_{M+2}, σ_{-2}, σ_{-1}, σ_{M+1}, σ_{M+2}. After eliminating the fictitious parameters in the system, we can uniquely solve the system which is the type of $(2M+2)\times(2M+2)$. Here, the essential equations are obtained by using the first and the second derivatives of approximate initial conditions based on trigonometric quintic B-Splines. So, the initial matrix systems are written with the following form

$$\begin{bmatrix} a_{11} & a_{12} & a_{13} & 0 & 0 & 0 & \dots & 0 \\ a_{21} & a_{22} & a_{23} & \alpha_1 & 0 & 0 & \dots & 0 \\ \alpha_1 & \alpha_2 & \alpha_3 & \alpha_2 & \alpha_1 & 0 & \dots & 0 \\ 0 & \alpha_1 & \alpha_2 & \alpha_3 & \alpha_2 & \alpha_1 & \dots & 0 \\ 0 & \ddots & \ddots & \ddots & \ddots & \ddots & \ddots & 0 \\ 0 & \dots & 0 & \alpha_1 & \alpha_2 & \alpha_3 & \alpha_2 & \alpha_1 \\ 0 & \dots & 0 & 0 & \alpha_1 & a_{2M+1,2M} & a_{2M+1,2M+1} & a_{2M,2M+2} \\ 0 & \dots & 0 & 0 & 0 & a_{2M+2,2M} & a_{2M+2,2M+1} & a_{2M+2,2M+2} \end{bmatrix} \begin{bmatrix} \delta_{m-2}^0 \\ \delta_{m-1}^0 \\ \vdots \\ \delta_M^0 \\ \sigma_{m-2}^0 \\ \sigma_{m-1}^0 \\ \vdots \\ \sigma_M^0 \end{bmatrix} = \begin{bmatrix} W(x_0,0) \\ W(x_1,0) \\ \vdots \\ W(x_M,0) \\ V(x_0,0) \\ V(x_1,0) \\ \vdots \\ V(x_M,0) \end{bmatrix},$$

where the entries of the matrix are given the following equations

$$a_{11} = a_{2M+2,2M+2} = \alpha_3 + \frac{\alpha_1\beta_2\gamma_3 - \alpha_2\beta_1\gamma_3}{\beta_1\gamma_2 - \beta_2\gamma_1},$$

$$a_{21} = a_{2M,2M+2} = \alpha_2 - \frac{\alpha_1\beta_1\gamma_3}{\beta_1\gamma_2 - \beta_2\gamma_1},$$

$$a_{12} = a_{2M+2,2M+1} = \frac{2\alpha_1\beta_2\gamma_2 - 2\alpha_2\beta_2\gamma_1}{\beta_1\gamma_2 - \beta_2\gamma_1},$$

$$a_{22} = a_{2M+1,2M+1} = \alpha_3 - \frac{\alpha_1\beta_1\gamma_2 + \alpha_1\beta_2\gamma_1}{\beta_1\gamma_2 - \beta_2\gamma_1},$$

$$a_{13} = a_{2M+2,2M} = \frac{2\alpha_1\beta_1\gamma_2 - 2\alpha_2\beta_1\gamma_1}{\beta_1\gamma_2 - \beta_2\gamma_1},$$

$$a_{23} = a_{2M+1,2M} = \alpha_2 - \frac{2\alpha_1\beta_1\gamma_1}{\beta_1\gamma_2 - \beta_2\gamma_1}.$$

4. Numerical Results and Discussion

In this section, the accuracy, efficiency and computational complexity of the present scheme is demonstrated on the model problem (2). To measure the accuracy of the present method and see how the approximation of the numerical solution approaches to exact ones, we used the error norms given as following equations

$$L_2 = \|W - W_M\|_2 \simeq \sqrt{h \sum_{j=0}^{M} \left|W_j - (W_M)_j\right|^2},$$

and

$$L_\infty = \|W - W_M\|_\infty \simeq \max_{j=0} \left|W_j - (W_M)_j\right|.$$

The exact soliton solution of the model problem Sawada-Kotera is

$$w(x,t) = 2k^2 \mathrm{sech}^2[k(x - 16k^4 t - \lambda)],$$

with the initial condition

$$w(x,0) = 2k^2 \mathrm{sech}^2[k(x - \lambda)],$$

where $\lambda = 0$ [4].

The numerical values obtained by applying the collocation finite element method are shown in Table 1. For the numerical calculations, the values are used as $\Delta t = 0.01,\ t = 10,\ k = 0.2$ and the solution region is taken as $[-20,20]$. In order to view the convergence of the method, L_2 and L_∞ error norms are given with the different values of t and smaller space steps $h = \Delta x = 0.25,\ 0.1,\ 0.05$ and 0.025. It is seen from Table 1 that the method provides a reasonable approximation for the increasing element numbers. The process can be associated with the efficiency of collocation method based on space knots. It should also be noted here, the method can be used with the accuracy desired for the smaller step sizes.

Table 1: Comparison of the error norms L_2 and L_∞ for the values $\Delta t = 0.01, k = 0.2$ and different values of t and Δx

	$\Delta x = 0.25$		$\Delta x = 0.1$	
t	L_2	L_∞	L_2	L_∞
2	3.896238×10^{-7}	1.632945×10^{-7}	2.377189×10^{-8}	1.285998×10^{-8}

4	7.100182×10^{-7}	2.888393×10^{-7}	3.421736×10^{-8}	1.695229×10^{-8}
6	1.063679×10^{-6}	4.651501×10^{-7}	4.672788×10^{-8}	2.163092×10^{-8}
8	1.506294×10^{-6}	6.774396×10^{-7}	5.614304×10^{-8}	2.370217×10^{-8}
10	2.036621×10^{-6}	8.864584×10^{-7}	7.370401×10^{-8}	3.021153×10^{-8}

	$\Delta x = 0.05$		$\Delta x = 0.025$	
t	L_2	L_∞	L_2	L_∞
2	5.279064×10^{-9}	3.082057×10^{-9}	1.306097×10^{-9}	7.658709×10^{-10}
4	7.279155×10^{-9}	4.075803×10^{-9}	1.787015×10^{-9}	1.010783×10^{-9}
6	9.740206×10^{-9}	5.405006×10^{-9}	2.364103×10^{-9}	1.338265×10^{-9}
8	1.163328×10^{-8}	6.400158×10^{-9}	2.928870×10^{-9}	1.637632×10^{-9}
10	1.284928×10^{-8}	6.645599×10^{-9}	3.050049×10^{-9}	1.597710×10^{-9}

In Table 1 which is composed of decreasing Δx and increasing final times t, it is aimed to see the variation of the error norms L_2 and L_∞ in a broad perspective. According to the obtained results, it is seen that the error norms L_2 and L_∞ are minimum at final time $t = 2$ and $\Delta x = 0.025$ spatial step size. In order to investigate the effect of temporal and spatial step sizes on the error norms L_2 and L_∞, the newly obtained error norms L_2 and L_∞ at different temporal and spatial step sizes based on a constant final time t are presented in Tables 2 and 3.

Table 2 shows the approximate solutions for the fixed values $t = 10$, $k = 0.2$, $\Delta x = 0.1$ and the decreasing values of time step Δt. It can be clearly seen from the table, the error norms L_2 and L_∞ have decreased with the temporal mesh Δt.

Table 2: Comparison of the error norms for the values $\mathrm{t} = 10$, $\Delta \mathrm{x} = 0.1$ and different values of Δt

Δt	L_2	L_∞
0.04	1.864118×10^{-7}	5.589674×10^{-8}
0.02	1.450729×10^{-7}	4.430777×10^{-8}
0.01	7.370401×10^{-8}	3.021153×10^{-8}
0.005	1.912650×10^{-8}	6.346669×10^{-8}

For the smaller space step, the error norms L_2 and L_∞ are given in Table 3 for different space steps Δx and the fixed values $t = 10$, $k = 0.2$, $\Delta t = 0.01$. The numerical results have smallest errors with the larger element numbers.

Table 3: Comparison of the error norms for the values $\mathrm{t} = 10$, $\Delta \mathrm{t} = 0.01$ and different values of $\Delta \mathrm{x}$.

Δx	L_2	L_∞
0.25	2.036621×10^{-6}	8.864584×10^{-7}
0.1	7.370401×10^{-8}	3.021153×10^{-8}
0.05	1.284928×10^{-8}	6.645599×10^{-9}
0.025	9.852056×10^{-10}	5.924715×10^{-10}

In Table 2 and Table 3, the error norms L_2 and L_∞ obtained by decreasing spatial and temporal time steps, respectively, are compared. As it can be seen from the tables, the decrease of the spatial step sizes seriously affects the shrinking of the the error norms L_2 and L_∞. Since the collocation finite element method based on location points has been used, it is expected that the error norms in Table 3 will also decrease significantly for much more smaller values of spatial step sizes.

The model problem Sawada-Kotera equation often accompanies the non-linear wave phenomena occur in shallow water, acoustic waves in plasma, fluid dynamics etc. In order to understand the behavior of the physical phenomena for Sawada-Kotera problem, the graphics and simulations of the problem are pictured for the different values of $k = 0.2$ and $k = 0.4$. Figure 1 and Figure 2 illustrate the wave's behavior for the $\Delta t = 0.01$, $\Delta x = 0.1$ and different values of t. Both of the parameters $k = 0.2$ and $k = 0.4$, the shape of the solutions do not change.

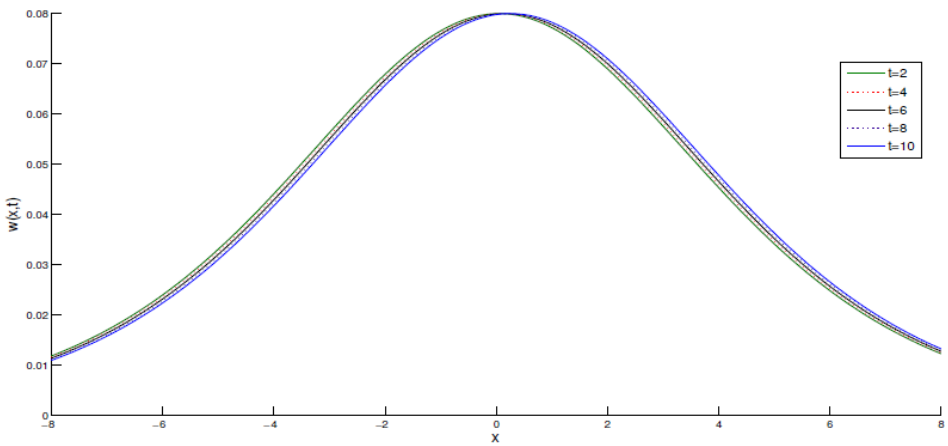

Figure 1: One solitary wave motion for the value $\mathrm{k} = 0.2$

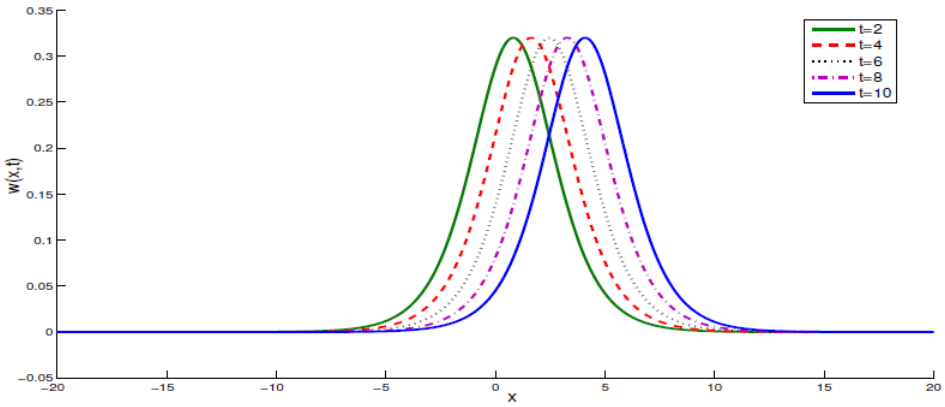

Figure 2: One solitary wave motion for the value k = 0.4

As it is seen in Figure 1, the graphs of the numerical solutions obtained at different times t are close to each other for the amplitude value of $k = 0.2$. In Figure 2, the graphs of the numerical solutions obtained for a larger amplitude value $k = 0.4$, shift significantly at different t times. Both of the figures are drawn at final times $t = 2, 4, 6, 8$ and 10. Also it is clearly seen that in the figures, solitary waves spread of the defination interval according to chosen amplitude.

The exact solutions and numerical solutions are depicted together in Figure 3 for the values $\Delta t = 0.01$, $\Delta x = 0.1, t = 10$ and different values of $k = 0.2$ and $k = 0.4$. In the figures, it can be verified how the approximate solutions are accurate.

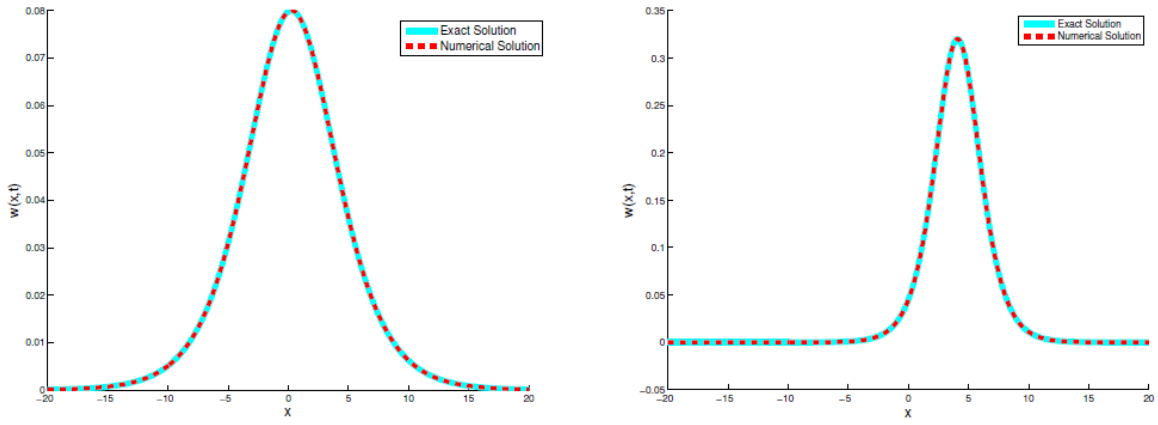

Figure 3: The numerical and exact solutions for k = 0.2 and k = 0.4, respectively

5. Conclusion

In this paper, we have considered the numerical solution of the Sawada-Kotera problem classified with the fifth order KdV equations. The finite element is combined scheme with the collocation finite element method based on the trigonometric quintic B-spline basis is formed and

analysed. The detailed analysis of the proposed method is given with the tables and graphs. It is found that the application of the collocation finite element method has high accuracy values for the larger element numbers. Concerning the spatial discretization use of the present method leads to quick convergences in the space. Also given as the graphs and simulations, the numerical solutions are in agreement with the exact ones. In that case, the present method is a useful numerical method for obtaining the numerical solutions to a wide range of non-linear problems in the theory of solitary waves.

Acknowledgment: The authors express their deep gratitude to editor-in-chief, his staff and anonymous referees for their invaluable contributions to a better content and reading of the manuscript.

References

[1] Nagashima, H., *Experiment on Solitary Waves in the Nonlinear Transmission Line Discribed by the Equation* $u_t + uu_\xi - u_{\xi\xi\xi\xi\xi} = 0$, Journal of the Physical Society of Japan, 47 (4), 1387-1388, 1979.

[2] Kawahara, T., *Oscillatory solitary waves in dispersive media*, Journal of the Physical Society of Japan, 33 (1), 260-264, 1972.

[3] Wazwaz, A.M., *Analytic Study on the Generalized KdV Equation: New Solution and Periodic Solutions*, Elsevier, Amsterdam, 2006.

[4] Bakodah, H.O., *Modified Adomian Decomposition Method for the Generalized Fifth Order KdV Equations*, American Journal of Computational Mathematics , 3, 53-58, 2013.

[5] Kaya, D., *The use of Adomian Decomposition Methods for Solving a Specific Nonlinear Partial Differential Equations*, Bulletin of the Belgian Mathematical Society Simon Stevin, 9 (3), 343-349, 2002.

[6] Wazwaz, A.M., *Partial Differential Equations and Solitary Waves Theory,* Higher Education Press, Beijing, Springer-Verlag, Berlin, 2009.

[7] He, J.H., Wu, X.H., *Construction of solitary solution and compacton-like solution by variational iteration method*, Chaos, Solitons and Fractals, 29 (1), 108-113, 2006.

[8] Odibat, Z., Momani, S., *Application of variational iteration method to nonlinear differential equations of fractional order*, International Journal of Nonlinear Science and Numerical Simulation, 7 (1), 27-34, 2006.

[9] Biazar, J., Hosseini, K., Gholamin, P., *Homotopy Perturbation Method for Solving KdV and Sawada-Kotera Equations*, Journal of Applied Mathematics, Islamic Azad University, 6, 2009.

[10] He, J.H., *Application of homotopy perturbation method to nonlinear wave equations*, Chaos, Solitons and Fractals, 26 (3), 695-700, 2005.

[11] Khan, Y., *An effective modification of the Laplace decomposition method for nonlinear equations*, International Journal of Nonlinear Sciences and Numerical Simulation, 10 (11-12), 1373-1376, 2009.

[12] Handibag, S., Karande, B.D., *Existence the solutions of some fifth-order kdv equation by laplace decomposition method*, American Journal of Computational Mathematics, 3, 80-85, 2013.

[13] Djidjeli, K., Price, W.G., Twizell, E.H., Wang, Y., *Numerical Methods for the Soltution of the Third and Fifth-Order Dispersive Korteweg-De Vries Equations*, Journal of Computational and Applied Mathematics, 58 (3), 307-336, 1995.

[14] Sawada, K., Kotera, T., *A method for finding N-soliton solutions of the KdV equation and KdV-like equation*, Progress of Theoretical Physics, 51 (5), 1355-1367, 1974.

[15] Prenter, P.M., *Splines and Variational Methods*, New York, John Wiley, 1975.

[16] Schoenberg, I.J., *On trigonometric spline interpolation*, Journal of Mathematics and Mechanics, 13, 795, 1964.

[17] Yagmurlu, N.M., Tasbozan, O., Ucar, Y., Esen, A., *Numerical solutions of the Combined KdV-mKdV Equation by a Quintic B-spline Collocation Method*, Applied Mathematics & Information Sciences Letters, 4 (1), 19-24, 2016.

[18] Hepson, O.E., *Numerical solutions of the Gardner equation via trigonometric quintic B-spline collocation method*, Sakarya University Journal of Science, 22 (6), 1576–1584, 2018.

[19] Rubin, S.G., Graves, R.A., *A Cubic Spline Approximation for Problems in Fluid Mechanics*, NASA, Washington, District of Columbia, October, 1975.

Adıyaman University Journal of Science
https://dergipark.org.tr/en/pub/adyujsci
DergiPark AKADEMİK
ISSN 2147-1630
e-ISSN 2146-586X

Computational Investigation of 5.5'',7''-trihydroxy-3,7-dimethoxy-4'-4'''-O-biflavone from Flavonoids Using DFT Calculations and Molecular Docking

Mehmet BAĞLAN[1,*], Ümit YILDIKO[2], Kenan GÖREN[1]

[1]*Kafkas University, Department of Chemistry, Kars 36100, Türkiye*
mehmetbaglan36@gmail.com , ORCID:0000-0002-7089-7111
kenangoren49@gmail.com , ORCID:0000-0001-5068-1762
[2]*Kafkas University, Department of Bioengineering, Kars 36100, Türkiye*
yildiko1@gmail.com , ORCID:0000-0001-8627-9038

Received: 25.05.2022 **Accepted:** 03.12.2022 **Published:** 30.12.2022

Abstract

The structural characterization of the 5.5'',7''-trihydroxy-3,7-dimethoxy-4'-4'''-*O*-biflavone (TDOB) molecule was done in this study. For the structural characterization of this molecule, based on the molecule's stable phase geometry, entire calculations were done using the CAM-B3LYP and PBEPBE approaches with SDD and LanL2DZ basis sets respectively. In our study, many calculations, such as HOMO-LUMO energy gaps, inter-orbital, and inter-orbital bond interactions, and electrostatic surface mapping processes of the TDOB molecule, have also been made. In the continuation of our study, the specific binding site and mechanism of the ligand on the protein were investigated using molecular docking. In the molecular docking study, affinity scores for TDOB- aldose reductase (PDB: 4ICC) and (PDB: 4IGS) were found to be -8.559 kcal/mol and -5.461 kcal/mol, respectively. The 4ICC receptor binding score was found to be greater. In the continuation of the molecular docking study, the inhibitory properties of TDOB were investigated against the aldose reductase enzymes (PDB: 4ICC) and (PDB: 4IGS), both of which showed effective inhibition, and it was seen that the TDOB molecule effectively inhibited the enzymes (PDB: 4ICC) and aldose reductase (PDB: 4IGS).

Keywords: Flavonoids; TDOB; HOMO-LUMO; Molecular docking.

* Corresponding Author DOI: 10.37094/adyujsci.1121018

5,5'',7''-trihidroksi-3,7-dimetoksi-4'-4'''-O-biflavon Bileşiğinde DFT ve Moleküler Doking Çalışması

Öz

Bu çalışmada, 5,5",7"-trihidroksi-3,7-dimetoksi-4'-4"'-*O*-biflavon (TDOB) molekülünün yapısal karakterizasyonu yapıldı. Bu molekülün yapısal karakterizasyonu için, molekülün kararlı faz geometrisine dayalı olarak, tüm hesaplamalar sırasıyla CAM-B3LYP ve PBEPBE metotlarını SDD ve LanL2DZ temel seti kullanılarak yapıldı. Çalışmamızda TDOB molekülünün HOMO-LUMO enerji boşlukları, yörüngeler arası ve yörüngeler arası bağ etkileşimleri, elektrostatik yüzey haritalama işlemleri gibi birçok hesaplamalarda yapılmıştır. Çalışmamızın devamında moleküler doking kullanılarak ligandın protein üzerindeki spesifik bağlanma yeri ve mekanizması araştırıldı. Doking çalışmasında, TDOB- aldoz reduktaz (PDB: 4ICC) ve TDOB- aldoz reduktaz (PDB: 4IGS) ile afinite skorları sırasıyla -8.559 kcal/mol ve -5.461 kcal/mol olarak bulundu. TDOB- aldoz reduktaz (PDB: 4ICC) reseptör bağlanma skoru daha büyük olduğu tespit edildi. Moleküler doking çalışmasının devamında TDOB'nin inhibitör özellikleri, her ikisi de etkili inhibisyon gösteren (PDB: 4ICC) ve (PDB: 4IGS) enzimlerine karşı araştırıldı ve TDOB molekülünün, (PDB: 4ICC) ve (PDB: 4IGS) aldoz reduktaz enzimlerini etkili bir şekilde inhibe ettiği görüldü.

Anahtar Kelimeler: Flavonoidler; TDOB; HOMO-LUMO; Moleküler doking.

1. Introduction

Flavonoids are natural substances that belong to a group of plant secondary metabolites with a polyphenolic structure found in vegetables, fruits, and certain beverages [1]. Flavonoids have biochemical and antioxidant capabilities that have been linked to diseases like Alzheimer's, atherosclerosis, and cancer [2, 3]. Flavonoids play a key role in a wide array of nutraceutical, pharmacological, medicinal, and cosmetic areas owing to their numerous health-promoting properties [4, 5]. Their antioxidant, anti-carcinogenic, anti-inflammatory, and anti-mutagenic qualities, with their potential to alter critical cellular enzyme activity, contribute to this [6]. Potent inhibitors of flavonoids include xanthine oxidase (XO), lipoxygenase, cyclo-oxygenase (COX), and phosphoinositide 3-kinase [7]. Flavonoids are plant-derived substances found in various plant parts. Flavonoids are essential for the growth of vegetables and protect themselves from plaque, so they are also known as low-molecular-weight phenolic compounds found in plants. Because flavonoids are one of the most recognized chemical groups in high plants, they are easily recognized as floral pigments found in most angiosperm groups [8, 9]. Yet they are not only found in flowers; they are also found in other plants like chalcones, flavones, flavonols, and isoflavones.

Computational chemistry has made significant progress as a tool to study organic and biological structures, especially in various fields of chemistry [10]. Theoretical chemical calculations have proven crucial in elucidating the molecule's architectures, properties, processes, and reaction selectivity. The most common theoretical approaches used to calculate various molecular properties include DFT (density functional theory), optimized molecular structures, vibrational frequencies, and chemical shifts [11-13].

The CAM-B3LYP/SDD and PBEPBE/LanL2DZ level of theory was used to investigate the theoretical spectroscopic features of the TDOB molecule in this research. The study was then subjected to molecular docking to determine the ligand's specific binding location over the protein as well as the binding's mechanism. Following the selection of the optimal pose for the entire ligand-enzyme docking, binding modalities were studied in order to better understand inhibitory mechanisms.

2. Materials and Methods

Entire calculations were made in Gaussian 09 software [14] by use of CAM-B3LYP/SDD and PBEPBE/LanL2DZ level of theory of DFT calculations. The first step in the computational analysis was to optimize the geometry of the generated molecule. The TDOB molecule, in particular, requires low energy sensitivity to molecular shape changes caused by core position displacement. Especially for TDOB, low energy sensitivity to changes in molecular structure is required due to core position displacement. Gaussian 09's DFT method was used to calculate the molecular structure, vibrational frequencies, and energies of optimal geometries of the TDOB molecule. The basic set is the Lee's-Yang-Parr correlation function (CAM-B3LYP) based on the SDD-based program package.

Molecular docking was done to look at the specific binding site and the ligand's mechanism over the protein (using the Maestro Molecular Modeling platform (version 11.8) of the Schrödinger, LLC model) [15]. High-resolution (0.85 Å) crystal structures were obtained from the enzymes aldose reductase (PDB: 4ICC) and aldose reductase (PDB: 4IGS) (https://www.rcsb.org/structure/4IGS/pdb). Ligand constructs were obtained as SDF files from the PubChem website. All compounds were synthesized according to the previous implementation of the Ligprep module [16, 17]. Using the wizard module, protein preparation was put on hold for data. At this point, all water molecules have been expelled from the crystal structure [18]. The protein ion balance was once again adjusted using this module, this time by identifying the active site of the protein for flexible binding. Mesh boxes were created as the basis of the receptor griding module and formed networks at the protein's binding sites, allowing

flexible docking. These studies followed the same procedures as previous studies. The slip insertion module was used to construct a ligand-protein docking strategy [19]. Optimal binding energies were calculated based on interactions between ligand and protein, π-π interactions, hydrogen bonds, and alkyl and π interactions. Maximum binding affinity is indicated by the lowest energy configurations. Discovery Studio 4.5 was used to demonstrate the 2D and 3D interactions as well as the resulting receptor model [20].

3. Results and Discussion

3.1. Structure details and analysis

The optimal structural parameters estimated using the DFT/CAM-B3LYP/SDD and PBEPBE/LanL2DZ level of theory are given in [21, 22] Table 1. The two methods and base sets were used to compare the bond lengths and angles between the optimized molecule atoms. The bond lengths between C - O atoms in the molecule were calculated as 1.395 Å in the CAM-B3LYP level of theory and 1.410 Å in the PBEPBE level of theory when compared with the two techniques. In the second procedure, the bond lengths were shorter. In aromatic and aliphatic structures, bond lengths can be used with both approaches. Due to the sensitivity of the procedures, there are slight differences between them. Both methods are compatible at Fig. 1.

Table 1: The bond lengths (Å) or bond angles (o) of the TDOB molecule calculated theoretically

Bond Lengths	**CAM-B3LYP/ SDD**	**PBEPBE/ LanL2DZ**	**Bond Lengths**	**CAM-B3LYP/ SDD**	**PBEPBE/ LanL2DZ**
C1-C2	1.399	1.412	**C2-O8**	1.395	1.410
C5-C7	1.472	1.473	**C16-O15**	1.391	1.404
C13-C14	1.397	1.406	**C18-O26**	1.276	1.304
C18-C19	1.449	1.450	**C23-O25**	1.361	1.372
C31-C32	1.462	1.467	**C32-O60**	1.385	1.397
C33-C34	1.405	1.419	**O8-C9**	1.400	1.417
C34-O39	1.376	1.394	**O39-C40**	1.449	1.469
C1-H41	1.083	1.093	**O25-H53**	1.006	1.045
C20-H50	1.081	1.090	**O37-C56**	1.004	1.041
C40-H57	1.089	1.106	**O60-C61**	1.466	1.488
Bond Angles	**CAM-B3LYP/ SDD**	**PBEPBE/ LanL2DZ**	**Bond Angles**	**CAM-B3LYP/ SDD**	**PBEPBE/ LanL2DZ**
C1-C2-C3	120.622	120.599	**C21-C22-H51**	122.013	121.928
C4-C5-C7	121.070	121.003	**C21-O24-H52**	113.194	111.159
C5-C7-C19	126.843	126.934	**C7-O15-C16**	121.135	120.175
C17-C18-O26	121.313	121.019	**C34-O39-C40**	119.379	118.057
C23-O25-H53	109.718	106.749	**H57-C40-H59**	109.760	109.891
Bond Angles	**CAM-B3LYP/ SDD**	**PBEPBE/ LanL2DZ**	**Bond Angles**	**CAM-B3LYP/ SDD**	**PBEPBE/ LanL2DZ**
C18-C17-C16-C20	-179.945	-179.921	**C35-C36-O37-H56**	179.243	178.928

C11-C12-C27-C32	-164.920	-166.661	**O28-C27-C32-O60**	177.309	176.626
C21-C22-C23- O25	179.981	179.946	**C12-C27-O28-C29**	-179.856	-178.716

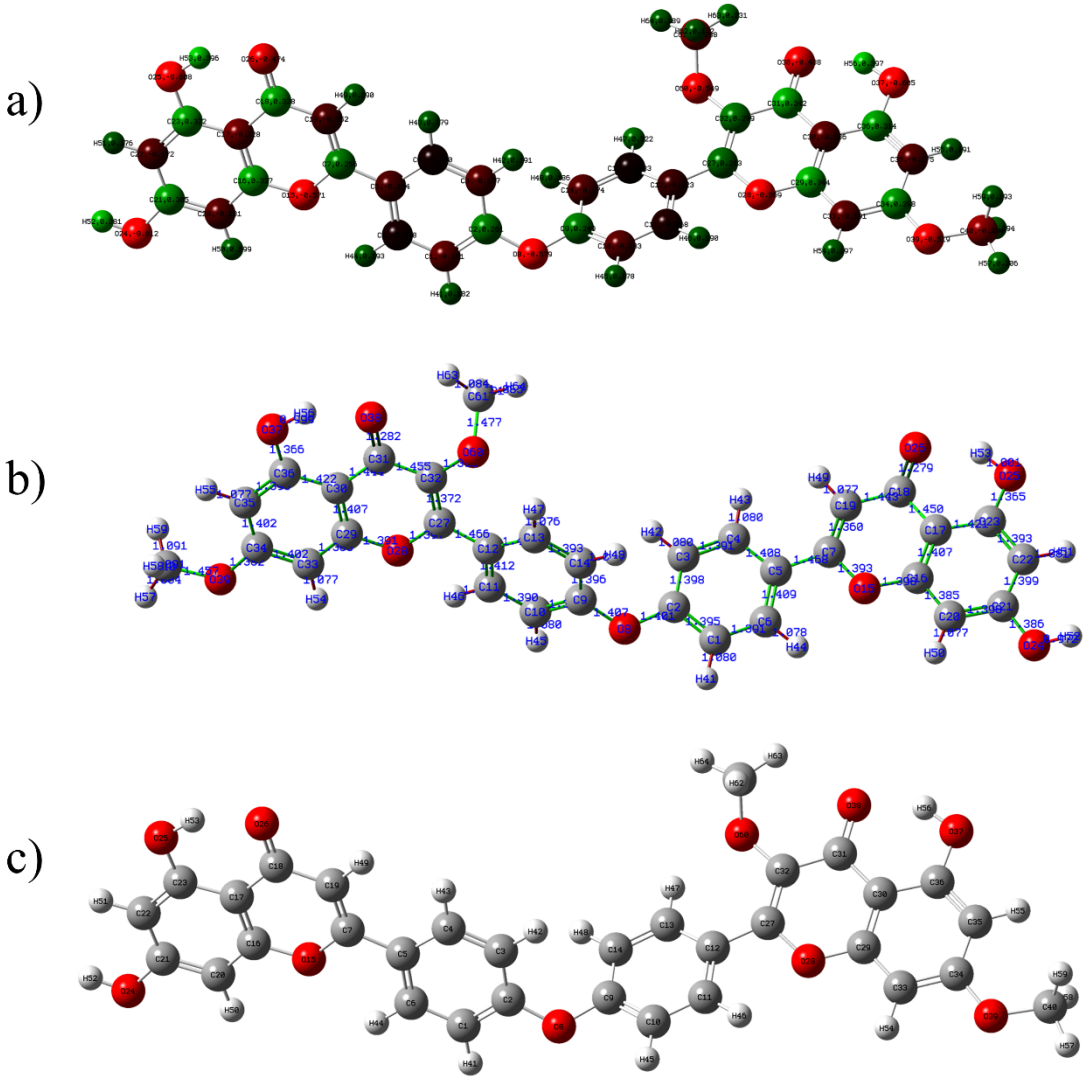

Figure 1: TDOB molecule with CAM-B3LYP/SDD level of theory a) Mulliken b) bond length c) structure optimization

3.2. Frontier molecular orbitals (FMOs)

The highest and occupied molecular orbitals (HOMOs) or the lowest and unoccupied molecular orbitals (LUMOs) are two types of frontier molecular orbitals [23, 24]. Apart from chemical interactions, FMOs have a key role in UV-Vis spectra, as well as electrical and optical properties [25]. The electron-donating ability of an inhibitor molecule is often linked to HOMO, according to the boundary orbital theory. The electron-donating ability of a molecule has been proven by high E_{HOMO} values. The electron-accepting ability of molecules has been proven by

ELUMO. TDOB molecule's CAM-B3LYP/SDD and PBEPBE/LanL2DZ level of theory and HOMO and LUMO boundary trajectories are shown in Fig. 2 and Fig. 3. While the E_{HOMO} = -7.5 eV-E_{LUMO} = -1.40 eV of the molecule was calculated by the DFT/CAM-B3LYP/SDD level of theory, the E_{HOMO} = -7.5 eV-E_{LUMO} = -1.41 eV of the DFT/ PBEPBE/ LanL2DZ level of theory was calculated. For other orbitals, E_{HOMO-1} = -7.8 eV-E_{LUMO+1} = -1.22 eV was calculated for the DFT/CAM-B3LYP/SDD level of theory, and E_{HOMO-1} = -7.8 eV-E_{LUMO+1} = -1.23 eV for DFT/ PBEPBE/LanL2DZ level of theory values were calculated. The HOMO and LUMO orbitals of the molecule determine how it will interact with other molecules. The energy band gap (E = ELUMO – EHOMO) has low absolute values indicating limited high chemical reactivity and kinetic stability [26]. The band gaps of the compound in both methods are high around 6.00 eV, indicating that it is an insulating material. The electronegativity of a small orbital gap indicates a molecule with polarization, stiffness, and other reactivated indices [27]. Chemical reactivity indices are shown in Table 2.

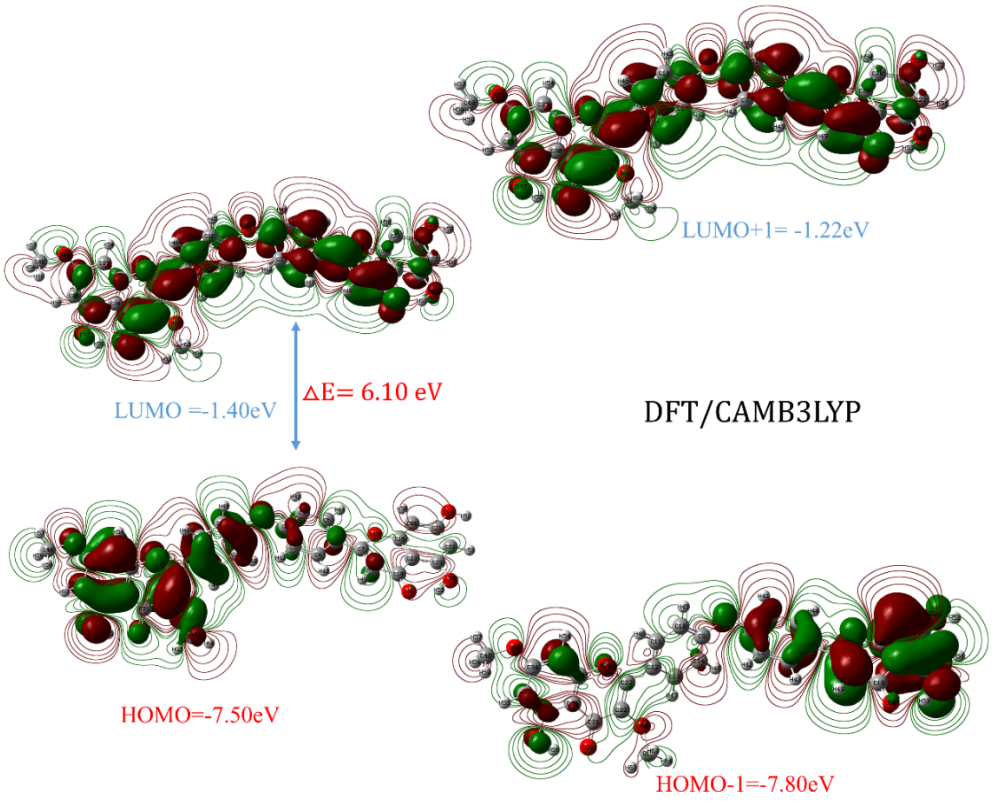

Figure 2: According to the DFT /CAM-B3LYP/SDD level of theory, the compound's boundary molecular orbitals

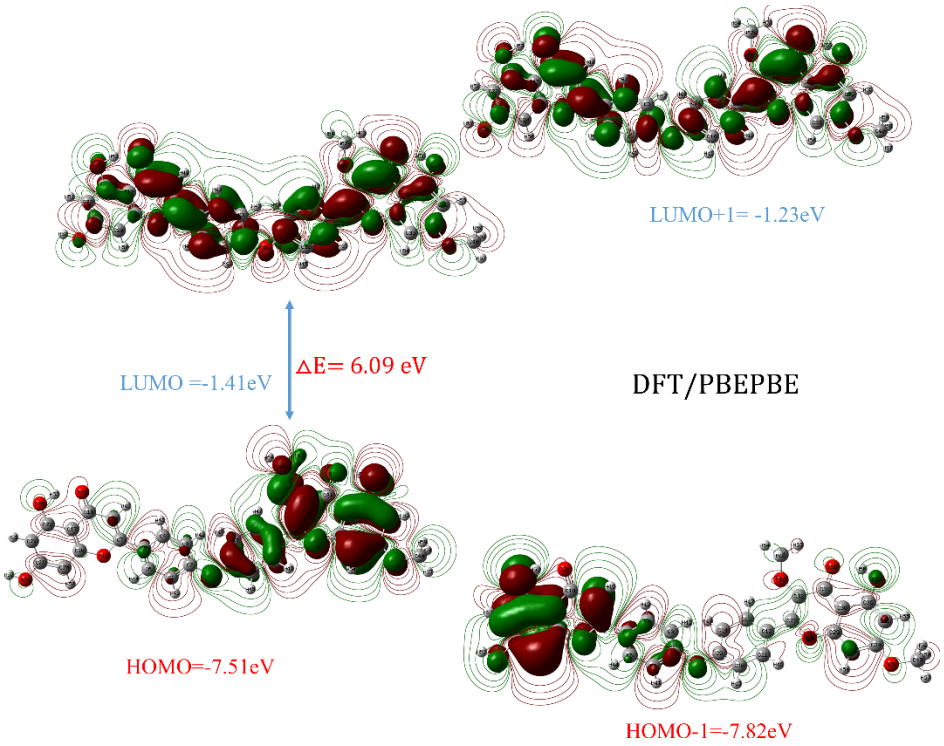

Figure 3: According to the DFT/PBEPBE/LanL2DZ level of theory, the compound's boundary molecular orbitals

Table 2: Calculation using DFT/CAM-B3LYP/SDD- DFT/PBEPBE/LanL2DZ level of theory to compare HOMO, LUMO, and chemical reactivity descriptors at 298.15 K in the base case

Molecules Energy	**DFT/CAM-B3LYP**	**DFT/ PBEPBE**
E_{LUMO}	-1.40	-1.41
E_{HOMO}	-7.50	-7.51
E_{LUMO+1}	-1.22	-1.23
E_{HOMO-1}	-7.80	-7.82
Energy Gap (Δ) $\lvert E_{HOMO}- E_{LUMO}\rvert$	6.10	6.09
Ionization Potential ($I = -E_{HOMO}$)	7.50	7.51
Electron Affinity ($A = -E_{LUMO}$)	1.40	1.41
Chemical hardness ($\eta = (I - A)/2$)	3.05	3.05
Chemical softness ($s = 1/2\ \eta$)	0.164	0.164
Chemical Potential ($\mu = -(I + A)/2$)	-4.45	-4.46
Electronegativity ($\chi = (1+ A)/2$)	1.2	1.21
Electrophilicity index ($\omega = \mu^2/2\ \eta$)	3.24	3.26

3.3. Non-linear optical properties (NLO)

Non-linear optical (NLO) materials having two substantial absorptions have sparked a lot of interest in recent years. Two-photon absorption' behavior can be influenced by factors like molecular weight, molecule symmetry, and solubility. In addition, The dipole moment provides a strong intermolecular attraction, containing dipole-dipole and van der Waals-type interactions, as well as a substantial characteristic of the energy associated with the electric field applied within

the molecule [28, 29]. Table 3 lists the calculated parameters for the electronic dipole moment and total dipole moment. In the gas phase, parameters for the CAM-B3LYP/SDD level of theory μ = 3.4723 D, α = 240.6017 au, β = 1.699x10^{-31} esu, and for the PBEPBE/LanL2DZ level of theory μ = 4.7335 D, α = 230.5635 au, β =2.316 x 10^{-31} was calculated as esu. From the data obtained for this molecule, theoretically high polarity values are considered to be good candidates for nonlinear optical materials [30].

Table 3: Polarizability (au), dipole moments (Debye), β sum, and β components of C-O value calculated with DFT/CAM-B3LYP/SDD and DFT/PBEPBE/LanL2DZ level of theory

Parameters	CAM-B3LYP/ SDD	PBEPBE/ LanL2DZ	Parameters	CAM-B3LYP/ SDD	PBEPBE/ LanL2DZ
μ_X	2.7749	2.4388	**β_{XXX}**	251.8406	261.7705
μ_Y	-2.0722	-3.0020	**β_{YYY}**	-58.2712	-53.0664
μ_Z	0.2505	0.6656	**β_{ZZZ}**	0.1694	0.1664
$\mu_{(D)}$	3.4723	4.7335	**β_{XYY}**	59.0378	60.5733
α_{XX}	-204.7813	-203.6619	**β_{XXY}**	-68.2085	-67.1160
α_{YY}	-268.1013	-267.7645	**β_{XXZ}**	1.1489	1.3641
α_{ZZ}	-243.3164	-247.2643	**β_{XZZ}**	19.5879	18.4797
A_{XY}	8.2697	7.6678	**β_{YZZ}**	17.0889	16.9470
α_{XZ}	18.9743	18.4972	**β_{YYZ}**	-14.1439	-12.2315
α_{YZ}	-2.5606	-2.4441	**β_{XYZ}**	5.7929	8.0334
α (au)	240.6017	230.5635	**β (esu)**	1.699 x10^{-31}	2.316x10^{-31}

3.4. Mulliken atomic charges

The application of quantum chemistry computations relies heavily on Mulliken atomic charge estimates. Mulliken can be used to get many ideas about atomic charge polarization, stability, electronic structure, etc [31]. It also shows how to charge sharing and molecular charge transfer help build electron donor-acceptor pairs. The CAM-B3LYP/SDD level of theory was used to calculate the Mulliken atom. The oxygen atom linked to the aromatic ring has a Mulliken charge of O24 (-0.458) - (-0.425), O26 (-0.359) - (-0.343), O38 (-0.377) - (-0.369), and O60 (-0.355) - (-0.314). Some C atoms were found to be positive, while others were found to be negative. Mulliken atomic charge calculation has an important role for the application of quantum chemical calculation of molecular system. Atomic charge affects the dipole moment, polarizability, electronic structure and other molecular properties of the system [32].

Table 4: Values found using DFT/CAM-B3LYP/SDD and DFT/PBEPBE/LanL2DZ level of theory to determine Mulliken atomic charges for TDOB molecule

	CAM-B3LYP/ SDD	PBEPBE/ LanL2DZ		CAM-B3LYP/ SDD	PBEPBE/ LanL2DZ
C1	-0.372	-0.383	**O24**	-0.458	-0.425
C2	0.334	0.328	**O25**	-0.454	-0.489
C4	-0.347	-0.368	**O26**	-0.359	-0.343

C7	0.275	0.225	**O28**	-0.333	-0.294
C9	0.330	0.324	**O38**	-0.377	-0.369
C13	-0.344	-0.362	**O39**	-0.299	-0.256
C19	-0.439	-0.402	**O60**	-0.355	-0.314
C22	-0.566	-0.572	**H41**	0.268	0.265
C27	0.162	0.111	**H43**	0.236	0.234
C29	0.323	0.266	**H46**	0.276	0.271
C30	-0.071	0.021	**H47**	0.313	0.303
C32	0.094	0.124	**H48**	0.271	0.271
C34	0.439	0.388	**H51**	0.259	0.254
C35	-0.533	-0.354	**H53**	0.412	0.383
C36	0.213	0.186	**H54**	0.293	0.283
C40	-0.475	-0.544	**H62**	0.199	0.219

3.5. Molecular electrostatic potential (MEP)

The molecular electrostatic potential (MEP) is plotted for the TDOB molecule and shows the molecule's shape, size, and electrostatic potential values. The investigation of the molecular structure's physicochemical properties has been substantially aided by molecular electrostatic potential (MEP) mapping [33, 34]. A portion of the molecule with a negative electrostatic potential is vulnerable to electrophilic assault. Different electrostatic potential levels on the surface are reflected in the changing colors; yellow and red indicate the highest negative zone, which is the preferred region for electrophilic reagents. The maximum positive range, which is the preferred range of nucleophilic reactivity, is expressed by the zero potential as shown in the blue and green regions. Here, the TDOB molecule's MEP map is mapped as shown in Fig. 4. The aromatic ring area appears to be neutral (green) in coloring.

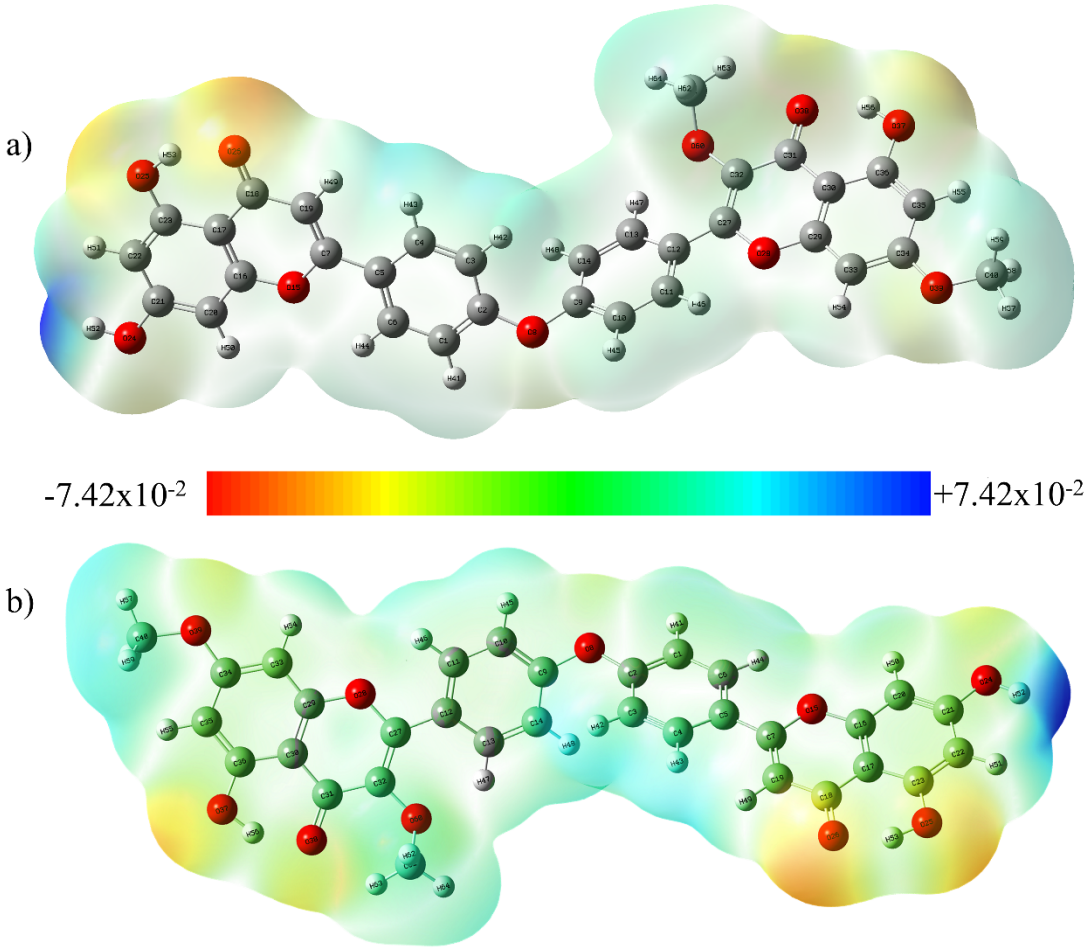

Figure 4: Molecular electrostatic potential surface calculated using the DFT/CAM-B3LYP/SDD **(a)** and PBEPBE/LanL2DZ **(b)** level of theory

3.6. Molecular docking studies

Molecular docking is a computer method that aims to forecast the non-covalent interaction between a macromolecule (receptor) and a small molecule (ligands). Automated docking is frequently used in structure/function analysis and molecular design for the prediction of bimolecular complexes. The structure-based drug design process includes steps such as docking small molecule compounds into a receptor's binding site and determining the complex's binding affinity [27, 35]. As a result of the TDOB - aldose reductase (PDB: 4ICC) docking study, Fig. 5 shows the 3D and 2D interaction. The shift score in binding affinity with TDOB - aldose reductase (PDB: 4ICC) was found to be -8.559 kcal/mol (Table 5). The binding mechanism is here, in the TRP-112 (5.49 Å) phenol binding mechanism with hydrogen-bonded water, ILE-261 (4.69 Å) hydrogen bonded to phenol, ILE-261 (3.65 Å), SER-211 (4.03 Å), ASP-44 (3.63 Å), THR-20 (5.30 Å), conventional hydrogen bond, GLY-19 (3.66 Å) conventional hydrogen bond attached to hydrogen in hydroxyl, SER-215 (3.40 Å) hydrogen bond attached to carbon, CYS-299 (7.41

Å) alkyl attached to the middle of the benzene ring, TYR-210 (5.69 Å), TRP-21 (5.09 Å) and TRP-21 (5.65 Å) π -alkyl attached to the core of the benzene are examples. Figure 5 shows additional interactions. Figure 5 depicts a 3D view of the SAS surface on the receptor.

Table 5: Docking score of TDOB - aldose reductase (PDB: 4ICC) and TDOB - aldose reductase (PDB:4IGS)

Compound	Docking Score	
	Aldose reductase (PDB:4ICC)	Aldose reductase (PDB:4IGS)
TDOB	-8.559 kcal/mol	-5.461 kcal/mol

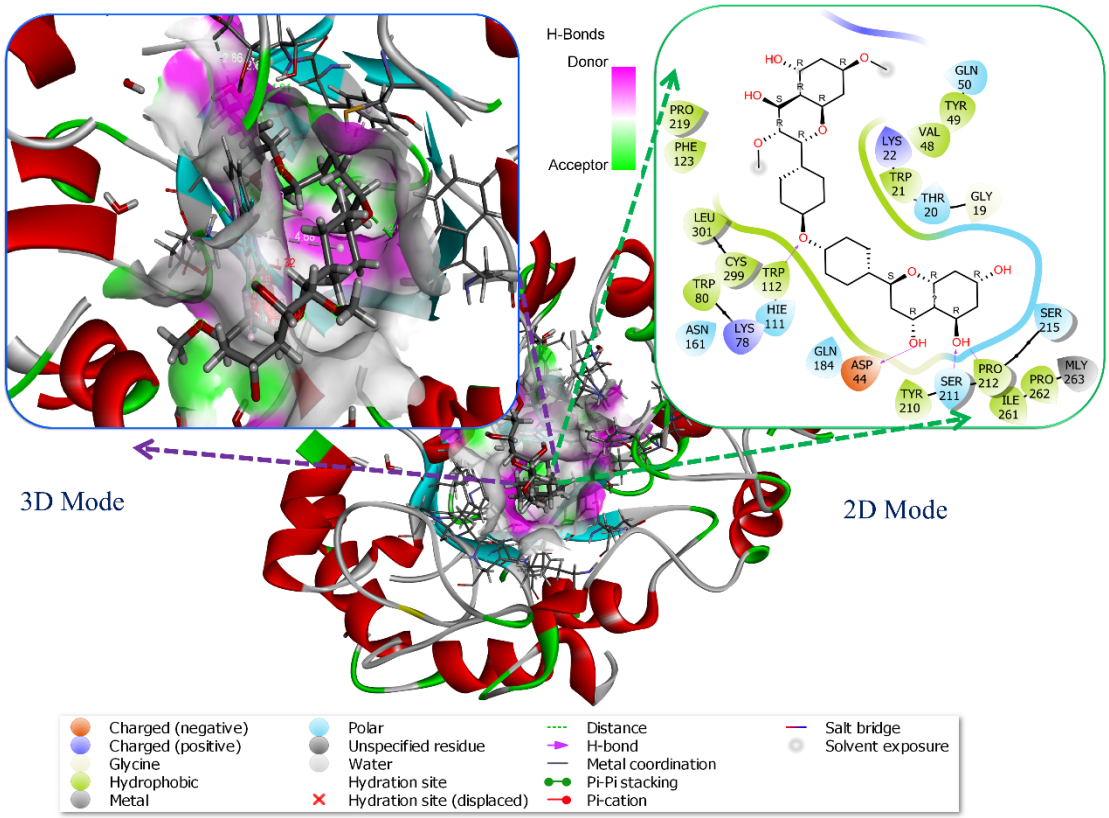

Figure 5: 2D picture of TDOB - aldose reductase (PDB: 4ICC) enzyme interactions and 3D view of the receptor's aromatic surface

As a result of AKR1B1 (PDB:4IGS) docking, the 3D and 2D interactions are shown in Fig. 6. The shift score in binding affinity with TDOB - aldose reductase (PDB:4IGS) was found as -5.461 kcal/mol (Table 5). The binding mechanism is here, PRO-225 (4.41 Å), ARG-217 (5.55 Å), GLU-229 (5.63 Å), ASP-216 (3.37 Å) conventional hydrogen bonding in hydroxyl, ASP-216

(4.63 Å) and ASP-216 (3.31 Å) carbon hydrogen bonds, ALA-220 (4.72 Å), ALA-220 (4.90 Å), PRO-222 (4.57 Å), and PRO-218 (5.17 Å) are examples of alkyl bonded to the middle of the benzene ring. Figure 6 shows other interactions. Figure 6 depicts a 3D view of the SAS surface on the receptor.

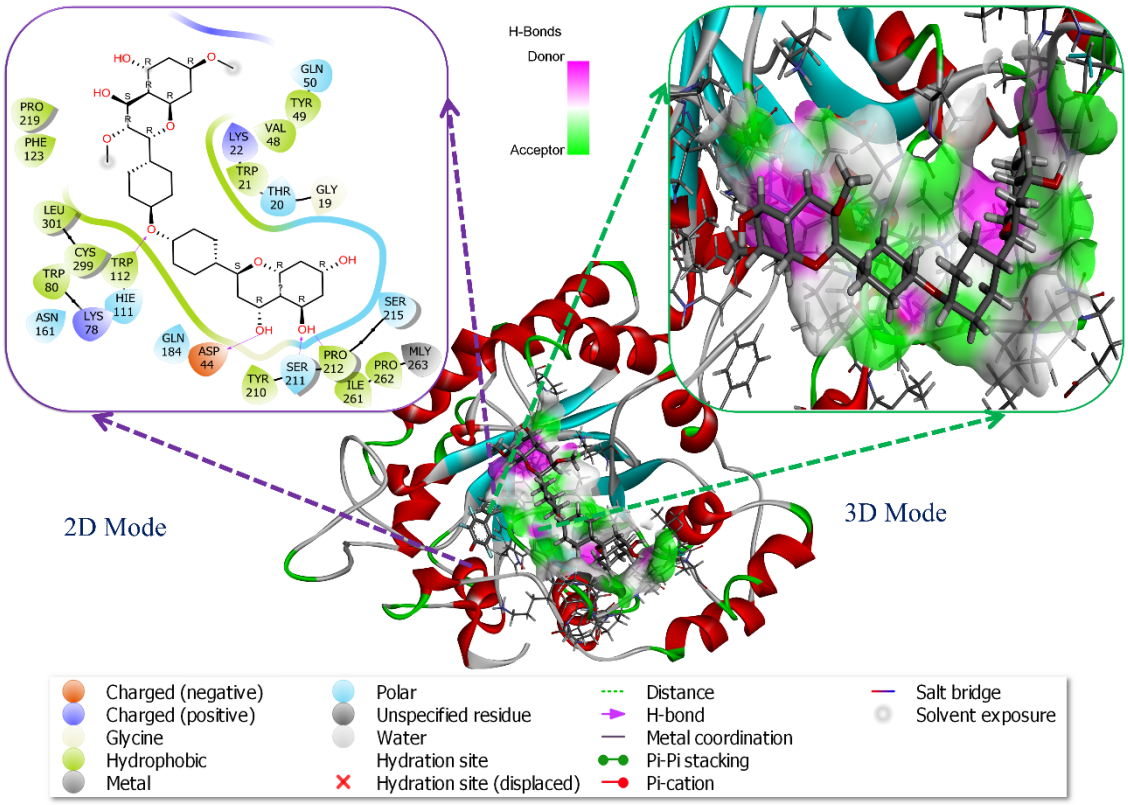

Figure 6: 2D picture of TDOB - aldose reductase (PDB: 4IGS) enzyme interactions and 3D view of the receptor's aromatic surface

4. Conclusion

Quantum chemical calculations were used to make detailed studies on TDOB molecule. The structural, electronic, and vibrational frequencies of the compound were estimated using the CAM-B3LYP/SDD and PBEPBE/LanL2DZ levels of theory. The compound's bond angles, bond lengths, and dihedral angles were theoretically defined structural parameters. The compound's Nonlinear optical properties were also examined. It was also determined that the studied compound could be used as an NLO material. HOMO-LUMO, MEP maps, and Mulliken atomic charges are also depicted. TDOB molecule's molecular docking was also done to look at the specific binding site and mechanism of the ligand on the protein. After finding the optimal exposure for all ligand-enzyme docking, binding modalities were studied to better understand inhibitory mechanisms. In the study, the shift scores in binding affinity with TDOB– aldose

reductase (PDB: 4ICC) and TDOB– aldose reductase (PDB: 4IGS) were determined to be -8.559 kcal/mol and -5.461 kcal/mol, respectively. It is more effective with TDOB – aldose reductase (PDB: 4ICC) receptor binding score. Since this compound has a high drug potential, it can be investigated in the design of new drugs in the treatment of Alzheimer's disease and as a new enzyme inhibitor candidate.

References

[1] Panche, A.N., Diwan, A.D., and Chandra, S.R., *Flavonoids: an overview,* Journal of Nutritional Science, 5 (47), 1-15, 2016.

[2] Oyeleke, M.B. and Owoyele, B.V., *Saponins and flavonoids from Bacopa floribunda plant extract exhibit antioxidant and anti-inflammatory effects on amyloid beta 1-42-induced Alzheimer's disease in BALB/c mice,* Journal of Ethnopharmacology, 288, 114997, 2022.

[3] Chauhan, B.S., Kumar, R., Kumar, P., Kumar, P., Sinha, S., Mishra, S.K., Kumar, P., Tiwari, K.N., Critchley, A.T., Prithiviraj, B., and Srikrishna, S., *Neuroprotective potential of flavonoid rich Ascophyllum nodosum (FRAN) fraction from the brown seaweed on an Aβ(42) induced Alzheimer's model of Drosophila,* Phytomedicine, 95, 153872, 2022.

[4] Wang, B., Ding, Y., Zhao, P., Li, W., Li, M., Zhu, J., and Ye, S., *Systems pharmacology-based drug discovery and active mechanism of natural products for coronavirus pneumonia (COVID-19): An example using flavonoids,* Computers in Biology and Medicine, 143, 105241, 2022.

[5] Mitra, S., Lami, M.S., Uddin, T.M., Das, R., Islam, F., Anjum, J., Hossain, M.J., and Emran, T.B., *Prospective multifunctional roles and pharmacological potential of dietary flavonoid narirutin,* Biomedicine and Pharmacotherapy, 150, 112932, 2022.

[6] Heimfarth, L., Nascimento, L.D.S., Amazonas da Silva, M.J., Lucca Junior, W., Lima, E.S., Quintans-Junior, L.J., and Veiga-Junior, V.F.D., *Neuroprotective and anti-inflammatory effect of pectolinarigenin, a flavonoid from Amazonian Aegiphila integrifolia (Jacq.), against lipopolysaccharide-induced inflammation in astrocytes via NFκB and MAPK pathways,* Food and Chemical Toxicology, 157, 112538, 2021.

[7] Onishi, S., Nishi, K., Yasunaga, S., Muranaka, A., Maeyama, K., Kadota, A., and Sugahara, T., *Nobiletin, a polymethoxy flavonoid, exerts anti-allergic effect by suppressing activation of phosphoinositide 3-kinase,* Journal of Functional Foods, 6, 606-614, 2014.

[8] Young, D.A. and Sterner, R.W., *Leaf flavonoids of primitive dicotyledonous angiosperms: Degeneria vitiensis and Idiospermum australiense,* Biochemical Systematics and Ecology, 9 (2), 185-187, 1981.

[9] Truchado, P., Ferreres, F., and Tomas-Barberan, F.A., *Liquid chromatography-tandem mass spectrometry reveals the widespread occurrence of flavonoid glycosides in honey, and their potential as floral origin markers,* Journal of Chromatography. A, 1216 (43), 7241-8, 2009.

[10] Solgun, D.G., Tanriverdi, A.A., Yildiko, U., and Ağirtaş, M.S., *Synthesis of axially silicon phthalocyanine substituted with bis- (3,4-dimethoxyphenethoxy) groups, DFT and molecular docking studies,* Journal of Inclusion Phenomena and Macrocyclic Chemistry, 102 (11), 851-860, 2022.

[11] Cui, W., Chen, J., *Insight into mineral flotation fundamentals through the DFT method,* International Journal of Mining Science and Technology, 31 (6), 983-994, 2021.

[12] Chauhan, A., Singh, K.M., *Recursive sliding DFT algorithms: A review,* Digital Signal Processing, 127, 103560, 2022.

[13] Shang, Y., Duan, X., Wang, S., Yue, Q., Gao, B., and Xu, X., *Carbon-based single atom catalyst: Synthesis, characterization, DFT calculations,* Chinese Chemical Letters, 33 (2), 663-673, 2022.

[14] Frisch, M.J., Trucks, G.W., Schlegel, H.B., and Scuseria, G.E., Gaussian 09, Revision E.01, 2016.

[15] Wang, G., Liu, W., Gong, Z., Huang, Y., Li, Y., and Peng, Z., *Design, synthesis, biological evaluation and molecular docking studies of new chalcone derivatives containing diaryl ether moiety as potential anticancer agents and tubulin polymerization inhibitors,* Bioorganic Chemistry, 95, 103565, 2020.

[16] Altun, K., Yildiko, Ü., Tanrıverdi, A.A., Tekeş, A.T., Ata, A.Ç., Kartal, B., and Çakmak, İ., *Structural and Spectral Properties of 4-(5-methyl-[1, 2, 4] triazolo [1, 5-a] pyrimidine-7-yloxy) phthalonitrile: Analysis by TD-DFT Method, ADME Analysis, and Molecular Docking Simulations,* Journal of the Institute of Science Technology, 12 (4), 2340-2351, 2022.

[17] Yildiko, Ü., Türkan, F., Tanriverdi, A.A., Ata, A.C., Atalar, M.N., and Cakmak, İ., *Synthesis, enzymes inhibitory properties and characterization of 2-(bis (4-aminophenyl) methyl) butan-1-ol compound: Quantum simulations, and in-silico molecular docking studies,* Journal of the Indian Chemical Society, 98 (11), 100206, 2021.

[18] Akinpelu, O.I., Lawal, M.M., Kumalo, H.M., and Mhlongo, N.N., *Drug repurposing: Fusidic acid as a potential inhibitor of M. tuberculosis FtsZ polymerization – Insight from DFT calculations, molecular docking and molecular dynamics simulations,* Tuberculosis, 121, 101920, 2020.

[19] Asadi, Z., Golchin, M., Eigner, V., Dusek, M., and Amirghofran, Z., *A detailed study on the interaction of a novel water-soluble glycine bridged zinc(II) Schiff base coordination polymer with BSA: Synthesis, crystal structure, molecular docking and cytotoxicity effect against A549, Jurkat and Raji cell lines,* Inorganica Chimica Acta, 465, 50-60, 2017.

[20] Marinho, E.M., Batista de Andrade Neto, J., Silva, J., Rocha da Silva, C., Cavalcanti, B.C., Marinho, E.S., and Nobre Júnior, H.V., *Virtual screening based on molecular docking of possible inhibitors of Covid-19 main protease,* Microbial Pathogenesis, 148, 104365, 2020.

[21] Solğun, D.G., Keskin, M.S., yıldıko, Ü., and Ağırtaş, M.S., *DFT analysis and electronic properties, and synthesis of tetra (9-phenyl-9H-xanthen-9-yl) oxy peripheral-substituted zinc phthalocyanine,* Chemical Papers, 74 (8), 2389-2401, 2020.

[22] Khajehzadeh, M. and Moghadam, M., *Molecular structure, FT IR, NMR, UV, NBO and HOMO–LUMO of 1-(3-(dimethylamino)propyl)-1-(4-fluorophenyl)-1,3-dihydroisobenzofuran-5-carbonitrile by DFT/B3LYP and PBEPBE methods with LanL2DZ and 6-311++G(d,2p) basis sets,* Spectrochimica Acta Part A: Molecular and Biomolecular Spectroscopy, 180, 51-66, 2017.

[23] Yildiko, Ü., Ata, A.Ç., Tanriverdi, A.A., and Çakmak, İ., *Investigation of novel diethanolamine dithiocarbamate agent for RAFT polymerization: DFT computational study of the oligomer molecules,* Bulletin of Materials Science, 44 (3), 186, 2021.

[24] Li, K., Xu, W., Han, M., Cheng, Y., Wen, G., and Huang, T., *Integration of iron-manganese co-oxide (FMO) with gravity-driven membrane (GDM) for efficient treatment of surface water containing manganese and ammonium,* Separation and Purification Technology, 282, 119977, 2022.

[25] Griesbeck, C., Hager-Braun, C., Rogl, H., and Hauska, G., *Quantitation of P840 reaction center preparations from Chlorobium tepidum: chlorophylls and FMO-protein,* Biochimica et Biophysica Acta (BBA) - Bioenergetics, 1365 (1), 285-293, 1998.

[26] Tanriverdi, A.A., Yildiko, U., Tekes, A.T., Cakmak, İ., and Ata, A.C., *Synthesis, characterization and affinity detection of sulfonated polyimides: confirmation of proton transfer in quantum theory simulations,* Polymer Bulletin, 2022. DOI: https://doi.org/10.1007/s00289-022-04536-0

[27] Tekeş, A.T., Ata, A.Ç., Tanriverdi, A.A., and Çakmak, İ., *Insilico Molecular Docking Studies of THBF Compound: TD-DFT Simulations and Drug Design,* Journal of the Institute of Science Technology, 11 (4), 2955-2966, 2021.

[28] Durgadevi, R., Suvitha, A., and Arumanayagam, T., *Growth, optical, electrical properties and DFT studies on piperidinium 4-nitrophenolate NLO single crystal in acetone,* Journal of Crystal Growth, 582, 126512, 2022.

[29] Derafa, W., Aggoun, D., Messasma, Z., Houchi, S., Bouacida, S., and Ourari, A., *An unexpected single crystal structure of nickel(II) complex: Spectral, DFT, NLO, magnetic and molecular docking studies,* Journal of Molecular Structure, 1264, 133190, 2022.

[30] Al Sabahi, A., Al Busafi, S.N., Suliman, F.O., and Al Kindy, S.M., *Photophysical and theoretical studies on the solvatochromic effects and dipole moments evaluation of substituted 1-phenyl-3-naphthyl-5- (4-ethyl benzoate)-2-pyrazoline,* Journal of Molecular Liquids, 307, 112967, 2020.

[31] Arivazhagan, M. and Senthil kumar, J., *Molecular structure, vibrational spectral assignments, HOMO–LUMO, MESP, Mulliken analysis and thermodynamic properties of 2,6-xylenol and 2,5-dimethyl cyclohexanol based on DFT calculation,* Spectrochimica Acta Part A: Molecular and Biomolecular Spectroscopy, 137, 490-502, 2015.

[32] Priya, M.K., Revathi, B.K., Renuka, V., Sathya, S., and Asirvatham, P.S., *Molecular Structure, Spectroscopic (FT-IR, FT-Raman, 13C and 1H NMR) Analysis, HOMO-LUMO Energies, Mulliken, MEP and Thermal Properties of New Chalcone Derivative by DFT Calculation,* Materials Today: Proceedings, 8, 37-46, 2019.

[33] Akman, M., Ata, A.C., Yildiko, U., and Çakmak, İ., *Molecular structure, frontier molecular orbitals, NBO, MESP and thermodynamic properties of 5,12-dibromo perylene with DFT calculation methods,* International Journal of Chemistry and Technology, 4 (1), 49-59, 2020.

[34] Boshaala, A., Said, M.A., Assirey, E.A., Alborki, Z.S., AlObaid, A.A., Zarrouk, A., and Warad, I., *Crystal structure, MEP/DFT/XRD, thione ⇔ thiol tautomerization, thermal, docking, and optical/TD-DFT studies of (E)-methyl 2-(1-phenylethylidene)-hydrazinecarbodithioate ligand,* Journal of Molecular Structure, 1238, 130461, 2021.

[35] Murugan, P., Jeyavijayan, S., Ramuthai, M., and Narmadha, R.B., *Structural, Spectroscopic, NBO and Molecular Docking Analysis of 5-Nitrobenzimidazole – A DFT Approach,* Polycyclic Aromatic Compounds, 2022. DOI: https://doi.org/10.1080/10406638.2022.2056621

Adıyaman University Journal of Science
https://dergipark.org.tr/en/pub/adyujsci
DergiPark AKADEMİK
ISSN 2147-1630
e-ISSN 2146-586X

Calculation of Dynamic Properties of Drug-Added Aqueous Solutions with T_1 and T_2 Relaxation Times

Sibel KORUNUR*

Munzur University, Tunceli Vocational School, Electric and Energy Department, Tunceli, Türkiye
skorunur@munzur.edu.tr, ORCID: 0000-0003-0682-2400

Received: 28.11.2022 **Accepted:** 07.12.2022 **Published:** 30.12.2022

Abstract

The development of modern spectroscopic methods has facilitated and accelerated structure analysis. The NMR method is the most popular way to perform structural analysis of compounds with very complex structures. D_2O is a solvent that is frequently used in NMR analysis of both chemical molecules and many biological molecules such as drugs, proteins, and enzymes. In this paper, the study of residual water in proton drug-added protein solutions was carried out via NMR relaxation. The spin-lattice (T_1) and the spin-spin relaxation (T_2) times of residual water in drug-added protein solutions were studied depending on temperature by Avance Bruker 400 MHz ^{1}H-NMR Spectrometer, and activation energies (E_a) and rotational correlation times (τ_0 and τ_c) have been determined for T_1 and T_2 relaxation times.

Keywords: D_2O; Proton NMR; Relaxation times; Activation energy; Flurouacil.

İlaç Katkılı Sulu Çözeltilerin Dinamik Özelliklerinin T_1 ve T_2 Rölaksasyon Zamanları ile Hesaplanması

Öz

* Corresponding Author DOI: 10.37094/adyujsci.1200682

Modern spektroskopik yöntemlerin gelişimi, yapı analizini kolaylaştırmış ve hızlandırmıştır. NMR yöntemi, çok karmaşık yapılara sahip bileşiklerin yapısal analizini gerçekleştirmenin en popüler yoludur. D_2O, hem kimyasal moleküllerin hem de ilaçlar, proteinler, enzimler gibi birçok biyolojik molekülün NMR analizinde sıklıkla kullanılan bir çözücüdür. Bu çalışmada, ilaç katkılı protein çözeltilerinde residual su çalışması, proton NMR rölaksasyonu yoluyla gerçekleştirilmiştir. Avance Bruker 400 MHz ^{1}H-NMR Spektrometresi ile ilaç katkılı protein çözeltilerinde residual suyun spin-örgü (T_1) ve spin-spin rölaksasyon (T_2) süreleri sıcaklığa bağlı olarak ölçülmüş, T_1 ve T_2 rölaksasyon süreleri için aktivasyon enerjileri (E_a) ile τ_0 ve τ_c dönme korelasyon zamanları belirlenmiştir.

***Anahtar Kelimeler*:** D_2O; Proton NMR; Rölaksasyon zamanları; Aktivasyon enerjisi; Flurouacil.

1. Introduction

The contribution of magnetic resonance to science and technology is one of the greatest discoveries of the century in the field of spectroscopy. Nuclear magnetic resonance technique (NMR) is a spectroscopic technique commonly used by researchers in many different fields to reveal the structures of chemicals, especially organic molecules, in liquid or solid form. After successful experiments by Purcell, Pound, Torrey at Harvard and Bloch, Hansen, Packard at Stanford in 1946, the field of application of magnetic resonance developed rapidly. The theoretical and technical development of this phenomenon, whose basic formulation is summarized by Abragam [1], is still ongoing.

The application of NMR relaxation times to understand the moving mechanisms of molecules in aqueous solutions has become an indispensable and frequently used method. The relaxation rates of water molecules are influenced by the local magnetic interactions between the nuclei of the water and the rate of molecular motion and proton exchange [2]. There are two mechanisms for the relaxation rates of water molecules: spin-lattice and spin-spin.

The relaxation time T_1, which defines the return to equilibrium in the magnetic field direction, is also known as spin-lattice relaxation or longitudinal relaxation and can be measured from the magnetization creation along the applied static magnetic field. T_1 relaxation can also be measured by the decay of a signal that creates a rotating magnetic field around the resonance frequency perpendicular to the static magnetic field. T_1 longitudinal or spin-lattice relaxation may be more sensitive to intramolecular mobility on flexible substrates, as it is associated with general rotational of the molecule in solution. The standard method for measuring T_1 is known as reversal recovery.

The relaxation time T_2, which describes the decay of induced magnetization perpendicular to the applied magnetic field, is also called spin-spin relaxation or transverse relaxation. It is known that the observed spectral line width is associated with the T_2 relaxation time, that is, spin-spin relaxation, and is also affected by magnetic inhomogeneity. The relaxation time T_2 is used to determine the decay rate of the magnetization in the xy plane. T_1 and T_2 relaxation times are long in rapidly rotating and small molecules such as free water. As in the case of proteins, as molecular motion slows down, T_2 relaxation gets shorter while T_1 increases. As a result, T_2 relaxation is faster than T_1 relaxation, and however, the T_1 relaxation time always takes a value longer than or equal to T_2 [3].

The rotational correlation time (τ_c), used in molecular-scale viscosity measurements and protein characterization, refers to the average time it takes for a molecule to rotate one radian, and its value in solutions is on the order of picoseconds and is known to be 1.7 ps for water [4]. The rotational correlation time can be determined for a molecule by T_1 and T_2 relaxation times and can be measured by methods such as microwave, dielectric, and nuclear magnetic resonance NMR spectroscopy [5, 6].

The most widely known mechanism is the magnetic dipole-dipole interaction. In this interaction, the mechanism between a nucleus and another nucleus or the magnetic moment of another environment such as the electron, atom, ion, or molecule is considered. Besides magnetic dipole-dipole interaction, there are different mechanisms for relaxation such as Chemical shift anisotropy (CSA) relaxation, Spin rotation (SR) relaxation mechanism, and quadrupole relaxation mechanism. In addition to these mechanisms, molecular reorientation or tumbling and the electrostatic interaction between nuclei can also lead to spin transitions and relaxation.

By analyzing aqueous solutions with NMR relaxation techniques, important data about rotational motion, molecular interactions and structure can be obtained. It was mentioned before that T_2 is smaller than T_1. The T_1 and T_2 curves overlap in the region called the extreme narrowing limit ($\omega^2 \tau_c^2 << 1$) which includes small rotational correlation times [7-14]. The expression “extreme narrowing” describes rapid molecular rotation on the order of picoseconds and simplifies the equations of rotational correlation [15].

Using proton resonance, the water dynamics has been extensively investigated for low frequencies by NMR relaxation methods, and it has been thought that the use of proton resonance is a major disadvantage [2-7]. However, several biological molecules, especially

proteins and enzymes have been studied in D_2O to decrease the water in the environment and increase the effectiveness of the bound water on the protein [16-25].

D_2O is one of the most important and widely preferred solvents used in NMR studies of chemical molecules. The standard water (H_2O) ratio in this solvent, which is tried to be purified but cannot be 100% pure, contains some residual hydrogen, which is called residual water.

The hydrogen-deuterium exchange reaction (H-D or H/D Exchange) between residual water molecules and D_2O is written as follows.

$$H_2O + D_2O \Leftrightarrow 2HDO$$

This expression indicates that the residual water in D_2O is in the HDO form. Therefore, it is very important to investigate HDO relaxation for information about the relaxation mechanism in drug-protein containing solutions.

Since the residual water in D_2O is in the form of HDO, investigation of HDO relaxation is valuable for understanding the mechanism of relaxation in several protein solutions. [26-30]. To easily calculate the input parameters of the chemical change-exchange formula, the proton relaxation of residual water must be known.

In this paper, to investigate residual water in drug-added protein solutions, proton NMR relaxation methods have been used. T_1 and the T_2 relaxation times of residual water in drug-added protein solutions were studied depending on temperature by Avance Bruker 400 MHz 1H-NMR Spectrometer, and activation energies (E_a) and rotational correlation times (τ_0 and τ_c) have been calculated for T_1 and T_2 relaxation times.

2. Theoretical Background

T_1 relaxation time is also called spin-lattice or longitudinal relaxation time. This relaxation time is a measure of the energy transfer from the core spin system to neighboring molecules or lattices. This relaxation takes place in the z-axis and causes the Boltzmann equilibrium to change.

The states of a dipole pair in a water molecule exposed to the external field B_0 applied in the z direction are as follows.

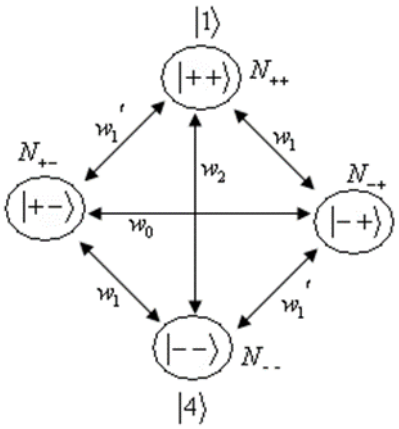

Figure 1: States of a dipole pair in a water molecule exposed to an external field in the z-direction

Figure 1 showing the eigenstates of I_z with respect to a spin pair are valid for all pairs in the example. Therefore, the population of each condition is shown above. If an RF field is applied to the water sample, there will be transitions between the above levels and saturation will occur. In other words, the magnetization in the z direction lies in the y direction. After the RF is cut off, the dipolar hamiltonian, which occurs due to the interaction of a couple among themselves, leads to transitions between states and eventually reaches the Boltzmann equilibrium. The dipolar hamiltonian leading to transitions between states can be written as;

$$H_D(t) = \left[I_z^{(1)}I_z^{(2)} - \tfrac{1}{4}(I_+^{(1)}I_-^{(2)} + I_-^{(1)}I_+^{(2)})\right]F_0(t) + [I_-^{(1)}I_z^{(2)} + I_z^{(1)}I_-^{(2)}]F_1(t) +$$
$$[I_+^{(1)}I_z^{(2)} + I_z^{(1)}I_+^{(2)}]F_{-1}(t) + [I_-^{(1)}I_-^{(2)}]F_2(t) + [I_+^{(1)}I_+^{(2)}]F_{-2}(t) \quad (1)$$

Here, the terms in square brackets denote the operators, while the terms abbreviated as F denote the time-dependent parts of the hamiltonian. It is known that the F terms expressing the time-dependent parts of the Hamiltonian are written as follows.

$$F_0(t) = \mathrm{d}\,(1 - 3cos^2\theta) \qquad d = \frac{\mu_0\ \gamma_1\gamma_2\hbar^2}{4\pi b^3}$$

$$F_1(t) = -\tfrac{3}{2}d\ \sin\theta\cos\theta\exp\ (i\phi) \qquad F_{-1}(t) = F_1(t)^* \quad (2)$$

$$F_2(t) = -\frac{3}{4}d\ \sin^2\theta\exp\ (\ 2i\phi) \qquad F_{-2}(t) = F_2(t)^*$$

To examine the transitions between the $|4\rangle$ and $|1\rangle$ states shown in Figure 1, it will be useful to start with Perturbation theory by considering the perturbation calculation between paired spins that Solomon's work in the past [13]. Accordingly, the transition probability between states $|4\rangle$ and $|1\rangle$can be written as,

$$a_{41}=\frac{1}{i\hbar}\int_0^t\langle 1|H'(t')|4\rangle\exp\left[i(\omega_1+\omega_2)t'\right]dt' \quad (3)$$

Continuing the quantum mechanical calculations and considering the $R_{22}(\tau)$ autocorrelation function w_{41} transition probability per unit time is written as,

$$w_2=\frac{1}{\hbar^2}\int_{-t}^{t}R_{22}(\tau)\,exp[-i(\omega_1+\omega_2)\tau]\,d\tau=\frac{2}{\hbar^2}\langle|F_2(t)|^2\rangle\frac{\tau_c}{1+(\omega_1+\omega_2)^2\tau_c^2}=\frac{1}{\hbar^2}J_2(\omega_1) \quad (4)$$

As can be seen from Eqn. (4), only F_2 is included in the process. That's why w_{41} is called w_2. If the transitions between other levels are calculated in a similar way, the following equations are obtained.

$$w_0=\frac{1}{8\,\hbar^2}\,\langle|F_0(t)|^2\rangle\,\frac{\tau_c}{1+(\omega_1-\omega_2)^2\,\tau_c^2} \quad (5)$$

$$w_1=\frac{1}{2\,\hbar^2}\,\langle|F_1(t)|^2\rangle\,\frac{\tau_c}{1+\omega_1{}^2\,\tau_c^2} \quad (6)$$

$$w_1{}'=\frac{1}{2\,\hbar^2}\,\langle|F_1(t)|^2\rangle\,\frac{\tau_c}{1+\omega_2{}^2\,\tau_c^2} \quad (7)$$

The importance of dipolar interaction in NMR relaxation has been proven in the past work of Bloembergen, Purcell and Pound [14]. By substituting these equations in $\frac{1}{T_1}=2\,(w_1+w_2)$ and $\frac{1}{T_1}=w_0+2\,(w_1+w_2)$ written for the relaxation time T_1 in similar spin and different spin states, $\frac{1}{T_1}$ relaxation rates are obtained for similar spin and different spin states, respectively.

$$\frac{1}{T_1}=\frac{6}{20}\left(\frac{\mu_0}{4\pi}\right)^2\frac{\gamma^4\,\hbar^2}{b^6}\left(\frac{\tau_c}{1+\omega^2\,\tau_c^2}+\frac{4\tau_c}{1+4\,\omega^2\,\tau_c^2}\right) \quad (8)$$

$$\frac{1}{T_1}=\frac{1}{10}\left(\frac{\mu_0}{4\pi}\right)^2\frac{\gamma_1^2\,\gamma_2^2\,\hbar^2}{b^6}\left(\frac{\tau_c}{1+(\omega_1-\omega_2)^2\,\tau_c^2}+\frac{3\,\tau_c}{1+\omega_2{}^2\,\tau_c^2}+\frac{6\tau_c}{1+(\omega_1+\omega_2)^2\,\tau_c^2}\right) \quad (9)$$

It is known that after an RF pulse is applied to a system, the magnetization lies in the y direction and this magnetization goes to zero by dephasing, and the process of this magnetization to zero is equal to the T_2 time. Therefore, T_2 is also called dephasing time. The same process followed to calculate the T_1 time in a dipole pair sample in a water molecule under the external field effect can also be followed to calculate the T_2 time. For similar spins and different spins, the equations for T_2 are written as follows, respectively.

$$\frac{1}{T_2}=2\,(u_1+u_2) \quad (10)$$

$$\frac{1}{T_2} = (u_0 + 2\ u_1 + u_2) \tag{11}$$

Considering Fig.1, the diagram showing all states and the transition probabilities between these states, by using the transition probabilities u_0, u_1 and $u_2$between states calculated for similar spins and different spins; $\frac{1}{T_2}$ relaxation rate for the two different situations are respectively written as follows.

$$\frac{1}{T_2} = \ 2\ (u_1 + u_2)\ = \frac{3}{20}\left(\frac{\mu_0}{4\pi}\right)^2 \frac{\gamma^4\ \hbar^2}{b^6}\left(\ 3\ \tau_c\ + \frac{5\ \tau_c}{1+\omega^2\ \tau_c^2}\ + \frac{2\tau_c}{1+4\ \omega^2\ \tau_c^2}\right) \tag{12}$$

$$\frac{1}{T_2} = u_0 + 2\ u_1 + u_2 = \frac{1}{20}\left(\frac{\mu_0}{4\pi}\right)^2 \frac{\gamma_1^2\ \gamma_2^2\ \hbar^2}{b^6}\left(\begin{matrix}4\ \tau_c + \frac{\tau_c}{1+(\omega_1-\omega_2)^2\ \tau_c^2}\ + \frac{3\ \tau_c}{1+{\omega_1}^2\ \tau_c^2} \\ + \frac{6\ \tau_c}{1+{\omega_2}^2\ \tau_c^2} + \frac{6\tau_c}{1+(\omega_1+\omega_2)^2\ \tau_c^2}\end{matrix}\right) \tag{13}$$

Considering Eqns. (9) and (13), T_1 and T_2 relaxation rates because of dipolar interaction between hydrogen (H) and deuterium (D) were determined by Solomon-Bloembergen.

$$\frac{1}{T_1} = \frac{1}{10}\left(\frac{\mu_0}{4\pi}\right)^2 \frac{\gamma_D^2\ \gamma_H^2\ \hbar^2}{b^6}\left(\frac{\tau_c}{1+(\omega_D-\omega_H)^2\ \tau_c^2}\ + \frac{3\ \tau_c}{1+{\omega_D}^2\ \tau_c^2}\ + \frac{6\tau_c}{1+(\omega_D+\omega_H)^2\ \tau_c^2}\right) \tag{14}$$

$$\frac{1}{T_2} = \frac{1}{20}\left(\frac{\mu_0}{4\pi}\right)^2 \frac{\gamma_D^2\ \gamma_H^2\ \hbar^2}{b^6}\left(\begin{matrix}4\ \tau_c + \frac{\tau_c}{1+(\omega_D-\omega_H)^2\ \tau_c^2}\ + \frac{3\ \tau_c}{1+{\omega_D}^2\ \tau_c^2}\ + \frac{6\ \tau_c}{1+{\omega_H}^2\ \tau_c^2} \\ + \frac{6\tau_c}{1+(\omega_D+\omega_H)^2\ \tau_c^2}\end{matrix}\right) \tag{15}$$

In Eqns. (14) and (15), γ_D and γ_H are the deuteron and proton gyromagnetic ratio, respectively, b is the distance between the H and D spins, $\hbar$ is Planck's constant divided by 2π, τ_c is rotational correlation time, ω_H and ω_D are Larmor frequencies of proton and deuteron, respectively and μ is the magnetic permeability.

The rotational correlation time τ_c in Eqns. (14) and (15) is given by the Arrhenius equation as follows.

$$\tau_c = \tau_0\ exp(E_a/RT) \tag{16}$$

Here, E_a is the activation energy for molecular motions, R is the gas constant, and T is the temperature, τ_0 and τ_c are rotational correlation time constant and rotational correlation time, respectively.

It is known that the T_1 and T_2 times in Eqns. (14) and (15) are equal to each other in the case of extreme narrowing, expressed as $\omega^2 \tau_c^2 << 1$. In this case, Eqns. (14) and (15) turn into Eqn. (17).

$$\frac{1}{T_1} = \frac{1}{T_2} = \left(\frac{\mu_0}{4\pi}\right)^2 \left(\frac{\gamma_D^2 \gamma_H^2 \hbar^2}{b^6}\right) \tau_c \tag{17}$$

Using Eqns. (16) and (17), Eqn. (18) is obtained.

$$\frac{1}{T_1} = \frac{1}{T_2} = \left(\frac{\mu_0}{4\pi}\right)^2 \left(\frac{\gamma_D^2 \gamma_H^2 \hbar^2 \tau_0}{b^6}\right) exp(E_a/RT) \tag{18}$$

Here, assuming that $A = \left(\frac{\mu_0}{4\pi}\right)^2 \left(\frac{\gamma_D^2 \gamma_H^2 \hbar^2 \tau_0}{b^6}\right)$ the Eqn. (18) is written as follows.

$$\frac{1}{T_1} = \frac{1}{T_2} = A \ exp(E_a/RT) \tag{19}$$

$$ln\, T_1 = ln\, T_2 = ln\frac{1}{A} - \left(\frac{E_a}{R}\right)\left(\frac{1}{T}\right) \tag{20}$$

According to Eqn. (20), it is seen that there is a linear dependence between $ln\, T_1$ and $\left(\frac{1}{T}\right)$ and it also has a slope with a negative sign.

3. Experimental

The most commonly used deuterated solvent in NMR experiments is D_2O. All chemicals used in this study were obtained from the Sigma-Aldrich catalog, together with the high purity D_2O (99.9%) used as the solvent in this study.

Albumin, the most abundant protein in human serum, is a monomeric structure with a molecular weight of 66 kD, consisting of three helical segments, each divided into two subregions, and has many ligand-binding abilities [31]. The most important factor affecting the distribution of intravenous drugs is the binding affinity of that drug to albumin in human blood serum, and therefore, the interaction between the drug and albumin must be optimal for the drug to reach the target organ and provide an effective treatment.

5-Fluorouracil, which is the active ingredient of the drug named Biosyn, is a fluorinated pyrimidine derivative and is a chemotherapy drug belonging to the group of antimetabolites.

Spin-Lattice Relaxation Times (T_1) and Spin-Spin Relaxation Times (T_2) were measured with a 400 MHz Bruker NMR Spectrometer. Measurements of Spin-Lattice Relaxation Times were performed with the Inversion Recovery technique using (180-τ-90) pulse steps.

Measurements of Spin-Spin Relaxation Times were carried out using CPMG (Carr-Purcell-Meiboom-Gill) technique with (90-τ-180-τ) pulse steps. After the solutions were prepared, they were placed in 5 mm NMR tubes to make NMR measurements. The delay times τ required for each measurement were chosen to match each peak observed in the spectrum. Temperature dependence measurements were made at 25, 30, 35, 40, 45 ^{0}C values by increasing the sample temperature by 5 ^{0}C.

4. Results and Discussion

The ^{1}H- NMR spectrum of FU solution for relaxation time measurements is given in Fig. 2. As seen in Fig. 2, the peak that appears as a single narrow line is the HDO peak at 4.7044 ppm and a doublet peak at 7.5978 ppm and 7.5845 ppm. The peak of the CH molecule seen in the chemical formula of FU was split in half due to the neighboring HN molecule and formed a doublet. The distance between the peaks of this doublet gives the coupling constant (j).

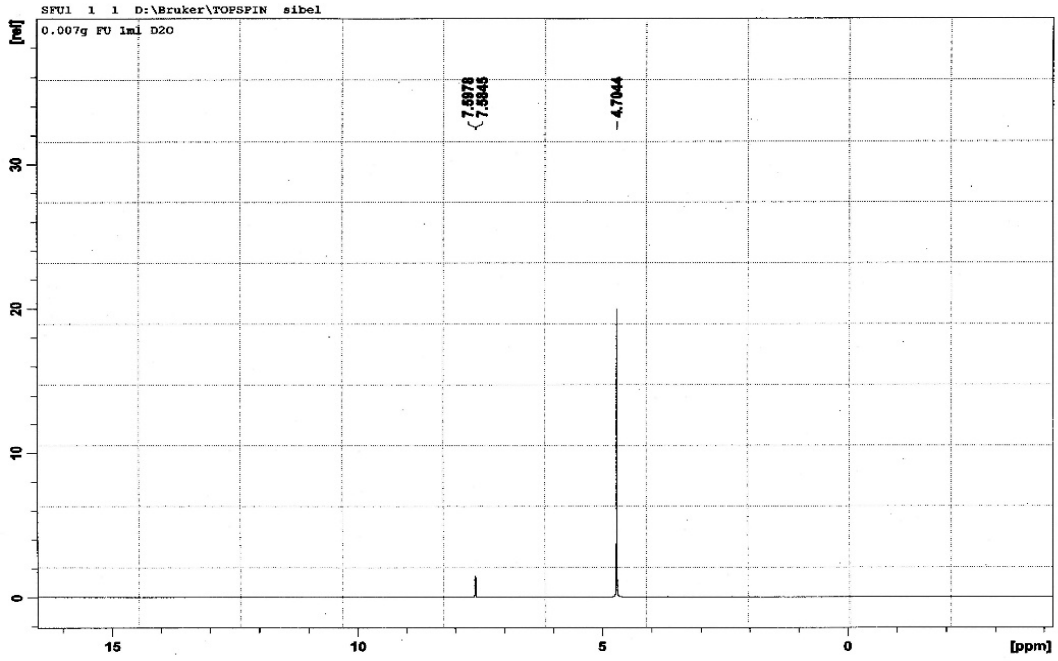

Figure 2: ^{1}H- NMR spectrum of FU in D_2O

T_1 and T_2 relaxation times graphs are shown in Fig. 3 a and b, respectively.

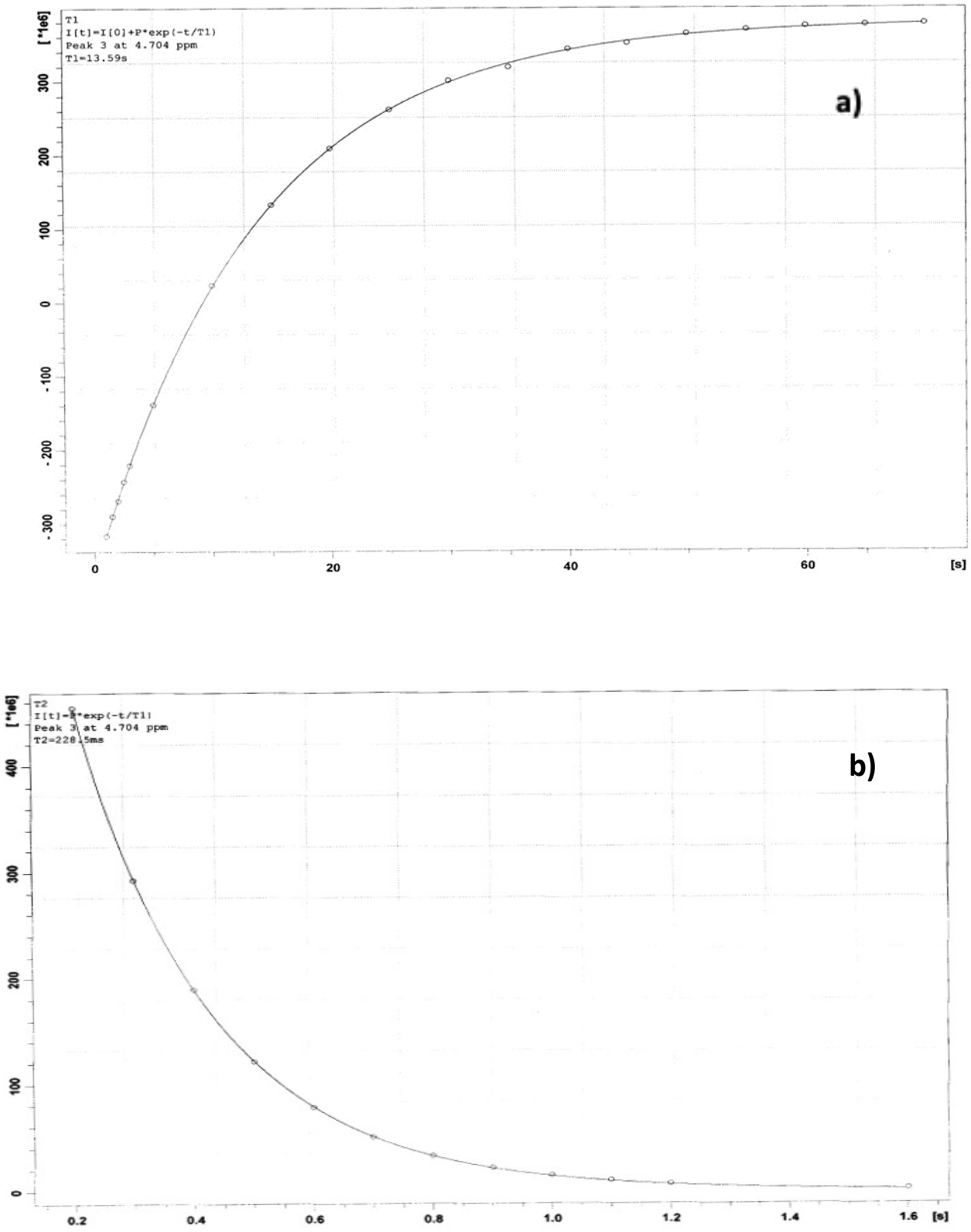

Figure 3: a) Inversion Recovery Spin-Lattice Relaxation Times (T_1), **b)** Spin Echo Spin-Spin Relaxation Times (T_2)

The measured T_1 and T_2 relaxation time values of HDO and doublet peaks in the spectrum shown in Fig. 2 for different temperatures are given in Table 1 and Table 2, respectively.

Table 1: T_1 and T_2 relaxation times of HDO peak in Fig. 2

T (K)	T_1 (s)	T_2 (ms)
298	7.815	118.6
303	7.991	111.0
308	8.486	109.8
313	8.885	108.6
318	8.994	107.3

Table 2: T_1 and T_2 relaxation times of Doublet peak in Fig. 2

T (K)	T_1 (s)	T_2 (ms)
298	1.728	114.2
303	2.063	147.4
308	2.297	193.4
313	2.573	261.4
318	2.591	340.1

As seen in Table 1 and Table 2, T_1 and T_2 values of Doublet peak and T_1 values of HDO peak increase depending on temperature, but T_2 values of HDO peak decrease depending on temperature. In addition, the case of $T_1 >> T_2$ in both tables draws attention. This clearly shows that the dynamics of the water molecule are complex and that intramolecular movements are also possible in the system [8, 12].

Temperature dependence graphs of ln T_1 and ln T_2 values for both peaks in the spectrum, shown in Fig. 4 and Fig. 5, respectively, were created to find the activation energies and rotational correlation times.

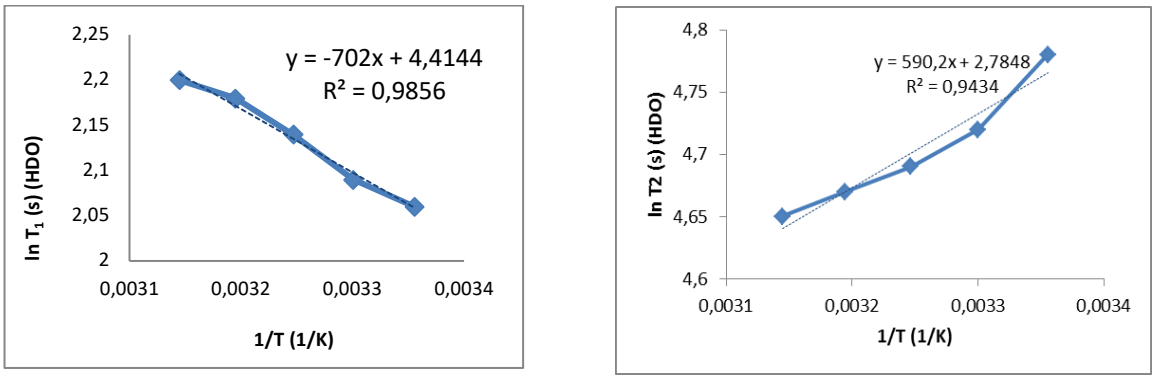

Figure 4: (**a**) ln T_1 and (**b**) ln T_2 vs. reciprocal temperature (1/T) for HDO peak measured at 400 MHz

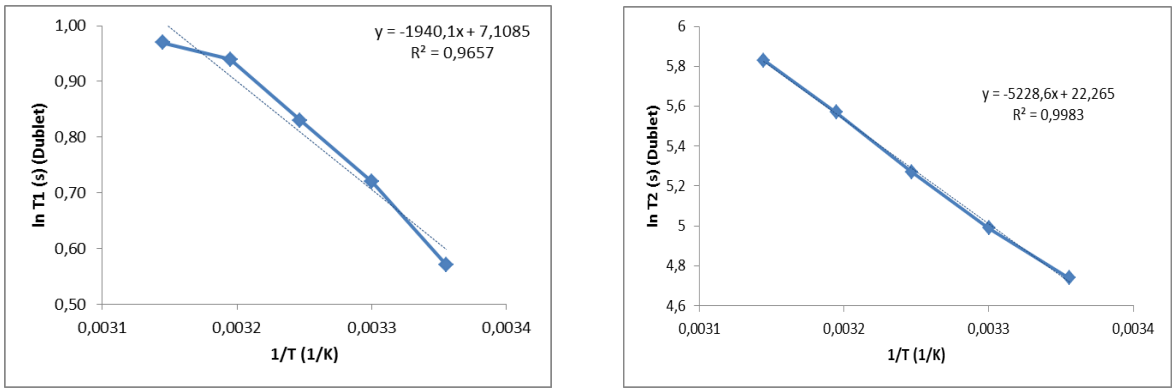

Figure 5: (**a**) ln T_1 and (**b**) ln T_2 vs. reciprocal temperature (1/T) for Doublet peak measured at 400 MHz

For the Doublet peak, both $\ln T_1$ and $\ln T_2$ decreased linearly with increasing 1/T. For the HDO peak, while $\ln T_1$ decreased linearly with increasing 1/T, $\ln T_2$ increased linearly. Therefore, in aqueous solutions, the T_1 and T_2 times are considered to be under high mobility. According to Eqn. (17), T_1 and T_2 relaxation times are inversely proportional to the rotational correlation time for molecular motion; According to Eqn. (19), it seems that T_1 and T_2 decrease as the temperature decreases.

In this case, the minimum T_1 relaxation appears to occur on the high-temperature side and τ_c provides the value $\omega\,\tau_c \ll 1$ of the correlation time characterizing the reorientation of the core. This approach should be applicable to some water molecules, or at least part of their dynamics. [11, 32, 37]. The intermolecular proton exchange affects the correlation time, and the spin-spin coupling causes the magnitude difference between T_1 and T_2 [32-36].

For the HDO peak, starting from the graph of T_1 and T_2 versus 1/T shown in Fig. 4, the following equations can be written, respectively.

$$\ln T_1 = -702\ (1/T) + 4.4144 \qquad R^2 = 0.9856 \qquad (21)$$

$$\ln T_2 = 590.2\ (1/T) + 2.7848 \qquad R^2 = 0.9434 \qquad (22)$$

Similarly, for the doublet peak, starting from the graph of of T_1 and T_2 versus 1/T shown in Fig. 5, the following equations can be written, respectively.

$$\ln T_1 = -1940.1\ (1/T) + 7.1085 \qquad R^2 = 0.9657 \tag{23}$$

$$\ln T_2 = -5228.6\ (1/T) + 22.265 \qquad R^2 = 0.9983 \tag{24}$$

According to Eqn. (20), activation energies (E_a) were calculated from the slopes of the curves in Fig. 4 and Fig. 5. Eqns. (16) and (17) were used to calculate the rotational correlation times (τ_0, τ_c). Ea and τ_0, τ_c values for HDO peak and Doublet peak are given in Table 3 and Table 4, respectively, at 25 ºC.

Table 3: E_a, and τ_0, τ_c values of HDO peak at 25 ºC

	T_1	T_2
E_a (kcal.mol^{-1})	1.39	1.17
τ_0 (s)	1.88×10^{-11}	1.038×10^{-9}
τ_c (s)	11.38×10^{-11}	7.49×10^{-9}

Table 4: E_a, and τ_0, τ_c values of Doublet peak at 25 ºC

	T_1	T_2
E_a (kcal.mol^{-1})	3.85	10.39
τ_0 (s)	8.697×10^{-10}	1.864×10^{-16}
τ_c (s)	5.15×10^{-10}	7.78×10^{-9}

5. Conclusion

For the HDO peak, the rotational correlation time and activation energy values were found as 1.14 ps, 1.39 kcal.mol^{-1} for T_1 and 7.5 ns, 1.17 kcal.mol^{-1} for T_2, respectively. For the Doublet peak, the rotational correlation time and activation energy values were found as 0.05 ps 3.85 kcal.mol^{-1} for T_1 and 7.8 ns, 10.39 kcal.mol^{-1} for T_2, respectively. As a result of the very fast molecular motion, the small τ_c value for T_1 was calculated and this result confirms the extreme narrowing condition mentioned above. However, the value of τ_c calculated for T_2 conforms to condition $\omega\tau_c > 1$. The reason for this situation can be considered as the effect of intermolecular proton exchange on shortening the correlation time and the spin-spin coupling that causes the difference in magnitude between T_1 and T_2. The calculated activation energies are compatible with the rotational activation energy of water given in the literature and are associated with the isotropic rotational motion of unbound water molecules. Consequently, the effective process for the spin-spin relaxation mechanism in an aqueous solution may be

chemical exchange and dipolar coupling between protons and deuterons, while spin-lattice relaxation may be caused by the molecular tumbling reorientation process. This indicates that two different molecular species exist in aqueous solutions with respect to reorientation dynamics.

References

[1] Abragam, A., *The Principles of Nuclear Magnetism*. Oxford: Clarendon Press, 32 ed., 599p. 1961.

[2] Mathur, R., Vré, D., *The NMR studies of water in biological systems*, Progress in Biophysics and Molecular Biology, 35, 103-134, 1980.

[3] Traficante, D.D., *Relaxation. Can T_2 be longer than T_1?*, Concepts in Magnetic Resonance, 3, 171-177, 1991.

[4] Lankhorst, D., Schriever, J., Leyte, J.C., *Determination of the Rotational Correlation Time of Water by Proton NMR Relaxation in $H_2{}^{17}O$ and Some Related Results*, Berichte der Bunsengesellschaft für physikalische Chemie, 86(3), 215–221, 1982.

[5] Bulla, I., Törmälä, P., Lindberg, J.J., *Spin Probe Studies on the Dynamic Structure of Dimethyl Sulfoxide-Water Mixtures*, Acta Chemica Scandinavica A, 29, 89–92, 1975.

[6] Reich, H.J. (2017). 8.1 Relaxation in NMR Spectroscopy

[7] Marchi, M., Sterpone, F., Ceccarelli, M., *Water Rotational Relaxation and Diffusion in Hydrated Lysozyme*, Journal of the American Chemical Society, 124(23), 6787–6791, 2002.

[8] Fung, B.M., Mcgaughy, T.W., *Study of Spin-Lattice and Spin-Spin Relaxation Times of ^1H, ^2H, and ^{17}O in Muscle Water*, Biophysical Journal, 28, 293- 304, 1979.

[9] Kiihne, S., Bryant, R.G., *Protein-bound water molecule counting by resolution of (1)H spin-lattice relaxation mechanisms*, Biophysical Journal, 78(4), 2163-2169, 2000.

[10] Kivelson, D., *Rotational correlation times for small molecules in liquids*, In: Dorfmüller, T., Pecora, R. Eds., *Rotational Dynamics of Small and Macromolecules. Lecture Notes in Physics*, 293. Springer, Berlin, Heidelberg, 1987.

[11] Cope, F.W., *Nuclear Magnetic Resonance Evidence using D_2O for Structured Water in Muscle and Brain*, Biophysical Journal, 9, 303-319, 1969.

[12] Woessner, D.E., Pettegrew, J.W. eds., *Relaxation Theory with Applications to Biological Studies*. In: NMR: *Principles and Applications to Biomedical Research*, Springer, New York, 618p. 1990.

[13] Solomon, I., *Relaxation Processes in a System of Two Spins*, Physical Review, 99(2), 559-565, 1955.

[14] Bloembergen, N., Purcell, E.M., Pound, R.V., *Relaxation Effects in Nuclear Magnetic Resonance Absorption*, Physical Review, 73(7), 679-712, 1948.

[15] Güven, M., Köylü, M.Z., *Dynamic Investigation of β-Hydroxy Amide Derivatives by 400 MHz ^1H-NMR*, International Journal of Science and Research, 7(10), 1130-1133, 2018.

[16] Bryant, R.G., Korb, J.P., *Nuclear magnetic resonance and spin relaxation in biological systems*, Magnetic Resonance Imaging, 23(2), 167-173, 2005.

[17] Van-Quynh, A., Willson, S., Bryant R.G., *Protein Reorientation and Bound Water Molecules Measured by ^{1}H Magnetic Spin-Lattice Relaxation*, Biophysical Journal, 84(1), 558-563, 2003.

[18] Halle, B., *Protein hydration dynamics in solution: a critical survey*, Philosophical Transactions of the Royal Society B, 359 (81448), 1207-1224, 2004.

[19] Venu, K., Denisov, V.P., Halle, B., *Water ^{1}H Magnetic Relaxation Dispersion in Protein Solutions. A Quantitative Assessment of Internal Hydration, Proton Exchange, and Cross-Relaxation*, Journal of the American Chemical Society, 119(13), 3122–3134, 1997.

[20] Tadimalla, S., Momot, K.I., *Effect of partial H_2O-D_2O replacement on the anisotropy of transverse proton spin relaxation in bovine articular cartilage*, PLoS One, 9(12), 2014.

[21] Gultekin, D.H., Gore, J.C., *Temperature dependence of nuclear magnetization and relaxation*, Journal of Magnetic Resonance, 172(1), 133- 141, 2005.

[22] Singer, P.M., Asthagiri, D., Chapman, W.G., Hirasaki, G.J., *Molecular dynamics simulations of NMR relaxation and diffusion of bulk hydrocarbons and water*, Journal of Magnetic Resonance, 277, 15-24, 2017.

[23] Zhang, L., Bouguet-Bonnet, S., Buck, M., *Combining NMR and molecular dynamics studies for insights into the allostery of small GTPase-protein interactions*, Methods in Molecular Biology, 796, 235-59, 2012.

[24] Korb, J.P., Bryant, R.G., *Magnetic Field Dependence of Proton Spin-Lattice Relaxation Times*, Magnetic Resonance in Medicine, 48, 21–26, 2002.

[25] Noskov, S.Y., Kiselev, M., Kolker, A.M., *Role of bound water in protein-ligand association processes*, Biophysics, 55(1), 29-34, 2010.

[26] Rezus, Y.L.A., Bakker, H.J., *On the orientational relaxation of HDO in liquid water*, The Journal of Chemical Physics, 123, 114502, 2005.

[27] Lawrence, C.P., Skinner, J.L., *Vibrational spectroscopy of HOD in liquid D_2O. III. Spectral diffusion, and hydrogen-bonding and rotational Dynamics*, The Journal of Chemical Physics, 118, 264, 2003.

[28] Duplan, J.C., Mahi, L., Brunet, J.L., *NMR determination of the equilibrium constant for the liquid H_2O–D_2O mixture*, Chemical Physics Letters, 413, 400-403, 2005.

[29] Thuduppathy, G.R., Hill, R.B., *Applications of NMR spin relaxation methods for measuring biological motions*, Methods in Enzymology, 384, 243-64, 2004.

[30] Gallot, G., Lascoux, N., Gale, G.M., Leicknam, J-Cl., Bratos, S., Pommeret, S., *Non-monotonic decay of transient infrared absorption in dilute HDO/D_2O solutions*, Chemical Physics Letters, 341, 535-539, 2001.

[31] Korunur, S., Zengin, B., Yilmaz, A., *Investigation of relaxation times in 5-fluorouracil and human serum albumin mixtures*, Turkish Journal of Biochemistry, 44(4), 524-529, 2019.

[32] Reuhl, M., Vogel, M., *Temperature-dependent dynamics at protein-solvent interfaces*, The Journal of Chemical Physics, 157(7), 074705, 2022.

[33] Halle, B., Denisov, V.P., *A new view of water dynamics in immobilized proteins,* Biophysical Journal, 69(1), 242-9, 1995.

[34] Goddard, Y.A., Korb, J.P., Bryant R.G., *Water molecule contributions to proton spin-lattice relaxation in rotationally immobilized proteins*, Journal of Magnetic Resonance, 199(1), 68-74, 2009.

[35] Charlier, C., Cousin, S.F., Ferrage, F., *Protein dynamics from nuclear magnetic relaxation, Chemical Society Reviews*, Royal Society of Chemistry, 45(9), 2410-2422, 2016.

[36] Mallamace, F., Corsaro, C., Mallamace, D., Baglioni, P., Stanley, H.E., Chen S.H., *A possible role of water in the protein folding process*, The Journal of Physical Chemistry B, 115(48), 14280-94, 2011.

[37] Köylü, M.Z., *Temperature Dependences of T_1 and T_2 of Residual Water in D_2O Determined at 400 MHz ^{1}H-NMR*, International Journal of Science and Research, 7(10), 40-43, 2018.

Adıyaman University Journal of Science
https://dergipark.org.tr/en/pub/adyujsci
DergiPark AKADEMİK
ISSN 2147-1630
e-ISSN 2146-586X

Electrochemical Properties of Low Bi Doped $La_{0.60}Dy_{0.10}Sr_{0.30}Mn_{(1-x)}Bi_xO_3$ Perovskite Materials

Mustafa Zeki KURT*

Cukurova University, Faculty of Art and Sciences, Department of Physics, 01330, Adana, Turkey
mzkurt@cu.edu.tr, ORCID: 0000-0002-3980-0692

Received: 28.11.2022 **Accepted:** 23.12.2022 **Published**: 30.12.2022

Abstract

Developing low-cost, high-durability and high-performance electrocatalytic materials are needed for hydrogen/oxygen evolution (HER/OER) and oxygen reduction reactions (ORR) which are crucial steps for regenerative fuel cells. Although Pt-based, RuO_2 and IrO_2 materials are widely used for these purposes, other alternative materials are required with desired properties. In this regard, we studied the electrochemical properties of lanthanum-based perovskites which were synthesized by sol-gel method. We investigated the substitution of 10% Dy and 30% Sr into the A site and a small amount of Bi (x: 0, 0.03 and 0.1) added into the B site of $La_{0.60}Dy_{0.10}Sr_{0.30}Mn_{(1-x)}Bi_xO_3$ perovskites on HER, OER and ORR in 1 M KOH alkaline media at room temperature. While undoped and 3% Bi doped samples exhibited poor HER activities, the effect of 10% Bi in the structure enhanced HER activities by lowering onset potential from -1.389 V to -1.036 V (vs. Ag/AgCl) and increasing specific current density from -13.3 mA cm^{-2} to -121.8 mA cm^{-2} at -1.4 V. Similarly, OER activity was also improved due to 10% Bi and onset potential and specific current density was found to be 0.758 V and 88.3 mA cm^{-2}, respectively. The large Tafel slopes indicate that the ORR mechanism is possible in the structure but at a slow rate. The addition of 10% Bi in the structure resulted in a very high resistance of 19.3 kΩ and it reduced to a desired value of 3.5 kΩ due to ion conducting paths developed in the catalysts.

* Corresponding Author DOI: 10.37094/adyujsci.1210860

***Keywords**:* La-based perovskite; Low Bi-doping; Electrochemistry; HER; OER; ORR.

Düşük Bi Katkılı Manyetikalorik $La_{0.60}Dy_{0.10}Sr_{0.30}Mn_{(1-x)}Bi_xO_3$ Perovskite Malzemelerin Elektrokimyasal Özellikleri

Öz

Rejeneratif yakıt hücreleri için çok önemli adımları olan hidrojen/oksijen evrimi (HER/OER) ve oksijen indirgeme reaksiyonlarının (ORR) düşük maliyetli, yüksek dayanıklılığa sahip ve yüksek performanslı elektrokatalitik malzemelerin geliştirilmesine ihtiyaç duyulmaktadır. Pt esaslı, RuO_2 ve IrO_2 malzemeler bu amaç için yaygın olarak kullanılsa da, istenilen özelliklerde alternatif malzemelere ihtiyaç duyulmaktadır. Bu bağlamda sol-jel yöntemi ile sentezlenen lantan bazlı perovskitlerin elektrokimyasal özelliklerini çalıştık. $La_{0.60}Dy_{0.10}Sr_{0.30}Mn_{(1-x)}Bi_xO_3$ perovskit yapısında, A bölgesine %10 Dy ve %30 Sr ve B bölgesine az miktarda Bi (x: 0, 0.03 ve 0.1) katkılanmasını oda sıcaklığında 1 M KOH alkali ortamda HER, OER ve ORR araştırdık. Katkılanmamış ve %3 Bi katkılanmış örnekler zayıf HER aktiviteleri sergilerken, yapıdaki %10 Bi'nin etkisi başlangıç potansiyelini -1,389 V'tan -1,036 V'a düşürerek (Ag/AgCl'ye karşı) ve spesifik akımı yoğunluğunu -13,3 mA cm^{-2}'den -121,8 mA cm^{-2}'ye -1,4 V'ta arttışını sağladı. Benzer şekilde OER aktivitesi de %10 Bi sayesinde iyileşmiş ve başlangıç potansiyeli ve özgül akım yoğunluğu sırasıyla 0,758 V ve 88,3 mA cm^{-2} olarak bulunmuştur. Büyük Tafel eğimleri, ORR mekanizmasının yapıda gerçekleşebildiğini ancak yavaş bir hızda olduğunu göstermektedir. Yapıya %10 Bi ilavesi 19,3 kΩ gibi çok yüksek bir direnç ile sonuçlanmış ve katalizörlerde oluşan iyon iletim yollarından dolayı 3,5 kΩ gibi istenen bir değere düşmüştür.

Anahtar Kelimeler: La bazlı perovskit; Düşük Bi-katkılama; Elektrokimya; HER; OER; ORR.

1. Introduction

Since the general structure of perovskites is identified as ABO_3 which has received significant attention in chemistry and physics and all $ABO_{3\pm\delta}$ structures similar to this structure are called perovskites [1, 2]. Here, A is a cation in the structure and has a larger ionic radius that makes 12 bonds with oxygen. On the other hand, the atom in the B position has a smaller radius and makes 6 bonds with oxygen. While A atom and oxygens form a cubic structure, B is located in the octahedral spaces in this closed cubic structure. For A and B elements to form the perovskite structure, the tolerance factor (*t*) must be between 0.75 and 1. The tolerance factor is calculated based on the radius of the ions of atoms [3]. The tolerance factor of many perovskite structures

studied in the literature ranges from 0.8 to 0.9. For the formation of perovskite structure, r_A>0.090 nm and r_B must be >0.051 nm [4]. The number of electrons of A and B ions in the structure must be balanced with oxygen which can be given with $A^{+1}B^{+5}O_3$, $A^{+2}B^{+4}O_3$ or $A^{+3}B^{+3}O_3$. With the second A and B elements added to the structure, the perovskite structure lose its ideal structure. In this case, orthorhombic, rhombohedral, tetragonal, monoclinic and triclinic structures can be formed.

Perovskites usually provide different physical properties, such as ferroelectric ($BaTiO_3$) ferromagnetic ($SrRuO_3$) superconductivity and thermal conductivity ($LaCoO_3$) behaviors which allows in many application areas in magnetic and electronic magnetocaloric effect [3, 5-8]. La-based materials were widely investigated to determine magnetocaloric properties and also studied doping these perovskites of A or B sites with Sr, Dy, Bi, Ba, K, Cu, Co, Ru, etc. [9-11]. For example, $La_{0.7}Sr_{0.3}MnO_3$ compound, which was synthesized by solid-state reaction method, increased the value of the magnetic entropy from 4.56 J/kg K for the undoped sample to 5.02 J/kg K with the substitution of Bi, but further increase the Bi ratio decreased the magnetic entropy [12]. Similarly, Dhahri et al. [13] studied the structural, magnetic and magnetocaloric properties of $La_{0.67-x}Bi_xBa_{0.33}MnO_3$ compound, which was synthesized by sol-gel method. They reported that all compounds exhibited a second-order magnetic phase transition and the transition temperature decreased with increasing Bi doping ratio.

Typically, noble metals (usually Pt, Pd-based) catalysts utilize for hydrogen evolution reaction (HER) and oxygen reduction reaction (ORR) while they exhibit rather poor activity for oxygen evolution reaction (OER) [14]. Besides, RuO_2 and IrO_2 have been also used for OER and ORR reactions [15]. However, efficient, low-cost, high-durability catalysts were required for mass production. One possible candidate for these purposes takes into account perovskite materials for OER and ORR processes with high-temperature durability and high conductivity [16]. For instance, bifunctional $La_{1-x}Sr_xFeO_{3-\delta}$ based perovskite has been used for cathodic and anodic material in high-temperature fuel cells and electrolyzes, respectively [17]. Here, reducing La and increasing Sr in the A site increases the oxygen vacancies which plays a crucial role for OER and also controlling the B site composition ratio in the structure enhances ORR.

Although the structural and magnetocaloric properties of $LaXMnO_3$-based perovskites have been widely investigated for different purposes, there is no detailed study of the catalytic properties of these perovskites. In this paper, we aimed to provide first principle investigations on the electrocatalytic properties of cost-effective $La_{0.60}Dy_{0.10}Sr_{0.30}Mn_{(1-x)}Bi_xO_3$ perovskites which are synthesized by sol-gel method. The electrocatalytic performance of $La_{0.60}Dy_{0.10}Sr_{0.30}Mn_{(1-}$

$_{x)}Bi_xO_3$ perovskites catalysts will be reported for HER, ORR and OER via cyclic voltammetry, linear sweep voltammetry, Tafel slope and impedance measurements.

2. Materials and Methods

2.1. Synthesis of Bi doped LDSM magnanites

$La_{0.60}Dy_{0.10}Sr_{0.30}Mn_{(1-x)}Bi_xO_3$ (x=0, 0.03 and 0.1) manganites with abbreviations as LDSM, LDSM+3% Bi and LDSM+10% Bi for x=0, 0.03 and 0.1, respectively, were produced by sol-gel method. Firstly, the appropriate amounts of the starting compounds were weighed and their aqueous solutions were prepared. These prepared solutions were mixed in a heated magnetic stirrer at 300. Appropriate agents, citric acid and ethylene glycol, were added to the mixture in appropriate amounts for the solution to gel. Then, the resulting mixture was heat treated at 550 for 1 h in order to be properly removed from the beaker. The material extracted from the beaker in powder form was then calcined 600 for 6 hours to remove the organic compounds from the structure. After the grinding and pressing processes, the material was sintered at 1200 for 24 h in air atmosphere.

2.2. Electrocatalysts preparation

The electrochemical measurements were performed using Gamry 1010E potentiostat/galvanostat three-electrode system in which carbon rode (5 mm dia, 0.1963 cm^2 area), platinum foil (66 mm^2) and Ag/AgCl in 3 M KCl solution were used as working, counter and references electrodes. We mixed 10 mg LDSM catalysts with 25 µl ethylene glycol (extra pure), 15 µl isopropanol and 5 µl 5% Nafion and sonicated for 30 min and then vortexed for 3 min. We loaded 1 mg catalysts ink on the working electrode and dried up the electrodes in a furnace at 55°C for 16 h prior to electrocatalytic performance.

3. Results

In order to investigate the electrocatalytic properties of Bi-doped $La_{0.60}Dy_{0.10}Sr_{0.30}Mn_{(1-x)}Bi_xO_3$ manganites, we first performed CV measurements. As seen in Figure 1, CV curves of LDSM (black), LDSM+3% Bi (red) and LDSM+10% Bi (blue) perovskites were recorded between -1 V and 1 V (vs. Ag/AgCl) with a scan rate of 50 mV s^{-1} in 1 M KOH alkaline media at room temperature. We can clearly distinguish the regions for HER, OER and ORR for all samples. Although, the substitution of 3% Bi (red) in LDSM structure did not affect the hydrogen gas evolution in the cathodic reduction region, increasing this ratio to 10% Bi (blue) enhanced HER activity with a clearly increased current density and lowered onset potential. In this region, we also observed modified ORR activity as a function of Bi substitution. Both the current density

and onset potential were improved by increasing the Bi ratio to 10% in the structure. On the other hand, the substitution of both 3% and 10% Bi samples provided better oxygen gas evolution in the anodic region in comparison with undoped-LDSM sample. These results indicate that 10% Bi-doped LDSM materials promise good electrocatalytic performance for HER and OER activities.

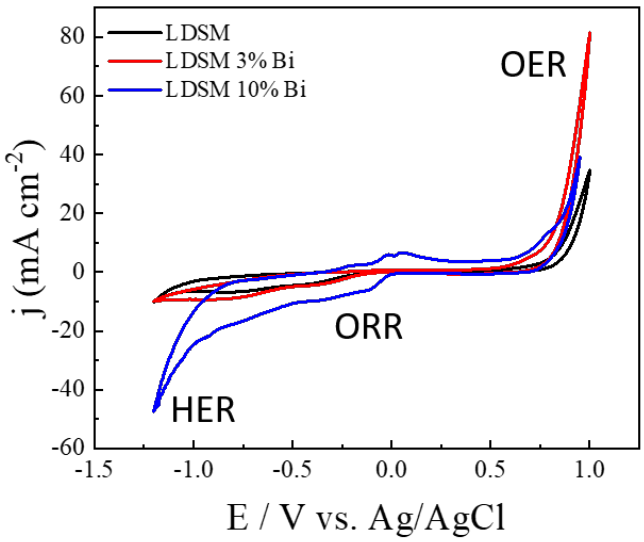

Figure 1: Cyclic voltammogram curves of LDSM (black), LDSM+3% Bi (red) and LDSM+10% Bi (blue) perovskites recorded between -1 V and 1 V (vs. Ag/AgCl) with a scan rate of 50 mV s^{-1} in 1 M KOH alkaline media at room temperature

We further performed a detailed investigation of current densities as a function of applied voltage for HER, ORR and OER activities for $La_{0.60}Dy_{0.10}Sr_{0.30}Mn_{(1-x)}Bi_xO_3$ manganites in 1 M KOH alkaline media at room temperature (see Figure 2(a-b)). The HER and OER performance of the manganites were illustrated in Figure 2(a) and the onset potential and specific current density were reported in Table 1. However, LDSM and LDSM+3% Bi catalysts exhibited highly poor HER activities of -1.389 V and -1.352 V, respectively. It can be clearly seen that the substitution of 10% Bi vastly improved HER performance with an onset potential of -1.036 V (vs. Ag/AgCl) and this value is close to HER activity of the commercially available Pt/C (20.7 mV vs. RHE) [18]. Moreover, the performance of ORR activity for LDSM and LDSM+3% Bi catalysts is highly low and required high activation voltage over -0.15 V. However, 10% Bi substitution lowered the potential by about 90 mV. The onset potential of LDSM, LDSM+3% Bi and LDSM+10% Bi were found to be 0.853 V, 0.769 V and 0.758 V, respectively. Here, 10% Bi substitution also improved the activity by about 100 mV. Similarly, the largest specific current density is measured as 88.3 mA cm^{-2} at 1 V for the substitution of the 10% Bi in LDSM structure. A similar result was reported in the literature as 80 mA cm^{-2} for $La_{0.6}Sr_{0.4}Fe_{0.8}Co_{0.2}O_3$/carbon composite [19].

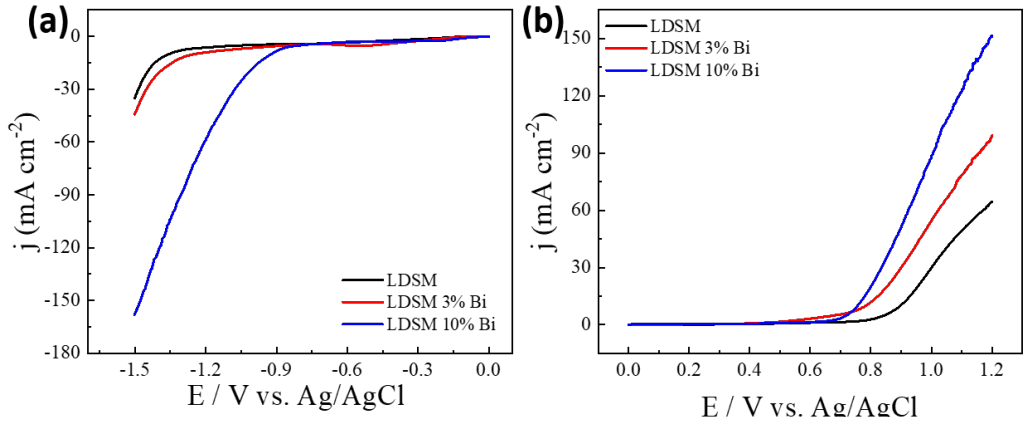

Figure 2: Current densities of LDSM (black), LDSM+3% Bi (red) and LDSM+10% Bi (blue) perovskites for (a) HER activity between 0 V and -1.5 V (vs. Ag/AgCl) and (a) OER activity between 0 V and 1.2 V (vs. Ag/AgCl) with a scan rate of 50 mV s^{-1} in 1 M KOH alkaline media at room temperature

Table 1: The summary of the electrochemical performance of LDSM, LDSM+3% Bi and LDSM+10% Bi manganite given with onset potential and specific current density at -1.4 and 1 V (vs. Ag/AgCl) for HER and OER, respectively

Sample	Onset Potential for HER (V)	Specific *j* for HER at -1.4 V (mA cm^{-2})	Onset Potential for OER (V)	Specific *j* for OER at 1 V (mA cm^{-2})
LDSM	-1.389	-13.3	0.853	29.8
LDSM+3% Bi	-1.352	-20.8	0.769	54.3
LDSM+10% Bi	-1.036	-121.8	0.758	88.3

The electrocatalytic performance of the as-synthesized catalysts as a function of Bi dope was also studied taking into account the Tafel slope (see Figure 3(a)). As seen in Table 2, corrosion potential is negative for 3% and 10% Bi-doped catalysts and this value became positive for undoped LDSM catalysts. We also considered the Tafel slope in cathodic region between -0.1 V and -0.3 V. The large Tafel slope indicates that the ORR mechanism is possible in the structure but at a slow rate. EIS data were also collected between 100 kHz and 0.01 Hz using AC signals of amplitude 10 mV peak to peak at open circuit potential in 1 M KOH solution and fitted with double layer capacitance method for LDSM (black), LDSM+3% Bi (red) and LDSM+10% Bi (blue) perovskites for which typical Nyquist plot is presented in Figure 3(b). The oxygen ion transfer and the surface kinetics occur at high frequency from LDSM sample to the electrolyte and at intermediate frequency, respectively. Here, a small alkali solution resistance, R_{sol}, was recorded between 5.1 Ω and 4.1 Ω [20]. The pore resistance, R_{po} which is ion-conducting paths developed in the catalysts, is reduced from very high resistance 19.3 kΩ to a desired value of 3.5 kΩ due to the substitution of 10% Bi in the structure. The increased C_c value indicates double-layer capacitance which is followed by charge-transfer reaction [21, 22].The effect of Bi doping resulted in oxygen vacancy so that increased adsorbed oxygen species in the structure. Similarly,

hydrogen evolution reaction is enhanced by Bi doping because water molecules are adsorbed by Bi sites. This can be related with reduced pore resistance in 10% Bi doped LDSM sample.

Table 2: Summary of Tafel and EIS curves. $E_{corr.}$ and β slope. The fit resistance and capacitance parameters of R_{sol}, R_{cor}, R_{po}, C_{cor} and C_c

Sample	$E_{corr.}$ (mV)	β (mV dec^{-1})	R_{sol} (Ω)	R_{cor} (kΩ)	R_{po} (kΩ)	C_{cor} (μF)	C_c (nF)
LDSM	39	261	5.1	3.9	19.3	2049	259
LDSM+3% Bi	-17	518	4.9	11.9	6.1	228	202
LDSM+10% Bi	-52	516	4.1	2.1	3.5	978	301

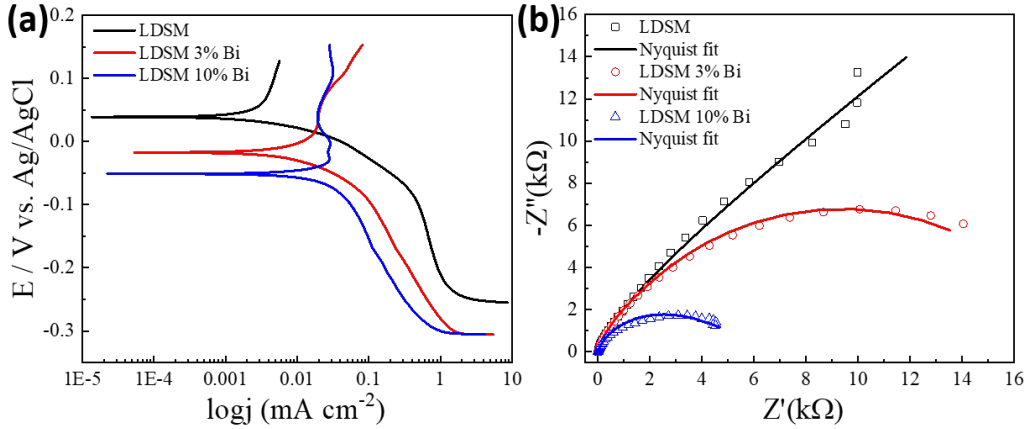

Figure 3: (a) Tafel plot and (b) EIS measurements of LDSM (black), LDSM+3% Bi (red) and LDSM+10% Bi (blue) perovskites in 1 M KOH at room temperature

4. Conclusions

In summary, we investigated the substitution of 10% Dy and 30% Sr into the A site and a small amount of Bi (x: 0, 0.03 and 0.1) added into the B site of $La_{0.60}Dy_{0.10}Sr_{0.30}Mn_{(1-x)}Bi_xO_3$ perovskites to understand the electrochemical properties for HER, OER and ORR processes. Undoped and 3% Bi doped LDSM samples exhibited poor HER activities, the effect of 10% Bi in the structure enhanced HER activities by lowering onset potential from -1.389 V to -1.036 V (vs. Ag/AgCl) and increasing specific current density at -1.4 V from -13.3 mA cm^{-2} to -121.8 mA cm^{-2}. Similarly, OER activity was also improved due to 10% Bi and onset potential and specific current density was found to be 0.758 V and 88.3 mA cm^{-2}, respectively. The large Tafel slopes indicate that the ORR mechanism is possible in the structure but at a slow rate. The substitution of 10% Bi in the structure resulted in a very high resistance of 19.3 kΩ and it reduced to a desired value of 3.5 kΩ due to ion conducting paths developed in the catalysts. So that La-based Bi-doped perovskites promise a low-cost and high-performance electrocatalytic materials candidate for regenerative fuel cells.

Acknowledgement

This work was supported by Cukurova University, Adana, Turkey, under Scientific Research Funding Grand No: FBA-2021-14197.

References

[1] Luo, D., Su, R., Zhang, W., Gong, Q., Zhu, R., *Minimizing non-radiative recombination losses in perovskite solar cells*, Nature Reviews Materials, 5(1), 44-60, 2020.

[2] Zhu, H., Zhang, P., Dai, S., *Recent Advances of Lanthanum-Based Perovskite Oxides for Catalysis*, ACS Catalysis, 5(11), 6370-6385, 2015.

[3] Tanaka, H., Misono, M., *Advances in designing perovskite catalysts*, Current Opinion in Solid State and Materials Science, 5(5), 381-387, 2001.

[4] Jiang, L.Q., Guo, J.K., Liu, H.B., Zhu, M., Zhou, X., Wu, P., Li, C.H., *Prediction of lattice constant in cubic perovskites*, Journal of Physics and Chemistry of Solids, 67(7), 1531-1536, 2006.

[5] Akça, G., Çetin, S., Ekicibil, A., *Composite* $xLa_{0.7}Ca_{0.2}Sr_{0.1}MnO_3/(1-x)La_{0.7}Te_{0.3}MnO_3$ *materials: magnetocaloric properties around room temperature*, Journal of Materials Science: Materials in Electronics, 31, 2020.

[6] Laouyenne, M.R., Baazaoui, M., Mahjoub, S., Cheikhrouhou-Koubaa, W., Oumezzine, M., *Enhanced magnetocaloric effect with the high tunability of bismuth in* $La_{0.8}Na_{0.2}Mn_{1-x}Bi_xO_3$ $(0 \leq x \leq 0.06)$ *perovskite manganites*, Journal of Alloys and Compounds, 720, 212-220, 2017.

[7] Gaur, A., Meenakshi, Nagpal, V., Bisht, P., Mahato, R.N., *Effect of Bi-doping on structural, magneto-caloric and magneto-resistive properties of* $La_{0.67-x}Bi_xCa_{0.33}MnO_3$ *perovskites*, Solid State Communications, 340, 114504, 2021.

[8] Khan, A.A., Hira, U., Sher, F., *Large relative cooling power of Bi-doped* $La_{0.8-x}Bi_xSr_{0.08}(Ca_{0.55}Ba_{0.45})_{0.12}MnO_3$ *(x=0.0, 0.1 and 0.3) perovskites: Magnetic and magnetocaloric properties*, Ceramics International, 43(9), 7351-7357, 2017.

[9] Przyslupski, P., Komissarov, I., Paszkowicz, W., Dluzewski, P., Minikayev, R., Sawicki, M., *Structure and magnetic characterization of* $La_{0.67}Sr_{0.33}MnO_3/YBa_2Cu_3O_7$ *superlattices*, Journal of Applied Physics, 95(5), 2906-2911, 2004.

[10] Qi, S., Zhang, W., Li, X., Wang, Q., Zhu, Z., Zhou, T., Wang, G., Xie, A., Luo, S., *Catalytic oxidation of toluene over B-site doped La-based perovskite* $LaNi_xB_{1-x}O_3$ *(B = Co, Cu) catalysts*, Environmental Progress Sustainable Energy, e13965, 2022.

[11] Kılıç Çetin, S., Akça, G., Kaya, D., Ayaş, A.O., Ekicibil, A., *Synthesis and characterization of bifunctional Ru doped La-based perovskites for magnetic refrigeration and energy storage systems*, International Journal of Hydrogen Energy, 47(97), 40999-41009, 2022.

[12] Barik, S.K., Mahendiran, R., *Effect of Bi Doping on Magnetoresistance in* $La_{0.7-x}Bi_xSr_{0.3}MnO_3$, Journal of Nanoscience and Nanotechnology, 11(3), 2603-2606, 2011.

[13] Dhahri, A., Dhahri, E., Hlil, E.K., *Large magnetocaloric effect in manganese perovskite* $La_{0.67-x}Bi_xBa_{0.33}MnO_3$ *near room temperature*, RSC advances, 9(10), 5530-5539, 2019.

[14] Kong, F.-D., Zhang, S., Yin, G.-P., Zhang, N., Wang, Z.-B., Du, C.-Y., *Preparation of* $Pt/Ir_x(IrO_2)_{10-x}$ *bifunctional oxygen catalyst for unitized regenerative fuel cell*, 210, 321-326, 2012.

[15] Du, K., Zhang, L., Shan, J., Guo, J., Mao, J., Yang, C.-C., Wang, C.-H., Hu, Z., Ling, T., *Interface engineering breaks both stability and activity limits of RuO_2 for sustainable water oxidation*, Nature Communications, 13(1), 5448, 2022.

[16] Patrakeev, M., Bahteeva, J., Mitberg, E., Leonidov, I., Kozhevnikov, V., Poeppelmeier, K., *Electron/hole and ion transport in $La_{1-x}Sr_xFeO_{3-\delta}$*, Journal of Solid State Chemistry, 172, 219-231, 2003.

[17] Silva, R.A., Soares, C.O., Afonso, R., Carvalho, M.D., Tavares, A.C., Jorge, M.E.M., Gomes, A., Pereira, M.I.d.S., Rangel, C.M., *Synthesis and electrocatalytic properties of $La_{0.8}Sr_{0.2}FeO_{3-\delta}$ perovskite oxide for oxygen reactions*, AIMS Materials Science, 4(4), 991-1009, 2017.

[18] Li, C., Baek, J.-B., *Recent Advances in Noble Metal (Pt, Ru, and Ir)-Based Electrocatalysts for Efficient Hydrogen Evolution Reaction*, ACS Omega, 5(1), 31-40, 2020.

[19] Alegre, C., Modica, E., Rodlert-Bacilieri, M., Mornaghini, F.C., Aricò, A.S., Baglio, V., *Enhanced durability of a cost-effective perovskite-carbon catalyst for the oxygen evolution and reduction reactions in alkaline environment*, International Journal of Hydrogen Energy, 42(46), 28063-28069, 2017.

[20] Co, A.C., Xia, S.J., Birss, V.I., *A Kinetic Study of the Oxygen Reduction Reaction at $LaSrMnO_3$-YSZ Composite Electrodes*, Journal of the Electrochemical Society, 152(3), A570, 2005.

[21] Jiang, S.P., Zhang, J.P., Foger, K., *Deposition of Chromium Species at Sr-Doped $LaMnO_3$ Electrodes in Solid Oxide Fuel Cells II. Effect on O_2 Reduction Reaction*, Journal of the Electrochemical Society, 147(9), 3195, 2000.

[22] Shafi, P.M., Bose, A.C., Vinu, A., *Electrochemical Material Processing via Continuous Charge-Discharge Cycling: Enhanced Performance upon Cycling for Porous $LaMnO_3$ Perovskite Supercapacitor Electrodes*, ChemElectroChem, 5(23), 3723-3730, 2018.

Adıyaman University Journal of Science
https://dergipark.org.tr/en/pub/adyujsci
DergiPark AKADEMİK
ISSN 2147-1630
e-ISSN 2146-586X

Investigation of Apoptotic Effect of Klotho Protein on Human Colorectal Cancer Cells via TRAIL Death Receptors

Sibel GÜNEŞ[1,2]*, Onur UYSAL[1,2], Merve Nur SOYKAN[1,2], Ayla Eker SARIBOYACI[1,2]

[1]*Eskisehir Osmangazi University, Cellular Therapy and Stem Cell Production Application and Research Centre, ESTEM, 26040, Eskisehir, Türkiye*

[2]*Eskisehir Osmangazi University, Institute of Health Sciences, Department of Stem Cell, 26040, Eskisehir, Türkiye*

gunesibel@gmail.com, ORCID: 0000-0003-0846-1170
ouysal1971@gmail.com, ORCID: 0000-0001-6800-5607
mervesykn@gmail.com, ORCID: 0000-0003-1231-9791
aylaekersariboyaci@yahoo.com, ORCID: 0000-0003-4536-9859

Received: 30.11.2022 **Accepted:** 23.12.2022 **Published:** 30.12.2022

Abstract

Klotho is a transmembrane protein whose deficiency has pleiotropic effects in a number of aging-related disease processes and various cancers. In some recent studies about klotho protein disorders, it has been shown that klotho is effective in various cancers including lung, liver, breast, kidney, and colon. TNF-related apoptosis-inducing ligand (TRAIL) a TNF family molecule, is a cytokine that stimulates apoptosis through death receptors in many cancer types and therefore attracts attention for tumor therapies in various preclinical models. Interaction with TRAIL death receptors create an apoptotic effect in cancer treatments by reducing the proliferation of cancer cells. In this study, it was aimed to investigate the effects of exogen klotho administration on cell viability and apoptosis on TRAIL death receptors (TRAIL1 and TRAILR2) in human healthy colon cells (CCD 841 CoN) and TRAIL-resistant human colorectal cancer cells (caco2). For this purpose, cells were treated with different concentrations

* Corresponding Author DOI: 10.37094/adyujsci.1212028

of klotho for 24 and 48 hours. To determine the cell viability, proliferation, and death receptors effects of klotho protein on cancer and healthy cells evaluations with WST-8 and real-time qRT-PCR analysis were performed. Our results showed that the increase in klotho protein concentration did not have a significant effect on cell viability in healthy colon cells, whereas it decreased cell viability and proliferation in apoptosis-resistant human colorectal cancer cells. Relative gene expression levels of TRAIL1 and TRAILR2 death receptors increased with klotho applied to the apoptosis-resistant colorectal cancer cell line Caco-2. Therefore, targeting TRAIL death receptors by klotho protein can be considered as a potential therapeutic approach for colorectal cancer therapy.

Keywords: Klotho; Cell viability; Colorectal cancer; Antitumor effect; TRAIL; Apoptosis.

Klotho Proteinin Insan Kolorektal Kanser Hücreleri Üzerindeki Apoptotik Etkisinin TRAIL Ölüm Reseptörleri Üzerinden İncelenmesi

Öz

Klotho, eksikliği bir dizi yaşlanma ile ilişkili hastalık sürecinde ve çeşitli kanserlerde pleiotropik etkilere sahip olan bir transmembran proteindir. Klotho protein bozuklukları ile ilgili son zamanlarda yapılan bazı araştırmalarda klothonun akciğer, karaciğer, meme, böbrek ve kolon dahil çeşitli kanserlerde etkili olduğu gösterilmiştir. Tümör nekroz faktör ilişkili apoptoz indükleyici ligand (TRAIL), birçok kanser türünde ölüm reseptörleri aracılığıyla apoptozu uyaran bir sitokindir ve bu nedenle çeşitli preklinik modellerde tümör terapileri için dikkat çekmektedir. TRAIL ölüm reseptörleri ile etkileşim, kanser hücrelerinin çoğalmasını azaltarak kanser tedavilerinde apoptotik bir etki yaratır. Bu çalışmada, eksojen klotho uygulamasının insan sağlıklı kolon (CCD 841 CoN) ve TRAIL dirençli insan kolorektal kanser hücreleri (Caco-2) üzerindeki hücre canlılığı ve apoptoz üzerine etkilerinin TRAIL ölüm reseptörleri (TRAIL1 ve TRAILR2) aracılığı ile araştırılması amaçlanmıştır. Bu amaçla hücreler, 24 ve 48 saat boyunca farklı konsantrasyonlarda klotho ile muamele edildi. Klotho proteinin kanser ve sağlıklı hücreler üzerindeki hücre canlılığı, proliferasyonu ve ölüm reseptörlerinin etkilerini belirlemek için WST-8 ve real-time qRT-PCR analizi ile değerlendirmeler yapıldı. Sonuçlarımız, klotho protein konsantrasyonundaki artışın sağlıklı kolon hücrelerinde hücre canlılığı üzerinde önemli bir etkiye sahip olmadığını, apoptoza dirençli insan kolorektal kanser hücrelerinde ise hücre canlılığını ve proliferasyonunu azalttığını gösterdi. Apoptoza dirençli kolorektal kanser hücre dizisi Caco-2'ye uygulanan klotho ile TRAIL1 ve TRAILR2 ölüm reseptörlerinin göreceli gen ekspresyonu arttı. Sonuç olarak, TRAIL ölüm reseptörlerinin klotho

proteini ile hedeflenmesi kolorektal kanser tedavisi için potansiyel bir terapötik yaklaşım olarak kabul edilebilir.

Anahtar Kelimeler: Klotho; Hücre canlılığı; Kolorektal kanser; Antitümör etki; TRAIL; Apoptoz.

1. Introduction

Klotho is a transmembrane beta-glucuronidase protein known for its anti-aging, anti-inflammatory, and antitumor properties [1, 2, 3]. Klotho has been shown to reduce the cell viability of tumor cells and induce apoptosis [4, 5]. Klotho protein deficiency plays a role in acute and chronic kidney disease [6], cancers [7], and hypertension [8]. Klotho is expressed in the renal proximal tubule, parathyroid gland, ovary, testis, and placenta [9, 10, 11, 12, 13]. In some studies, it has been reported that the klotho protein level is low in many cancer types, including colon cancer, compared to normal tissues [14, 15, 16, 17]. Studies showing the relationship of the klotho protein, which has known antitumor activity in colorectal cancer, with the apoptosis-inducing ligand TRAIL signaling pathway and death receptors are limited [18,19].

TRAIL, also known as Apo2L, stands out with its ability to activate both pathways of apoptosis by binding to death receptors (TRAILR1 and TRAILR2) on the cell surface. TRAILR1 and TRAILR2 are types I transmembrane proteins that recruit apoptosis signaling molecules to induce cell death [20]. TRAILR1 and TRAILR2 located in the cell membrane receive cellular death signals produced by TRAIL and initiate programmed cell death. These receptors act as regulators of the TRAIL death pathway [21]. TRAIL death receptors (TRAILR1 and TRAILR2) are regulated by the p53 transcription factor. TRAILR1 and TRAILR2 receptors not only trigger apoptosis in TRAIL-sensitive cells but also activate survival pathways in tumor cells that resist induction of cell death when exposed to TRAIL [22]. In a study conducted in three different colon cancers (SW948, Caco-2, and Colo320), the TRAIL sensitivities of the cells were analyzed. It was determined that there are more TRAILR2 receptors than TRAILR1 in colon cancer cell lines where the TRAIL signaling pathway is effective. Similar levels of TRAILR1 and TRAILR2 receptors were found to be expressed in resistant colon cancer cell lines [23, 24, 25].

Klotho protein plays an important role in relation to anticancer treatments. There are limited studies of recombinant klotho protein causing cytotoxic effects on human colorectal adenocarcinoma or healthy colon cells. We aimed to investigate the anticancer effects of klotho protein against the human colorectal adenocarcinoma cells and the selectivity using healthy colon cells by adding exogen klotho protein to the medium of Caco-2 cancer and the CCD 841

CoN healthy cell lines and analyzing its effect on cell viability and apoptosis process. Additionally, we aimed to evaluate the effects of klotho protein as a potential antiproliferative and an apoptotic inducer factor on TRAIL death receptors (TRAILR1 and TRAILR2).

2. Materials and Methods

2.1. Cell culture and morphological analysis

Colorectal cancer (ATCC® HTB-37) and healthy colon cells (ATCC® CRL-1790™) were purchased commercially (ATCC, Washington DC, USA). The cells were cultured in Dulbecco's Modified Eagle's Medium (DMEM ; Biochrom, Holliston, MA, USA) and incubated at 37°C in a humidified atmosphere containing 5%CO_2 and 5%O_2. The medium was changed every other 3 days over a 5-6-day period. For each passage, the cells were plated similarly and grown to a confluency of 70%.

2.2. WST-8 cell viability assay

Human recombinant klotho protein was purchased from Sigma (Sigma-Aldrich, Darmstadt, Germany, catalog no: SRP3102-20UG). The effect of klotho protein on the viability of Caco-2 and CCD 841 CoN cells was tested with (WST)-8 (AAT Bioquest, California, USA) [26]. Recombinant klotho protein was treated in a doses range 0.04, 0.15 and 0.3 μg/ml [2, 27, 28].

After 24 and 48h, 10 μl/well of WST-8 solution was added, subsequently, cells were incubated at 37°C in a humidified atmosphere containing 5%CO_2 for 3 days. Then the absorbance values were measured at 460 nm in a microplate reader with a monochromator system (BIOTEK ELx808IU, Vermont, USA). Next, the viability of the klotho-treated cells was calculated, assuming the viability of untreated cells to be 100%. The following formula was used to calculate the percent viability:

[(OD klotho-treated cells-OD blank)/(OD untreated cells-OD blank)] × 100.

The OD refers to the optical density.

2.3. Analysis of death receptors by real-time qRT-PCR

Real-time qRT-PCR analysis was performed in order to determine the gene expression changes of TRAIL death receptors (TRAILR1 and TRAILR2) in CCD 841 CoN and Caco-2 cells. Total RNA was isolated using the extraction total RNA kit (Blirt S.A., Gdańsk, Poland) in accordance with the manufacturer's protocol. Complementary DNA (cDNA) was obtained from

the obtained mRNAs by using a cDNA synthesis kit (Transcriptome RNA kit, Blirt S.A., Gdansk, Poland). The obtained cDNA was stored at -20°C.

After obtaining cDNA, gene amplification in real-time qRT-PCR device (One-Step Thermo Scientific™ Carlsbad, USA) using probe-primers suitable for target genes (Table 1) and SYBR Green RT-PCR kit (Blirt S.A., Gdansk, Poland). The target genes were amplified and analyzed.

Table 1: Sense and antisense primers for qRT-PCR analysis

Gene	Primer (5' – 3')	
	Forward	Reverse
Klotho (KL)	ACT CCC CCA GTC AGG TGG CGG TA	TGG GCC CGG GAA ACC ATT GCT GTC
TRAILR1 (TNFRSF10)	CTG AGC AAC GCA GAC TCG CTG TCC AC	TCC AAG GAC ACG GCA GAG CCT GTG CCA T
TRAILR2 (TNFRSF10B)	CAC CAC GAC CAG AAA CAC AG	AAT CAC CGA CCT TGA CCA TC
GAPDH	CAC CCT GTT GCT GTA GCC ATA TTC	GAC ATC AAG AAG GTG GTG AAG CAG

2.4. Statistical Analysis

Statistical analyses were performed using SPSS software 20.0. Categorical and continuous variables were displayed as means ± standard deviation (SD) and percentages, respectively. $p<0.05$ were considered to be statistically significant.

3. Results

3.1. Morphological analysis of cells

During the culture period, CCD 841 CoN and Caco-2 cells were examined and photographed daily by phase-contrast microscopy (Fig. 1).

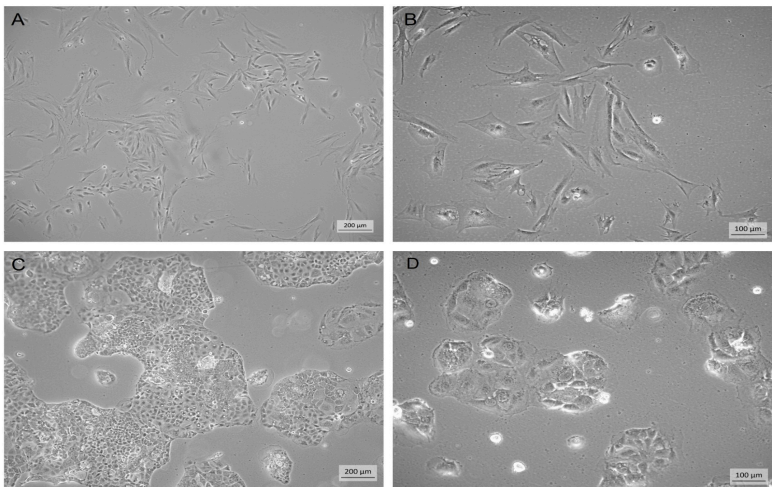

Figure 1: Phase-contrast microscopic views of healthy colon and colorectal cancer cells in early and late passages in culture (A-D) (Scale bars: A-C 200 µm; B-D 100 µm)

In microscopic examinations, CCD 841 CoN cells were attached to culture flasks as clusters, and most cells displayed a fibroblast-like, spindle-shaped morphology during the days of incubation. These cells began to proliferate in approximately 4–5 days and gradually grew as in diffuse monolayer morphology (Figure 1A and B). Caco-2 cells attached to culture flasks sparsely, and most cells displayed an epithelial-like, polygonal-shaped morphology during the days of incubation. These cells began to proliferate in approximately 6–7 days and gradually grew as non-homogenized and monolayer islets to form wide and big colonies (Figure 1C and D). Throughout 15 passages, no changes in their morphology, growth patterns, or immunophenotype were observed.

3.2. Determination of cell viability with WST-8

As a result of the doses of exogen klotho protein treated to healthy colon cells (CCD841 CoN) for 24 hours, cell viability was detected in the cells at the rates of 95%, 97% and 88%, respectively (p>0.05). At the doses of 0.04 µg/mL, 0.15 µg/mL, and 0.3 µg/mL klotho applied to healthy colon cells for 48 hours, the viability rates of the cells were 89%, 105%, and 89%, respectively (p>0.05) (Table 2, Fig. 2).

Table 2: Viability values of CCD 841 CoN cells (%)

	Cell viability (%)			
	24 hours		48 hours	
Klotho (µg/mL)	mean±SD	*p value*	mean±SD	*p value*
0.04 µg/mL	95,3±1,8	p>0.05	89,7±1,9	p>0.05
0.15 µg/mL	97,0±2,4	p>0.05	105,2±3,7	p>0.05
0.3 µg/mL	88,8±0,5	p>0.05	89,8±2,6	p>0.05

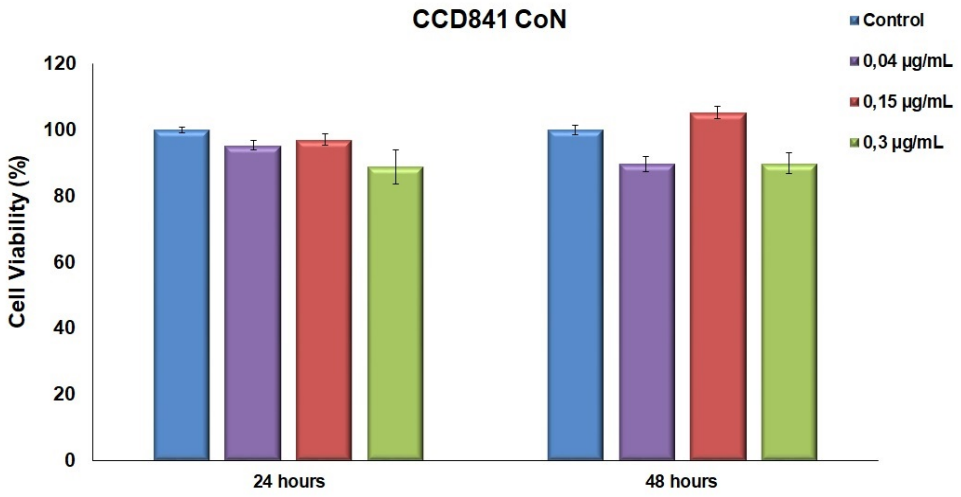

Figure 2: Detection of the effect of klotho on CCD841 CoN cells by WST-8 cell viability assay (n=3)

After 24-hour application of different doses of recombinant klotho protein to colorectal cancer cell line (Caco-2), the viability values of the cells were 81%, 68%, and 60%, respectively (p<0.001). When klotho was applied to Caco-2 cells at doses of 0.04 µg/mL, 0.15 µg/mL, and 0.3 µg/mL for 48 hours, the cells were viable at 92%, 83%, and 75%, respectively (p<0.001) (Table 3, Fig. 3).

Table 3: Viability values of Caco-2 cells (%)

Klotho (µg/mL)	Cell viability (%) 24 hours mean±SD	*p value*	48 hours mean±SD	*p value*
0.04 µg/mL	81,7±1,6	***p<0.001	92,6±1,9	p>0.05
0.15 µg/mL	68,8±1,4	***p<0.001	83,8±2,2	***p<0.001
0.3 µg/mL	60,1±0,9	***p<0.001	75,2±1,4	***p<0.001

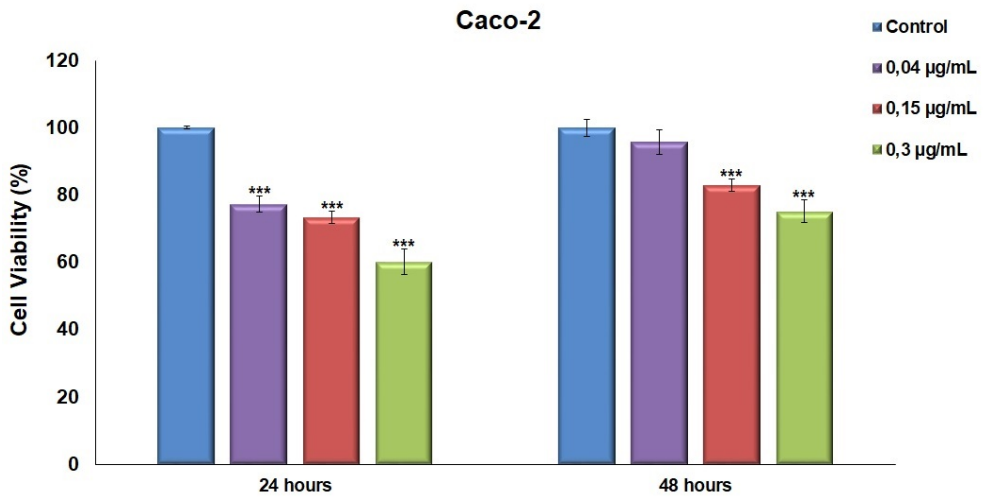

Figure 3: The results of the viability effect of recombinant klotho protein on Caco-2 cells by WST-8 analysis (n=3, ***p<0.001)

3.3. Real-Time qRT-PCR analysis of TRAIL receptors

Real-time qRT-PCR analysis was performed in order to determine the gene expression changes of TRAIL death receptors (TRAILR1 and TRAILR2) in cells. When CCD841 CoN cells were treated with recombinant klotho for 24 hours, there were changes in TRAILR1 (44.91 fold) and TRAILR2 (30.49 fold) gene expressions compared to the control group (CCD841 CoN cells not treated with klotho) (p<0.001). When CCD841 CoN cells were treated with exogen klotho for 48 hours, there was a change in TRAILR1 (34.45-fold) and TRAILR2 (32.51-fold) gene expressions compared to the control group (p<0.001) (Fig. 4 and Fig.5).

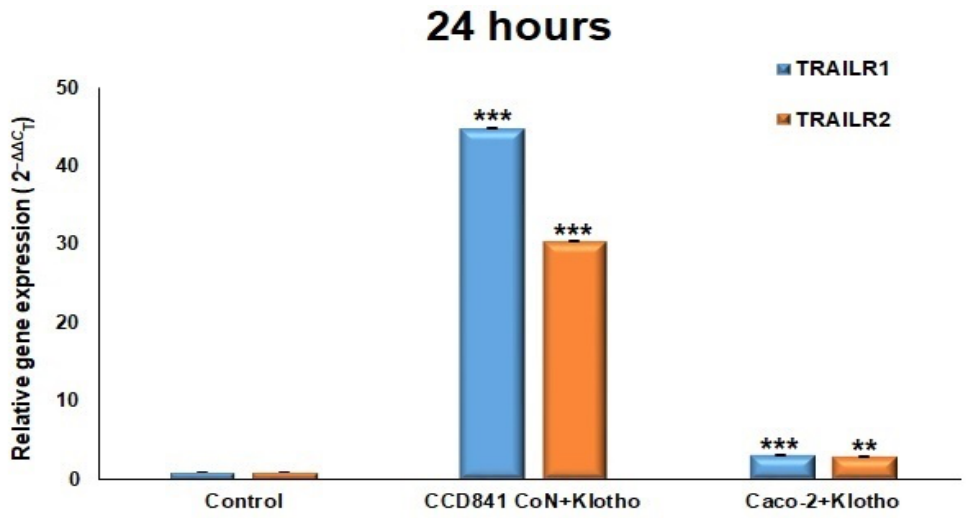

Figure 4: The effect of klotho protein (0.3 µg/mL) applied to healthy and colorectal cancer cells for 24 hours on TRAILR1 and TRAILR2 gene expression changes (n=3, **p<0.01, ***p<0.001)

When 0.3 µg/mL klotho was treated to colorectal cancer cells (Caco-2) for 24 hours, there was a change in TRAILR1 (3.22 fold) and TRAILR2 (3.01 fold) gene expressions compared to the control group (Caco-2 cells without klotho protein treatment) (p<0.01). When Caco-2 colorectal cancer cells were treated with klotho for 48 hours, there was a change in TRAILR1 (0.93 fold) and TRAILR2 (0.74 fold) gene expressions compared to the control group (p<0.01) (Fig. 4 and Fig. 5).

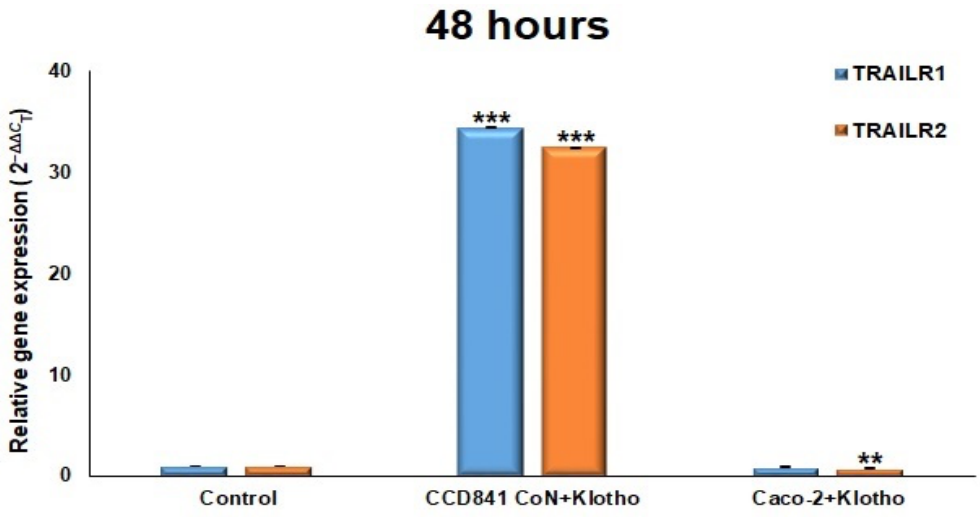

Figure 5: The gene expression changes of TRAILR1 and TRAILR2 gene expression levels after treatment of klotho protein on healthy colon and colorectal cancer cells for 48 hours (n=3, **p<0.01, ***p<0.001)

4. Discussion

Klotho protein has many well-known functions such as anti-aging, anti-inflammatory, and antitumor. Alterations in klotho gene expression affect cellular events such as cell viability and programmed cell death. While klotho protein function contributes to apoptotic cell death in normal cells, it acts as an inducer of apoptosis in cancer cells in combination with multiple signaling pathways [17, 29, 33]. Studies have shown that klotho deficiency may be a marker that can be used in the early diagnosis of colorectal cancer [5, 16]. The aim of this study was to evaluate the apoptotic effects of recombinant klotho in chemotherapeutic-resistant human adenocarcinoma colorectal cancer cell line (Caco-2) and healthy colon cells (CCD841 CoN). It has been shown that in vitro application of recombinant klotho in cancer cells reduces cell viability by stopping the cell cycle and leads to cell death [30]. Although the role of klotho in these mechanisms is not clear yet, studies have shown that it has a tumor-suppressive property [5]. It has been shown that klotho significantly suppresses cell proliferation and invasion in hepatocellular carcinoma cells and induces apoptosis of cells or autophagy [31]. Klotho protein levels have been found to be decreased in colorectal cancer [33, 34]. In studies with various colorectal cancer cells, it was found that klotho significantly decreased the viability of cells and induced cell death [35].

In our study, we found that the use of klotho protein in cells has a dose-dependent cytotoxic effect and the most effective dose in apoptosis was 0.3 µg/ml. As a result of klotho treatment to healthy cells for 24 and 48 hours, the viability values of the cells at all doses decreased compared to the control group, although it was not statistically significant ($p>0.05$). It was determined that klotho significantly reduced cell viability and stimulated apoptosis in cancer cells treated with klotho protein ($p<0.001$). These results indicated that klotho induced apoptosis in resistant Caco-2 cells and contributed to the normal apoptotic process in healthy colon cells.

The relationship between TRAILR1 and TRAILR2 death receptors is crucial in the activation of the TRAIL signaling pathway for the death of colorectal cancer cells. In cells, TRAILR1 and TRAILR2 death receptors are initiators of TRAIL-induced programmed cell death [36]. In studies conducted with TRAIL sensitivity in colon cancer cells, it was found that TRAIL-sensitive cell line SW948 expressed more TRAILR2 than TRAILR1 on the cell membrane, while two relatively resistant cell lines, Caco-2 and Colo320, expressed similar levels of TRAILR1 and TRAILR2 [37]. It has been shown that the majority of colorectal cancer cells are resistant to TRAIL. Therefore, Caco-2 cells, which are highly resistant to TRAIL-induced cell death, were selected in this study. In a study on the elimination of cancer cells of

TRAIL death receptors (TRAILR1 and TRAILR2), TRAILR2 was shown to be more effective for caspase activation than TRAILR1 [38]. In our study, we found that the relative gene expression levels of TRAILR2 in colorectal cancer cells were significantly increased at 24 and 48 hours after klotho administration. This result can be interpreted as that klotho activates the cell death receptor TRAILR2 and thus can cause apoptosis of cancer cells by causing caspase activation.

It has been reported that some clinically used drugs make cancer cells sensitive to TRAIL by increasing the protein level of TRAILR1 and TRAILR2 [39]. Previous studies have shown that DAT1, one of the diaminothiazole drugs known to have antimitotic effects on colon cancer cells (HCT-116), activates the MEK/ERK signaling pathway, increasing the expression of the TRAILR2 receptor independent of p53. In another study, it was found that Azithromycin, which is widely used in the clinic, increases the expression of TRAILR1 and TRAILR2 in HCT116 and SW480 colon cancer cells and sensitizes cancer cells to TRAIL [40]. In another study, the chemotherapeutic drug gemcitabine was shown to increase the expression of death receptors in HCT116 [41].

5. Conclusion

In our findings, it was observed that klotho protein decreased cell viability in cancer cells and had a cytotoxic effect by inducing apoptotic cell death via receptors. The fact that klotho protein increases the numbers of TRAILR1 and TRAILR2 death receptors can be interpreted as klotho may sensitize colorectal cancer cells to TRAIL. In conclusion, we think that exogen klotho protein can be used as a dose dependent adjuvant therapy in the treatment of human colorectal adenocarcinoma. In addition, we think that extrinsic and intrinsic apoptotic caspases and proapoptotic protein levels should be investigated in order to demonstrate the apoptotic effects of exogenous klotho on death receptors.

Funding

This study was supported by grants Eskisehir Osmangazi University, Scientific Research Projects (ESOGU-BAP, Code: 202046A113).

Author Contributions

Sibel Gunes is the main author in this study and contributed to the study conception and design. Material preparation, data collection and analysis were performed by Sibel Gunes and Merve Nur Soykan. The first draft of the manuscript was written by Onur Uysal and Ayla Eker

Sariboyaci. All authors commented on previous versions of the manuscript. Corresponding author read and approved the final manuscript.

Ethical statement

This study is not approval required for the ethics committee.

Declaration of interest:

The authors report no conflicts of interest. The authors alone are responsible for the content and writing of the paper.

References

[1] Zhou, X., Wang X., *Klotho: a novel biomarker for cancer*. J Cancer Res Clin Oncol. 2015;141(6):961-9. doi: 10.1007/s00432-014-1788-y.

[2] Tang, X., Wang, Y., Fan, Z., Ji, G., Wang, M., Lin, J., Huang, S., Meltzer, SJ., *Klotho: a tumor suppressor and modulator of the Wnt/β-catenin pathway in human hepatocellular carcinoma*. Lab Invest. 2016;96(2):197-205. doi: 10.1038/labinvest.2015.86.

[3] Shu, G., Xie, B., Ren, F., Liu, DC., Zhou, J., Li, Q., Chen, J., Yuan, L., Zhou, J., *Restoration of klotho expression induces apoptosis and autophagy in hepatocellular carcinoma cells*. Cell Oncol (Dordr). 2013;36(2):121-9. doi: 10.1007/s13402-012-0118-0.

[4] Chen, B., Wang, X., Zhao, W., Wu, J., *Klotho inhibits growth and promotes apoptosis in human lung cancer cell line A549*. J Exp Clin Cancer Res. 2010;29(1):99. doi: 10.1186/1756-9966-29-99.

[5] Li, XX., Huang, LY., Peng, JJ., Liang, L., Shi, DB., Zheng, HT., Cai, SJ., *Klotho suppresses growth and invasion of colon cancer cells through inhibition of IGF1R-mediated PI3K/AKT pathway*. Int J Oncol. 2014;45(2):611-8. doi: 10.3892/ijo.2014.2430.

[6] Hu, MC., Shi, M., Zhang, J., Quiñones, H., Griffith, C., Kuro-o, M., Moe, OW., *Klotho deficiency causes vascular calcification in chronic kidney disease*. J Am Soc Nephrol. 2011;22(1):124-36. doi: 10.1681/ASN.2009121311.

[7] Gunes, S., Soykan, MN., Sariboyaci, AE., Uysal, O., Sevimli, TS., *Enhancement of Apo2L/TRAIL signaling pathway receptors by the activation of Klotho gene with CRISPR/Cas9 in Caco-2 colon cancer cells*. Med Oncol. 2021;38(12):146. doi: 10.1007/s12032-021-01595-7.

[8] Zhou, X., Chen, K., Lei, H., Sun, Z., *Klotho gene deficiency causes salt-sensitive hypertension via monocyte chemotactic protein-1/CC chemokine receptor 2-mediated inflammation*. J Am Soc Nephrol. 2015;26(1):121-32. doi: 10.1681/ASN.2013101033.

[9] Matsumura, Y., Aizawa, H., Shiraki-Iida, T., Nagai, R., Kuro-o, M., Nabeshima, Y., *Identification of the human klotho gene and its two transcripts encoding membrane and secreted klotho protein*. Biochem Biophys Res Commun. 1998;242(3):626-30. doi: 10.1006/bbrc.1997.8019.

[10] Shiraki-Iida, T., Aizawa, H., Matsumura, Y., Sekine, S., Iida, A., Anazawa, H., Nagai, R., Kuro-o, M., Nabeshima, Y., *Structure of the mouse klotho gene and its two*

transcripts encoding membrane and secreted protein. FEBS Lett. 1998;424(1-2):6-10. doi: 10.1016/s0014-5793(98)00127-6.

[11] Kuro-o, M., Matsumura, Y., Aizawa, H., Kawaguchi, H., Suga, T., Utsugi, T., Ohyama, Y., Kurabayashi, M., Kaname, T., Kume, E., Iwasaki, H., Iida, A., Shiraki-Iida, T., Nishikawa, S., Nagai, R., Nabeshima, YI., *Mutation of the mouse klotho gene leads to a syndrome resembling ageing*. Nature. 1997;6;390(6655):45-51. doi: 10.1038/36285.

[12] Imura, A., Tsuji, Y., Murata, M., Maeda, R., Kubota, K., Iwano, A., Obuse, C., Togashi, K., Tominaga, M., Kita, N., Tomiyama, K., Iijima, J., Nabeshima, Y., Fujioka, M., Asato, R., Tanaka, S., Kojima, K., Ito, J., Nozaki, K., Hashimoto., N, Ito., T, Nishio., T, Uchiyama., T, Fujimori., T, Nabeshima., Y., *alpha-Klotho as a regulator of calcium homeostasis*. Science. 2007; 316(5831):1615-8. doi: 10.1126/science.1135901.

[13] Hu, MC., Shi, M., Zhang, J., Pastor, J., Nakatani, T., Lanske, B., Razzaque, MS., Rosenblatt, KP., Baum, MG., Kuro-o, M., Moe, OW., *Klotho: a novel phosphaturic substance acting as an autocrine enzyme in the renal proximal tubule*. FASEB J. 2010;24(9):3438-50. doi: 10.1096/fj.10-154765.

[14] Urakawa, I, Yamazaki, Y, Shimada, T, Iijima, K, Hasegawa, H, Okawa, K, Fujita, T, Fukumoto, S, Yamashita, T., *Klotho converts canonical FGF receptor into a specific receptor for FGF23*. Nature. 2006;444(7120):770-4. doi: 10.1038/nature05315.

[15] Ben-Dov, IZ., Galitzer, H., Lavi-Moshayoff, V., Goetz, R., Kuro-o, M., Mohammadi, M., Sirkis, R., Naveh-Many, T., Silver J., *The parathyroid is a target organ for FGF23 in rats*. J Clin Invest. 2007;117(12):4003-8. doi: 10.1172/JCI32409.

[16] Ritter, CS., Zhang, S., Delmez, J., Finch, JL., Slatopolsky, E., *Differential expression and regulation of Klotho by paricalcitol in the kidney, parathyroid, and aorta of uremic rats*. Kidney Int. 2015;87(6):1141-52. doi: 10.1038/ki.2015.22.

[17] Pan, J., Zhong, J., Gan, LH., Chen, SJ., Jin, HC., Wang, X., Wang, LJ., *Klotho, an anti-senescence related gene, is frequently inactivated through promoter hypermethylation in colorectal cancer*. Tumour Biol. 2011;32(4):729-35. doi: 10.1007/s13277-011-0174-5.

[18] Ligumsky, H., Rubinek, T., Merenbakh-Lamin, K., Yeheskel, A., Sertchook, R., Shahmoon, S., Aviel-Ronen, S., Wolf I., *Tumor Suppressor Activity of Klotho in Breast Cancer Is Revealed by Structure-Function Analysis*. Mol Cancer Res. 2015;13(10):1398-407. doi: 10.1158/1541-7786.MCR-15-0141.

[19] Refaat, A., Abd-Rabou, A., Reda, A., *TRAIL combinations: The new 'trail' for cancer therapy (Review)*. Oncol Lett. 2014;7(5):1327-1332. doi: 10.3892/ol.2014.1922.

[20] Corazza, N., Kassahn, D., Jakob, S., Badmann, A., Brunner, T., *TRAIL-induced apoptosis: between tumor therapy and immunopathology*. Ann N Y Acad Sci. 2009;1171:50-8. doi: 10.1111/j.1749-6632.2009.04905.x.

[21] Ma, L., Wei, HL., Wang, KJ., Meng, XY., Ni, SQ., Zhou, C., Li, Y., Yu, R., Ma, Q., *Rhein promotes TRAIL-induced apoptosis in bladder cancer cells by up-regulating DR5 expression*. Aging (Albany NY). 2022;14(16):6642-6655. doi: 10.18632/aging.204236.

[22] R, Mishra DP., *Trailing TRAIL Resistance: Novel Targets for TRAIL Sensitization in Cancer Cells*. Front Oncol. 2015;5:69. doi: 10.3389/fonc.2015.00069.

[23] Yildiz, Y., Yaylim-Eraltan, I., Arikan, S., Ergen, H.A., Küçücük, S., Isbir, T., *Is there any correlation between TNF-related apoptosis-inducing ligand (TRAIL) genetic variants and breast cancer?* Arch Med Sci. 2010;6(6):932-6. doi: 10.5114/aoms.2010.19304.

[24] van Geelen, CM., Pennarun, B., Le, PT., de Vries, EG., de Jong, S., *Modulation of TRAIL resistance in colon carcinoma cells: different contributions of DR4 and DR5*. BMC Cancer. 2011;11:39. doi: 10.1186/1471-2407-11-39.

[25] Li, X.B., Deng, Y.G., Hu, J.P., Wang, Z., Xie, R.Z., Luo, H., Hu, X.Y., *Resveratrol overcomes TRAIL resistance in human colon cancer cells*. Bangladesh Journal of Pharmacology, 2015;10(3), 568-576. doi: 10.3329/bjp.v10i3.21208.

[26] Stoddart, MJ., *WST-8 analysis of cell viability during osteogenesis of human mesenchymal stem cells*. Methods Mol Biol. 2011;740:21-5. doi: 10.1007/978-1-61779-108-6_4.

[27] Sun, H., Gao, Y., Lu, K., Zhao, G., Li, X., Li, Z., Chang, H., *Overexpression of Klotho suppresses liver cancer progression and induces cell apoptosis by negatively regulating wnt/β-catenin signaling pathway*. World J Surg Oncol. 2015 Oct 24;13:307. doi: 10.1186/s12957-015-0717-0. PMID: 26499380; PMCID: PMC4619481.

[28] Chen, C.D., Li, H., Liang, J., Hixson, K., Zeldich, E., Abraham, C.R., *The anti-aging and tumor suppressor protein Klotho enhances differentiation of a human oligodendrocytic hybrid cell line*. J Mol Neurosci. 2015 Jan;55(1):76-90. doi: 10.1007/s12031-014-0336-1. Epub 2014 Jun 8. PMID: 24907942; PMCID: PMC5154549.

[29] Sariboyaci, A.E, Uysal, O., Soykan, M.N., Gunes, S. ,*The potential therapeutic effect of klotho on cell viability in human colorectal adenocarcinoma HT-29 cells*. Med Oncol. 2022 Sep 7;39(12):191. doi: 10.1007/s12032-022-01793-x. PMID: 36071274.

[30] Rubinek, T., Wolf, I. (2015). *Klotho Tumor Suppressor*. In: Schwab, M. (eds) Encyclopedia of Cancer. Springer, Berlin, Heidelberg. https://doi.org/10.1007/978-3-642-27841-9_7219-1

[31] Chen, CD., Li, H., Liang, J., Hixson, K., Zeldich, E., Abraham, C.R., *The anti-aging and tumor suppressor protein Klotho enhances differentiation of a human oligodendrocytic hybrid cell line*. J Mol Neurosci. 2015;55(1):76-90. doi: 10.1007/s12031-014-0336-1.

[32] Sun, H., Gao, Y., Lu, K., Zhao, G., Li, X., Li, Z., Chang, H., *Overexpression of Klotho suppresses liver cancer progression and induces cell apoptosis by negatively regulating wnt/β-catenin signaling pathway*. World J Surg Oncol. 2015;13:307. doi: 10.1186/s12957-015-0717-0.

[33] Zhou, X., Fang, X., Jiang, Y., Geng, L., Li, X., Li, Y., Lu, K., Li, P., Lv, X., Wang, X., *Klotho, an anti-aging gene, acts as a tumor suppressor and inhibitor of IGF-1R signaling in diffuse large B cell lymphoma*. J Hematol Oncol. 2017;10(1):37. doi: 10.1186/s13045-017-0391-5.

[34] Xie, B., Zhou, J., Yuan, L., Ren, F., Liu, DC., Li, Q., Shu, G., *Epigenetic silencing of Klotho expression correlates with poor prognosis of human hepatocellular carcinoma*. Hum Pathol. 2013;44(5):795-801. doi: 10.1016/j.humpath.2012.07.023.

[35] Arbel Rubinstein, T., Shahmoon, S., Zigmond, E., Etan, T., Merenbakh-Lamin, K., Pasmanik-Chor, M., Har-Zahav, G., Barshack, I., Vainer, GW., Skalka, N., Rosin-Arbesfeld, R.,

Varol, C., Rubinek, T., Wolf, I., *Klotho suppresses colorectal cancer through modulation of the unfolded protein response*. Oncogene. 2019;38(6):794-807. doi: 10.1038/s41388-018-0489-4.

[36] Zhang, Z., Li, Z., Wu, X., Zhang, CF., Calway, T., He, TC., Du, W., Chen, J., Wang, CZ., Yuan, CS., T*RAIL pathway is associated with inhibition of colon cancer by protopanaxadiol*. J Pharmacol Sci. 2015;127(1):83-91. doi: 10.1016/j.jphs.2014.11.003.

[37] Zhang, B., Liu, B., Chen, D., Setroikromo, R., Haisma, HJ., Quax, WJ., *Histone Deacetylase Inhibitors Sensitize TRAIL-Induced Apoptosis in Colon Cancer Cells*. Cancers (Basel). 2019;11(5):645. doi: 10.3390/cancers11050645.

[38] Nahacka, Z., Svadlenka, J., Peterka, M., Ksandrova, M., Benesova, S., Neuzil, J., Andera, L., *TRAIL induces apoptosis but not necroptosis in colorectal and pancreatic cancer cells preferentially via the TRAIL-R2/DR5 receptor*. Biochim Biophys Acta Mol Cell Res. 2018;1865(3):522-531. doi: 10.1016/j.bbamcr.2017.12.006.

[39] Thamkachy, R., Kumar, R., Rajasekharan, K.N., Sengupta, S., *ERK mediated upregulation of death receptor 5 overcomes the lack of p53 functionality in the diaminothiazole DAT1 induced apoptosis in colon cancer models: efficiency of DAT1 in Ras-Raf mutated cells*. Mol Cancer. 2016;15:22. doi: 10.1186/s12943-016-0505-7.

[40] Qiao, X., Wang, X., Shang, Y., Li, Y., Chen, S.Z., *Azithromycin enhances anticancer activity of TRAIL by inhibiting autophagy and up-regulating the protein levels of DR4/5 in colon cancer cells in vitro and in vivo*. Cancer Commun (Lond). 2018;38(1):43. doi: 10.1186/s40880-018-0309-9.

[41] Gravett, A.M., Dalgleish, A.G., Copier, J., *In vitro culture with gemcitabine augments death receptor and NKG2D ligand expression on tumour cells*. Sci Rep. 2019;9(1):1544. doi: 10.1038/s41598-018-38190.